

NORTHWESTERN UNIVERSITY

Electronic Coupling and Morphology in Organic - Two Dimensional Heterostructures

A DISSERTATION

SUBMITTED TO THE GRADUATE SCHOOL  
IN PARTIAL FULFILLMENT OF THE REQUIREMENTS

for the degree

DOCTOR OF PHILOSOPHY

Field of Chemistry

By

Samuel Amsterdam

EVANSTON, ILLINOIS

June 2021

## Abstract

Mixed-dimensional heterojunctions between two-dimensional (2D) materials and organic semiconductors is a rapidly growing field. This is motivated by the promise of leveraging the extraordinary properties of 2D materials with the synthetic tunability and reconfigurability of organic electronics, allowing the realization of new physics or devices that are not possible in either constituent material alone. Early approaches to understanding these interfaces relied on simple band alignment considerations, approximating the organic molecule as two orbital energies in a vacuum. While this approach is useful, fully realizing the possibilities of this material combination require understanding how organic molecules couple to 2D materials, and in turn how 2D materials affect the structure of the organic thin films.

This thesis presents several examples of organic / 2D heterojunctions whose unique properties cannot be explained solely by considering the constituent materials in isolation. The electronic coupling between metallophthalocyanines (MPc) and molybdenum disulfide ( $\text{MoS}_2$ ) shows emergent states due to mixing of the molecular orbitals with band states, and Raman enhancement in this system is found to depend on the energy of non-frontier orbitals. MPc are also found to interact with defects in the  $\text{MoS}_2$ , quenching their low temperature photoluminescence (PL). Density functional theory calculations reveal this quenching to be a result of the MPc stabilizing dark, negatively charged defect states over bright, neutral ones. Finally, optical – morphological relationships are characterized in the heterojunction between pentacene and hexagonal boron nitride (hBN). hBN is found to template a new thin-film phase of

pentacene which has lower energy free excitons, lower interfacial strain, and long-lived PL decay compared to the typical thin-film phase observed on SiO<sub>2</sub>.

Taken together, these results show the importance of detailed characterization of organic / 2D heterostructures beyond their band alignment. While this increases complexity in the design of these systems, it also provides many opportunities. Controlling electronic coupling, defect trapping, and thin film phase provide a wide range of tools for exploring new physics and fine-tuning the properties of organic / 2D heterojunctions. Understanding and controlling these interactions are necessary to fully leverage the unique opportunities provided by such mixed-dimensional interfaces.

## Acknowledgements

I would first like to thank Prof. Mark Hersam and Prof. Tobin Marks for giving me the opportunity to work in their research groups. Their guidance (and funding) has been essential to this work, and their scientific approach has forever changed how I look at the world. The collaborative spirit and interdisciplinary curiosity they have instilled in their groups have made these past five years the most intellectually exciting of my life. Thank you to my thesis committee members, Prof. Emily Weiss and Prof. Mercuri Kanatzidis, for their feedback, insightful questions, and tolerance of my last minute scheduling. Additional thanks to my qualifying exam committee chair Prof. Samuel Stupp for asking difficult (but not impossible) questions. He also shares my name, and I feel this is important.

A big thank you to my many collaborators over the years, especially Teodor Stanev, Dr. Qunfei Zhou, Dr. Pierre Darancet, and Prof. Nate Stern. Without your contributions and feedback none of this work would have happened. A further thank you to the other phthalocyanine collaborators, Dr. Luqing Wang, Dr. Maria Chan, Shawn Zhao, and Dr. Alex Lou. Thank you to collaborators on other projects: Dr. Trevor LaMountain, Dr. Michael Heiber, Dr. Weigang Zhu, and Dr. Steven Swick. Also thank you and good luck to the future phthalocyanine crew: Carin, Ethan, Tommy, and Brendan. Thank you to my mentors at Northwestern: Dr. Vinod Sangwan, Dr. Tejas Shastry, Sarah Clark, and Dr. Kyle Luck, and to my mentors before graduate school: Prof. David Yaron, Prof. Tomasz Kowalewski, Dr. Jacob Mohan, and Prof. Yoel Ohayon. And thank you to my high school chemistry teachers, Mr. Deal,

who loved to light methanol on fire, and Mr. Mauer, who let us handle all the concentrated acids. A few small burns were worth a lifetime of fun.

I have relied on the support and friendship of so many people at Northwestern. In no particular order: the 1055 office, past and present (Nathan Bradshaw, David Lam, Sarah Clark, Sonal Rangnekar, Julia Downing, Ana Moraes, Norman Luu, Ethan Secor, Kan-sheng Chen, Jin-Myoung Lim, Dominic Goronzy), Suyog Padgaonkar, Tyler Gish, Anushka Dasgupta, Brendan Kerwin, Joaquin Alzola, Eden Aklile, Stephanie Liu, Mike Park, Tommy Song, Karl Putz, Dima Lebedev, Iqbal Utama, Paul Brown, Aritra Sil, Shaowei Li, Matthew Rahn, Shay Wallace, Jade Balla, Spencer Wells, Megan Beck, Hadallia Bergeron, Katherine Su, Linda Guiney, Hocheon Yoo, Chengmei Zhong, Wei Huang, Michael Moody, Jack Olding, Alex Silver, Joohoon Kang, Will Gaviria, Xiaolong Liu, and many others I have forgotten to mention. If you are missing from the list, it is a reflection of sleep deprivation and not the quality of your friendship.

Outside of the lab I have been lucky to make many excellent friends in Chicago and Evanston. A big shout out to my Dungeons and Dragons companions: Arigale Silvertongue, Jules of Enragement, Geoff Boyardee (RIP), Edetha “Siren” Sheeran, Zob Vila, and Agent Scarnelius. Hudson and Sam – you have made these past five years much more fun, and it was probably worth all of the liver damage. Natalia, you were adequate as a roommate, and more than adequate as a friend. Thanks to the Broad Street Boys and the 1B Sausagefest for the many welcome distractions over the years.

Thank you to my family – Mom, Dad, Louisa, Joe, Shana, Moe - for their support through this journey. A big thank you to Reyna, my partner in love and borborygmus, who not only kept me sane, but has made me so happy in this challenging year.

And finally, thank you to anyone who is reading this in the future. I'm so sorry.

## List of Abbreviations

0D	Zero Dimensional
1D	One Dimensional
2D	Two Dimensional
3D	Three Dimensional
A	Ampere
Å	Angstrom
AFM	Atomic Force Microscopy
ALD	Atomic Layer Deposition
ARPES	Angle-resolved Photoelectron Spectroscopy
B3LYP	Becke, 3-parameter, Lee-Yang-Parr functional
CBM	Conduction Band Minimum
cm	Centimeter
cm <sup>-1</sup>	Wavenumber
cm <sup>2</sup> V <sup>-1</sup> s <sup>-1</sup>	Carrier Mobility
cps	Counts Per Second
CVD	Chemical Vapor Deposition
CVT	Chemical Vapor Transport
DFT	Density Functional Theory
DOS	Density of States

eV	Electron Volt
f-	Femto (prefix)
FE	Free Exciton
FET	Field-effect Transistor
G-	Giga (prefix)
Gr	Graphene
hBN	Hexagonal Boron Nitride
HOMO	Highest Occupied Molecular Orbital
K	Kelvin
k-	Kilo (prefix)
LUMO	Lowest Unoccupied Molecular Orbital
m	Meter
m-	Milli (prefix)
M-	Mega (prefix)
MPc	Metal Phthalocyanine
n-	Nano (prefix)
NN	Nearest Neighbor
OFET	Organic Field-effect Transistor
OPV	Organic Photovoltaics
Osub	Oxygen Substitution

p-	Pico (prefix)
Pa	Pascal
PBE	Perdew-Burke-Ernzerhof functional
Pc	Phthalocyanine
pDOS	Projected Density of States
PL	Photoluminescence
PLQY	Photoluminescence Quantum Yield
Pn	Pentacene
PTB7	Poly [[4,8-bis[(2-ethylhexyl)oxy]benzo[1,2-b:4,5-b']dithiophene-2,6-diyl]][3-fluoro-2-[(2-ethylhexyl)carbonyl]thieno[3,4-b]thiophenediyl ]]
PTCDA	Perylenetetracarboxylic dianhydride
PTCDI	3,4,9,10-perylenedicarboximide
QY	Quantum Yield
RT	Room Temperature
s	Second
SAM	Self-Assembled Monolayer
SEM	Scanning Electron Microscopy
STE	Self-Trapped Exciton
STM	Scanning Tunneling Microscopy
Svac	Sulfur Vacancy

TCSPC	Time Correlated Single Photon Counting
TEM	Transmission Electron Microscopy
TFT	Thin-film Transistor
TMDC	Transition Metal Dichalcogenide
UHV	Ultra-high Vacuum
V	Volt
VBM	Valence Band Minimum
vdW	Van der Waals
XPS	X-ray Photoelectron Spectroscopy
XRR	X-ray Reflectivity
μ-	Micro (prefix)

*Perhaps my old age and fearfulness deceive me, but I suspect that the human species -- the unique species -- is about to be extinguished, but the Library will endure: illuminated, solitary, infinite, perfectly motionless, equipped with precious volumes, useless, incorruptible, secret.*

-Jorge Louis Borges, *The Library of Babel* (trans. J. E. I)

## Table of Contents

Abstract.....	2
Acknowledgements.....	4
List of Abbreviations .....	7
List of Figures.....	14
List of Tables .....	24
1. Chapter 1 Introduction and Literature Review .....	25
1.1. Motivation .....	25
1.2. Two-dimensional Materials.....	26
1.2.1. Molybdenum Disulfide and the Transition Metal Dichalcogenides .....	30
1.2.2. Hexagonal boron nitride .....	43
1.3. Phthalocyanines.....	50
1.4. Pentacene.....	55
1.5. Organic / 2D Heterostructures.....	61
1.5.1. Electronic Structure .....	61
1.5.2. Morphology.....	65
1.5.3. Spectroscopy .....	68
1.5.4. Devices.....	70
2. Electronic Coupling in Metal Phthalocyanine – MoS <sub>2</sub> Heterojunctions .....	74
2.1. Abstract .....	74
2.2. Introduction .....	74
2.3. Results and Discussion.....	76
2.4. Methods.....	92
3. Quenching of MoS <sub>2</sub> Defect Photoluminescence by Non-Frontier Orbitals in Metal Phthalocyanines .....	95
3.1. Abstract .....	95
3.2. Introduction .....	96
3.3. Results and Discussion.....	100
3.4. Conclusion.....	114

3.5. Methods.....	114
3.6. Supporting Information – Charge and Energy Transfer.....	119
4. Tailoring the Optical Response of Pentacene Thin Films via Templated Growth on Hexagonal Boron Nitride.....	125
4.1. Abstract .....	125
4.2. Introduction .....	125
4.3. Results and Discussion.....	128
4.4. Conclusions .....	138
4.5. Experimental Methods .....	139
5. Summary and Future Outlook .....	141
5.1. Thesis Summary .....	141
5.2. Future Directions: Tuning Organic / 2D Heterojunctions Beyond Band Alignment... 144	
5.2.1. Hybridization and Electrostatics.....	146
5.2.2. Adlayer Orientation and Morphology.....	148
5.2.3. Non-Frontier Orbitals.....	150
5.2.4. Excitonic States.....	153
5.2.5. Spin Degree of Freedom .....	157
5.2.6. Chirality Effects .....	161
5.2.7. Summary of Future Directions.....	164
6. References .....	166
7. Vita .....	206

## List of Figures

- Figure 1.1 2D material classes and production. (a) Classes of 2D materials sorted by bandgap. (b) Major 2D material production methods sorted by quality and price / scalability. (a) reproduced from <sup>16</sup>. Copyright 2016 Springer Nature. (b) adapted from <sup>17</sup>. Copyright 2012 Springer Nature. .... 28
- Figure 1.2 Phases of TMDs. (a) 1H monolayer with metal in a trigonal prismatic coordination (b) 1T phase, with metal in an octahedral coordination. (c) Distorted 1T phase, in an asymmetric octahedral coordination. (d) AB stacking of 2H phase MoS<sub>2</sub>. (e) ABC stacking of 3R phase MoS<sub>2</sub>. Figure reproduced from <sup>38</sup>. Copyright 2015 The Royal Society of Chemistry..... 31
- Figure 1.3 MoS<sub>2</sub> band diagrams. Qualitative band diagram of (a) 2H MoS<sub>2</sub> and (b) 1T MoS<sub>2</sub>. The highest occupied band ( $d_z^2$ ) in the 2H phase is filled, making it semiconducting. In the 1T case, the  $t_{2g}$  band is only partially filled, making it metallic. (c) Band structure and charge densities of 1H MoS<sub>2</sub> at selected areas near band edges. The VBM at  $\Gamma$  and CBM at K are primarily Mo  $d_z^2$  orbitals, with some S  $p_z$  character. The VBM at K is primarily  $d_{xy}$  and  $d_{x^2-y^2}$ , as does the local minimum of the CBM between K and  $\Gamma$  (the  $\Lambda$  point). (a) and (b) adapted from <sup>49</sup>, Copyright 1993 The Royal Society of Chemistry. (c) reproduced from <sup>52</sup>. Copyright 2013 American Physical Society. .... 33
- Figure 1.4 Valley polarization and point defects. (a) Schematic of valley polarization by coupling of degenerate K valleys to opposite circularly polarized light. (b) Polarization of MoS<sub>2</sub> emission by pumping with near-band edge circularly polarized light at low temperature. P is a measure of the efficiency of valley polarization in the MoS<sub>2</sub>, calculated by  $P = [I(\sigma+) - I(\sigma-)] / [I(\sigma+) + I(\sigma-)]$ , where  $I(\sigma\pm)$  is the intensity of the left (right)-handed circularly polarized component of the PL. (c) Project density of states (pDOS) of MoS<sub>2</sub> with a sulfur vacancy ( $S_{vac}$ ) or and oxygen substitution ( $O_{sub}$ ). The red nearest neighbor (NN) components of the pDOS represent the localized states adjacent to the point defect. (a) and (b) reproduced from <sup>55</sup>. Copyright 2012 Springer Nature. Calculations in (c) performed by Luqing Wang. Further details will be discussed in Chapter 3. .... 35
- Figure 1.5 MoS<sub>2</sub> spectroscopy. (a) UV-Vis absorption spectrum and PL spectrum at room temperature. (b) Schematic of different excitonic states in MoS<sub>2</sub> and their relative energies. (c) Low temperature PL spectrum of MoS<sub>2</sub> showing deconvolution of different excitonic states. (d) Schematic of trapping and radiative recombination pathways illustrating temperature dependence of defect PL. (e) Layer dependent Raman spectra of the MoS<sub>2</sub>  $E_{2g}$  and  $A_{1g}$  modes. (f) Change of peak position in (e) versus thickness, as well as the change in  $A_{1g} - E_{2g}$ . (a) reproduced from <sup>68</sup>. Copyright 2016 American Chemical Society. (b) and (c) reproduced from <sup>80</sup>. Copyright 2019 Elsevier. (d) reproduced from <sup>81</sup>. Copyright 2017 American Physical Society. (e) and (f) reproduced from <sup>82</sup>. Copyright 2010 American Chemical Society..... 38
- Figure 1.6 MoS<sub>2</sub> electrical and optical devices. (a) Temperature dependence of conductivity of a monolayer MoS<sub>2</sub> FET on SiO<sub>2</sub>. Linear dependence on  $T^{1/3}$  is characteristic of variable range hopping. Inset shows mobility versus temperature behavior. (b) Partial I-V plot of an intersecting

MoS<sub>2</sub> grain boundary memristor. Inset shows the full I-V characteristics of on switching cycle. (c) Absorbance spectra of thin MoS<sub>2</sub> flakes of different thicknesses with a micrometer-scale ring electrode. The semiconductor/metal interface increases the local density of states, resulting in near-unity absorption from ultrathin films. (d) Linear sweep voltammetry curves illustrating the relative performance of 2H and 1T MoS<sub>2</sub> electrocatalysts at the hydrogen evolution reaction versus platinum. (a) is reproduced from <sup>100</sup>. Copyright 2011 American Chemical Society. (b) is reproduced from <sup>107</sup>. Copyright 2015 Springer Nature. (c) is reproduced from <sup>111</sup>. Copyright 2016 American Chemical Society. (d) is reproduced from <sup>114</sup>. Copyright 2018 Wiley-VCH..... 42

Figure 1.7 Structure of hBN. (a) Crystal structure of hBN. (b) Valence band structure of monolayer hBN grown on Ni(111), Pd(111), and Pt(111), measured by angle-resolved ultraviolet photoelectron spectroscopy (ARUPS). (b) reproduced from 71. Copyright 1995 American Physical Society. .... 44

Figure 1.8 Spectroscopy of hBN. (a) Absorption and cathodoluminescence spectra of bulk hBN taken at low temperature. The absorption spectrum shows higher wavelength peaks corresponding to the excitonic Rydberg series, with the direct bandgap absorption occurring at 207 nm. The peaks 215 nm and below in the cathodoluminescence spectrum are due to the excitonic recombination, while the lower energy peaks are due to defect-bound excitons. (b) PL spectrum of hBN defect center in monolayer hBN, taken at 77 K. The inset shows the zero phonon line. (c) FTIR spectrum of few layer hBN grown on Si/SiO<sub>2</sub>. (d) Position of the hBN E<sub>2g</sub> Raman mode versus thickness for mechanically exfoliated hBN. (a) adapted from <sup>120</sup>. Copyright 2004 Springer Nature. (b) reproduced from <sup>127</sup>. Copyright 2016 Springer Nature. (c) reproduced from <sup>125</sup>. Copyright 2010 American Chemical Society. (d) reproduced from <sup>128</sup>. Copyright 2011 Wiley-VCH. .... 45

Figure 1.9 hBN production and devices. (a) Photograph of large area CVD hBN transferred onto an Si substrate. (b) White light microscope image of mechanically exfoliated monolayer and few-layer hBN. (c) Temperature dependent resistance versus gate voltage of hBN-encapsulated Graphene. Inset shows the corresponding conductivity. (d) Temporal response of a drop cast hBN photodetector with 254 nm illumination. (a) adapted from <sup>130</sup>. Copyright 2010 American Chemical Society. (b) adapted from <sup>128</sup>. Copyright 2011 Wiley-VCH. (c) reproduced from <sup>134</sup>. Copyright 2010 Springer Nature. (d) reproduced from <sup>139</sup>. Copyright 2021 American Chemical Society..... 48

Figure 1.10 Phthalocyanine structure. (a) Chemical structure of MPc molecule. (b-i) Electron density of frontier and near-frontier orbitals of MPc molecules. (j) Orbital energy levels for H<sub>2</sub>Pc, MPc (M = Fe, Co, Ni, Cu, Zn, Mg) and select fluorinated derivatives. (b-i) Electron density of frontier and near-frontier orbitals of MPc molecules. (j) Orbital energy levels for H<sub>2</sub>Pc, MPc (M = Fe, Co, Ni, Cu, Zn, Mg) and select fluorinated derivatives. (b)-(j) reproduced from <sup>151</sup>. Copyright 2020 the authors, licensed under CC BY-NC-ND. .... 51

Figure 1.11 Phthalocyanine absorption and Raman spectra. (a) example UV-vis absorption spectrum of ZnPc in chloroform. The Soret and Q bands are labelled. (b) Raman spectrum of ZnPc and (c) CuPc. (d) Polarized Raman spectra of CuPc and H<sub>2</sub>Pc films on MoS<sub>2</sub> with the A<sub>1g</sub> modes highlighted. The change in parallel versus cross polarization in CuPc suggests a π-face-on

orientation to MoS<sub>2</sub> while the H<sub>2</sub>Pc is unchanged, suggesting an edge-on orientation. (a) adapted from <sup>163</sup>. Copyright 2017 Elsevier. (b) and (c) reproduced from <sup>164</sup>. Copyright 2001 The Royal Society of Chemistry. (d) adapted from <sup>165</sup>. Copyright 2019 American Chemical Society. .... 53

Figure 1.12 Pentacene structure and film morphology. (a) Chemical structure of pentacene. (b) Comparison of the Siegrist, Campbell, and thin-film phases of pentacene based on their (001) distances. (c) Atomic force microscopy (AFM) images of the morphology contrast between thin-film and  $\pi$ -face-on phases of pentacene. The dendritic thin-film phase grows on the SiO<sub>2</sub> while the needle-like  $\pi$ -face-on phase grows on hBN. (d) Comparison of deposition rate and substrate bandgap of representative studies of pentacene film growth. Epitaxial growth typically occurs on metallic or vdW substrates at very slow growth rates. Sources: a, <sup>184</sup> b, <sup>185</sup> c, <sup>186</sup> d, <sup>187</sup> e, <sup>188</sup> f, <sup>189</sup> g, <sup>190</sup> h, <sup>191</sup> i, <sup>192</sup> j, <sup>193</sup> k, <sup>183</sup> l, <sup>194</sup> m, <sup>195</sup> n, <sup>195</sup> o, <sup>196</sup> p, <sup>197</sup> q, <sup>198</sup> r. <sup>199</sup> (a) reproduced from <sup>200</sup>. Copyright 2016 The Royal Society of Chemistry. (c) reproduced from <sup>201</sup>. Copyright 2021 American Chemical Society..... 56

Figure 1.13 Pentacene spectroscopy. (a) UV-Vis absorption spectrum of solution phase and single crystal pentacene. (b) PL spectra of thin-film pentacene (on SiO<sub>2</sub>) and  $\pi$ -face-on pentacene (on hBN) showing the free- and self-trapped excitonic emission peaks at 1.8 and 1.65 eV respectively. (c) Jablonski diagram of optical processes in pentacene, illustrating the relevant energy levels for singlet fission. (a) reproduced from <sup>207</sup>. Copyright 2011 American Institute of Physics. (b) reproduced from <sup>201</sup>. Copyright 2021 American Chemical Society. (c) reproduced from <sup>208</sup>. Copyright 2013 American Chemical Society. .... 59

Figure 1.14 Electronic structure in organic – 2D heterojunctions. (a) Band alignment and heterojunction types. (i) Schematic of a band alignment diagram, with the frontier orbitals of the molecule and band edges of the 2D material labelled. The z axis is implicitly energy in these diagrams. Possible alignments for a (ii) type-I straddling gap heterojunction, (iii) type-II staggered gap heterojunction, and (iii) type-III broken gap heterojunction. (b) Schematic of a MoS<sub>2</sub> transistor on a self-assembled monolayer (SAM) and a plot of the change in carrier concentration in the MoS<sub>2</sub> transistor with different SAM end groups, plotted versus the amount of transferred charge and the dipole moment. (c) Structures of PTCDA, PTCDI-Ph, schematic of their heterojunctions with MoS<sub>2</sub>, and the z-direction charge difference in PTCDA and PTCDI-Ph/MoS<sub>2</sub> heterojunctions with isosurface plots of the charge density difference. The red and green isosurfaces represent electron accumulation and depletion, respectively. The LUMO  $\pi$ -orbital energies determine the direction of the charge transfer. (d,e) Energy-momentum angle-resolved photoelectron spectroscopy (ARPES) intensity maps ( $h\nu = 75$  eV) of (d) pristine MoS<sub>2</sub> and (e) 0.6 nm of FePc on MoS<sub>2</sub>. The lowest binding energy features of FePc have intensity maxima close to *K* and *M*, indicating hybridization between MoS<sub>2</sub> states and those of the adsorbed molecule. (b) Adapted from <sup>234</sup>. Copyright 2014 American Chemical Society. (c) adapted from <sup>235</sup>. Copyright 2020 Wiley-VCH. (d) and (e) reprinted with permission from <sup>154</sup>. Copyright 2020 American Chemical Society. .... 62

Figure 1.15 Organic – 2D morphology (a) Transient absorption traces of monolayer MoS<sub>2</sub> and its heterojunction with CuPc and H<sub>2</sub>Pc. A long-lived charge separated state is present only in the CuPc heterojunction. (b) Polarized Raman spectra of CuPc and H<sub>2</sub>Pc on MoS<sub>2</sub>. The change in

intensity of the highlighted modes in parallel and perpendicular polarizations indicates that CuPc has a face-on orientation with respect to the MoS<sub>2</sub> plane, whereas H<sub>2</sub>Pc has a significant tilt angle. (c) Optical microscopy image of a 20 nm pentacene film deposited on multilayer hBN and a SiO<sub>2</sub> substrate. Pentacene forms a typical dendritic thin-film phase on SiO<sub>2</sub> but grows in a unique needle-like  $\pi$ -face-on phase on hBN. (d) HOMO-VBM energy offset as a function of ZnPc thickness at the interface of ZnPc-monolayer-MoS<sub>2</sub> and ZnPc-bulk-MoS<sub>2</sub> heterostructures as deduced from photoelectron spectra. The film thickness can change the band alignment in this organic-2D heterostructure by several hundred meV. (a) and (b) adapted from <sup>165</sup>. Copyright 2019 American Chemical Society. (c) reproduced from <sup>201</sup>. Copyright 2021 American Chemical Society. (d) reproduced from <sup>241</sup>. Copyright 2019 American Chemical Society..... 66

Figure 1.16 Spectroscopy of organic – 2D heterojunctions. (a) UV-Vis absorption of a CuPc – MoS<sub>2</sub> heterojunction shows a new peak associated with delocalization of the CuPc Q band into the MoS<sub>2</sub>. This will be discussed in more detail in Chapter 2. (b) Raman spectra of an equal thickness of CuPc deposited on graphene, hBN, MoS<sub>2</sub>, and SiO<sub>2</sub>, showing Raman enhancement of the CuPc on different the 2D substrates. (c) PL spectra of the OPV polymer PTB7, MoS<sub>2</sub>, and their heterojunction shows mutual PL quenching characteristic of photoinduced charge transfer in a type-II heterojunction. Inset shows the small remnant PL signal from the heterojunction. (a) reproduced from <sup>66</sup>. Copyright 2019 American Chemical Society. (b) reproduced from <sup>247</sup>. Copyright 2014 American Chemical Society. (c) reproduced from <sup>68</sup>. Copyright 2016 American Chemical Society. .... 69

Figure 1.17 Organic – 2D devices. (a) Threshold voltage and carrier concentration in an MoS<sub>2</sub> as a function of CuPc thickness. CuPc depletes carriers in MoS<sub>2</sub>, increasing the threshold voltage and acting effectively as a p-dopant. (b) Transfer curves of an MoS<sub>2</sub>, pentacene, and overlapping pentacene - MoS<sub>2</sub> transistors. MoS<sub>2</sub> and pentacene act as typical n- and p-type FETs, respectively, but when a gating electric field can penetrate both components, their overlapping film produces a unique anti-ambipolar transfer curve. (c) J-V curve of a PTB7 – MoS<sub>2</sub> 20 nm thick photovoltaic cell shows an open circuit voltage of 0.2 V and short circuit current of  $\sim 2$  mA/cm<sup>2</sup>. (d) Photoresponse of MoS<sub>2</sub> only and H<sub>2</sub>Pc – MoS<sub>2</sub> hybrid photodetector, normalized to the performance at 2.5 eV. Absorption and excited state charge transfer by the H<sub>2</sub>Pc greatly improves the photoresponse and spectral range of the photodetector. (a) reproduced from <sup>243</sup>. Copyright 2015 The Royal Society of Chemistry. (b) reproduced from <sup>233</sup>. Copyright 2016 American Chemical Society. (c) reproduced from <sup>68</sup>. Copyright 2016 American Chemical Society. (d) reproduced from <sup>255</sup>. Copyright 2020 American Chemical Society..... 71

Figure 2.1 (a) Optical image of an exfoliated MoS<sub>2</sub> film. (b) The AFM profile indicates monolayer thickness. (c) Raman signal of a MoS<sub>2</sub> film corresponding to monolayer response. (d) Structure of an MPc molecule where M = Co, Ni, Cu, Zn or metal-free H<sub>2</sub>Pc. (e) Schematic cross-sectional structure of single-layer MoS<sub>2</sub>. (f) Schematic of the anticipated adsorption geometry of MPc molecules on the MoS<sub>2</sub> basal plane..... 77

Figure 2.2 X-ray photoelectron spectra (XPS) of MPc metal core electrons (a, b: Co 2p; c, d: Ni 2p; e, f: Cu 2p; g, h: Zn 2p) with identical film thickness on sapphire or CVD MoS<sub>2</sub> – sapphire substrates. Peak integrations indicate similar amounts of MPc is deposited on sapphire vs. MoS<sub>2</sub>.

- Due to the insulating substrate and long collection times, significant charging effects occur despite the use of a charge compensation gun. This causes large shifts in the peak positions, meaning subtle changes in chemical state on sapphire vs MoS<sub>2</sub> are not observable. The charge compensation also causes reduction of the Cu<sup>2+</sup> species over time, which yields the different peak structure in the Cu 2p spectra on sapphire vs MoS<sub>2</sub>. ..... 79
- Figure 2.3 (a) Optical absorption spectra of pristine MoS<sub>2</sub>, CuPc, and CuPc – MoS<sub>2</sub> heterojunction films. The new transition at 710 nm is denoted A<sup>CT</sup>. (b) Optical absorption spectra of a pristine CuPc film, the CuPc – MoS<sub>2</sub> heterojunction, and the difference spectrum of the CuPc – MoS<sub>2</sub> heterojunction and pristine MoS<sub>2</sub> absorption. (c) Proposed origin of A<sup>CT</sup> as a direct transition from the MPc HOMO to the MoS<sub>2</sub> CBM. .... 81
- Figure 2.4 Absorption spectra of monolayer chemical vapor deposition grown MoS<sub>2</sub>, 0.4 nm of Pc, and MoS<sub>2</sub> with 0.4 nm Pc deposited. The emergent charge-transfer absorption is labeled A<sup>CT</sup>. All spectra were taken on sapphire substrates. .... 82
- Figure 2.5 (a) Electronic structure of Co, Ni, Cu, Zn, and metal-free phthalocyanines in the gas phase computed using the HSE functional. For all molecules, the HOMO has a strong  $\pi$ -character. Orbital symmetries are labelled for the MPc (H<sub>2</sub>Pc has a lower symmetry and distinct irreducible representations). All molecules are found in their low-spin configuration with the b<sub>2g</sub> (d<sub>xy</sub>) and b<sub>1g</sub> (d<sub>x<sup>2</sup>-y<sup>2</sup>) orbitals being singly occupied for CoPc and CuPc, respectively. The density of states of MoS<sub>2</sub> with respect to vacuum energy is shown at the right, along with the change in level alignment (PBE) of an H<sub>2</sub>Pc molecule upon forming a heterojunction with MoS<sub>2</sub>. (b) Representative electron densities of the indicated orbitals as well as their symmetry labels. .... 83</sub>
- Figure 2.6 (a) AFM image of SiO<sub>2</sub>, monolayer, and bilayer MoS<sub>2</sub> flakes before deposition of MPc. (b) AFM of the same location following deposition of 0.4 nm CuPc. Note the circle of larger CuPc aggregates due to prolonged exposure to the Raman laser. (b inset) The same location following a 30 minute anneal at 250 °C under an N<sub>2</sub> atmosphere. Note that the CuPc particles have coalesced into larger aggregates. .... 85
- Figure 2.7 (a) Relative MPc-MoS<sub>2</sub> heterojunction Raman enhancement factors (633 nm laser excitation) showing a decrease with increasing M atomic number. (top inset) Excitation wavelength-dependent enhancement shows a steady increase as the wavelength is changed from non-absorbing (473 nm) to on-resonance with the MPc Q-band  $\pi \rightarrow \pi^*$  absorption and MoS<sub>2</sub> exciton absorption. (b) Dependence of CuPc Raman spectra (532 nm laser source) on MoS<sub>2</sub> thickness. .... 88
- Figure 2.8 (a) Mean Raman enhancement factors for CoPc- and NiPc-MoS<sub>2</sub> heterojunctions using 532 nm and 633 nm lasers reveal the general trend of decreasing enhancement as the MoS<sub>2</sub> layer number increases from monolayer to bulk. (b) Optical image of a MoS<sub>2</sub> flake with areas of single-layer (1L), bilayer (2L), trilayer (3L), and multilayer (ML) (> 30 nm). (c) Corresponding map of Raman intensity of the CuPc B<sub>2g</sub> ring stretching mode at 1530 cm<sup>-1</sup>. .... 90
- Figure 3.1 (a) Structure of the MPc molecule. (b) Schematic of the MPc – MoS<sub>2</sub> heterojunction. .... 98
- Figure 3.2 (a) Optical micrograph of mechanically exfoliated MoS<sub>2</sub> with the monolayer region highlighted. (b) Raman spectra of monolayer MoS<sub>2</sub> before and after deposition of 1 nm CoPc.

The separation of the  $A_{1g}$  and  $E_{2g}$  is  $\sim 19 \text{ cm}^{-1}$ , indicating monolayer  $\text{MoS}_2$ . Raman modes that appear in the  $1100 - 1500 \text{ cm}^{-1}$  range are characteristic of CoPc. (c) 300 K PL spectra of mechanically exfoliated  $\text{MoS}_2$  and  $\text{MoS}_2 - 1 \text{ nm CoPc}$ . The A-exciton and associated trion are prominent at 675 nm, and a small higher-energy shoulder is visible due to the B-exciton (d) 10 K photoluminescence of  $\text{MoS}_2$  and  $\text{MoS}_2 - 1 \text{ nm CoPc}$ . At this temperature, the  $\text{MoS}_2$  defect emission becomes apparent at 700 nm in addition to the A- and B- excitons at 660 nm and 600 nm, respectively. The defect PL is completely quenched by the CoPc and the A- exciton is partially quenched. .... 101

Figure 3.3 (a) Optical microscopy of representative MPc films on monolayer CVD  $\text{MoS}_2$ . PL spectra of  $\text{MoS}_2$  were collected near the edges of the MPc film to ensure the observed quenching was not due to inhomogeneity in CVD growth. (b) Low temperature photoluminescence spectra of representative CVD  $\text{MoS}_2$  and  $\text{MoS}_2$  with 1 nm films of  $\text{H}_2\text{Pc}$ ,  $\text{ZnPc}$ ,  $\text{CuPc}$ , and  $\text{CoPc}$ . The spectra are normalized to the intensity of the  $\text{MoS}_2$  A exciton peak. (c) Comparison of quenching fraction of each MPc. .... 103

Figure 3.4 Non-normalized PL spectra comparing (a) CoPc, (b) CuPc, (c) ZnPc, and (d)  $\text{H}_2\text{Pc}$  with a nearby clean  $\text{MoS}_2$ . There is a clear trend in quenching efficiency, with  $\text{CoPc} > \text{CuPc} > \text{ZnPc} > \text{H}_2\text{Pc}$ . Within the MPc, the quenching efficiency follows the Periodic Table, becoming less efficient as d-electrons are added to the central metal center in the MPcs. Note that the shape of the defect emission does vary between spectra due to inhomogeneity in the CVD  $\text{MoS}_2$ . All comparisons in this figure are done for  $\text{MoS}_2 - \text{Pc}$  areas within  $10 \mu\text{m}$  of the representative pristine  $\text{MoS}_2$  in a given spectrum. Thus the  $\text{MoS}_2$  varies between panels but is comparable within a given panel. .... 104

Figure 3.5 Time correlated single photon counting (TCSPC) traces collected at 10 K with a 450 nm laser showing the photoluminescence decay for  $\text{MoS}_2$  and the  $\text{MoS}_2 - \text{MPc}$  systems. Due to instrumentation limits, the  $\mu\text{s}$ -scale decay of the defect emission cannot be accurately fit but can allow qualitative comparisons by using a linear fit to the median intensity for times  $> 100 \text{ ns}$ . 105

Figure 3.6 Low temperature PL with applied gate voltages of (a) mechanically exfoliated  $\text{MoS}_2$  alone and (b)  $\text{CoPc} - \text{MoS}_2$ . Negative gate voltages enhance the defect emission in  $\text{MoS}_2$ , but this effect is suppressed by CoPc. (c) Comparison of defect PL integration for  $\text{MoS}_2$  and  $\text{CoPc} - \text{MoS}_2$  at the measured gate voltages. .... 108

Figure 3.7 (a)  $\text{MoS}_2$  with positive voltages shows no change in the defect PL except for lower energy emission from trions. (b)  $\text{MoS}_2 - \text{CoPc}$  at positive voltages show a larger shift to lower energy emission at high gate voltages, suggesting a lower initial population of trions at 0 V due to p-doping from CoPc. .... 109

Figure 3.8 Normalized room temperature photoluminescence comparison with and without MPc films for (a) CoPc (b) CuPc (c) ZnPc and (d)  $\text{H}_2\text{Pc}$ . For all spectra there is either no change to the energy of the exciton emission or a slight shift to lower wavelengths due to a decrease in trion emission characteristic of p-doping. This is also consistent with the low temperature results in Fig 2. .... 110

Figure 3.9 Binding energy calculation of Pc on  $\text{MoS}_2$  defects at different locations relative to the Pc. (a) Schematic of the MPc structure on  $\text{MoS}_2$  used for the binding energy calculations. The

yellow sulfurs correspond to the yellow dots, which indicate the location of the defect used in each binding energy calculation for (b) H <sub>2</sub> Pc on S <sub>vac</sub> , (c) CuPc on S <sub>vac</sub> , (d) ZnPc on S <sub>vac</sub> , (e) H <sub>2</sub> Pc on an oxygen substitution (O <sub>sub</sub> ), and (f) ZnPc on O <sub>sub</sub> . .....	111
Figure 3.10 Formation energy of neutral and charged S <sub>vac</sub> vs Fermi energy for MoS <sub>2</sub> alone, CoPc - MoS <sub>2</sub> and H <sub>2</sub> Pc - MoS <sub>2</sub> . For a given Fermi energy, the dominant defect state is the charged state corresponding to the lowest energy line. For the MoS <sub>2</sub> case, at the VBM this is neutral, while at the CBM this is -1. At a Fermi level near the CBM, the formation energy of the negative S <sub>vac</sub> is CoPc < H <sub>2</sub> Pc < MoS <sub>2</sub> only. The Fermi energy where the defect charge changes from neutral to negative is highlighted with a gray arrow.....	113
Figure 3.11 Formation energy of charged and neutral O <sub>sub</sub> versus Fermi energy for MoS <sub>2</sub> alone and CoPc - MoS <sub>2</sub> . (b) pDOS of MoS <sub>2</sub> with charged and neutral oxygen substitutions (O <sub>sub</sub> )... ..	114
Figure 3.12 Spectra of MoS <sub>2</sub> defect PL and MPC absorption, normalized to a maximum value of 1.0 for ease of comparison, of (a) CoPc, (b) CuPc, (c) ZnPc, (d) H <sub>2</sub> Pc. The overlap area is highlighted in blue. Absorption spectra were collected by subtracting the absorption of CVD MoS <sub>2</sub> on sapphire and 4 Å of the MPC on MoS <sub>2</sub> on sapphire. This was done to account for the large shift in Pc absorption upon deposition on MoS <sub>2</sub> documented elsewhere. <sup>66</sup> MoS <sub>2</sub> defect PL spectra are the same as presented in Figures 3.2b-e, using CVD MoS <sub>2</sub> on SiO <sub>2</sub> at 10 K. Both absorption and PL spectra were normalized to 1.0 as their maxima. ....	119
Figure 3.13 Ratio of NRET rates of the MoS <sub>2</sub> defect to A exciton induced by H <sub>2</sub> Pc and CuPc as a function of Pc thickness. The greater expected quenching of the defect by H <sub>2</sub> Pc vs CuPc contradicts the observed patterns. ....	121
Figure 3.14 (a) Projected density of states (pDOS) of MoS <sub>2</sub> with sulfur vacancies or oxygen substitutions of different charge. The S <sub>vac</sub> or O <sub>sub</sub> nearest neighbor (NN) orbitals correspond to the localized states induced by the S <sub>vac</sub> or O <sub>sub</sub> . (b) Band alignment diagram showing the energy of the out-of-plane MPC d <sub>xz</sub> and d <sub>yz</sub> orbitals moving from the valence band edge in the case of CoPc to lower energy in the case of CuPc and ZnPc, while H <sub>2</sub> Pc has no such orbitals. ....	122
Figure 4.1 (a) Optical images showing the assembly of thermally evaporated pentacene into needle-like grains on 5-10 nm hBN. (b) AFM topographic image showing the transition from predominantly needle-like pentacene on hBN to the dendritic structure on SiO <sub>2</sub> . (c) Raman spectra of pentacene grown on hBN and SiO <sub>2</sub> using a 532 nm excitation wavelength, normalized to the respective maxima at 1370 cm <sup>-1</sup> and vertically offset to highlight the different modes. Arrows indicate the A <sub>g</sub> vibration at 1533 cm <sup>-1</sup> in pentacene/SiO <sub>2</sub> and the B <sub>3g</sub> vibration at 1597 cm <sup>-1</sup> in pentacene/hBN. (d) Schematic illustration of the π-face-on growth of pentacene/hBN and the edge-on growth of the pentacene/SiO <sub>2</sub> thin-film phase.....	128
Figure 4.2 (a) AFM profilometry of large pentacene needles on hBN showing heights of 10 – 20 nm and widths of 1 – 2 μm. (b) AFM profilometry of pentacene terraces on SiO <sub>2</sub> . The step height is 1.6 nm, consistent with the thin-film phase. ....	130
Figure 4.3 π-Face-on and thin-film phase of pentacene on semiconducting vdW materials. (a,c) Optical images at 100x magnification of pentacene on WS <sub>2</sub> (a) and MoS <sub>2</sub> (c). (b, d) AFM scans of (a, c) respectively. Needle-like structures are apparent on both. They also show a greater coverage of nanoscale grains and dendritic thin-film phase than on hBN. ....	131

- Figure 4.4 (a) Comparison of the 298 K photoluminescence spectra of  $\pi$ -face-on pentacene/hBN and thin-film phase pentacene/SiO<sub>2</sub>. (b) Photoluminescence spectral comparison of pentacene/hBN and pentacene/SiO<sub>2</sub> at 10 K. The higher and lower energy peaks are assigned to pentacene free exciton (FE) emission and self-trapped exciton (STE) emission, respectively. Emission from pentacene/hBN (blue) has a narrower linewidth and a lower energy relative to pentacene/SiO<sub>2</sub> (gray). (c) Temperature dependence of the FE emission energy for the two pentacene phases extracted from Gaussian fits. (d) Temperature dependence of the FE emission full-width at half maximum (FWHM), showing that both phases have narrower emission at lower temperatures. .... 133
- Figure 4.5 (a,b) PL spectra at 10 K of pentacene thin films on the indicated vdW substrates compared to SiO<sub>2</sub>. Red-shift of the pentacene peak on WS<sub>2</sub> is apparent since the WS<sub>2</sub> exciton is well-separated from the pentacene emission. The pentacene/MoS<sub>2</sub> spectrum is more complicated since the pentacene emission overlaps spectrally with the MoS<sub>2</sub> emission.  $X_A$  denotes the A-exciton emission of the vdW material,  $X_{FE}$  denotes the pentacene free exciton emission, and  $X_{STE}$  denotes the pentacene self-trapped exciton. The STE emission of pentacene on WS<sub>2</sub> is hidden by the large intensity of the A-exciton emission. (c) The pentacene/MoS<sub>2</sub> spectrum broken down by a series of peak functions in order to better identify the constituent components of the broad, convoluted emission. In addition to the peaks in (b), there is contribution from the MoS<sub>2</sub> B-exciton ( $X_B$ ), the MoS<sub>2</sub> defect emission ( $X_D$ ), and both the thin-film and  $\pi$ -face-on phase pentacene FE emission ( $X_{FE}$  and  $X_{FE'}$  respectively). .... 134
- Figure 4.6 Temperature-dependent PL of pentacene/WS<sub>2</sub>. (a) PL plots of the pentacene thin films on WS<sub>2</sub> and SiO<sub>2</sub>. The WS<sub>2</sub> exciton emission at 2 eV is more efficient than the pentacene free exciton at 1.8 eV. (b) Energy of pentacene free exciton emission versus temperature. The epitaxial film on WS<sub>2</sub> behaves similarly to the film on hBN, although with a lower overall energy shift. The in-plane thermal expansion coefficient of WS<sub>2</sub> is on the order of  $10^{-6} \text{ K}^{-1}$ , based on temperature-dependent Raman measurements.<sup>346</sup> This thermal expansion coefficient is between hBN ( $2 - 4 \times 10^{-5} \text{ K}^{-1}$ )<sup>344</sup> and SiO<sub>2</sub> ( $5 \times 10^{-7} \text{ K}^{-1}$ ),<sup>345</sup> which aligns with the temperature-dependent PL shift of pentacene/WS<sub>2</sub> being between those two other substrates. .... 135
- Figure 4.7 (a) PL map of the pentacene/hBN thin film, acquired with an excitation wavelength of 570 nm and detection range 650-950 nm. The grayscale bar indicates the signal intensity and the color bar indicates the average PL lifetime (ns) at each pixel. (b) Decay of PL intensity at representative spots of the map ON (green) and OFF (blue) the hBN flake, along with IRF (gray). The “fastest” two components of PL decay (i.e., <50 ps and 400 ps; convolved with the IRF) in both phases correspond to a singlet fission process, while the 3.2 ns component of the PL from pentacene deposited on top of hBN arises from triplet-triplet recombination. .... 136
- Figure 5.1 Summary of molecular characteristics beyond frontier orbital energy level alignment that can provide tunability over the electronic and optical properties of organic-2D mixed-dimensional heterojunctions. .... 145
- Figure 5.2 Proposed hybridization-driven direct-to-indirect bandgap transition in monolayer MoS<sub>2</sub> or indirect-to-direct bandgap transition in bilayer MoS<sub>2</sub>. Repulsion between out-of-plane MoS<sub>2</sub>  $p_z$  orbitals drives the direct-to-indirect transition in monolayer to bilayer MoS<sub>2</sub>. Similarly,

by designing molecular systems that have strong bonding or antibonding interactions with the MoS<sub>2</sub> p<sub>z</sub> orbitals, the energy at  $\Gamma$  in the valence band structure can be raised or lowered while leaving  $K$  relatively unchanged..... 147

Figure 5.3 (a) Calculated density of states (DOS) of a pentacene-MoS<sub>2</sub> heterojunction at 300 K using the HSE06 functional. (b) Calculated time-dependent state populations from nonadiabatic dynamic simulations of interfacial hole transfer in a pentacene-MoS<sub>2</sub> heterojunction. Hole transfer proceeds from the MoS<sub>2</sub> VBM to the pentacene HOMO-1 on ultrafast timescales before relaxing to the pentacene HOMO over the following picoseconds. (c) Schematic proposal of an azulene-2D heterojunction that utilizes ping-pong electron transfers to allow gate-tunable emission at two wavelengths. (d) Azulene exhibits bright fluorescence from its S<sub>2</sub> state in isolation. (e) If the S<sub>1</sub> state is within the bandgap of a 2D semiconductor, photoexcited azulene would likely undergo back electron transfer via S<sub>2</sub> → CB → S<sub>1</sub>, allowing emission from the S<sub>1</sub> state. (f) At high gate voltages, band bending may prevent electron transfer from the azulene, allowing it to fluoresce from its S<sub>2</sub> state as it does under normal conditions. (g,h)

Photoluminescence intensity and wavelength histograms of WS<sub>2</sub> treated with (g) Oleic acid and (f) Bis(trifluoromethane)sulfonimide (TFSI). Both treatments dramatically increase the WS<sub>2</sub> photoluminescence quantum yield (PLQY), but the narrowness of the emission from the oleic acid treatment suggests chemical specificity in the defect passivation. (a) and (b) reprinted with permission from <sup>363</sup>. Copyright 2019 American Chemical Society. (g) and (h) reprinted with permission from <sup>253</sup>. Copyright 2019 American Chemical Society..... 151

Figure 5.4 (a) Schematic band diagram of a graphene-WS<sub>2</sub>-hBN heterostructure for excited-state biexciton formation. Electrons from photoexcited neutral excitons in the WS<sub>2</sub> transfer to the graphene, leaving behind free holes that can combine with negative trions (light grey shaded area) to form an excited-state biexciton (light orange shaded area). (b) Integrated PL intensity of the excitonic emission from the heterostructure in (a) as a function of gate voltage. Higher gate voltage increases the negative trion population, promoting formation and emission of biexcitons (X). (c) Schematic of a tetracene-WS<sub>2</sub> heterojunction, its energy level alignment, and the energy levels of a charge transfer exciton. (d) Photoluminescence spectrum of the tetracene-WS<sub>2</sub> heterojunction. An extra peak is present near 1.7 eV that is attributed to recombination of the charge transfer exciton. (e,f) Exciton population profiles of (e) WS<sub>2</sub> and (f) tetracene-WS<sub>2</sub>. The excitons diffuse further in the case of the tetracene-WS<sub>2</sub> heterojunction due to equilibrium with the long-lived charge transfer exciton. (a) and (b) reproduced from <sup>371</sup>. Copyright 2019 Royal Society of Chemistry. (c), (d), (e) and (f) reproduced from <sup>252</sup>. Copyright 2018 The Authors, American Association for the Advancement of Science, licensed under CC BY-NC. .... 155

Figure 5.5 (a) Constant height AFM images of FePc molecules on nitrogen-doped graphene show a change in electron density in the FePc adsorbed above an N-dopant, corresponding to triplet FePc on graphene and singlet FePc above the dopant. (b) Proposed change in electronic structure of Fe<sup>2+</sup> d-orbitals when adsorbed on an N-dopant. On graphene, the d<sub>yz</sub>, d<sub>xz</sub>, and d<sub>z</sub><sup>2</sup> orbitals are not strongly split and form a high-spin triplet ground state. Repulsion from the N-dopant results in a higher energy d<sub>z</sub><sup>2</sup> orbital and a low-spin singlet ground state. (c) Two-photon photoemission spectra at selected delay times in a ZnPc-MoS<sub>2</sub> heterostructure. Upon

photoexcitation, the emission evolves through three states as depicted in (d). Upon photoexcitation of ZnPc (i), charge transfer occurs (ii), followed by back electron transfer to the ZnPc triplet state (iii). (e) Structure of quinoidal dithienyl perylenequinodimethane (QDTP) and SQUID measurements showing a spin transition around 360 K as QDTP switches from a singlet to a triplet state. (f) Temperature-dependent magnetoconductivity of a QDTP-MoS<sub>2</sub> heterojunction. A clear transition from negative to positive magnetoconductivity is observed as the QDTP switches from a singlet to a triplet spin state. (a) and (b) reprinted from <sup>384</sup>. Copyright 2018 The Authors, Springer Nature under a CC-BY license. (c) and (d) reprinted with permission from <sup>284</sup>. Copyright 2017 American Chemical Society. (e) and (f) reprinted from <sup>386</sup>. Copyright 2017 The Authors, Springer Nature, under a CC-BY license..... 158

Figure 5.6 (a) Liquid phase exfoliation of MoS<sub>2</sub> in the presence of chiral penicillamine induces chiral bending in the resulting nanoplatelets. (b) Circular dichroism spectra of these platelets shows that the bent nanoplatelets are optically active and oppositely polarized for the D- and L-enantiomers. (c) Schematic of patterned chiral  $\alpha$ -helix polyaniline molecules (AHPA-L and AHPA-D) on a ferromagnetic thin film, separated by a conductive gold layer. (d,e) Magnetic force microscopy (MFM) of patterned AHPA-L and AHPA-D, respectively, show opposite magnetization orientation of the Co thin film induced by the chiral molecule. (f,g) Schematic proposals to use chirality to manipulate magnetically ordered 2D materials. (f) CrI<sub>3</sub> bilayers are known to be antiferromagnetically (AFM) oriented in the z-direction. By coating both sides of a CrI<sub>3</sub> bilayer with a conductive layer of molecules of the same chirality in a manner similar to (c), it may be possible to induce a ferromagnetic (FM) phase transition. (g) A ferromagnetic monolayer is patterned with a conductive layer and domains of opposite chirality. (a) and (b) reprinted with permission from <sup>398</sup>. Copyright 2018 American Chemical Society. (c), (d), and (e) reprinted from <sup>404</sup>. Copyright 2017 American Chemical Society. .... 163

## List of Tables

Table 2.1 $E_{REL}$ (standard deviation) for each phthalocyanine and layer number with 633 nm excitation laser .....	91
Table 2.2 $E_{REL}$ (standard deviation) for each phthalocyanine and layer number with 532 nm excitation laser .....	91
Table 3.1 Calculated Overlap Integrals and Quenching Factors .....	120
Table 4.1 Fitting parameters for the photoluminescence decay histograms of pentacene deposited on an hBN flake and on a non-hBN part of the substrate, excited at 570 nm. Three spots were evaluated at each region on the image. The IRF was fitted to a Gaussian ( $a_1, \tau_1$ ) and a biexponential decay ( $a_2, \tau_2, a_3, \tau_3$ ). .....	137

# 1. Chapter 1 Introduction and Literature Review

## 1.1. Motivation

Two-dimensional (2D) materials have experienced a massive growth in research interest due to their extraordinary optical and electrical properties. Individual 2D layers are held together by van der Waals (vdW) forces rather than covalent or ionic bonds. The weakness and non-specificity of this interaction means that arbitrary stacks of vdW materials can be layered without regard to epitaxy, which is a major obstacle in the fabrication of conventional 3D heterostructures. This enables new paradigms in the design of physical systems and electronic devices, potentially allowing measurement and control of new phenomena with unprecedented precision.

In contrast to the relative recency of work on 2D materials, organic semiconductors have been an active area of research for decades. While many of the fundamental rules for designing high-performance organic electronics are well understood, the central importance of interfaces and morphology are only now being elucidated. With this knowledge comes opportunities in hybrid systems, whereby the decades of experience of organic synthesis can be used to finely tune the interactions between organic molecules and inorganic components.

Given that both organic and 2D materials are held together in the solid state by vdW interactions, their interaction in mixed-dimensional heterojunctions is a natural next step in fabricating and understanding vdW heterojunctions. While many individual examples of organic

- 2D heterojunctions and devices exist in the literature, there has been little systematic work on understanding the fundamental rules by which the two materials couple. Given that organic synthesis allows the tuning of molecular electronic structure in ways that are not accessible to other material systems, systematic exploration of electronic coupling and other structure-property relationships in organic – 2D heterojunctions can be done with finer control than in many other mixed-dimensional heterojunctions. Elucidating the interactions between molecules and 2D materials is needed to extend this field from exploratory – that is, demonstrations of new systems with a single molecule and 2D material – to rationally designing heterojunctions that interact in specific and controlled ways.

The following literature review will give background information on 2D materials broadly, as well as the two materials that will be the focus of later chapters: molybdenum disulfide ( $\text{MoS}_2$ ) and hexagonal boron nitride (hBN). Following the 2D material discussion, the organic molecules that will be discussed in later chapters, phthalocyanines and pentacene, will be introduced in detail here. Next, the literature of mixed-dimensional organic – 2D heterojunctions will be reviewed. Within each section of the this introduction chapter, special attention will be given to the electronic structure, production, spectroscopic characterization, and device applications of each material or heterojunction being discussed.

## 1.2. Two-dimensional Materials

2D materials are a broad class of atomically thin solids. The study of these materials began in 2004 with the isolation of graphene, a single layer of  $\text{sp}^2$  bonded carbon, by Novoselov and

Geim.<sup>1,2</sup> After graphene, many other 2D materials were quickly isolated, spanning a wide range of chemical, electrical, optical, and magnetic properties (Figure 1.1a). Just as graphene was exfoliated from layered graphite, nearly any layered vdW crystal can be exfoliated. Other 2D materials have no layered crystal analogue, with their only layered phase existing at the ultrathin limit, as is the case of borophene,<sup>3</sup> or only existing confined between other material layers, as is the case of 2D GaN.<sup>4</sup> Major classes include transition metal monochalcogenides,<sup>5</sup> dichalcogenides,<sup>6</sup> phosphorus chalcogenides,<sup>7</sup> oxides,<sup>8</sup> halides,<sup>9</sup> carbides or nitrides (MXenes),<sup>10</sup> as well as layered monoelementals like black phosphorus,<sup>11</sup> and other synthesized monoelementals like borophene or stanene.<sup>12</sup> In addition, many new materials have structures that share many similarities with 2D materials despite not typically being considered within the 2D literature. These include metal-organic frameworks,<sup>13</sup> covalent organic frameworks,<sup>14</sup> and 2D perovskites.<sup>15</sup> All together, 2D materials represent a wide range of potential chemistries and properties, with many more waiting to be discovered. Work in later chapters will focus on a transition metal dichalcogenide, MoS<sub>2</sub>, as well as the 2D insulator hexagonal boron nitride (hBN). These two materials will be discussed in greater detail later in this chapter.

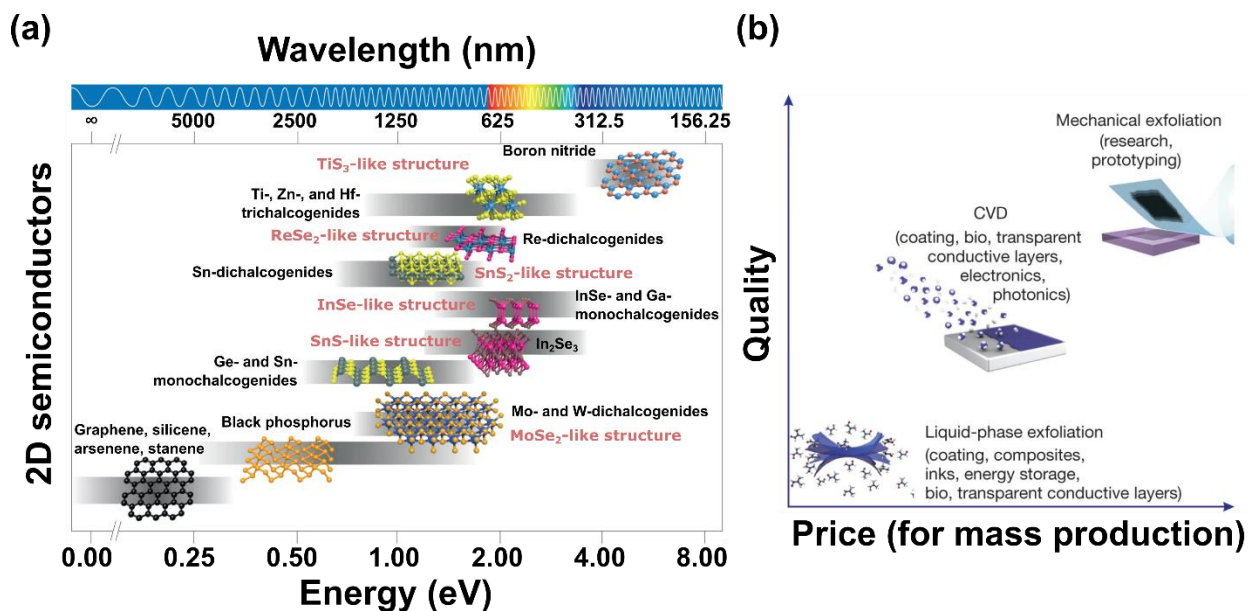


Figure 1.1 2D material classes and production. (a) Classes of 2D materials sorted by bandgap. (b) Major 2D material production methods sorted by quality and price / scalability. (a) reproduced from <sup>16</sup>. Copyright 2016 Springer Nature. (b) adapted from <sup>17</sup>. Copyright 2012 Springer Nature.

There are a wide array of methods to prepare 2D materials. They can be broadly classified as top-down exfoliation or bottom-up growth, with numerous methods in each category. Not every material is compatible with every method. For example, 2D materials with no corresponding bulk layered crystal cannot be exfoliated, and certain growth methods only work with a limited range of materials, like SiC graphitization to produce graphene. All methods have tradeoffs in material quality, scalability, and time investment. Figure 1.1b summarizes these tradeoffs for the three most widely used classes of 2D production methods: mechanical exfoliation (the ‘Scotch Tape’ method), chemical vapor deposition (CVD), and liquid phase exfoliation (LPE).

Mechanical exfoliation involves taking a bulk layered crystal and removing individual layers using adhesive tape,<sup>2</sup> solid polymers,<sup>18</sup> or gold films<sup>19</sup> to peel off individual 2D layers. This method requires the interaction between the crystal and tape is strong enough to peel off layers, but weak enough that the layers can be placed on another substrate and without tearing or fracturing the exfoliated layers.<sup>20</sup> This produces a random selection of flake thicknesses and lateral sizes, with monolayers typically needing to be found manually by microscope. These exfoliated flakes can subsequently be picked up and stacked to form vdW heterostructures with other materials.<sup>21</sup> Automating this process through robotics and computer vision is an active area of research.<sup>21</sup>

CVD production refers to the growth of 2D materials by flowing gaseous precursors over a substrate. Production of 2D materials by CVD can produce wafer scale ( $> 1 \text{ cm}^2$ ) monolayers, though often with more defects than those produced by mechanical exfoliation.<sup>22,23</sup> The precursors, substrates, and methods of CVD are too numerous to list here, with some materials having dozens of published processes.<sup>24–26</sup>

LPE refers to a broad class of exfoliation methods in which a powder of the bulk 2D crystal is suspended in a solvent and then subject to a process that exfoliates the individual layers.<sup>27</sup> This can include high energy processes such as sonication,<sup>28</sup> shear mixing,<sup>29</sup> and wet-jet milling,<sup>30</sup> or intercalation based methods like lithiation<sup>31</sup> or electrochemical exfoliation.<sup>32</sup> The larger scale of production and solvent-dispersed product enable the use of 2D materials in applications like printable electronics<sup>33,34</sup> and battery additives.<sup>35,36</sup>

### 1.2.1. Molybdenum Disulfide and the Transition Metal Dichalcogenides

The transition metal dichalcogenides (TMDs) are a broad class of layered materials of the form  $\text{MX}_2$ , where M is a transition metal (typically Mo or W) and X is a chalcogen (S, Se, Te). The metal has an oxidation state of +4 and the chalcogen is -2. Of the ~60 materials with this form, about two-thirds have layered structures that can potentially be exfoliated to the monolayer limit.<sup>37</sup> The electronic properties of the TMDs are largely dependent on the d-orbital filling and splitting of the metal.<sup>38</sup> A filled d-band will result in semiconducting behavior, while partial filling results in a metallic material. TMDs can also exhibit more exotic conduction behaviors such as superconductivity<sup>39</sup> and the quantum spin Hall effect.<sup>40</sup>

The crystal structure and d-orbital filling of a TMD are linked. A TMD layer will typically adopt either a trigonal prismatic coordination structure with  $D_{3h}$  symmetry (called the 2H phase, or 1H in the monolayer limit), or an octahedral coordination with  $D_{3d}$  symmetry (called the 1T phase).<sup>38</sup> The coordination of the TMD metal will determine its d-orbital splitting, with the trigonal prismatic phase creating three degenerate states split by ~1 eV ( $d_z^2$ ,  $d_{x^2-y^2, xy}$ ,  $d_{xz, yz}$ ), while the octahedral phase creates two degenerate states – the  $t_{2g}$  ( $d_{xy, yz, xz}$ ) and  $e_g$  ( $d_z^2, x^2-y^2$ ). Group 4 and 6 TMDs typically adopt the 2H phase, while group 10 will typically have a 1T phase. Group 5 can have either phase, and group 7 TMDs form distorted 1T phases.<sup>38</sup> Figure 1.2a-c summarizes these possible structures.

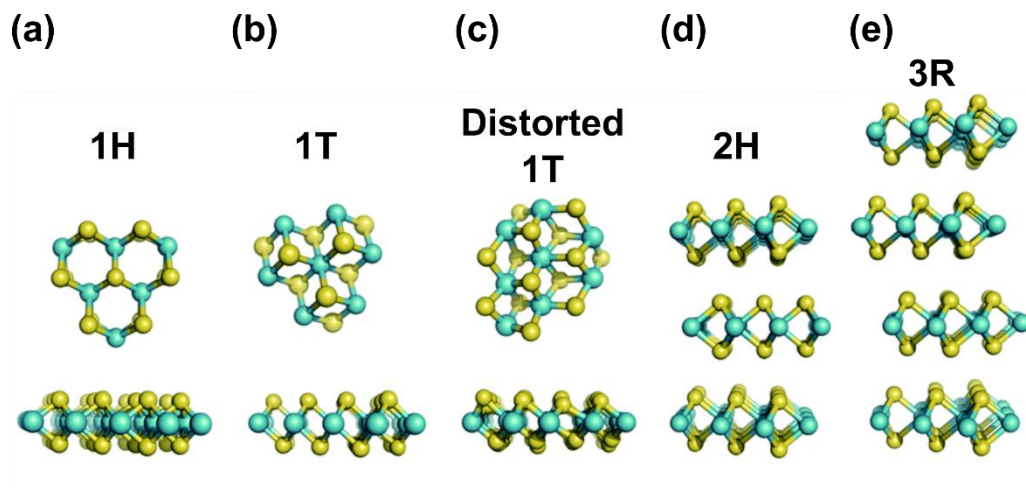


Figure 1.2 Phases of TMDs. (a) 1H monolayer with metal in a trigonal prismatic coordination (b) 1T phase, with metal in an octahedral coordination. (c) Distorted 1T phase, in an asymmetric octahedral coordination. (d) AB stacking of 2H phase MoS<sub>2</sub>. (e) ABC stacking of 3R phase MoS<sub>2</sub>. Figure reproduced from <sup>38</sup>. Copyright 2015 The Royal Society of Chemistry.

Of the TMDs isolated at the monolayer limit, MoS<sub>2</sub> is perhaps the most studied. It was among the first 2D semiconductors exfoliated to a monolayer and as such has a large body of work on its optical and electrical properties.<sup>41</sup> In many ways MoS<sub>2</sub> is representative of the semiconducting TMDs, and it will be the focus of later work in this thesis, so the rest of this chapter will focus on it. Many of the chemical, optical, and electronic trends discussed are also applicable to the other Mo – and W – based TMDs.

### *MoS<sub>2</sub> Structure*

As expected of a TMD with a group 4 metal, MoS<sub>2</sub> adopts a trigonal prismatic phase. The layer stacking can also vary. In MoS<sub>2</sub> crystals, the most common stacking order is 2H phase (Figure 1.2d), with an AB packing between the layers resulting in hexagonal symmetry.<sup>42</sup> An ABC layering, called the 3R phase (Figure 1.2e), is also possible, resulting in rhombohedral symmetry.<sup>38</sup> Creating the 3R phase requires either specialized synthesis methods<sup>43</sup> or folding of exfoliated MoS<sub>2</sub>.<sup>44</sup> The bandgap of the 3R phase is similar to the 2H phase,<sup>44</sup> but its broken inversion symmetry above the monolayer limit makes 3R MoS<sub>2</sub> a potentially useful material for nonlinear optics.<sup>45</sup>

It is also possible to change the phase of MoS<sub>2</sub> through chemical treatment. Adding excess charge of 0.2 – 0.4 electrons per Mo will make the 1T phase more stable than the 2H phase.<sup>46</sup> This is typically done in the liquid phase by lithium intercalation (using n-butyllithium in hexane)<sup>31</sup> or in the solid state using lithium borohydride.<sup>47,48</sup> In either case, the lithium intercalated MoS<sub>2</sub> is then exposed to water, which dissolves the powder into sheets of monolayer or few-layer 1T phase material. The 2H to 1T transition changes the MoS<sub>2</sub> from a filled d<sub>z</sub><sup>2</sup> band to a partially filled t<sub>2g</sub> band, resulting in a semiconducting to metallic transition (Figure 1.3a).<sup>49</sup> This results in enhanced conductivity<sup>49,50</sup> as well as quenching of photoluminescence.<sup>31</sup>

The band structure of semiconducting 2H MoS<sub>2</sub> changes drastically as it is thinned from bulk to monolayer. Its bandgap transitions from indirect to direct and widens from 1.3 eV to 1.9 eV,<sup>41,51,52</sup> which results in a drastic blue-shift and brightening of its photoluminescence (PL) in

the monolayer form.<sup>41</sup> Orbital analysis of the MoS<sub>2</sub> band structure explains this crossover (Figure 1.3b). The K point, composed mostly of in-plane Mo d-orbitals and S p-orbitals, is the

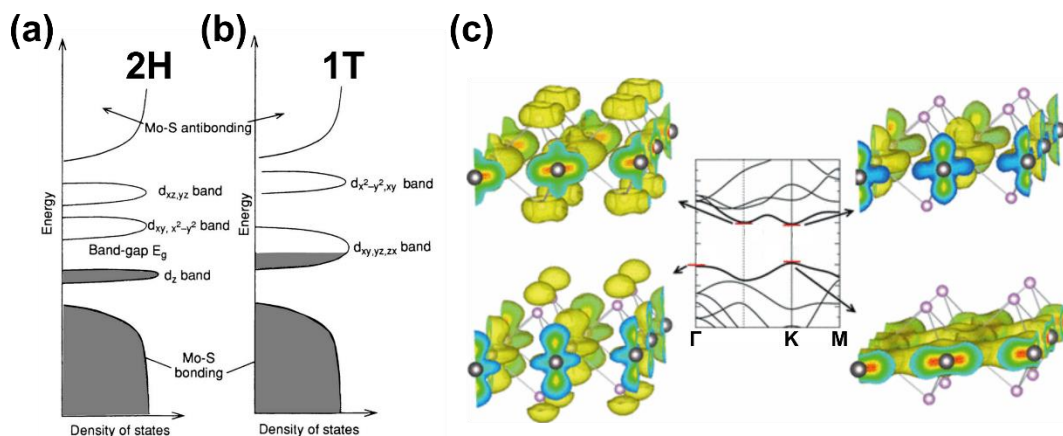


Figure 1.3 MoS<sub>2</sub> band diagrams. Qualitative band diagram of (a) 2H MoS<sub>2</sub> and (b) 1T MoS<sub>2</sub>. The highest occupied band ( $d_z^2$ ) in the 2H phase is filled, making it semiconducting. In the 1T case, the  $t_{2g}$  band is only partially filled, making it metallic. (c) Band structure and charge densities of 1H MoS<sub>2</sub> at selected areas near band edges. The VBM at  $\Gamma$  and CBM at K are primarily Mo  $d_z^2$  orbitals, with some S  $p_z$  character. The VBM at K is primarily  $d_{xy}$  and  $d_{x^2-y^2}$ , as does the local minimum of the CBM between K and  $\Gamma$  (the  $\Lambda$  point). (a) and (b) adapted from<sup>49</sup>, Copyright 1993 The Royal Society of Chemistry. (c) reproduced from<sup>52</sup>. Copyright 2013 American Physical Society.

conduction band minimum (CBM) and valence band maximum (VBM) of monolayer MoS<sub>2</sub>.<sup>52</sup>

When moving from a monolayer to a bilayer of MoS<sub>2</sub>, repulsion between out-of-plane S  $p_z$  orbitals drives the energy of the valence band  $\Gamma$  higher such that it becomes the new VBM.<sup>52</sup> The conduction band is less affected, become lower energy at  $\Lambda$  but still maintaining a minimum at K. Thus bilayer has an indirect bandgap, with the CBM at K and the VBM at  $\Gamma$ .<sup>52</sup>

Spin effects also play a prominent role in the electronic structure of MoS<sub>2</sub>. Large spin-orbit coupling causes large spin splitting of the valence band by more than 100 meV.<sup>53</sup> This

causes the K points of the CBM and VBM to split into degenerate valleys of opposite spin, denoted as K and K' (or K<sup>+</sup> and K<sup>-</sup>). In the absence of inversion symmetry, the valley and spin degrees of freedom become coupled in MoS<sub>2</sub> such that  $E_{\downarrow}(k) = E_{\uparrow}(-k)$ , where E is the energy of the given spin projection (up or down) and k is the crystal momentum.<sup>53</sup> This leads to optical selection rules in which circularly polarized light will couple to a specific spin-valley, allowing optical control of the spin – valley degree of freedom (Figure 1.4a and 1.4b).<sup>54–56</sup> This ability to manipulate spin-valley information through optical and magnetic control has led to interest in MoS<sub>2</sub> and other TMDs for valleytronics, in which the valley degree of freedom is manipulated for computing applications.<sup>57,58</sup> The primary appeal of such systems is that valley information is momentum protected, thus allowing very low power consumption information processing assuming that intervalley scattering can be minimized.<sup>58</sup>

When discussing structure-property relations in MoS<sub>2</sub>, it is important to include defects. Of the common point defects in MoS<sub>2</sub>, sulfur vacancies ( $S_{\text{vac}}$ ) are observed to be the most common defect in MoS<sub>2</sub> due to their low energy of formation.<sup>59–61</sup> The  $S_{\text{vac}}$  is predicted to create a donor-like state near the CBM of MoS<sub>2</sub> and thus it is commonly invoked to explain n-type transport observed in MoS<sub>2</sub>. This view is complicated by recent observations that many apparent  $S_{\text{vac}}$  are actually oxygen substitutions ( $O_{\text{sub}}$ ).<sup>62,63</sup> These  $O_{\text{sub}}$  appear to form upon exposure to O<sub>2</sub> or H<sub>2</sub>O,<sup>64</sup> and this reaction is sped by light,<sup>64</sup> making it likely that some of the previous experimental literature on MoS<sub>2</sub> defects will need to be reevaluated.  $O_{\text{sub}}$ s are predicted to create acceptor-like states near the VBM, where they would act as p-dopants.<sup>63</sup> The electronic structure of these point defects in MoS<sub>2</sub> is shown in Figure 1.4c. Reconciling these observations, the

higher than expected population of  $O_{\text{subs}}$  and the ubiquitous n-type transport in  $\text{MoS}_2$ , will be an important research question in the near future.

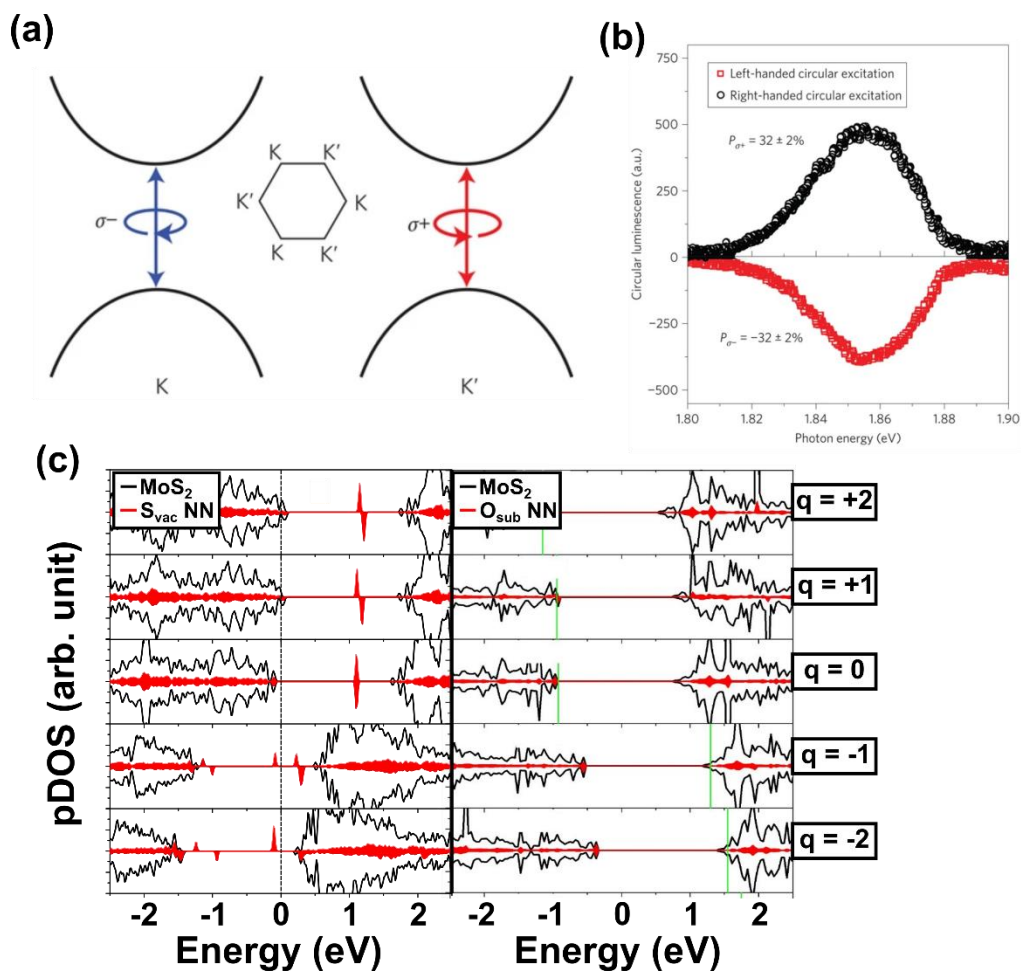


Figure 1.4 Valley polarization and point defects. (a) Schematic of valley polarization by coupling of degenerate K valleys to opposite circularly polarized light. (b) Polarization of  $\text{MoS}_2$  emission by pumping with near-band edge circularly polarized light at low temperature.  $P$  is a measure of the efficiency of valley polarization in the  $\text{MoS}_2$ , calculated by  $P = [I(\sigma^+) - I(\sigma^-)] / [I(\sigma^+) + I(\sigma^-)]$ , where  $I(\sigma_{\pm})$  is the intensity of the left (right)-handed circularly polarized component of the PL. (c) Project density of states (pDOS) of  $\text{MoS}_2$  with a sulfur vacancy ( $S_{\text{vac}}$ ) or and oxygen

substitution ( $O_{\text{sub}}$ ). The red nearest neighbor (NN) components of the pDOS represent the localized states adjacent to the point defect. (a) and (b) reproduced from <sup>55</sup>. Copyright 2012 Springer Nature. Calculations in (c) performed by Luqing Wang. Further details will be discussed in Chapter 3.

### *MoS<sub>2</sub> Production*

Micromechanical exfoliation from high quality crystals is the most common method to produce single crystal flakes of 2D MoS<sub>2</sub>. While scotch tape is still the standard, gold film-based exfoliation processes have in certain conditions shown superior results.<sup>65</sup> Heating in hydrogen is often used to remove tape residues to produce clean interfaces.<sup>66</sup>

When large area monolayers are needed, chemical vapor deposition (CVD) is used. There are two broad methods of CVD production of MoS<sub>2</sub>: powder, and metal-organic.<sup>67</sup> Powder CVD uses solid sulfur and MoO<sub>3</sub> heated in an inert carrier gas upstream from the target substrate,<sup>68</sup> while metal-organic CVD uses more reactive gaseous precursors such as Mo(CO)<sub>6</sub> and H<sub>2</sub>S.<sup>69</sup> Further development of precursors and substrate treatments are an active area of research.<sup>70–72</sup> Other related production methods include atomic layer deposition (ALD)<sup>73</sup> and heating solution-based precursors,<sup>74</sup> though these methods tend to produce nanocrystalline or amorphous material.

Large scale production of 2D MoS<sub>2</sub> is possible by liquid phase exfoliation (LPE),<sup>27</sup> though often with a tradeoff in material quality. The most common lab-scale method is sonication in a high-boiling solvent like N-methyl-2-pyrrolidone (NMP)<sup>75</sup> or a mixture of ethanol

and water.<sup>28</sup> Chemical exfoliation by intercalating Li atoms, followed by dissolving/exploding in water produces largely monolayer 1T MoS<sub>2</sub>.<sup>31</sup> Other LPE methods include shear mixing<sup>76</sup> and electrochemical exfoliation.<sup>32</sup>

### *MoS<sub>2</sub> Spectroscopy*

The UV-Vis absorption spectrum of MoS<sub>2</sub> has two primary peaks, corresponding to its excitonic absorption. They are centered at 670 nm and 620 nm for monolayer MoS<sub>2</sub> (Figure 1.5a) and are referred to as the A and B excitons, respectively. Both of these peaks are due to direct K→K transitions, and are split in energy due to spin-orbit coupling.<sup>77,78</sup> MoS<sub>2</sub> absorbs strongly in the visible spectrum due to large overlap between the orbitals in the CBM and VBM resulting in high oscillator strengths.<sup>79</sup> The high absorption makes MoS<sub>2</sub> attractive for photovoltaic applications – it has been estimated that a monolayer of MoS<sub>2</sub> can absorb as much as 10% of incoming solar radiation with a layer less than one nm thick.<sup>79</sup>

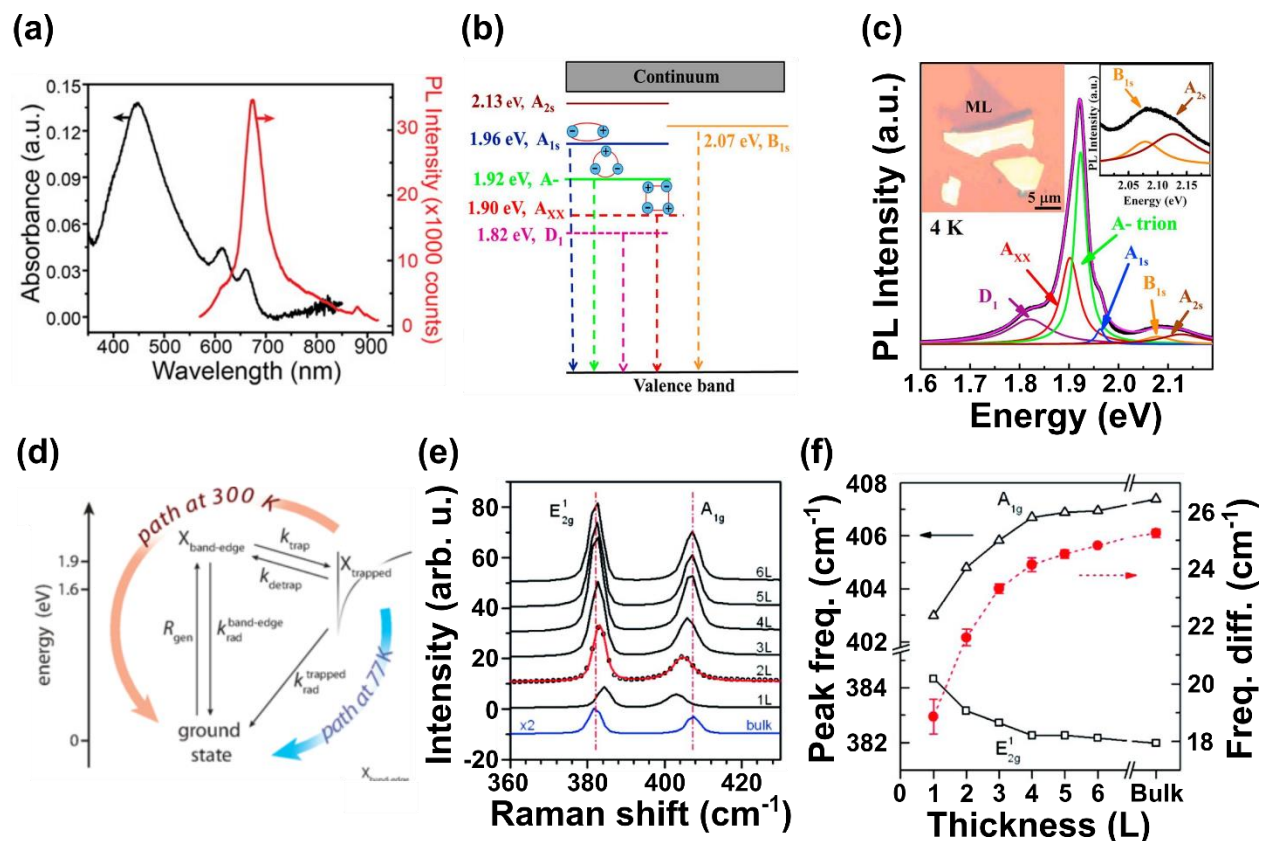


Figure 1.5 MoS<sub>2</sub> spectroscopy. (a) UV-Vis absorption spectrum and PL spectrum at room temperature. (b) Schematic of different excitonic states in MoS<sub>2</sub> and their relative energies. (c) Low temperature PL spectrum of MoS<sub>2</sub> showing deconvolution of different excitonic states. (d) Schematic of trapping and radiative recombination pathways illustrating temperature dependence of defect PL. (e) Layer dependent Raman spectra of the MoS<sub>2</sub> E<sub>2g</sub> and A<sub>1g</sub> modes. (f) Change of peak position in (e) versus thickness, as well as the change in A<sub>1g</sub> - E<sub>2g</sub>. (a) reproduced from <sup>68</sup>. Copyright 2016 American Chemical Society. (b) and (c) reproduced from <sup>80</sup>. Copyright 2019 Elsevier. (d) reproduced from <sup>81</sup>. Copyright 2017 American Physical Society. (e) and (f) reproduced from <sup>82</sup>. Copyright 2010 American Chemical Society.

As expected from its direct bandgap, MoS<sub>2</sub> has relatively bright PL,<sup>83</sup> with photoluminescence quantum yields (PLQY) up to 100% following chemical treatments and at low incident powers.<sup>84</sup> The photoluminescence (PL) spectrum of MoS<sub>2</sub> contains a multitude of information about a given flake. Due to geometric confinement reducing out-of-plane dielectric

screening, excited electrons and holes have a strong Coulomb interaction which results in very high exciton binding energies on the scale of 100s of meV.<sup>85</sup> In addition to neutral excitons, other bound states also exist at room temperature in MoS<sub>2</sub> such as trions,<sup>86</sup> biexcitons,<sup>87</sup> and defect-bound excitons.<sup>81</sup> A schematic representation of each of these species is shown in Figure 1.5b, and their contribution to the PL spectrum shown in Figure 1.5c.

The trion is a bound state of three charge carriers, in MoS<sub>2</sub> usually two electrons and a hole. This species is usually convoluted with the A exciton PL and must be extracted by careful fitting of the PL spectrum. The binding energy of negative trions in MoS<sub>2</sub> is 20 – 50 meV<sup>86</sup> and both their binding energy and population are strongly responsive to gate voltages.<sup>86</sup> The neutral exciton to trion ratio is also sensitive to doping and can be changed using molecular dopants.<sup>88</sup> As a result, the ratio of neutral exciton to trion emission is typically used as a proxy for doping in MoS<sub>2</sub> samples, with red-shifted PL typical of increased trion emission (n-doping) while blue-shifted PL typical of dominant A-exciton emission (intrinsic or p-doping).<sup>89</sup> Trions also have higher rates of nonradiative decay than neutral excitons, so many strategies to improve PLQY revolve around doping TMDs to be closer to intrinsic semiconductors.<sup>90–92</sup>

Interest in biexcitons has increased in recent years because their recombination produces entangled photon pairs,<sup>93</sup> which has potential applications in quantum information science. The biexciton is a bound state of four carriers, two electrons and two holes. These exist a few meV lower than trions, but are typically only observable at very high excitation power and their spectra must be carefully deconvoluted from trions and defect-bound excitons.<sup>80,87,94</sup> While

biexcitons can be formed by the combination of two neutral excitons, experimentally they have been shown to form more readily from the combination of a trion and a free carrier of opposite charge, forming an excited-state biexciton.<sup>80,95</sup>

The defects in MoS<sub>2</sub> are also optically active. The most prominent of these is a PL peak that appears at low temperatures (< 100 K) centered around 1.7 eV, originating from localized states of mixed 0D-2D character.<sup>96</sup> The temperature dependence of the defect emission is due to thermal equilibrium with the neutral exciton, shown schematically in Figure 1.5d.<sup>81</sup> The defect bound exciton has a long PL lifetime on the order of ten microseconds, so despite being heavily favored thermodynamically compared to the neutral exciton, the much faster recombination of the neutral exciton makes it dominate PL at high temperatures.<sup>81</sup> The defect PL will be discussed in greater detail in Chapter 3.

Raman scattering is widely used to characterize the thickness of MoS<sub>2</sub>. There are two prominent Raman active modes, the E<sub>2g</sub> (near 380 cm<sup>-1</sup>) and A<sub>1g</sub> (near 405 cm<sup>-1</sup>).<sup>82</sup> The E<sub>2g</sub> corresponds to in-plane shear modes while the A<sub>1g</sub> is an out-of-plane chalcogen vibration.<sup>82</sup> The A<sub>1g</sub> decreases in energy as MoS<sub>2</sub> is thinned below six layers, while the E<sub>2g</sub> stiffens, and as a result the difference between these two peaks reduces from 25 cm<sup>-1</sup> in bulk MoS<sub>2</sub> to 19 cm<sup>-1</sup> at the monolayer limit (Figure 1.5e, f).<sup>82</sup> This difference is a common method of determining MoS<sub>2</sub> thickness. Strain can also shift the position of these peaks by a 1 – 3 cm<sup>-1</sup>.<sup>97</sup>

Much of the early interest in MoS<sub>2</sub> was around its application as a 2D semiconductor in electronic devices. Early monolayer MoS<sub>2</sub> field-effect transistors (FETs) fabricated on SiO<sub>2</sub> had mobilities on the order of 0.1 - 10 cm<sup>2</sup> V<sup>-1</sup> s<sup>-1</sup>, but notably high on/off ratios of 10<sup>8</sup>.<sup>98,99</sup> This mobility limitation is likely due to scattering from traps in the SiO<sub>2</sub> substrate which cause the conduction mechanism in to be thermally-activated, with variable range hopping transport at low temperatures (Figure 1.6a).<sup>98,100</sup> Mobilities above 100 cm<sup>2</sup> V<sup>-1</sup> s<sup>-1</sup> have been measured in hBN – encapsulated MoS<sub>2</sub> FETs,<sup>101</sup> but these are still far below the predicted room-temperature phonon-limited mobility of 410 cm<sup>2</sup> V<sup>-1</sup> s<sup>-1</sup>.<sup>102</sup> Due to its mechanical strength and flexibility,<sup>103</sup> MoS<sub>2</sub> has also found application in flexible electronics,<sup>104</sup> and LPE MoS<sub>2</sub> has been used in inks for printed electronics.<sup>105</sup>

Other electrical devices have been fabricated which use the unique physical properties of MoS<sub>2</sub>. Heterojunctions with graphene have exploited the dimensionality of MoS<sub>2</sub> to create tunneling FETs.<sup>106</sup> Mobile grain boundaries and point defects in MoS<sub>2</sub> have been used to fabricate memristors<sup>107</sup> and memtransistors (Figure 1.6b).<sup>108</sup> Porous composites of MoS<sub>2</sub> with nanocarbons have found use as supercapacitors<sup>109</sup> and battery electrodes.<sup>110</sup>

The high absorption of MoS<sub>2</sub> has also motivated its application in photonic and optoelectronic devices.<sup>79</sup> Efforts at photonic engineering have shown near-unity absorption of solar radiation in ultrathin films (Figure 1.6c).<sup>111</sup> Bulk MoS<sub>2</sub> was explored as a photovoltaic material as far back as the 1980s, and ultrathin photovoltaics of MoS<sub>2</sub> p-n junctions have

achieved a modest power conversion efficiency (PCE) of 2.8%.<sup>112</sup> MoS<sub>2</sub> – 2D photovoltaic heterojunctions have also shown modest performance,<sup>113</sup> and TMDs have also been explored as a

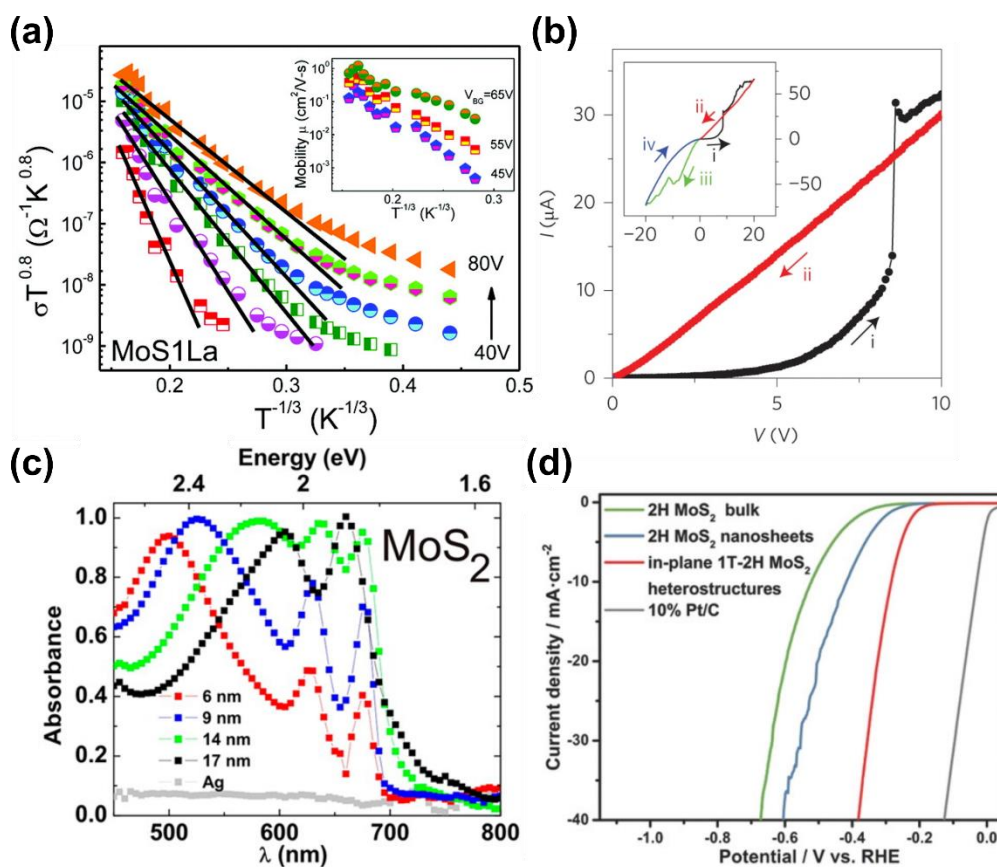


Figure 1.6 MoS<sub>2</sub> electrical and optical devices. (a) Temperature dependence of conductivity of a monolayer MoS<sub>2</sub> FET on SiO<sub>2</sub>. Linear dependence on  $T^{-1/3}$  is characteristic of variable range hopping. Inset shows mobility versus temperature behavior. (b) Partial I-V plot of an intersecting MoS<sub>2</sub> grain boundary memristor. Inset shows the full I-V characteristics of on switching cycle. (c) Absorbance spectra of thin MoS<sub>2</sub> flakes of different thicknesses with a micrometer-scale ring electrode. The semiconductor/metal interface increases the local density of states, resulting in near-unity absorption from ultrathin films. (d) Linear sweep voltammetry curves illustrating the relative performance of 2H and 1T MoS<sub>2</sub> electrocatalysts at the hydrogen evolution reaction versus platinum. (a) is reproduced from<sup>100</sup>. Copyright 2011 American Chemical Society. (b) is

reproduced from <sup>107</sup>. Copyright 2015 Springer Nature. (c) is reproduced from <sup>111</sup>. Copyright 2016 American Chemical Society. (d) is reproduced from <sup>114</sup>. Copyright 2018 Wiley-VCH

ternary additive in organic photovoltaic (OPV) active layers.<sup>115</sup> The excellent optical and electrical properties of MoS<sub>2</sub> has also motivated its use in high performance photodetectors.<sup>116</sup> MoS<sub>2</sub> has also seen tremendous interest as a photoelectrocatalyst,<sup>117</sup> particularly in the application of the 1T phase for the hydrogen evolution reaction (Figure 1.6d).<sup>118</sup>

### 1.2.2. Hexagonal boron nitride

Aside from TMDs, hexagonal boron nitride (hBN) will be used prominently in this work, particularly in Chapter 4. hBN is widely used as a 2D insulator, acting as an inert substrate or a dielectric layer. Its low density of defects compared to substrates like SiO<sub>2</sub>, as well as its ability to encapsulate materials and expel adsorbed molecules, make it attractive for studying the high-performance limits of 2D materials.<sup>25,119</sup> It also possesses a wide bandgap of 5-6 eV,<sup>25,120</sup> making it useful as an electrical insulator. While outside the topic of this dissertation, hBN also has extraordinary thermal and mechanical properties, with a measured thermal conductivity of 360 W m<sup>-1</sup> K<sup>-1</sup> <sup>121</sup> and a Young's modulus above 1 TPa.<sup>122</sup>

#### *hBN Structure*

HBN is a honeycomb lattice of sp<sup>2</sup>-hybridized B and N. Bulk hBN is a layered crystal with the individual layers held together by vdW forces at a spacing of 0.333 nm (Figure 1.7a).<sup>120</sup> Theory has predicted both indirect- and direct- bandgaps in hBN at a variety of bandgaps, but experimentally its optical properties are dominated by a direct bandgap of 5-6 eV, depending on

the hBN quality and thickness.<sup>25,120</sup> The valence band of hBN is composed of overlapping  $\sigma$  and  $\pi$  bands,<sup>123</sup> and both the VBM and CBM have strong  $\pi$  character, with the VBM localized on the nitrogen atoms while the CBM is localized on the boron atoms.<sup>124</sup> The experimentally measured valence band structure is shown in Figure 1.7b.

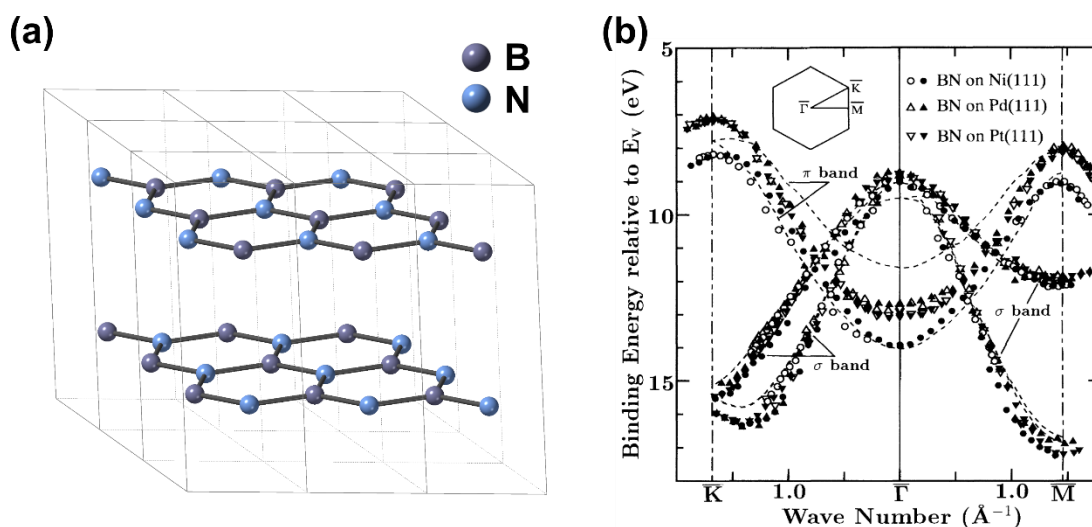


Figure 1.7 Structure of hBN. (a) Crystal structure of hBN. (b) Valence band structure of monolayer hBN grown on Ni(111), Pd(111), and Pt(111), measured by angle-resolved ultraviolet photoelectron spectroscopy (ARUPS). (b) reproduced from 71. Copyright 1995 American Physical Society.

### *hBN Spectroscopy*

HBN is transparent through the visible range, only absorbing light in the deep UV above 5 eV.<sup>125</sup> Its absorption spectrum shows a series of peaks from 5.822 eV to 5.968 eV, in a progression characteristic of free-exciton s-like absorption.<sup>120</sup> Bulk hBN shows a single PL peak 5.765 eV due to direct bandgap recombination of free excitons.<sup>120</sup> Figure 1.8a shows representative absorption and emission spectra of bulk hBN. In contrast to many other 2D materials, the PL energy of hBN is not strongly thickness dependent – in the monolayer form it is

still 5.76 eV,<sup>126</sup> likely due to strongly localized excitons. In addition to direct-bandgap PL, lower quality hBN will also exhibit defect-associated PL in the 1.5 – 4 eV range,<sup>126,127</sup> At low temperatures, narrow defect PL in hBN has been investigated as a single-photon emitter for quantum information technologies.<sup>127</sup> Representative defect PL spectra are shown in Figure 1.8b.

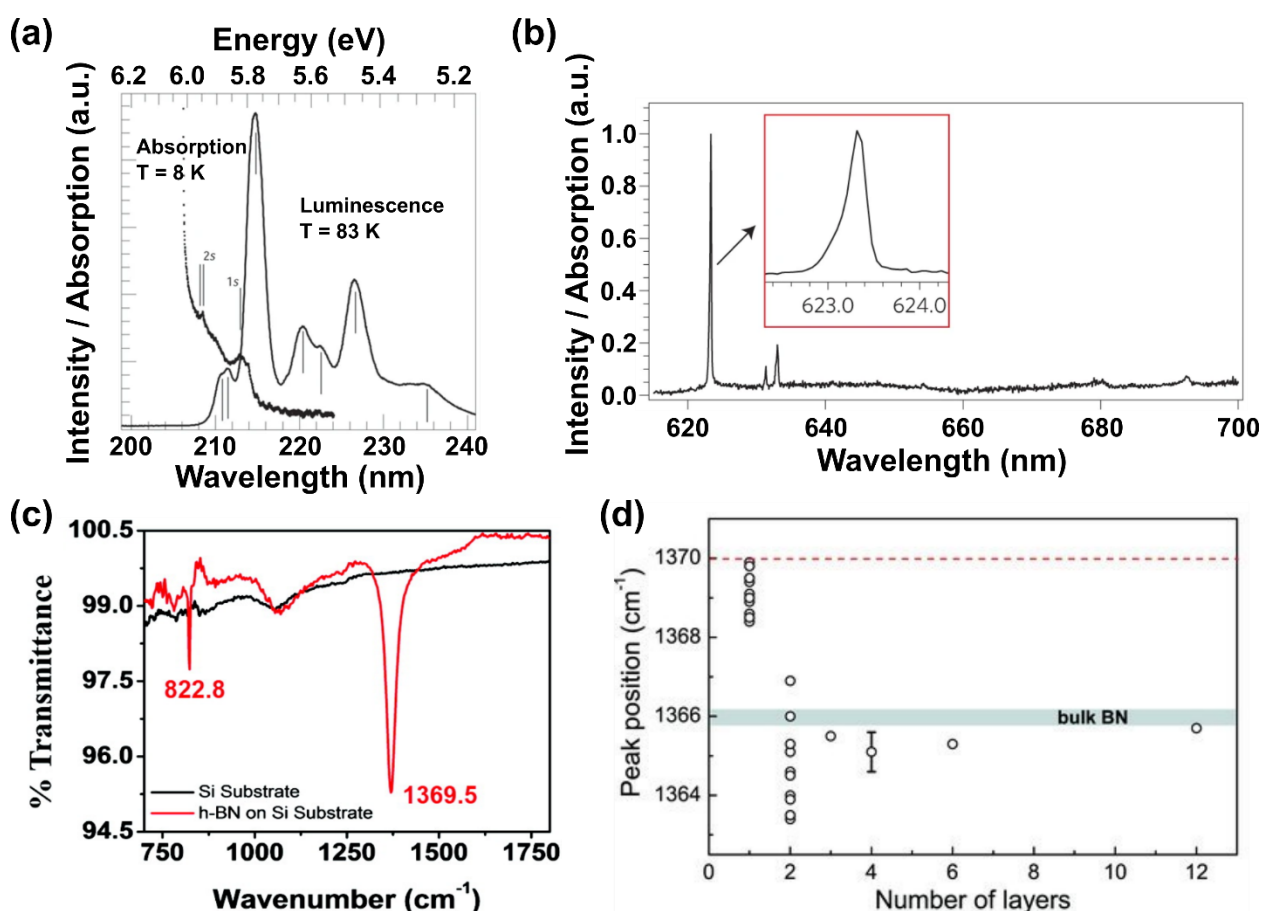


Figure 1.8 Spectroscopy of hBN. (a) Absorption and cathodoluminescence spectra of bulk hBN taken at low temperature. The absorption spectrum shows higher wavelength peaks corresponding to the excitonic Rydberg series, with the direct bandgap absorption occurring at 207 nm. The peaks 215 nm and below in the cathodoluminescence spectrum are due to the excitonic recombination, while the lower energy peaks are due to defect-bound excitons. (b) PL spectrum of hBN defect center in monolayer hBN, taken at 77 K. The inset shows the zero phonon line. (c) FTIR spectrum of few layer hBN grown on Si/SiO<sub>2</sub>. (d) Position of the hBN E<sub>2g</sub>

Raman mode versus thickness for mechanically exfoliated hBN. (a) adapted from <sup>120</sup>. Copyright 2004 Springer Nature. (b) reproduced from <sup>127</sup>. Copyright 2016 Springer Nature. (c) reproduced from <sup>125</sup>. Copyright 2010 American Chemical Society. (d) reproduced from <sup>128</sup>. Copyright 2011 Wiley-VCH.

The vibrational spectra of hBN show relatively few features, showing two IR absorptions and one characteristic Raman peak in addition to weaker two-phonon peaks.<sup>125,129</sup> The two IR modes are an  $E_{1u}$  in-plane ring vibration at  $1369\text{ cm}^{-1}$  and an out-of-plane  $A_{2u}$  mode at  $823\text{ cm}^{-1}$ ,<sup>125,129</sup> shown in Figure 1.8c. The Raman spectrum shows a single peak near  $1370\text{ cm}^{-1}$  (Figure 1.8d) associated with an  $E_{2g}$  B-N vibration.<sup>125,130</sup> The position of this peak will vary by several wavenumbers in response to stress on the hBN due to growth conditions, interactions with the substrate, and applied external forces.<sup>130</sup> Following mechanical exfoliation, the Raman peak will be  $1368\text{-}1370\text{ cm}^{-1}$  for monolayer hBN and  $1363\text{--}1367\text{ cm}^{-1}$  for thicker layers.<sup>128</sup>

### *hBN Production*

As with other 2D materials, hBN is produced by either top-down exfoliation (mechanical, liquid-phase) or bottom-up growth (CVD). At the moment, mechanical exfoliation of high-quality crystals produces the best results when the crystal source and cleaning procedure are optimized.<sup>131</sup> Large area growth is typically done by CVD using borazine<sup>132</sup> or ammonia borane<sup>133</sup> precursors on a Cu film, though improved large-area monolayer growth using other methods, precursors, and substrates is an active area of research.<sup>25</sup> Typical 2D hBN films by these two production methods are shown in Figure 1.9a and 1.9b.

### *hBN Devices*

As mentioned at the beginning of this section, hBN is often used as an inert substrate for other nanomaterials. Its large bandgap and high energy surface optical phonons reduce substrate induced carrier scattering, and its dielectric constant of 3-4 make it usable as a gate dielectric in transistors.<sup>25</sup> As an example of the advantages of hBN in this context, the first hBN-gated graphene FET had a mobility of  $60,000 \text{ cm}^2 \text{ V}^{-1} \text{ s}^{-1}$ , a large improvement over the state-of-the-art on  $\text{SiO}_2$  (Figure 1.9c).<sup>134</sup> In addition to better performance, hBN encapsulated materials, making it an attractive capping layer for ambient reactive 2D materials such as InSe,<sup>135</sup>  $\text{CrI}_3$ ,<sup>136</sup> and 2D perovskites.<sup>137</sup> This inertness has also found application as a substrate for templating the epitaxial growth of organic molecules,<sup>138</sup> which will be discussed in detail in a later section.

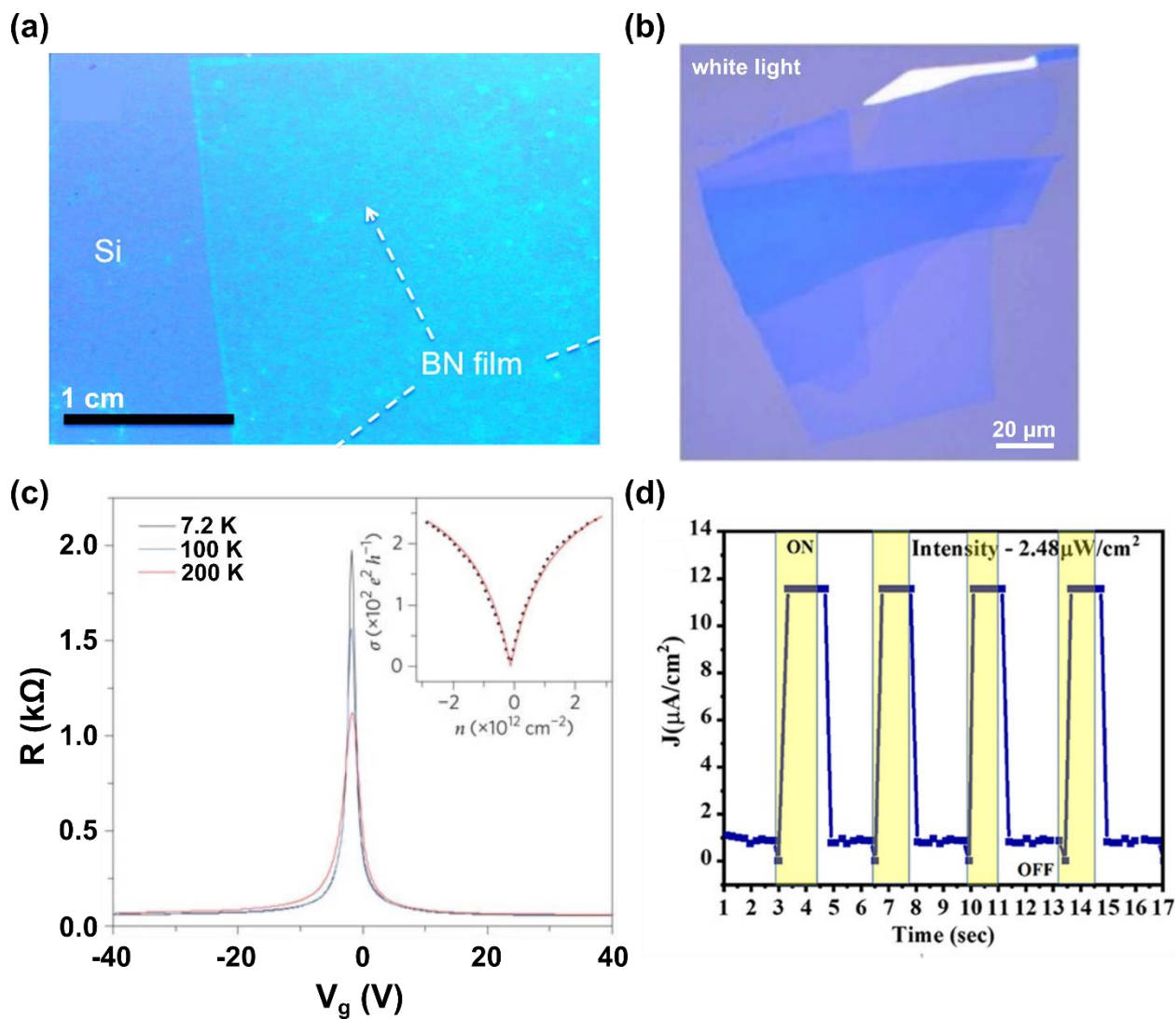


Figure 1.9 hBN production and devices. (a) Photograph of large area CVD hBN transferred onto an Si substrate. (b) White light microscope image of mechanically exfoliated monolayer and few-layer hBN. (c) Temperature dependent resistance versus gate voltage of hBN-encapsulated Graphene. Inset shows the corresponding conductivity. (d) Temporal response of a drop cast hBN photodetector with 254 nm illumination. (a) adapted from <sup>130</sup>. Copyright 2010 American Chemical Society. (b) adapted from <sup>128</sup>. Copyright 2011 Wiley-VCH. (c) reproduced from <sup>134</sup>. Copyright 2010 Springer Nature. (d) reproduced from <sup>139</sup>. Copyright 2021 American Chemical Society.

Its direct, wide bandgap has also made hBN a promising material for UV optoelectronics. Photodetectors using an hBN absorber have demonstrated high performance (Figure 1.9d).<sup>139,140</sup> As mentioned above, engineering the defect PL in hBN for single-photon emission is a promising area of research in quantum information sciences.<sup>127,141</sup> hBN has also been suggested as a candidate material for deep ultraviolet lasing,<sup>120</sup> but to date this has not been conclusively demonstrated.

### 1.3. Phthalocyanines

Phthalocyanines (Pc) are a broad class of conjugated macrocycles with the structural framework shown in Figure 1.10a. Pc are most commonly synthesized from o-phthalonitrile, with the metal phthalocyanines (MPc) formed by the addition of a metal salt to the synthesis.<sup>142</sup> They are widely produced industrially as pigments, with annual production of nearly  $10^8$  kg per year.<sup>143</sup> Copper phthalocyanine (CuPc) is widely used as a textile dye and is the single largest volume colorant sold, and other Pc have found use in ink toners, plastic plastic coloring, and other applications.<sup>144</sup> Their popularity as a dye stems from their facile synthesis and exceptional stability to high temperatures, light, and solvents.<sup>142</sup>

#### *Phthalocyanine Chemistry*

The variety of synthetic modifications possible on Pc has contributed to their variety of uses. The fully organic Pc has two hydrogens in the center bonded to opposite nitrogens with a  $D_{2h}$  symmetry and is referred to as  $H_2Pc$ . These hydrogens are tautomeric and readily move between the central nitrogens.<sup>142</sup> MPc can be formed from nearly any metal atom (formally a 2+ cation) with smaller metal cations forming planar complexes of  $D_{4h}$  symmetry. Larger metals can form nonplanar puckered structures, as is the case of  $PbPc$ ,<sup>145</sup> or form larger sandwich complex as with many rare-earth metals.<sup>146</sup> In the case of smaller, trivalent cations such as boron, three-fold symmetric subphthalocyanines will form.<sup>147</sup>

In addition to changing the central metal, MPc can be chemically modified at several points in their structure. Axial bonding of ligands to the central metal can be performed in many

cases,<sup>148,149</sup> and coordinating solvents like pyridine are known to transiently bond with central MPc metals.<sup>150</sup> The aromatic periphery of the MPc is also a point for modification. Solubility

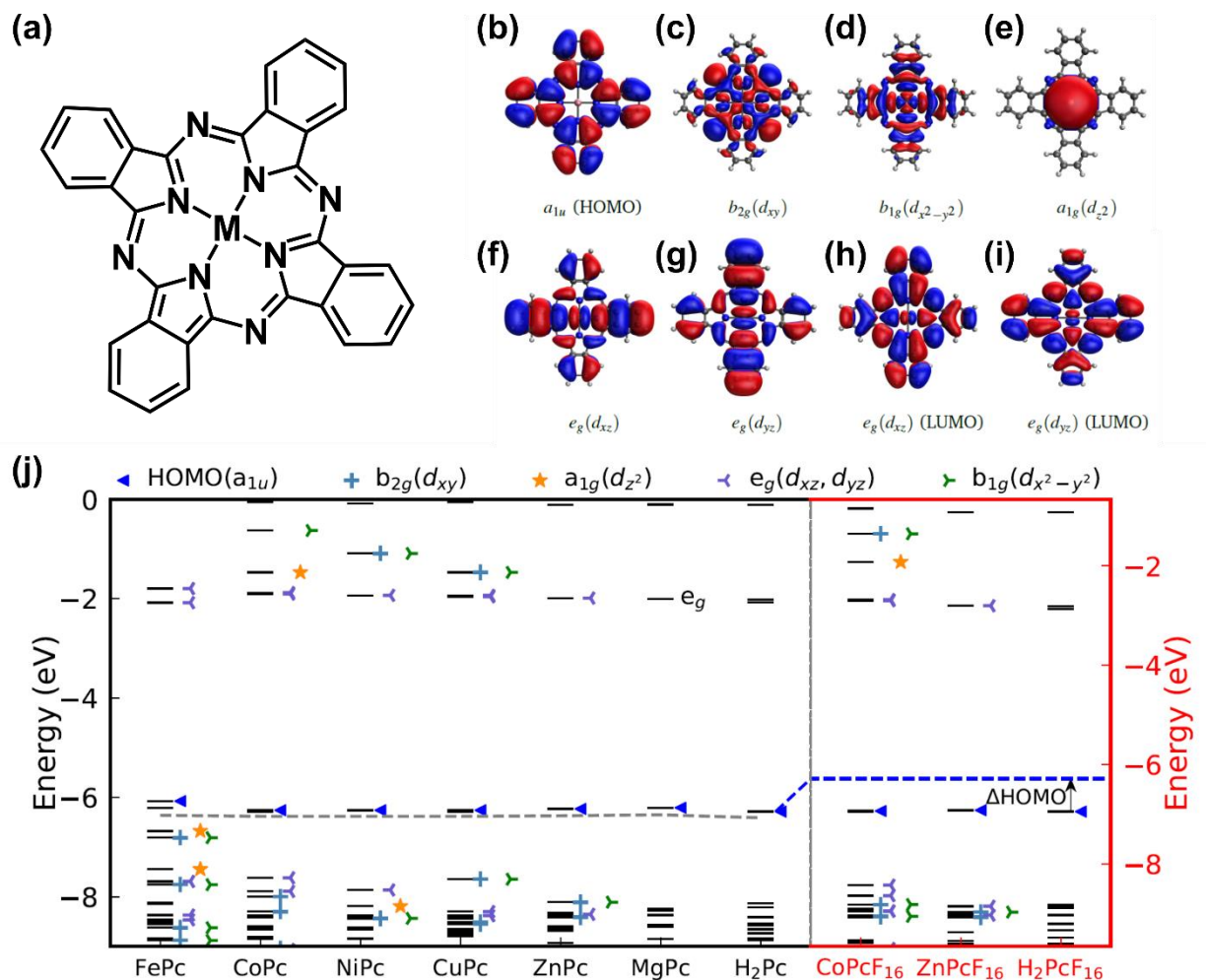


Figure 1.10 Phthalocyanine structure. (a) Chemical structure of MPc molecule. (b-i) Electron density of frontier and near-frontier orbitals of MPc molecules. (j) Orbital energy levels for H<sub>2</sub>Pc, MPc (M = Fe, Co, Ni, Cu, Zn, Mg) and select fluorinated derivatives. (b)-(j) reproduced from<sup>151</sup>. Copyright 2020 the authors, licensed under CC BY-NC-ND.

modifying side chains such as alkyl chains<sup>152</sup> and sulfonic acids<sup>153</sup> are routinely added many unmodified MPc are only soluble in concentrated sulfuric acid.<sup>142</sup> Fluorine is another common peripheral functionalization group, which generally raises the work function of the MPc<sup>154</sup> and switches its conduction from p-type to n-type.<sup>155</sup> Due to their optical and electronic properties, there has also been work on incorporating MPc in polymers<sup>156</sup> and 2D networks.<sup>157,158</sup>

Due to their planar structure, synthetic diversity, and facile vapor phase deposition, Pc molecules are used extensively as model compounds in surface science.<sup>159</sup> Films prepared in ultrahigh vacuum (UHV) are can imaged by scanning tunneling microscopy (STM) at atomic or molecular resolution, and often form ordered monolayers on a variety of surfaces.<sup>159</sup> The out-of-plane orbitals of the MPc metal can interact with surfaces, inducing a “surface-trans effect” on axial ligands, or even changing the spin state of the metal.<sup>160</sup>

### *Phthalocyanine Electronic Structure, Spectroscopy*

The highest occupied molecular orbital (HOMO) and lowest unoccupied molecular orbital (LUMO) orbitals are primarily aromatic  $\pi$  orbitals with little metal character. The contributions of the out-of-plane d-orbitals ( $d_{xz}$ ,  $d_{yz}$ , and  $d_z^2$ ) are important to consider as they can interact with surfaces. The d-orbital contribution to the electronic structure varies with the choice of metal, with illustrated by the late 3d block metals (Fe through Zn) and is shown in Figure 1.10c. The HOMO is entirely C and N  $\pi$ -orbitals, while the LUMO has a small contribution from  $d_{xz,yz}$  that decreases from 6.5% to 0.3% going across the period from FePc to ZnPc.<sup>151</sup> The energy and d-character of the HOMO-1 orbital varies strongly with central metal, going from

70%  $d_{xz,yz}$  and 0.6 eV below the HOMO in FePc to 30%  $d_{xz,yz}$  and 1.9 eV below the HOMO for ZnPc.<sup>151</sup> It is notable that proper prediction of these trends requires careful DFT calculations. Standard functionals like B3LYP do not properly balance long-range Coulomb interactions and shorter range exchange, resulting in errors in the d-character of orbitals and orbital energies that disagree with experiment.<sup>151,161</sup>

Pc molecules have strong absorption features, as expected given their applications as dyes. Their primary absorption (the Q band,  $S_0 \rightarrow S_1$ ) is near 670 nm for most MPc in solution, with a secondary peak (the Soret or B band,  $S_0 \rightarrow S_2$ ) near 340 nm.<sup>162</sup> Both of these bands are  $\pi \rightarrow \pi^*$  transitions. An representative absorption spectrum is shown in Figure 1.11a. The Q band typically shifts to lower energy in the solid state due to coupling between Pc transition dipoles (J-aggregates),<sup>162</sup> and shifts in the Q band can also be induced by redox, potentially introducing new metal to ligand or ligand to metal charge transfer bands.<sup>162</sup>

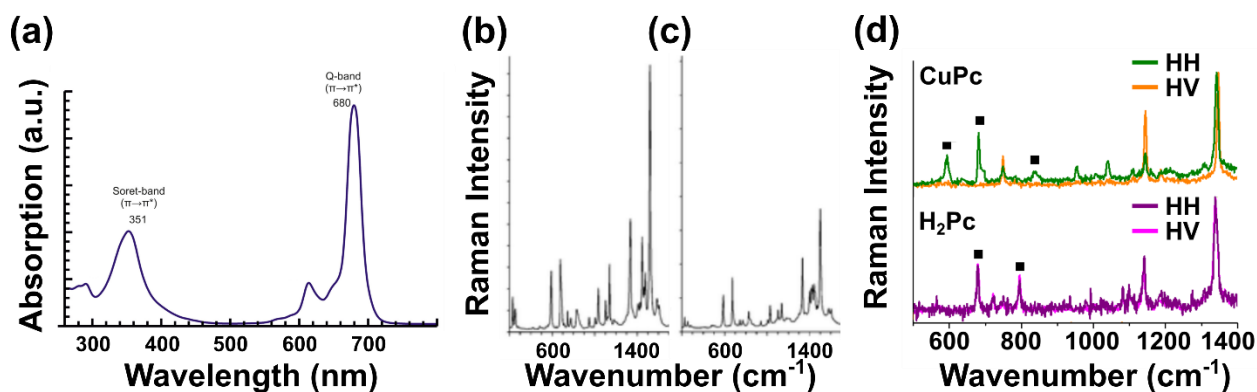


Figure 1.11 Phthalocyanine absorption and Raman spectra. (a) example UV-vis absorption spectrum of ZnPc in chloroform. The Soret and Q bands are labelled. (b) Raman spectrum of ZnPc and (c) CuPc. (d) Polarized Raman spectra of CuPc and H<sub>2</sub>Pc films on MoS<sub>2</sub> with the A<sub>1g</sub> modes highlighted. The change in parallel versus cross polarization in CuPc suggests a  $\pi$ -face-on

orientation to MoS<sub>2</sub> while the H<sub>2</sub>Pc is unchanged, suggesting an edge-on orientation. (a) adapted from <sup>163</sup>. Copyright 2017 Elsevier. (b) and (c) reproduced from <sup>164</sup>. Copyright 2001 The Royal Society of Chemistry. (d) adapted from <sup>165</sup>. Copyright 2019 American Chemical Society.

Raman spectroscopy is used extensively to characterize Pc films. The Pc aromatic framework is very polarizable, giving rise to intense Raman bands in the region of 600 – 1600 cm<sup>-1</sup> that can uniquely identify each Pc molecule (Figure 1.11b).<sup>164,166,167</sup> Group theory can be used to deduce the molecular orientation of Pc thin films by collecting Raman spectra in parallel and perpendicular polarizations.<sup>165,168</sup> The mathematical basis of this method is as follows: D<sub>4h</sub> Pc vibrations of A<sub>1g</sub> and B<sub>1g</sub> symmetry have Raman tensors with only diagonal elements. When the laser polarization is in the same plane as the Pc molecule, those diagonal vibrations will not alter the polarization of Raman scattered photons. This condition is met when the Pc molecule is lying  $\pi$ -face-on for a linear polarized laser normal to the surface. As a result, Raman modes of A<sub>1g</sub> and B<sub>1g</sub> vibrations will have full intensity when the collected spectrum is parallel polarized to the incident laser, and zero intensity when the collection is perpendicularly polarized. When those modes have non-zero intensity, the Pc molecule is not lying  $\pi$ -face-on. This method can be used to qualitatively compare Pc films as ‘face-on’ or ‘edge-on’, as in Figure 1.11c.

### *Phthalocyanine Optoelectronic Devices*

Due to their intense absorption, Pc molecules have been the subject of intense study for organic photovoltaics (OPVs).<sup>169</sup> In fact, the first OPV with a non-negligible efficiency was fabricated by Tang using a CuPc donor molecule and a perylene acceptor.<sup>170</sup> The Pc - C<sub>60</sub> heterojunction was used as a model system for many years after higher efficiency systems were

discovered due to the fine control in fabrication that is enabled by vapor deposition.<sup>171,172</sup> Pc molecules have also found use in photodetectors,<sup>173</sup> organic light-emitting diodes (OLEDs),<sup>174</sup> and organic field-effect transistors (OFETs).<sup>175</sup> They have also been used in heterojunctions with 2D materials, which will be discussed in more detail in Chapter 1.4.

#### 1.4. Pentacene

Pentacene is a simple five membered fused ring, as shown in Figure 1.12a. It is among the most heavily studied organic semiconductors due to its high p-type mobility above  $1 \text{ cm}^2 \text{ V}^{-1} \text{ s}^{-1}$ .<sup>176</sup> It has also drawn intense interest from the spectroscopy and organic photovoltaics communities due to its ability to undergo ultrafast singlet fission on the 100-fs timescale,<sup>177</sup> which may be used for multiexciton generation in solar cells to exceed the Shockley-Queisser limit.<sup>178</sup>

##### *Structure*

Two polymorphs of single crystal pentacene are discussed in the literature – the Campbell phase<sup>179</sup> and the Siegrist phase,<sup>180</sup> as well as a few minor variations.<sup>181</sup> These are characterized by their  $d(001)$ -spacings, with  $14.1 \text{ \AA}$  corresponding to the Campbell phase and  $14.5 \text{ \AA}$  corresponding to the Siegrist phase.<sup>181</sup> In both phases the pentacene forms a herringbone structure with molecules packed edge-to-face to their nearest neighbors. As a thin film, pentacene adopts different structures, the most common of which is the aptly named thin-film phase.<sup>182,183</sup> Figure 1.12b shows a comparison of these three primary phases. Other thin film phases are possible, differing mostly in the orientation of the pentacene molecules with the

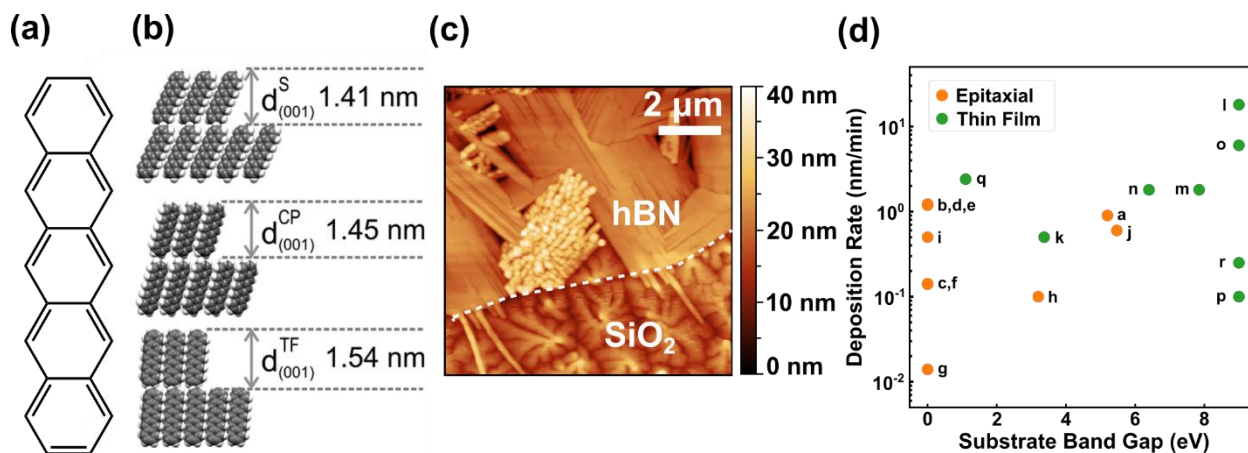


Figure 1.12 Pentacene structure and film morphology. (a) Chemical structure of pentacene. (b) Comparison of the Siegrist, Campbell, and thin-film phases of pentacene based on their (001) distances. (c) Atomic force microscopy (AFM) images of the morphology contrast between thin-film and  $\pi$ -face-on phases of pentacene. The dendritic thin-film phase grows on the SiO<sub>2</sub> while the needle-like  $\pi$ -face-on phase grows on hBN. (d) Comparison of deposition rate and substrate bandgap of representative studies of pentacene film growth. Epitaxial growth typically occurs on metallic or vdW substrates at very slow growth rates. Sources: a,<sup>184</sup> b,<sup>185</sup> c,<sup>186</sup> d,<sup>187</sup> e,<sup>188</sup> f,<sup>189</sup> g,<sup>190</sup> h,<sup>191</sup> i,<sup>192</sup> j,<sup>193</sup> k,<sup>183</sup> l,<sup>194</sup> m,<sup>195</sup> n,<sup>195</sup> o,<sup>196</sup> p,<sup>197</sup> q,<sup>198</sup> r.<sup>199</sup> (a) reproduced from<sup>200</sup>. Copyright 2016 The Royal Society of Chemistry. (c) reproduced from<sup>201</sup>. Copyright 2021 American Chemical Society.

substrate – the thin-film phase has pentacene’s long axis nearly perpendicular to the substrate while other phases show  $\pi$ -face-on growth with the long axis parallel to the substrate.<sup>201,202</sup>

In addition to impacting the crystal structure, the thin film morphology is also impacted by substrate and growth conditions.<sup>182</sup> The thin-film phase typically appears on oxide substrates and grows in a dendritic manner,<sup>203,204</sup> while face-on growths will tend instead to form long, needle-like structures.<sup>201,205</sup> Figure 1.12c illustrates these phases with pentacene grown on both SiO<sub>2</sub> and hBN. In certain cases, it is possible to grow epitaxial phases of pentacene, where the orientation and spacing of the pentacene is determined by the underlying substrate. These films are typically grown on a metallic or vdW substrates by molecular beam epitaxy in ultrahigh

vacuum.<sup>138,192,206</sup> Figure 1.12d summarizes a variety of different substrates, growth rates, and the resulting pentacene phase.

### *Pentacene Spectroscopy*

The UV-Vis absorption spectrum of solution and crystalline pentacene is shown in Figure 1.13a. The lowest energy features at 675 nm and 630 nm correspond to the singlet absorption with a large Davydov splitting.<sup>207</sup> The magnitude of this splitting and the large energy shift from liquid to solid phase indicates strong intermolecular coupling in films.<sup>208</sup> The nature of the higher energy peaks below 600 nm is debated, with the leading candidates being charge transfer excitations<sup>209</sup> and vibrational sidebands.<sup>207</sup>

The steady-state photoluminescence spectrum of solid pentacene is dominated by excitonic recombination. At high temperatures, only the free exciton recombination is measurable at 1.8 eV, while at cryogenic temperatures a lower energy feature at 1.65 eV appears that is attributed to the self-trapped exciton.<sup>210-212</sup> In addition, higher and lower energy features are sometimes measured, corresponding to recombination of charge transfer states<sup>197</sup> and excitons trapped at extrinsic defects, respectively.<sup>212</sup> The structure of pentacene effects the energy of these states, with the single crystal pentacene free exciton emitting 40 meV lower energy than thin-film free exciton.<sup>210,211</sup> This difference is shown clearly in Figure 1.13b, which shows the low temperature PL of thin-film pentacene (grown on SiO<sub>2</sub>) versus a  $\pi$ -face-on phase grown on hBN.

Most of the interest in pentacene's optical properties stems from its ability to undergo ultrafast triplet fission. In this process, a singlet excited state will relax into two triplet excited

states on adjacent molecules. To obey conservation of energy, these triplet states must have less than half of the energy of the singlet state. Aside from fundamental photochemical interest, this process is interesting in organic photovoltaics. A major assumption of the Shockley-Queisser limit is that one absorbed solar photon generates one charge carrier. By creating more than one charge carrier per absorbed photon (multiexciton generation), pentacene can theoretically achieve photovoltaic efficiencies higher than the Shockley-Queisser limit.<sup>178</sup> For triplet fission to be efficient, it must occur faster than competing excited-state process (summarized in Figure 1.13c), and thus extensive effort has been made into understanding the ultrafast dynamics of pentacene.<sup>199,208,213</sup>

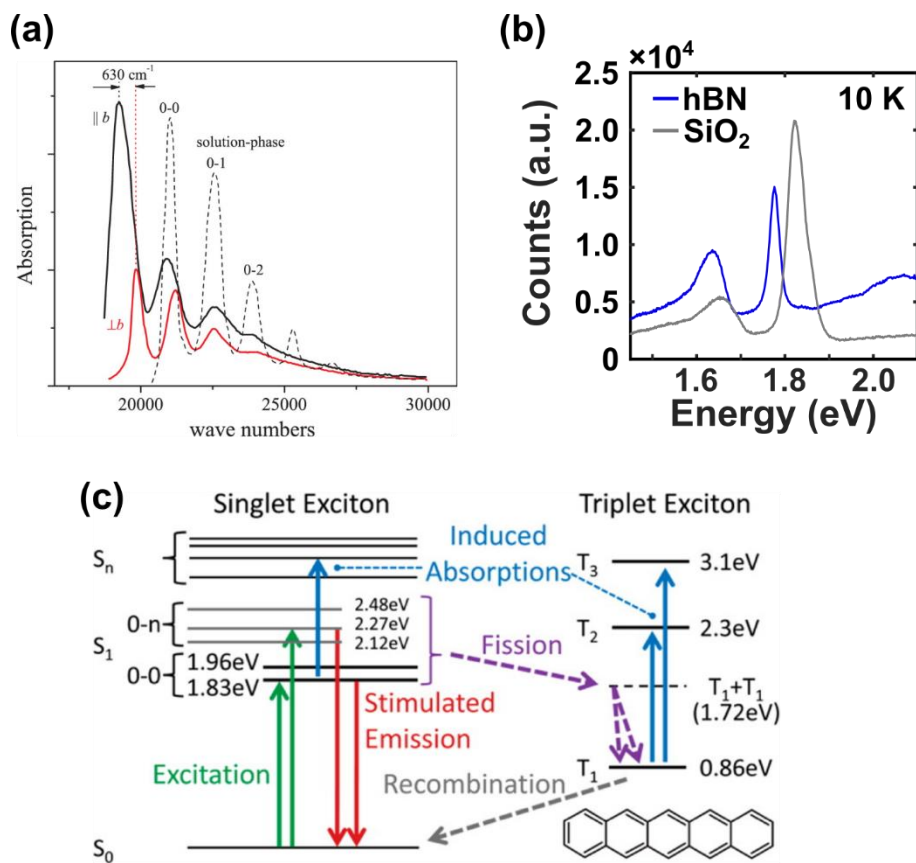


Figure 1.13 Pentacene spectroscopy. (a) UV-Vis absorption spectrum of solution phase and single crystal pentacene. (b) PL spectra of thin-film pentacene (on SiO<sub>2</sub>) and  $\pi$ -face-on pentacene (on hBN) showing the free- and self-trapped excitonic emission peaks at 1.8 and 1.65 eV respectively. (c) Jablonski diagram of optical processes in pentacene, illustrating the relevant energy levels for singlet fission. (a) reproduced from <sup>207</sup>. Copyright 2011 American Institute of Physics. (b) reproduced from <sup>201</sup>. Copyright 2021 American Chemical Society. (c) reproduced from <sup>208</sup>. Copyright 2013 American Chemical Society.

### Optoelectronic Devices

Pentacene has been studied heavily in the context of organic electronics due to its high p-type mobility. The morphology and purity of pentacene plays an important role in its transport. Single crystals produced by chemical vapor transport (CVT) have shown OFET charge mobilities up to 58 cm<sup>2</sup> V<sup>-1</sup> s<sup>-1</sup>.<sup>214</sup> While single crystal CVT pentacene shows the best

performance, it is not practical for most applications, which focus on pentacene films produced by thermal evaporation. Though early OFETs showed poor performance, shifting focus to the pentacene – dielectric interface in the 90s caused a rapid increase in mobilities,<sup>215</sup> with self-assembled monolayer (SAM) – treated SiO<sub>2</sub> pentacene OFETs showing mobilities above 1 cm<sup>2</sup> V<sup>-1</sup> s<sup>-1</sup>.<sup>216</sup> More recent improvements have incorporated advances to dielectric engineering, such as lanthanum niobium oxide (La<sub>x</sub>Nb<sub>1-x</sub>O<sub>y</sub>)<sup>217</sup> or ionic liquids,<sup>218</sup> achieving mobilities as high as 10.6 cm<sup>2</sup> V<sup>-1</sup> s<sup>-1</sup> on LaNbO on Pd-coated Si.<sup>219</sup> Another major trend is in synthetic modification of pentacene for n-type conductivity.<sup>220</sup>

While other molecules now dominate the top performance in OPVs, pentacene continues to be studied in this context as a model system.<sup>221–223</sup> There is also continued interest in pentacene for multiexciton generation.<sup>224</sup> These include OPVs with greater than 100% external quantum efficiency (EQE),<sup>225</sup> as well as application in hybrid organic – nanoparticle<sup>226</sup> and dye-sensitized systems.<sup>227</sup>

## 1.5. Organic / 2D Heterostructures

While organic and 2D materials have exceptional properties on their own, there are significant opportunities in combining the two into mixed-dimensional heterostructures.<sup>228</sup> The goal for these interfaces is to synergistically combine the useful properties of the constituent materials, as well as to realize new physical phenomena that are not possible in either constituent system alone. Both material classes bring different advantages that can be leveraged in such heterointerfaces. Organics are synthetically tunable and easy to process through solution or vacuum based methods, while 2D materials bring in high electrical performance, strong optical responses, and a number of exotic physical phenomena. When combined, organic molecules can allow tuning of 2D properties with finer control than is possible in other heterostructures, and they enable new device concepts that are not possible with other material systems.

### 1.5.1. Electronic Structure

When considering the electronic structure of a heterojunction, it is easiest to start by considering the materials in isolation. This is used to produce a band alignment diagram, which can give a first-order approximation of how the electrons will move when put into the heterostructure. A schematic of a band alignment diagram and the types of band alignment is shown in Figure 1.14a. This can be used to predict properties like ground state charge transfer,<sup>229,230</sup> photoinduced charge or energy transfer,<sup>165,231,232</sup> photovoltaic effects,<sup>68,233</sup> and others.

While band alignment is useful as a first order prediction, it assumes that the electronic structure of the heterojunction constituents does not change after they are put together. This seems to be a reasonable assumption at first glance, given that there is no chemical bonding occurring at

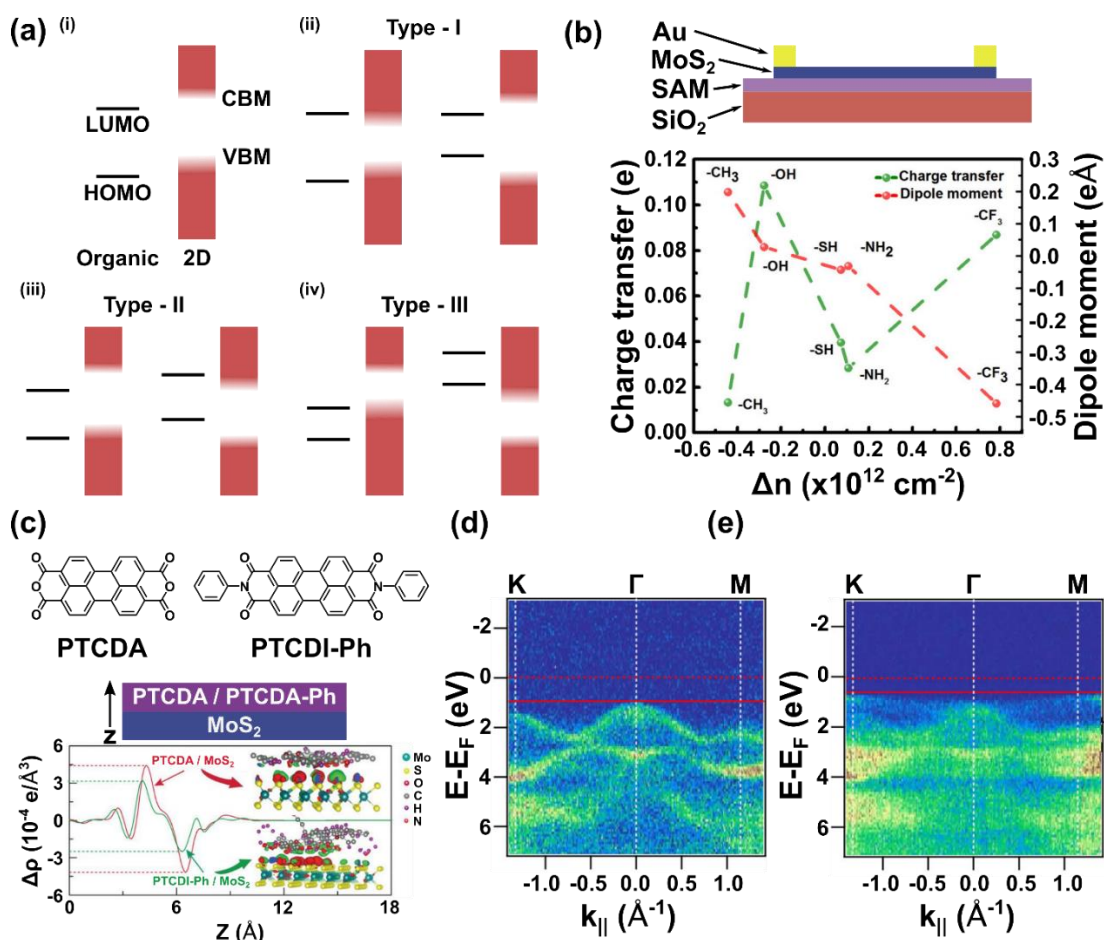


Figure 1.14 Electronic structure in organic – 2D heterojunctions. (a) Band alignment and heterojunction types. (i) Schematic of a band alignment diagram, with the frontier orbitals of the molecule and band edges of the 2D material labelled. The z axis is implicitly energy in these diagrams. Possible alignments for a (ii) type-I straddling gap heterojunction, (iii) type-II staggered gap heterojunction, and (iii) type-III broken gap heterojunction. (b) Schematic of a MoS<sub>2</sub> transistor on a self-assembled monolayer (SAM) and a plot of the change in carrier concentration in the MoS<sub>2</sub> transistor with different SAM end groups, plotted versus the amount of transferred charge and the dipole moment. (c) Structures of PTCDA, PTCDI-Ph, schematic of

their heterojunctions with MoS<sub>2</sub>, and the z-direction charge difference in PTCDA and PTCDI-Ph/MoS<sub>2</sub> heterojunctions with isosurface plots of the charge density difference. The red and green isosurfaces represent electron accumulation and depletion, respectively. The LUMO  $\pi$ -orbital energies determine the direction of the charge transfer. (d,e) Energy-momentum angle-resolved photoelectron spectroscopy (ARPES) intensity maps ( $h\nu = 75$  eV) of (d) pristine MoS<sub>2</sub> and (e) 0.6 nm of FePc on MoS<sub>2</sub>. The lowest binding energy features of FePc have intensity maxima close to *K* and *M*, indicating hybridization between MoS<sub>2</sub> states and those of the adsorbed molecule. (b) Adapted from <sup>234</sup>. Copyright 2014 American Chemical Society. (c) adapted from <sup>235</sup>. Copyright 2020 Wiley-VCH. (d) and (e) reprinted with permission from <sup>154</sup>. Copyright 2020 American Chemical Society.

the interface. But strong interactions can occur even across van der Waals gaps. Consider, as an example, the large change to the MoS<sub>2</sub> band structure that occurs as it is thinned to the monolayer limit, which occurs due to repulsion of orbitals between layers.<sup>52</sup> Perturbations to the state band-alignment model include orbital-specific effects such as hybridization, as well as more general effects due to charge transfer and electrostatics. Hybridization in this case refers to the formation of emergent mixed-character electronic states in the combined organic-2D system that contain contributions to their density from both the organic molecule and the 2D material. If this hybridization results in a net change in electron density distribution, then ground state charge transfer occurs, effectively donating a fraction of an electron from one material to the other. Dipoles and charges in molecules can also change the electronic structure of the 2D material in a manner similar to a gate voltage in a transistor, causing the 2D material Fermi level to be displaced up or down in energy. All of these effects are interdependent and challenging to deconvolute. An informative system for studying the interdependence of electrostatic and hybridization effects are 2D materials exfoliated onto self-assembled monolayers (SAM).<sup>234,236</sup> The end group of the SAM can be altered with various substituents, which has predictable effects on both charge transfer and electrostatics, while its orientation and packing density remain constant. By systematically

investigating the change in carrier density in an MoS<sub>2</sub> field-effect transistor (FET) versus the calculated dipole and charge transfer from the SAM, the relative impact of these two effects can be assessed with dipoles typically dominating over ground state charge transfer (Figure 1.14b).<sup>5</sup> Beyond dipole effects, control over molecular charge provides opportunities for dynamically tuning organic-2D heterostructure electronic properties. For example, redox of ferrocene<sup>237</sup> and manipulation of molecular zwitterions<sup>238</sup> have been leveraged to alter the electronic response of 2D material substrates. In addition, molecules with high or low redox potentials can also directly transfer charge to 2D material substrates, as shown for benzyl viologen.<sup>229</sup>

Many commonly used organic semiconductors such as planar phthalocyanines, acenes, and perylenes are neutrally charged and have either small dipoles or no net dipole moment. In these cases, hybridization and ground state charge transfer determine the movement of charge carriers. For instance, in perylenetetracarboxylic dianhydride (PTCDA)/MoS<sub>2</sub> heterojunctions (Figure 1.14c), hybridization mixes the S p<sub>z</sub> and Mo d<sub>z<sup>2</sup></sub> orbitals near the CBM and the conjugated C p<sub>z</sub> orbitals.<sup>239</sup> This hybridization results in a narrowing of the MoS<sub>2</sub> bandgap and increases the density of states (DOS) near the band edges, causing a large intensity increase and red shift in its photoluminescence (PL) spectrum. A net charge transfer also occurs due to redistribution of electron density in the resulting hybrid orbitals. This effect becomes more evident when the behavior of PTCDA is contrasted with other perylene derivatives such as N,N'-diphenyl-3,4,9,10-perylenedicarboximide (PTCDI-Ph). In contrast to the planar geometry of PTCDA, PTCDI-Ph possesses a bent structure, which results in reduced overlap of the molecular  $\pi$ -orbitals with the out-of-plane orbitals in the MoS<sub>2</sub> conduction band.<sup>235</sup> As a result, the net charge transfer between

PTDCI-Ph and MoS<sub>2</sub> is reduced (Figure 1.14c), and the surface binding energy calculated from density functional theory (DFT) is 30% lower for PTCDI-Ph compared to PTCDA.<sup>235</sup> In another example, angle-resolved photoelectron spectroscopy (ARPES) has shown that iron phthalocyanine (FePc) hybridizes with MoS<sub>2</sub> near the K point (Figures 1.14d and 1.14e).<sup>154</sup>

### 1.5.2. Morphology

The same techniques that are used for organic and 2D materials on their own are used in combination to fabricate organic – 2D mixed-dimensional heterojunctions. As with any multi-step fabrication process, care must be taken to insure material compatibility. Aqueous deposition of an organic molecule onto a water-soluble 2D material, for example, is not advisable.

While fabrication of organic – 2D interfaces is relatively straightforward, predicting and understanding the interface structure is more of a challenge. Organic film thickness, morphology, and molecular orientation are important but often neglected factors in organic-2D heterojunctions. The essential role of these parameters in all-organic electronics is well known. Thus, vdW materials provide a unique platform for tuning these properties, even enabling the growth of organic phases not observed on other substrates. The orientation of a molecule on a surface is a key parameter in controlling its interactions with the surface. The role of orientation has been shown in H<sub>2</sub>Pc and CuPc films on MoS<sub>2</sub> (Figures 1.15a and 1.15b). These two similar molecules have different orientations on MoS<sub>2</sub>, with CuPc lying  $\pi$ -face-on while H<sub>2</sub>Pc stands approximately edge-on on MoS<sub>2</sub>.<sup>165</sup> This orientational difference affects recombination times upon photoexcitation, with excitons more readily dissociating into long-lived free carriers in the CuPc-MoS<sub>2</sub> case. Many other large  $\pi$ -conjugated molecules have been shown to orient face-on to 2D

materials including pentacene<sup>201</sup> and perylenes.<sup>240</sup> This orientation is often in contrast to the edge-on orientations on more common surfaces such as SiO<sub>2</sub> and sapphire.<sup>165,201</sup> This qualitative difference in thin-film growth has led to the emergence of vdW materials, particularly hexagonal boron nitride (hBN), as promising substrates for templating the epitaxial growth of functional organic molecules.<sup>138</sup>

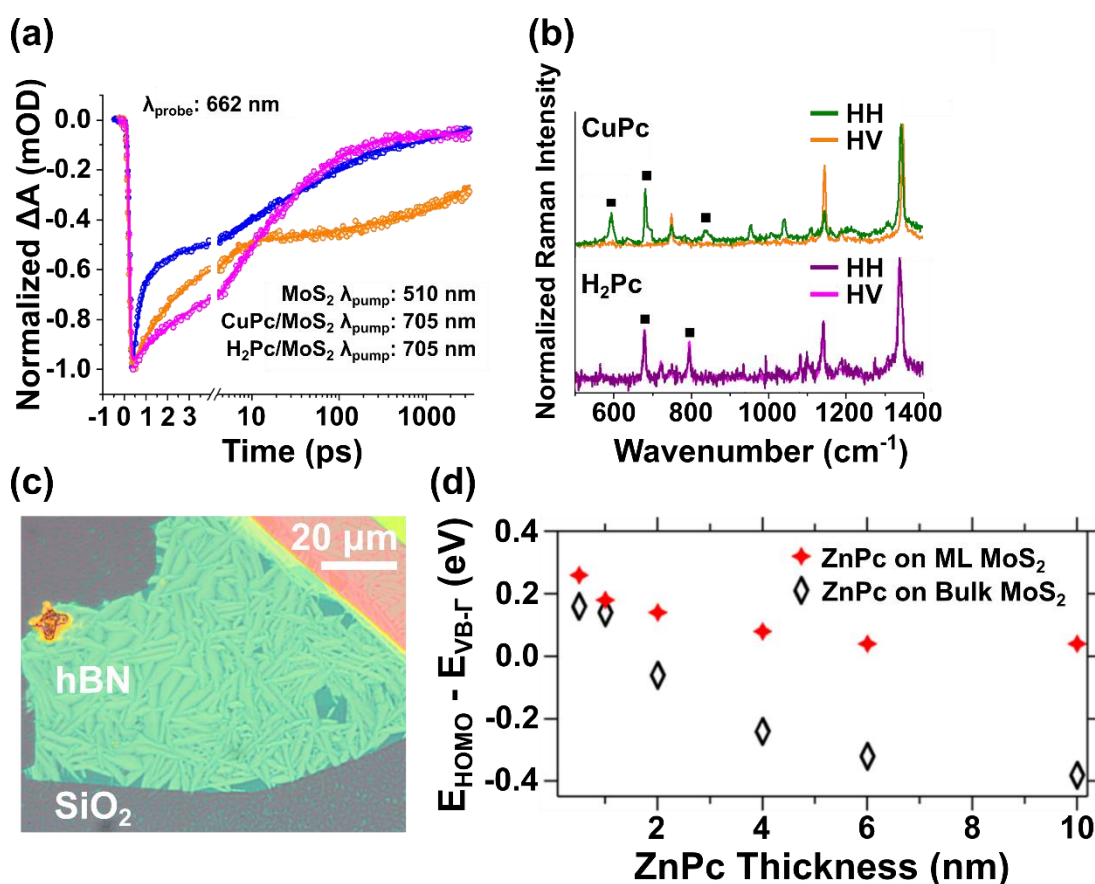


Figure 1.15 Organic – 2D morphology (a) Transient absorption traces of monolayer MoS<sub>2</sub> and its heterojunction with CuPc and H<sub>2</sub>Pc. A long-lived charge separated state is present only in the CuPc heterojunction. (b) Polarized Raman spectra of CuPc and H<sub>2</sub>Pc on MoS<sub>2</sub>. The change in intensity of the highlighted modes in parallel and perpendicular polarizations indicates that CuPc has a face-on orientation with respect to the MoS<sub>2</sub> plane, whereas H<sub>2</sub>Pc has a significant tilt angle. (c) Optical microscopy image of a 20 nm pentacene film deposited on multilayer hBN and a SiO<sub>2</sub> substrate.

Pentacene forms a typical dendritic thin-film phase on SiO<sub>2</sub> but grows in a unique needle-like  $\pi$ -face-on phase on hBN. (d) HOMO-VBM energy offset as a function of ZnPc thickness at the interface of ZnPc-monolayer-MoS<sub>2</sub> and ZnPc-bulk-MoS<sub>2</sub> heterostructures as deduced from photoelectron spectra. The film thickness can change the band alignment in this organic-2D heterostructure by several hundred meV. (a) and (b) adapted from <sup>165</sup>. Copyright 2019 American Chemical Society. (c) reproduced from <sup>201</sup>. Copyright 2021 American Chemical Society. (d) reproduced from <sup>241</sup>. Copyright 2019 American Chemical Society

The orientation of organic adlayers has clear effects on the resulting properties of organic-2D heterostructures. As noted above, pentacene grows  $\pi$ -face-on for hBN substrates versus edge-on for SiO<sub>2</sub> substrates.<sup>184,201,242</sup> Thus, hBN templates a unique thin-film phase for pentacene that exhibits a needle-like morphology in contrast to the dendritic motif typical of the thin-film phase of pentacene on SiO<sub>2</sub> (Figure 1.15c).<sup>201</sup> Interestingly, the optical response of the  $\pi$ -face-on phase is notably different from the edge-on phase, showing PL more closely resembling that of single-crystal pentacene than that of thin-film pentacene, as well as different temperature dependencies and decay times.<sup>201</sup> At thicknesses greater than 10-20 nm, pentacene growth on hBN can transition from  $\pi$ -face-on to an edge-on phase similar to its bulk crystalline phase. Ambipolar transport is also observed in pentacene FETs on hBN due to differing charge transport characteristics in the edge-on compared to face-on regions of the film.<sup>184</sup> This transition in orientation also depends on the growth method. In particular, pentacene grown by organic molecular beam epitaxy on MoS<sub>2</sub> does not exhibit the face-on to edge-on transition and instead grows  $\pi$ -face-on uniformly.<sup>242</sup> The deterministic growth of different organic thin-film phases on vdW materials is just beginning to be explored and thus represents significant opportunities at the intersection of organic optoelectronics and 2D inorganic materials.

Beyond orientation and morphology, the thickness of the organic film is another critical parameter in organic-2D heterojunctions. For example, the performance of CuPc-MoS<sub>2</sub> photodetectors is dependent on the thickness of the CuPc adlayer with the performance peaking at a CuPc thickness of 2 nm, which suggests that it is not limited by optical absorption or exciton diffusion.<sup>243</sup> Instead, band bending can be a major thickness-dependent factor. Specifically, photoelectron spectroscopic measurements on the ZnPc-MoS<sub>2</sub> heterojunction in Figure 1.15d show that the ZnPc HOMO energy changes by over 100 meV in the range of 0.5 - 5.0 nm ZnPc thickness, with an even greater change on bulk MoS<sub>2</sub> compared to monolayer MoS<sub>2</sub>.<sup>241</sup> This band bending influences the dynamics of photoinduced charge transfer, changing the energies of charge transfer states, the energetic barriers to electron transfer, and the dynamics of back electron transfer.<sup>241</sup> Organic bandwidth also varies with thickness. Thicker molecular layers create a greater density of states for donating or accepting electrons, which can significantly influence charge transfer.<sup>244,245</sup> It should be emphasized that these effects are not captured in simple energy level alignment diagrams since these models are typically based on isolated molecules and thus do not include the influence of molecular adlayer thickness.

### 1.5.3. Spectroscopy

The formation of an organic – 2D interface will alter the photonic response of the materials and potential host emergent phenomena.<sup>246</sup> These spectroscopic changes contain rich information about the coupling between the two materials, and can potentially be used in novel applications.

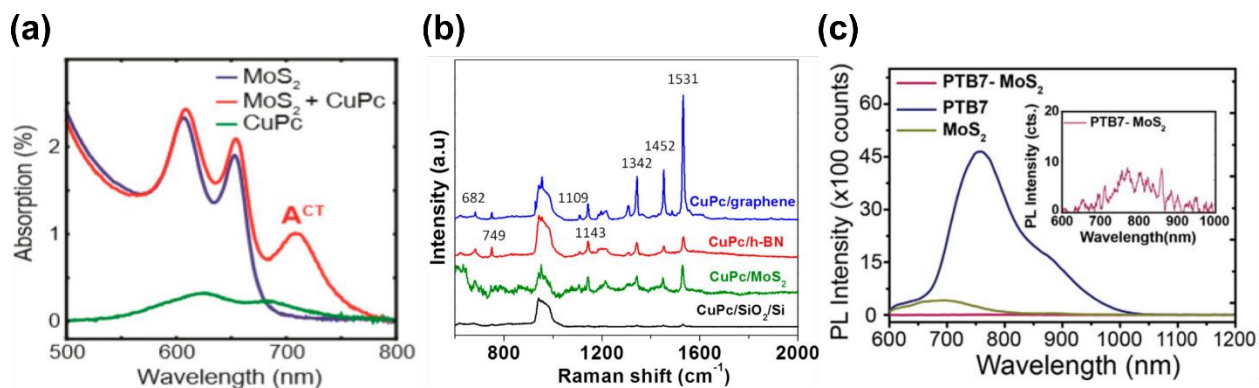


Figure 1.16 Spectroscopy of organic – 2D heterojunctions. (a) UV-Vis absorption of a CuPc – MoS<sub>2</sub> heterojunction shows a new peak associated with delocalization of the CuPc Q band into the MoS<sub>2</sub>. This will be discussed in more detail in Chapter 2. (b) Raman spectra of an equal thickness of CuPc deposited on graphene, hBN, MoS<sub>2</sub>, and SiO<sub>2</sub>, showing Raman enhancement of the CuPc on different the 2D substrates. (c) PL spectra of the OPV polymer PTB7, MoS<sub>2</sub>, and their heterojunction shows mutual PL quenching characteristic of photoinduced charge transfer in a type-II heterojunction. Inset shows the small remnant PL signal from the heterojunction. (a) reproduced from <sup>66</sup>. Copyright 2019 American Chemical Society. (b) reproduced from <sup>247</sup>. Copyright 2014 American Chemical Society. (c) reproduced from <sup>68</sup>. Copyright 2016 American Chemical Society.

Electronic coupling between the molecule and 2D material, for example, can alter various spectra. Pc deposited on MoS<sub>2</sub>, for example, shows a significant red-shift of its Q band as electrons in the Pc delocalize on the MoS<sub>2</sub> (Figure 1.16a).<sup>66</sup> New absorption peaks can appear due to charge transfer excitations.<sup>248</sup> Raman enhancement of molecules on 2D materials is also inherently related to this electronic coupling via the ‘chemical’ mechanism of surface enhanced Raman scattering.<sup>249,250</sup> The results in moderate enhancement factors (10-100) when the molecular orbitals are coupling to the 2D bands (Figure 1.16b),<sup>66,247</sup> and even higher enhancement (>10<sup>5</sup>) when the Raman laser is tuned to a charge transfer excitation.<sup>248</sup>

The PL spectra of heterojunctions also contains a multitude of information about the flow of charges in the system. Mutual PL quenching in a type-II heterojunction is a tell-tale sign of

charge transfer, (Figure 1.16c)<sup>68</sup> which has been shown to occur in organic – 2D systems on ultrafast (<1 ps) timescales.<sup>165,231</sup> In addition, type-I heterojunctions can also enhance the PL of narrow bandgap component through energy transfer.<sup>251</sup> Existing PL peaks can shift due to doping or charge addition/depletion changing neutral exciton to trion ratios in TMDs. New peaks can also emerge in PL spectra that correspond to formation of unique organic phases<sup>201</sup> or recombination of charge-transfer excitons.<sup>252</sup> Molecular adsorbates can also enhance PLQY by passivating defects,<sup>84,253</sup> though this process only works at low powers and above cryogenic temperatures.<sup>81,254</sup>

#### 1.5.4. Devices

Organic materials are often used to modify the properties of a 2D material-based device. They can be used as dopants by directly transferring charge due to high or low redox potential,<sup>229,230</sup> or they may alter the carrier density of a 2D device through ground state charge

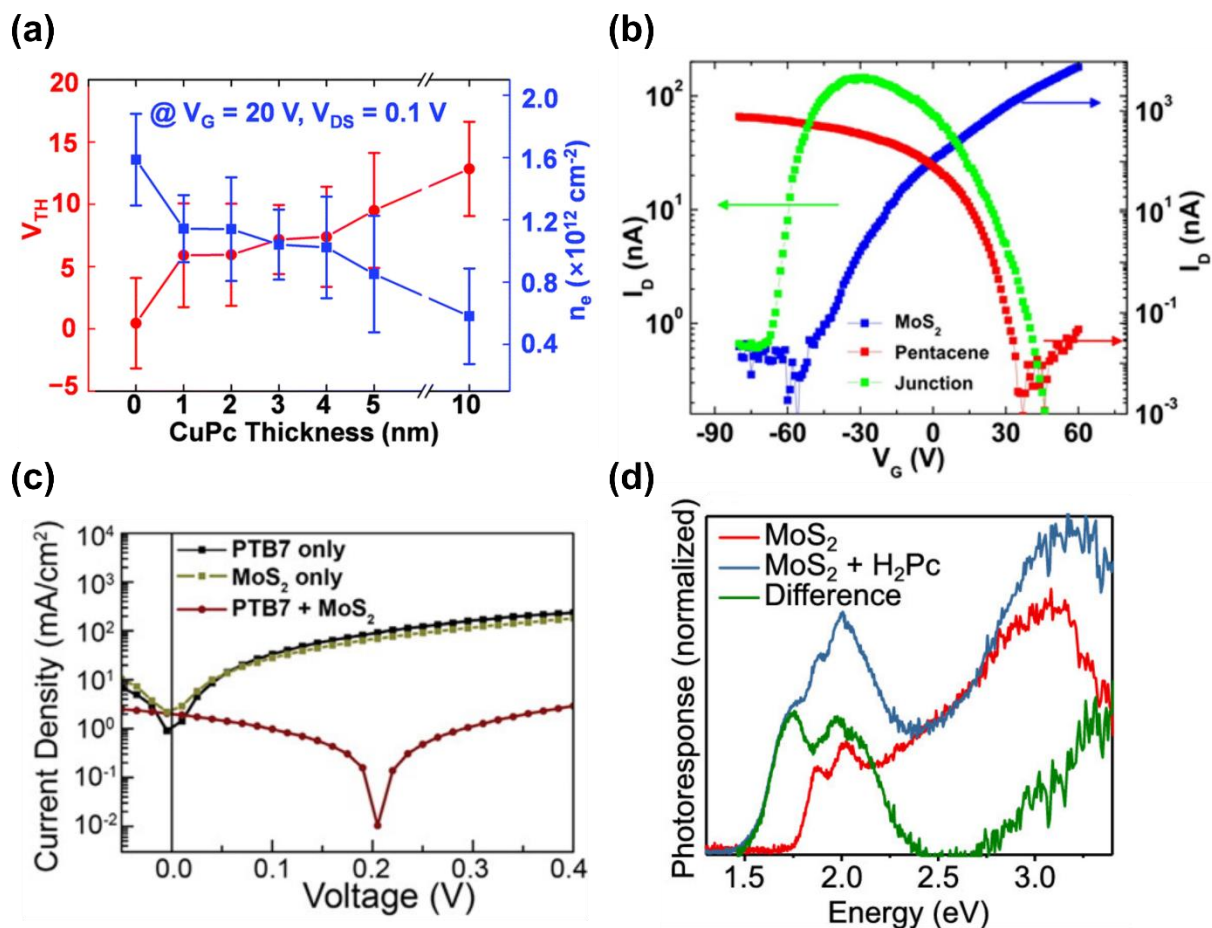


Figure 1.17 Organic – 2D devices. (a) Threshold voltage and carrier concentration in an MoS<sub>2</sub> as a function of CuPc thickness. CuPc depletes carriers in MoS<sub>2</sub>, increasing the threshold voltage and acting effectively as a p-dopant. (b) Transfer curves of an MoS<sub>2</sub>, pentacene, and overlapping pentacene - MoS<sub>2</sub> transistors. MoS<sub>2</sub> and pentacene act as typical n- and p-type FETs, respectively, but when a gating electric field can penetrate both components, their overlapping film produces a unique anti-ambipolar transfer curve. (c) J-V curve of a PTB7 – MoS<sub>2</sub> 20 nm thick photovoltaic cell shows an open circuit voltage of 0.2 V and short circuit current of  $\sim 2 \text{ mA/cm}^2$ . (d) Photoresponse of MoS<sub>2</sub> only and H<sub>2</sub>Pc – MoS<sub>2</sub> hybrid photodetector, normalized to the performance at 2.5 eV. Absorption and excited state charge transfer by the H<sub>2</sub>Pc greatly improves the photoresponse and spectral range of the photodetector. (a) reproduced from <sup>243</sup>. Copyright 2015 The Royal Society of Chemistry. (b) reproduced from <sup>233</sup>. Copyright 2016 American Chemical Society. (c) reproduced from <sup>68</sup>. Copyright 2016 American Chemical Society. (d) reproduced from <sup>255</sup>. Copyright 2020 American Chemical Society.

transfer or charge depletion (Figure 1.17a).<sup>256</sup> Molecular layers have also been used extensively in the semiconductor – dielectric and semiconductor – contact interface to passivate traps, unpin Fermi levels, and improve performance.<sup>257</sup> The ability to apply a gate voltage through the 2D layer also enables novel device concepts in mixed-dimensional heterojunctions, such as antiambipolar transistors, as shown in Figure 1.17b.<sup>233</sup>

The charge and energy transfer characteristics of organic – 2D heterojunctions can also be used in optoelectronic devices. Ultrathin polymer – MoS<sub>2</sub> junctions have shown high record performance per unit thickness, (Figure 1.17c)<sup>68</sup> and 2D materials have been used as a mobility-improving additive in bulk heterojunction OPVs.<sup>115</sup> Deposition of molecules can be used to extend the spectral range of 2D photodetectors (Figure 1.17d)<sup>243,255</sup> as well as speed their performance.<sup>258</sup> Using photoswitches or photochromic molecules in devices also enables reconfigurable responses.<sup>259</sup> This can be used to alter the electronic coupling between two heterojunction components,<sup>260</sup> or to change the electrostatic environment of an FET.<sup>261</sup>

\*Chapters 1.5.1 and 1.5.2 were adapted with permission from <sup>262</sup>. Copyright 2021 American Chemical Society.

## 2. Electronic Coupling in Metal Phthalocyanine – MoS<sub>2</sub> Heterojunctions

### 2.1. Abstract

Mixed-dimensional heterojunctions, such as zero-dimensional (0D) organic molecules deposited on two-dimensional (2D) transition metal dichalcogenides (TMDCs), often exhibit unique interfacial effects that enhance the properties of the individual constituent layers. Here we report a systematic study of interfacial charge transfer in metallophthalocyanine (MPc) – MoS<sub>2</sub> heterojunctions using optical absorption and Raman spectroscopy to elucidate M core (M = first row transition metal), MoS<sub>2</sub> layer number, and excitation wavelength effects. Observed phenomena include the emergence of heterojunction-specific optical absorption transitions and strong Raman enhancement that depends on M identity. In addition, the Raman enhancement is tunable by excitation laser wavelength and MoS<sub>2</sub> layer number, ultimately reaching a maximum enhancement factor of 30x relative to SiO<sub>2</sub> substrates. These experimental results, combined with density functional theory (DFT) calculations, indicate strong coupling between non-frontier MPc orbitals and the MoS<sub>2</sub> band structure as well as charge transfer across the heterojunction interface that varies as a function of the MPc electronic structure.

### 2.2. Introduction

Transition metal dichalcogenides (TMDCs) are an emerging class of two-dimensional (2D) materials with many desirable semiconducting characteristics.<sup>263–265</sup> In particular, their tunable

optical and electronic properties offer applications in diverse nanoscale optoelectronic devices, ranging from field-effect transistors (FETs)<sup>266</sup> to photonic circuits.<sup>267</sup> The van der Waals bonding between the 2D layers of TMDCs also facilitates the realization of lateral<sup>233,268,269</sup> and vertical<sup>270–272</sup> heterojunctions composed of TMDC layers and other distinctive low-dimensional materials.<sup>243,248,267,273</sup> Organic  $\pi$ -electron molecules are attractive components of such heterojunctions due to their facile film processing as well as widely tunable structural and electronic properties.<sup>228</sup> Within this class, metallophthalocyanines (MPcs) are particularly intriguing due to their planar, conjugated structures and well-defined surface chemistries,<sup>159</sup> which offer significant electronic tunability as a function of the metal M<sup>274,275</sup> or peripheral substituents, while maintaining near-constant molecular core geometries.<sup>161,276</sup>

Mixed-dimensional heterojunctions based on zero-dimensional (0D) organic dye molecules and 2D TMDC heterojunctions have been realized for diverse classes of TMDCs,<sup>247,248,277–280</sup> where the organic dye molecules have often been used to enhance the response of photodetectors.<sup>243,258</sup> While these early studies revealed the potential utility of organic–TMDC heterojunctions in optoelectronic applications, the underlying physical mechanisms that govern electronic and optical properties are not fully understood. For example, the optical cross-sections and Raman response of MPc–TMDC heterojunctions as a function of TMDC layer number and transition metal (M) identity have been sparsely investigated.<sup>247,281,282</sup>

Here we systematically probe MPc–MoS<sub>2</sub> heterojunctions with ultraviolet-visible (UV–Vis) optical absorption spectroscopy and Raman scattering. The emergence of new optical transitions arising from the formation of the MPc–MoS<sub>2</sub> heterojunction provides insight into charge transfer

that is sensitive to the MPc transition metal ( $M = \text{Co, Ni, Cu, Zn}$ ). Furthermore, density functional theory (DFT) modeling of the phthalocyanine– $\text{MoS}_2$  heterojunction reveals a type-II band alignment with the highest occupied molecular orbital localized on the Pc ligand and the lowest unoccupied orbital on  $\text{MoS}_2$  in addition to further details concerning charge transfer. Raman enhancement of key MPc skeletal modes upon heterojunction formation is also observed, and is similarly dependent on the  $M$  identity, the excitation laser wavelength (473 nm, 532 nm, and 633 nm), and the number of  $\text{MoS}_2$  layers (monolayer, bilayer, trilayer, and bulk). The electronic structure calculations provide molecular-scale insight into these phenomena, including a correlation between the Raman enhancement and the energy of the MPc out-of-plane d-orbitals. Overall, this work highlights the role of the MPc electronic structure in modulating charge transfer across MPc-TMDC heterojunctions, which will inform ongoing efforts to utilize these mixed-dimensional heterojunctions in both fundamental studies and optoelectronic applications.

### 2.3. Results and Discussion

$\text{MoS}_2$  samples were prepared by chemical vapor deposition (CVD) on sapphire substrates or micromechanical “Scotch Tape” exfoliation on  $\text{SiO}_2$  substrates (see Methods for details). The resulting samples were characterized by optical microscopy (Figure 2.1a), atomic force microscopy (AFM) (Figure 2.1b), and Raman spectroscopy (Figure 2.1c) to identify the number of  $\text{MoS}_2$  layers. Films of various metallophthalocyanines (CoPc, NiPc, CuPc, ZnPc) and metal-free phthalocyanines ( $\text{H}_2\text{Pc}$ ) were purified by vacuum temperature gradient sublimation, and then deposited by thermal evaporation on the  $\text{MoS}_2$  samples in addition to pristine reference  $\text{SiO}_2$  and single-crystal sapphire substrates (see Methods for details). After deposition, the presence of the

Pc was confirmed by Raman spectroscopy,<sup>247</sup> and X-ray photoelectron spectroscopy (XPS) quantification was performed to verify that the Pc sticking coefficients are equal on MoS<sub>2</sub> and sapphire (Figure 2.2). Figures 2.1d-f schematically depict the MPc and MoS<sub>2</sub> atomic-level structures and the anticipated face-on adsorption geometry of MPc molecules on the MoS<sub>2</sub> surface.<sup>283</sup>

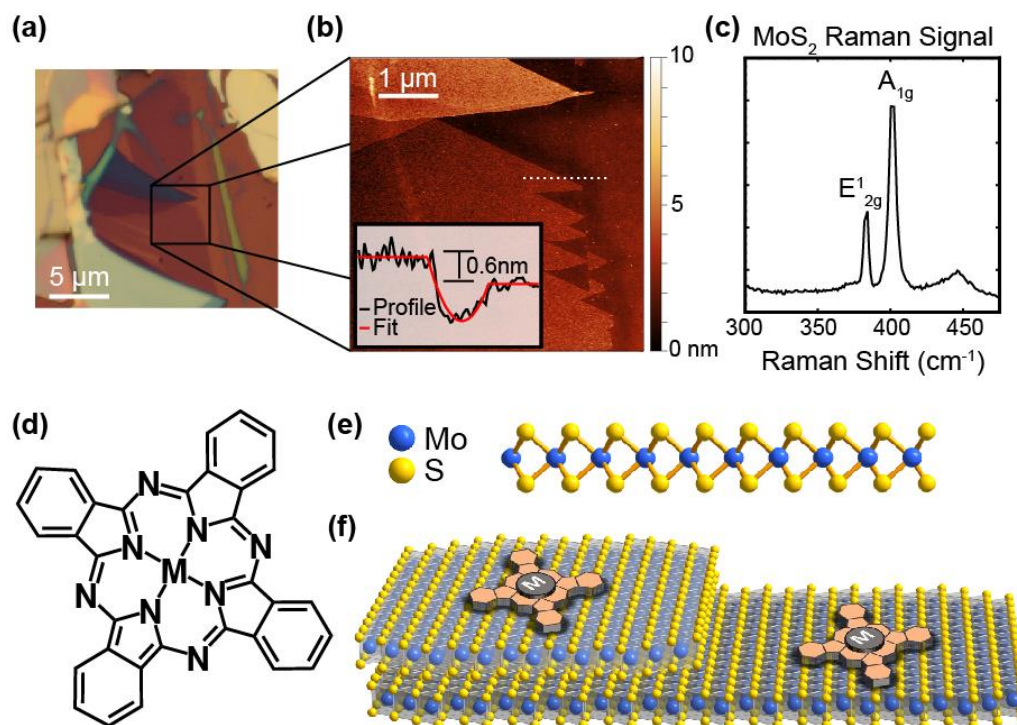
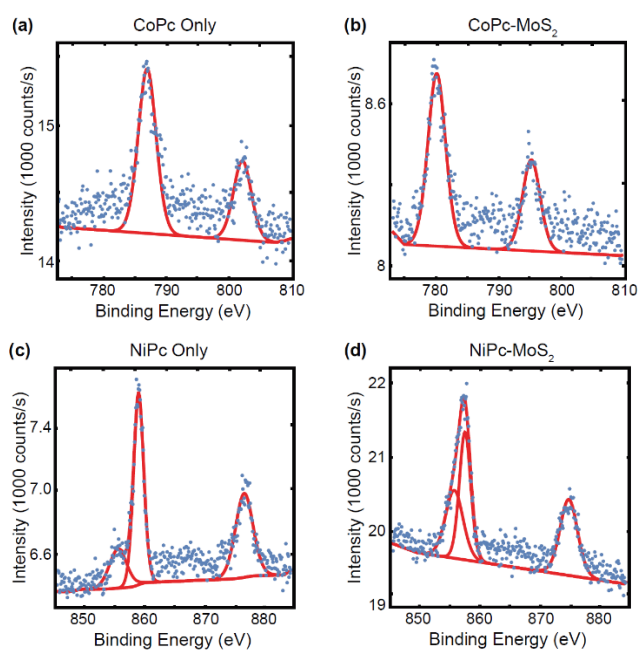


Figure 2.1 (a) Optical image of an exfoliated MoS<sub>2</sub> film. (b) The AFM profile indicates monolayer thickness. (c) Raman signal of a MoS<sub>2</sub> film corresponding to monolayer response. (d) Structure of an MPc molecule where M = Co, Ni, Cu, Zn or metal-free H<sub>2</sub>Pc. (e) Schematic cross-sectional structure of single-layer MoS<sub>2</sub>. (f) Schematic of the anticipated adsorption geometry of MPc molecules on the MoS<sub>2</sub> basal plane.

Optical absorption measurements were performed on CVD-derived MoS<sub>2</sub> films grown on sapphire substrates. UV–Vis spectra of the MPc – MoS<sub>2</sub> heterojunctions show an emergent feature

near 700 nm that is absent in both the MoS<sub>2</sub> and MPc reference spectra (Figure 2.3a). Subtraction of the pre-deposition MoS<sub>2</sub> spectrum from the heterojunction shows features similar to the pristine MPc absorption in addition to the new peak (Figure 2.3b), confirming that this is a new transition rather than an extreme redshift of the MPc absorption. The gas-phase type-II alignment of the MPc



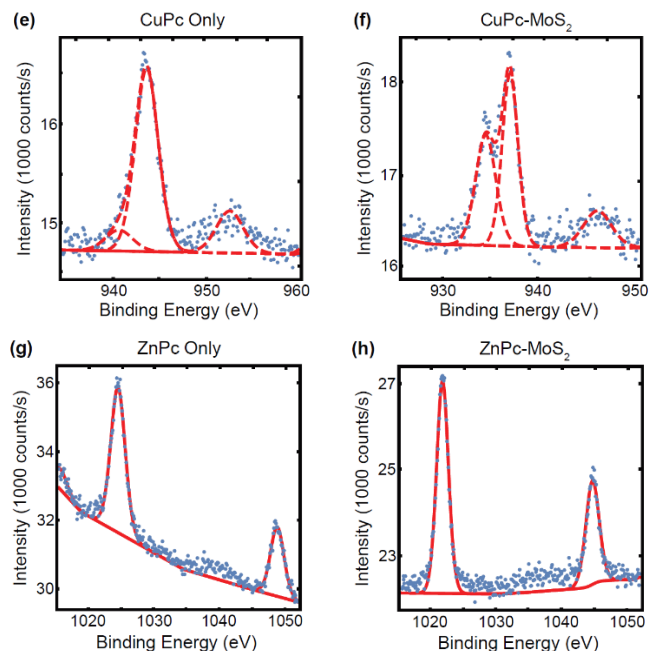


Figure 2.2 X-ray photoelectron spectra (XPS) of MPC metal core electrons (a, b: Co 2p; c, d: Ni 2p; e, f: Cu 2p; g, h: Zn 2p) with identical film thickness on sapphire or CVD MoS<sub>2</sub> – sapphire substrates. Peak integrations indicate similar amounts of MPC is deposited on sapphire vs. MoS<sub>2</sub>. Due to the insulating substrate and long collection times, significant charging effects occur despite the use of a charge compensation gun. This causes large shifts in the peak positions, meaning subtle changes in chemical state on sapphire vs MoS<sub>2</sub> are not observable. The charge compensation also causes reduction of the Cu<sup>2+</sup> species over time, which yields the different peak structure in the Cu 2p spectra on sapphire vs MoS<sub>2</sub>.

orbitals with respect to the MoS<sub>2</sub> bands (Figure 2.3c)<sup>41,258,274,275</sup> suggests that this feature is a charge-transfer transition from the MPC highest occupied molecular orbital (HOMO) to the MoS<sub>2</sub> conduction band minimum (CBM), in agreement with a previous assignment based on MoS<sub>2</sub> quantum dots suspended in an H<sub>2</sub>Pc solution<sup>284</sup> and photoelectron spectroscopy of ZnPc on MoS<sub>2</sub>.<sup>285</sup> The present A<sup>CT</sup> peak is also evident in metal-free H<sub>2</sub>Pc–MoS<sub>2</sub> heterojunctions, which suggests that the MPC HOMOs participating in the charge transfer have a primarily  $\pi$ -character. The A<sup>CT</sup> peak energy weakly depends on the metal in the MPC, varying from 730 nm for metal-

free H<sub>2</sub>Pc to 700 nm for CoPc and NiPc, with Cu and Zn slightly redshifted (~710 nm). See Figure 2.4 for the full absorption spectra. This 80 meV shift in the A<sup>CT</sup> peak energy correlates with the frontier Pc metal d-orbital, with Co (d<sup>7</sup>) and Ni (d<sup>8</sup>) at similar wavelengths. Likewise, Cu (d<sup>9</sup>) and Zn (d<sup>10</sup>) have similar energies. The dependence on orbital filling indicates that d-electrons, while only weakly involved in the A<sup>CT</sup> transition, play a role in the electronic band-offsets between the MPc and MoS<sub>2</sub>. Similar effects have been reported for the coupling of MPc molecules to other semiconductor surfaces.<sup>286</sup>

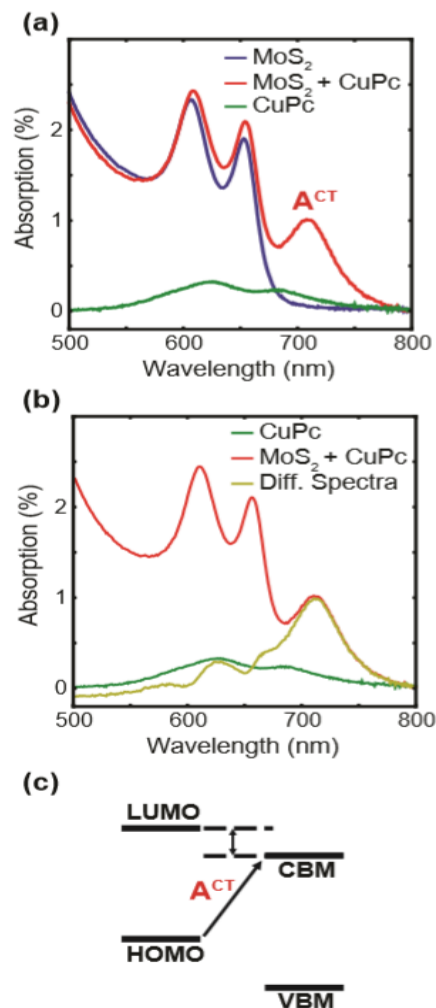


Figure 2.3 (a) Optical absorption spectra of pristine MoS<sub>2</sub>, CuPc, and CuPc – MoS<sub>2</sub> heterojunction films. The new transition at 710 nm is denoted A<sup>CT</sup>. (b) Optical absorption spectra of a pristine CuPc film, the CuPc – MoS<sub>2</sub> heterojunction, and the difference spectrum of the CuPc – MoS<sub>2</sub> heterojunction and pristine MoS<sub>2</sub> absorption. (c) Proposed origin of A<sup>CT</sup> as a direct transition from the MPc HOMO to the MoS<sub>2</sub> CBM.

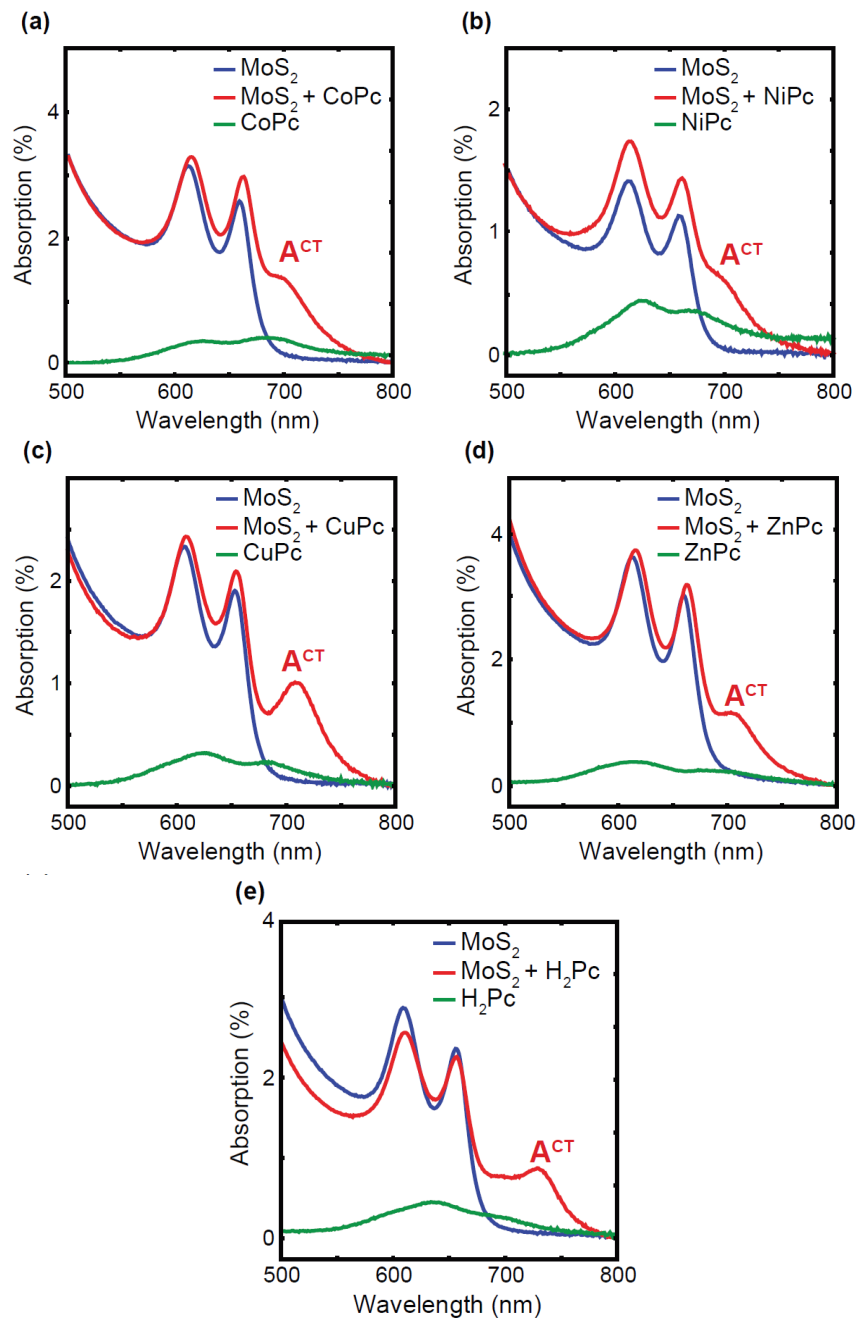


Figure 2.4 Absorption spectra of monolayer chemical vapor deposition grown MoS<sub>2</sub>, 0.4 nm of Pc, and MoS<sub>2</sub> with 0.4 nm Pc deposited. The emergent charge-transfer absorption is labeled A<sup>CT</sup>. All spectra were taken on sapphire substrates.

Further evidence for this interpretation of the optical absorption spectra is provided by DFT modeling. Figure 2.5 shows the computed vacuum level alignment of the individual phthalocyanine–MoS<sub>2</sub> system components. Following literature approaches,<sup>275</sup> the HSE hybrid functional<sup>287</sup> was employed to describe the MPc gas-phase electronic structures. For all cases, we find that the HOMO is localized primarily on the organic sublattice (a<sub>1u</sub>). All molecules are found to be in their low-spin configurations with the b<sub>2g</sub> (d<sub>xy</sub>) and b<sub>1g</sub> (d<sub>x<sup>2</sup>-y<sup>2</sup>) orbitals singly occupied for CoPc and CuPc, respectively, in agreement with experiment. While consistent with previous hybrid functional descriptions of MPc, these results differ qualitatively from local and semilocal density functional descriptions that predict a change in the HOMO composition based on the d-shell</sub>

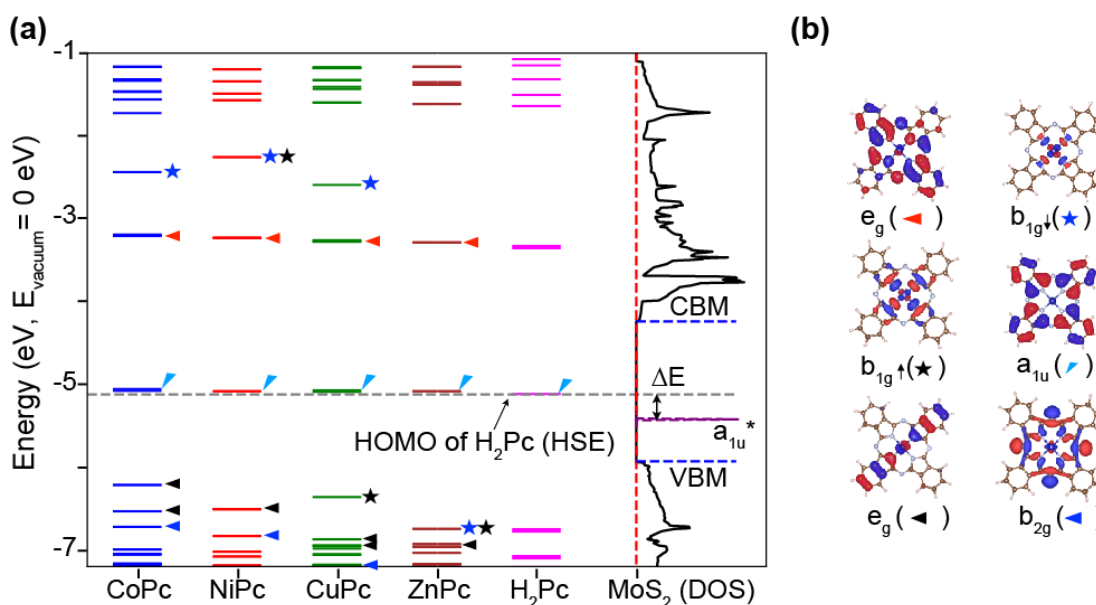


Figure 2.5 (a) Electronic structure of Co, Ni, Cu, Zn, and metal-free phthalocyanines in the gas phase computed using the HSE functional. For all molecules, the HOMO has a strong  $\pi$ -character. Orbital symmetries are labelled for the MPc (H<sub>2</sub>Pc has a lower symmetry and distinct irreducible representations). All molecules are found in their low-spin configuration with the b<sub>2g</sub> (d<sub>xy</sub>) and b<sub>1g</sub>

( $d_{x^2-y^2}$ ) orbitals being singly occupied for CoPc and CuPc, respectively. The density of states of MoS<sub>2</sub> with respect to vacuum energy is shown at the right, along with the change in level alignment (PBE) of an H<sub>2</sub>Pc molecule upon forming a heterojunction with MoS<sub>2</sub>. (b) Representative electron densities of the indicated orbitals as well as their symmetry labels.

occupancy, indicating the significant effect of self-interaction corrections. The HOMO–LUMO gap in the gas phase contracts weakly with the d-shell occupancy, from 1.85 eV in CoPc to 1.80 eV in ZnPc. In contrast, the HOMO – HOMO-1 energy difference strongly varies with d occupancy from 1.14 eV in CoPc to 1.43, 1.29, and 1.66 eV in NiPc, CuPc, and ZnPc, respectively.

Using Tkatchenko-Scheffler van-der-Waals corrections,<sup>288</sup> we find that the H<sub>2</sub>Pc molecule adsorbs with a binding energy of 1.635 eV/molecule and an equilibrium distance of 3.3 Å above MoS<sub>2</sub> basal plane. The resulting electronic structure is fully consistent with the present experiments since H<sub>2</sub>Pc/MoS<sub>2</sub> is found here to be a type-II heterojunction, with a HOMO energy ~0.4 eV lower than in the gas phase and well within the MoS<sub>2</sub> band gap (see Figures 2.3c and 2.5). This energy difference is a consequence of the pronounced interface dipole, with all molecular levels experiencing a similar downshift.

To further probe the nature of the MPc – MoS<sub>2</sub> coupling at smaller length scales and without the spatial variability in defect density and doping inherent in CVD-derived MoS<sub>2</sub> films, we investigated the MPc dependence in the heterojunction by surface-enhanced Raman spectroscopy (SERS) on mechanically exfoliated (“Scotch Tape”) MoS<sub>2</sub>. SERS has been observed in similar organic–MoS<sub>2</sub> and MPc–MoS<sub>2</sub> systems,<sup>247,248,277,278</sup> where the semiconductor is known to be strongly responsive to charge transfer dynamics.<sup>248,249,273,289–292</sup> The MoS<sub>2</sub> in this case was

exfoliated onto 285 nm thick SiO<sub>2</sub> (see Methods) to increase optical contrast and allow collection of sufficient MPc Raman signal on this substrate as compared to sapphire substrates. AFM images of the MoS<sub>2</sub> before and after deposition of MPc (Figure 2.6) show the presence of ~50 nm diameter aggregates uniformly distributed across the surface, though more precise characterization is limited by strong AFM tip – MPc interactions that cause extensive streaking and tip artifacts in the images. The laser spot used for prolonged Raman and photoluminescence collection (> 120 sec) is readily apparent in Figure 2.6b as a circle of larger aggregates. To prove that heating is the cause of this increased aggregation, the sample was then placed on a 250 °C hot plate in an inert N<sub>2</sub> atmosphere for 30 min. This treatment caused the small CuPc particles to coalesce into a few large aggregates as seen in Figure 2.6b inset. To avoid this local heating induced aggregation, the laser excitation conditions were maintained below 150 μW and 60 sec.

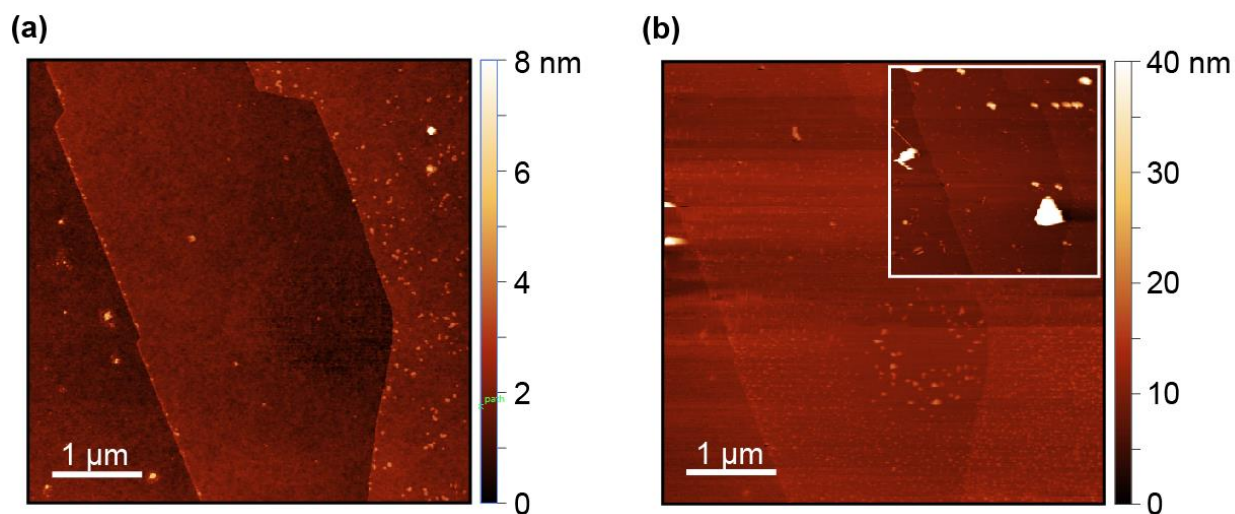


Figure 2.6 (a) AFM image of SiO<sub>2</sub>, monolayer, and bilayer MoS<sub>2</sub> flakes before deposition of MPc. (b) AFM of the same location following deposition of 0.4 nm CuPc. Note the circle of larger CuPc aggregates due to prolonged exposure to the Raman laser. (b inset) The same location following a

30 minute anneal at 250 °C under an N<sub>2</sub> atmosphere. Note that the CuPc particles have coalesced into larger aggregates.

The Raman intensity enhancement factor,  $E_{REL}$ , is calculated by dividing the signal intensity of a given MPc vibrational mode on the MoS<sub>2</sub> by the signal intensity on bare SiO<sub>2</sub> (eq. 1).

$$E_{REL} = \frac{I_{MoS_2}}{I_{SiO_2}} \quad (1)$$

Based on prior XPS quantification (Figure 2.2), we assume that the MPc coverage is nearly equal on MoS<sub>2</sub> and SiO<sub>2</sub>. Previous work has shown that the first deposited layer of MPc on bulk MoS<sub>2</sub> lies face-on.<sup>283</sup> Since the MPc Raman peaks maintain identical intensity ratios for all thicknesses, we expect the same orientation for the Pc molecules from bulk down to monolayer MoS<sub>2</sub>.<sup>293</sup> Representative spectra and layer-dependent enhancement results are presented in Figure 2.6.

The effects of laser wavelength and MPc metal identity on Raman scattering are summarized in Figure 2.6a.  $E_{REL}$  is far greater at 633 nm than at shorter wavelengths. The observed enhancement near the resonance at 633 nm follows an M atomic number trend (Figure 2.7a). Going across the period, CoPc shows the highest  $E_{REL}$  followed by NiPc and then CuPc, with ZnPc and H<sub>2</sub>Pc exhibiting essentially negligible Raman enhancement. In terms of wavelength dependence, the Raman enhancement factor increases with increasing wavelength. At 473 nm, the intensity of most MPc Raman modes is immeasurably low, whereas at 532 nm excitation, the enhancement is 2 – 4x that of the signal on SiO<sub>2</sub>. Ultimately, at 633 nm excitation, the enhancement at the heterojunction increases by another 10x, up to an overall 30x for CoPc. This wavelength coincides with major optical absorption features of both the CoPc and MoS<sub>2</sub>. Prior work and theory has

shown that large Raman enhancement factors of other organic dye molecules on MoS<sub>2</sub> can be achieved by matching the laser excitation energy to excitonic or charge transfer resonances in the dye–MoS<sub>2</sub> system,<sup>248,249</sup> in agreement with the present observations. The trend in resonant enhancement is not correlated with the MPc optical absorption but does track the Periodic Table first-row transition metal progression with a maximum  $E_{REL}$  for CoPc, decreasing for NiPc and CuPc, and with almost no enhancement for ZnPc. This trend can be understood in terms of the decreasing energy of orbitals with strong out-of-plane d-character (i.e.,  $d_{xz}$ ,  $d_{yz}$ , and  $d_z^2$ ) lying below the predominantly  $\pi$ -HOMO, which should also fall in energy relative to vacuum due to the is further confirmed by Raman spectroscopy of metal-free H<sub>2</sub>Pc similarly deposited on MoS<sub>2</sub>, which shows negligible enhancement of the Raman signal despite 633 nm being resonant with the intense H<sub>2</sub>Pc optical absorption.

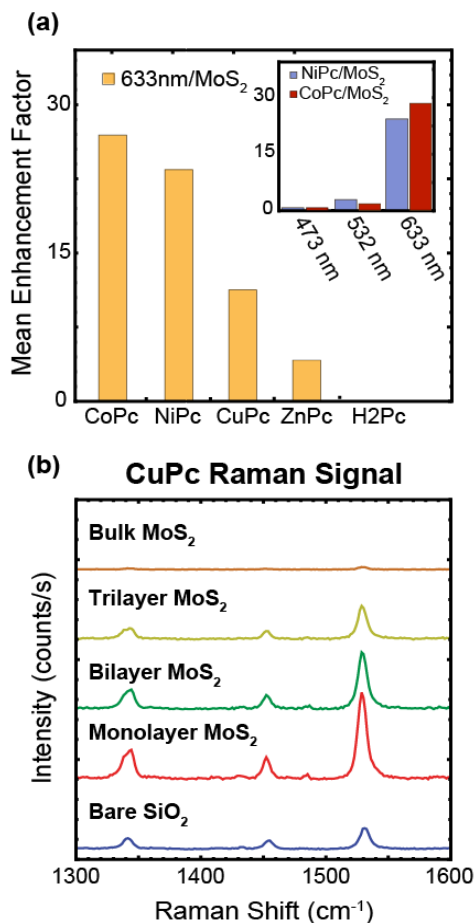


Figure 2.7 (a) Relative MPc-MoS<sub>2</sub> heterojunction Raman enhancement factors (633 nm laser excitation) showing a decrease with increasing M atomic number. (top inset) Excitation wavelength-dependent enhancement shows a steady increase as the wavelength is changed from non-absorbing (473 nm) to on-resonance with the MPc Q-band  $\pi \rightarrow \pi^*$  absorption and MoS<sub>2</sub> exciton absorption. (b) Dependence of CuPc Raman spectra (532 nm laser source) on MoS<sub>2</sub> thickness.

The d-orbital hypothesis is also supported by DFT calculations (Figure 2.5a), which show that the energy of the  $e_g$  ( $d_{xz}$ ,  $d_{yz}$ ) orbitals decreases from 1.14 eV below the HOMO in CoPc to 1.43, 1.78, and 1.85 (eV) below the HOMO for NiPc, CuPc, and ZnPc, respectively (Figure 2.5a). We hypothesize that the energy of these orbitals relative to the MoS<sub>2</sub> valence band maximum controls the mixing of the optical excitations of MoS<sub>2</sub> and MPc, which becomes less effective as the d-

orbital energies decrease. A similar but lesser trend is evident in the MPc LUMO, which also has out-of-plane d-orbital character ( $e_g$ ) and decreases in energy across the period from -3.19 eV in CoPc to -3.28 eV for ZnPc. Consequently, mixing/back-bonding from the MoS<sub>2</sub> CBM to the MPc LUMO may also play a role.

Theoretical and experimental work on non-plasmonic (chemical) SERS points to the important role of hybridization between adsorbed molecules and the surface in increasing polarizability and thus increasing the Raman signal enhancement.<sup>249,273,292</sup> A similar trend has also been observed in the high-resolution electron energy loss Raman spectrum of MPcs on graphene–Ni(111),<sup>294</sup> which show decreasing metal–graphene bonding character as the MPc d-orbitals are filled. This behavior highlights the important role of non-frontier orbitals (i.e., not HOMO or LUMO) in tuning the properties of mixed-dimensional heterojunctions.

As shown in previous work, Raman enhancement of adsorbate spectra on TMDCs depends on the number of TMDC layers, with decreasing enhancement as TMDC layer number increases as studied under 532 nm illumination.<sup>247,248,295</sup> This behavior has been attributed to increased absorption by the underlying MoS<sub>2</sub>.<sup>247</sup> Similar trends are noted in the present study with CuPc, ZnPc, and H<sub>2</sub>Pc. In these cases, as exemplified by the CuPc data (Figure 2.8), the trend of decreasing Raman enhancement with increasing MoS<sub>2</sub> layer number is clearly evident. A notable exception to this trend is the CoPc- and NiPc–MoS<sub>2</sub> heterojunction under 633 nm excitation, which both increases in enhancement on bilayer MoS<sub>2</sub>, to 48.2 and 26.5 respectively, before ultimately decreasing at the bulk limit. This exception has not been reported in the previous literature since MPc–MoS<sub>2</sub> heterojunction systems have not been studied systematically under near-resonant

conditions. We hypothesize that this divergence from previously reported trends is due to particularly favorable charge transfer between CoPc and MoS<sub>2</sub>. A full listing of E<sub>REL</sub> values of the MPc at different MoS<sub>2</sub> thicknesses are found in Table 2.1 (633 nm excitation) and Table 2.2 (532 nm excitation).

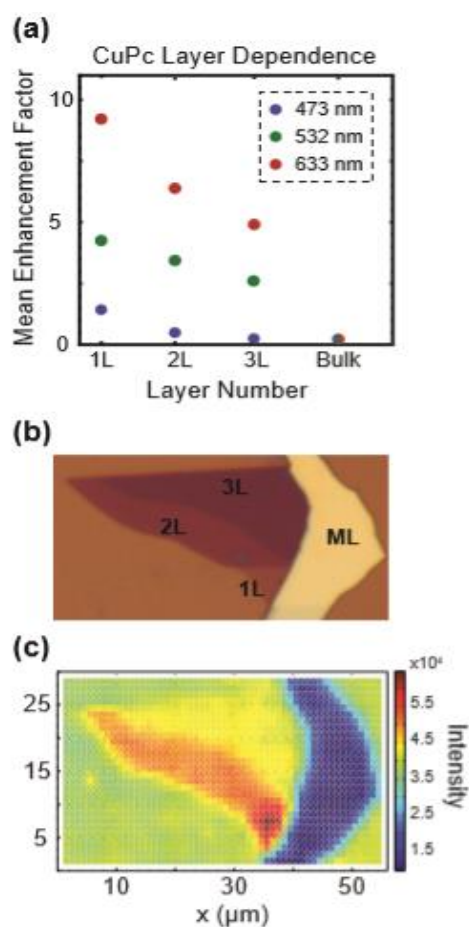


Figure 2.8 (a) Mean Raman enhancement factors for CoPc- and NiPc-MoS<sub>2</sub> heterojunctions using 532 nm and 633 nm lasers reveal the general trend of decreasing enhancement as the MoS<sub>2</sub> layer number increases from monolayer to bulk. (b) Optical image of a MoS<sub>2</sub> flake with areas of single-layer (1L), bilayer (2L), trilayer (3L), and multilayer (ML) (> 30 nm). (c) Corresponding map of Raman intensity of the CuPc B<sub>2g</sub> ring stretching mode at 1530 cm<sup>-1</sup>.

Table 2.1  $E_{REL}$  (standard deviation) for each phthalocyanine and layer number with 633 nm excitation laser

	1L	2L	3L	Bulk
CoPc	25.8 (3.2)	48.2 (10.2)	14.8 (2.1)	1.7
NiPc	23.4 (3.6)	26.5 (7.2)	14.1 (1.3)	0.5
CuPc	9.2 (0.9)	6 (0.8)	5.1 (1.0)	*
ZnPc	4.9 (0.7)	4.9 (1.7)	2.1 (0.3)	0.6
H <sub>2</sub> Pc	*	*	*	*

\*Signal too weak to measure

Table 2.2  $E_{REL}$  (standard deviation) for each phthalocyanine and layer number with 532 nm excitation laser

	1L	2L	3L	Bulk
CoPc	2.5 (0.3)	2.1 (0.1)	1.7 (0.2)	*
NiPc	2.9(0.2)	1.8 (0.2)	2.2(0.1)	*
CuPc	3.9 (0.1)	2.7 (0.2)	1.6 (0.1)	*
ZnPc	0.6 (0.1)	0.5 (0.2)	*	*
H <sub>2</sub> Pc	1.6 (0.4)	1.4 (0.6)	0.9 (0.3)	*

\*Signal too weak to measure

In summary, we have systematically probed the coupling in mixed-dimensional heterojunctions between 0D metallophthalocyanine molecules and 2D MoS<sub>2</sub> using UV–Vis absorption, Raman spectroscopy, and DFT modeling. The appearance of a new optical absorption feature arising from MPc–MoS<sub>2</sub> heterojunctions demonstrates optically-stimulated charge transfer that is dependent on the MPc transition metal core identity. Raman enhancement studies further characterize the interfacial charge transfer and reveal a trend correlating with MPc metal d-orbital occupancy, which is analogous to a charge transfer absorption model. Together these results point to the critical role of non-frontier orbitals in mediating the exchange of charge across the interface in phthalocyanine–MoS<sub>2</sub> heterojunctions. By providing mechanistic insight into charge transfer between MPcs and TMDCs, this work provides direct guidance to ongoing efforts to utilize mixed-dimensional heterojunctions in electronic and optoelectronic applications.

## 2.4. Methods

Monolayer to few-layer samples of MoS<sub>2</sub> were prepared using the “Scotch Tape” method of micromechanical exfoliation onto SiO<sub>2</sub> substrates. This technique ensures single crystal quality and clean surfaces as mono to few layer stacks are left behind in cleaving the bulk crystal. Following exfoliation, samples were annealed at 300 °C in an inert Ar/H<sub>2</sub> atmosphere to remove any remnant tape residues. Monolayer CVD MoS<sub>2</sub> films were grown directly on single-crystal sapphire substrates (MTI) using MoO<sub>3</sub> (Millipore Sigma) and sulfur (Millipore Sigma) powder precursors, following a previously reported procedure.<sup>68</sup> Samples were characterized before MPc deposition using AFM, Raman, and photoluminescence measurements at room temperature to confirm their quality and pre-deposition behavior. AFM was used to confirm smooth surface morphology as well as to determine the flake thickness (Asylum Cypher AFM, tapping mode with NanoWorld Si cantilever NCHR-W, resonant frequency ~300 kHz). Raman and photoluminescence measurements were carried out with 473 nm, 532 nm, or 633 nm laser excitation (Horiba Raman XPlora for 473 nm and 532 nm, Princeton Instruments Acton TriVista Raman System for 633 nm), with less than 150 μW power and an 1800 grooves/mm diffraction grating.

Metallophthalocyanines were purchased from Sigma Aldrich and purified by temperature gradient sublimation. Films were deposited by thermal evaporation following published methods:<sup>243</sup> a bell jar containing the Pc in an alumina boat under a shutter was pumped below 10<sup>-5</sup> Torr, after which current was passed through the boat until a steady deposition rate of 0.10 to 0.20 Å/s was reached, as monitored by a quartz crystal microbalance (QCM). Once a steady rate was reached, the shutter was opened and 4 Å of MPc was deposited, which is approximately one

monolayer. Following MPc deposition, the films were again evaluated by AFM and Raman. Due to the strong interactions between the MPc molecules and the AFM tip, post-deposition images were difficult to collect and as a result can only qualitatively verify the presence of MPc but provide no quantitative information about film thickness. Sticking coefficients were evaluated by monitoring typical depositions on sapphire substrates and thin layers of MoS<sub>2</sub> grown by CVD. The amount deposited was quantified by X-ray photoelectron spectroscopy by comparing the integration of the M peak from the MPc on the different substrates following charge correction to the adventitious C 1s peak at 284.8 eV.

Density functional theory calculations were carried out using the plane wave basis set code Quantum-Espresso.<sup>296</sup> Exchange and correlation interactions were described using the Perdew-Burke-Ernzerhof (PBE) of the generalized gradient approximation (GGA)<sup>297</sup> unless otherwise stated. Optimized norm-conserving pseudopotentials<sup>298</sup> were used to describe electron-nuclei interactions. A wavefunction cutoff of 85 Ry and Gamma-centered k-point sampling was used. K-point mesh of  $9 \times 9 \times 1$ , and  $2 \times 2 \times 1$  were used for monolayer MoS<sub>2</sub> with unit cell dimension of  $3.18 \times 3.18 \times 31.13$  (Å), and H<sub>2</sub>Pc – MoS<sub>2</sub> system with supercell of  $16.43 \times 15.81 \times 31.13$  (Å), respectively, both with vacuum region larger than 24 Å. All parameters were tested in order to achieve convergence of 0.001 eV/atom in total energy and  $10^{-6}$  eV in electronic energy. The supercell dimension and number of atoms (30 Mo and 60 S atoms) for H<sub>2</sub>Pc – MoS<sub>2</sub> system were similar to a previous study.<sup>299</sup> Tkatchenko-Scheffler dispersion corrections<sup>288</sup> were used to describe van der Waals interactions between H<sub>2</sub>Pc and MoS<sub>2</sub>. MPc molecules were calculated using Heyd–Scuseria-Ernzerhof<sup>287</sup> (HSE06) screened hybrid functional as it could predict correct

HOMO–LUMO gaps, closest to experimental results, as opposed to PBE or other hybrid functionals for those systems.<sup>275</sup>

\*This chapter was originally published in *ACS Nano* in 2019. Reprinted with permission from <sup>66</sup>.

Copyright 2019 American Chemical Society.

### **3. Quenching of MoS<sub>2</sub> Defect Photoluminescence by Non-Frontier Orbitals in Metal Phthalocyanines**

#### **3.1. Abstract**

Point defects play an important role in determining the optical and electrical properties of monolayer semiconductors such as MoS<sub>2</sub>. Although structure of various defects in monolayer MoS<sub>2</sub> is well studied, very little is known about the optical properties of fluorescent defect species in MoS<sub>2</sub>. Here we demonstrate quenching of the low-temperature defect photoluminescence (PL) in MoS<sub>2</sub> by the deposition of metallophthalocyanines (MPc). The quenching is found to significantly depend on the identity of the phthalocyanine metal, with the quenching efficiency decreasing in the order CoPc, CuPc, ZnPc, with almost no quenching by metal-free H<sub>2</sub>Pc. Time correlated single photon counting (TCSPC) measurements corroborate the observed trend, showing decreased defect PL lifetime in MPc – MoS<sub>2</sub>, and gate voltage dependent PL also reveals suppression of the defect emission even at large Fermi level shifts. Computational analysis reveals that the MPc complexes stabilizes dark, negatively charged defects over luminescent neutral defects. Furthermore, there is a correlation between the observed PL quenching and the energy of the out-of-plane MPc d-orbitals, suggesting that resonant hole tunneling provides a secondary nonradiative decay pathway for defect-bound excitons. These results demonstrate the possibility of controlling excited state pathways of specific defects via molecular electronic structure tuning and thus have implications in the design of mixed-dimensional optoelectronic devices.

### 3.2. Introduction

The transition metal dichalcogenides (TMDs) have emerged as an important class of two-dimensional (2D) semiconductors,<sup>263</sup> with applications as diverse as flexible electronics,<sup>300</sup> biosensors,<sup>301</sup> photovoltaics,<sup>113</sup> and other photonic devices,<sup>302</sup> neuromorphic computing,<sup>108</sup> as well as catalysis.<sup>303</sup> Among the TMDs, MoS<sub>2</sub> is the most widely studied and serves as a model system for exploring the fundamental physics and chemistry of the TMDs.<sup>265</sup> While MoS<sub>2</sub> has exceptional inherent optoelectronic properties, there are new opportunities in combining it with other classes of materials to form mixed-dimensional heterojunctions.<sup>246</sup> These interfaces leverage the unique capabilities of their constituent materials to realize new performance metrics, novel heterojunction device concepts, and emergent phenomena that are not possible in either isolated system. In this regard, the interface of organic molecular materials with monolayer MoS<sub>2</sub> is of particular interest due to the broad synthetic tunability, controllable assembly, and facile processing of the former, as well as the exceptional optical and electrical properties of the latter.<sup>304-306</sup> Molecular heterojunctions have been used extensively to modulate the photoluminescence (PL) of monolayer MoS<sub>2</sub>, including quenching of PL by charge transfer,<sup>68,307</sup> enhancing of emission via energy transfer,<sup>251</sup> enhancing Raman scattering,<sup>66</sup> and increasing PL quantum yield (PLQY) by defect passivation.<sup>84</sup>

Understanding and controlling the defect-related optical response in monolayer MoS<sub>2</sub> is essential to realizing its potential in electronic, optoelectronic, and quantum technologies.<sup>257,308</sup> Defects in MoS<sub>2</sub> play an important role in electronic transport,<sup>309,310</sup> doping,<sup>64</sup> and exciton recombination.<sup>81</sup> At low temperatures (<150 K), the defects in MoS<sub>2</sub> become luminescent,

exhibiting PL at wavelengths greater than 700 nm of similar or greater intensity than the MoS<sub>2</sub> A exciton at 650 - 670 nm. While this defect PL is ubiquitous in MoS<sub>2</sub> at low temperatures, the structural and chemical origin of these bright defects is still unclear.<sup>89,311</sup> While these emissive defect states are expected to have a negative impact on conventional optoelectronic devices, under certain circumstances they have also been shown to be efficient single photon emitters for quantum information applications.<sup>312,313</sup>

To date no molecular strategy has been devised to quench the defect PL in MoS<sub>2</sub>. Encapsulation with hexagonal boron nitride (hBN) can reduce the background defect PL,<sup>314</sup> but this strategy is labor intensive and not scalable. Molecular approaches to MoS<sub>2</sub> defect passivation have been explored,<sup>60,256,299</sup> but these strategies do not efficiently quench the defect PL.<sup>81</sup> Understanding the interactions of molecular adsorbates with defects in MoS<sub>2</sub> will be essential to any future attempts at rational chemical modification of these defects.

Based on theoretical predictions and experimental observation, the most common intrinsic point defect in MoS<sub>2</sub> is thought to be sulfur vacancy (S<sub>vac</sub>), which creates localized states near the conduction band edge.<sup>59,61</sup> Recent work has shown that previously undetected oxygen substitutions (O<sub>sub</sub>) also represent a significant fraction of the point defects in MoS<sub>2</sub>.<sup>62,63</sup> While point defects in MoS<sub>2</sub> are correlated with defect PL, there is some evidence of the partially extrinsic character of this emission peak. For example, helium ion bombardment induces point defects in MoS<sub>2</sub> with bright and narrow PL,<sup>22,313</sup> but these defects are not luminescent until exposed to gases.<sup>315</sup> Furthermore, defect emission is enhanced by exposure to water and light, but not O<sub>2</sub> alone.<sup>316</sup> The location of the Fermi level plays a critical role in the PLQY of MoS<sub>2</sub> defects by changing the



Metallophthalocyanines (MPcs) present an ideal system for exploring the chemical control of optically-active defects in monolayer MoS<sub>2</sub>. The electronic structure of MPcs can be altered in systematic ways by changing the central metal atom while retaining its aromatic macrocycle framework (Figure 3.1a).<sup>151</sup> Thus, phthalocyanine-MoS<sub>2</sub> mixed dimensional heterojunctions, shown schematically in Figure 3.1b, have been studied to probe PL quenching,<sup>307</sup> Raman enhancement,<sup>66</sup> ultrafast dynamics,<sup>165,241</sup> and interfacial charge transfer and hybridization.<sup>154</sup> On the subject of MoS<sub>2</sub> defects, adsorbed titanyl phthalocyanine (TiOPc) has been investigated for passivating mid gap states in MoS<sub>2</sub>,<sup>256,299</sup> and adsorbed ZnPc has been shown to suppress persistent photocurrent in MoS<sub>2</sub> photodetectors originating from trap states.<sup>258</sup>

In this work, we systematically explore the interactions of various metallophthalocyanines (MPc) with defects in monolayer MoS<sub>2</sub> to better understand defect – adsorbate interactions. It will be shown that MPcs quench the defect emission of MoS<sub>2</sub>, with the quenching efficiency decreasing in the order CoPc, CuPc, ZnPc, and H<sub>2</sub>Pc. Experimental data rule out charge depletion and nonradiative energy transfer as the mechanism of this defect PL quenching, while theoretical considerations rule out charge transfer. Gate voltage-dependent measurements reveal that this quenching persists to very low Fermi energies. Moreover, computation of the defect formation energies shows that the adsorbed MPcs render negatively charged defects more favorable than neutral defects, and the relative defect formation energies agree with the experimentally observed trends. The results provide a molecular level understanding of emergent adsorbate interactions with luminescent defects in MoS<sub>2</sub> and suggest routes for further control of this PL through molecular design.

### 3.3. Results and Discussion

In initial experiments, CoPc was deposited to a thickness of 1.0 nm on mechanically exfoliated monolayer MoS<sub>2</sub> as shown in Figure 3.2a. The monolayer thickness of the MoS<sub>2</sub> was verified by Raman spectroscopy (Figure 3.2a), while the CoPc deposition was confirmed by its characteristic Raman modes in the region of 1100 – 1600 cm<sup>-1</sup>. The Raman modes of CoPc are visible despite the nm film thickness due to known Raman enhancement by the underlying monolayer MoS<sub>2</sub>.<sup>66,247</sup> PL spectra were collected before and after CoPc deposition on the same MoS<sub>2</sub> flake. At 300 K,

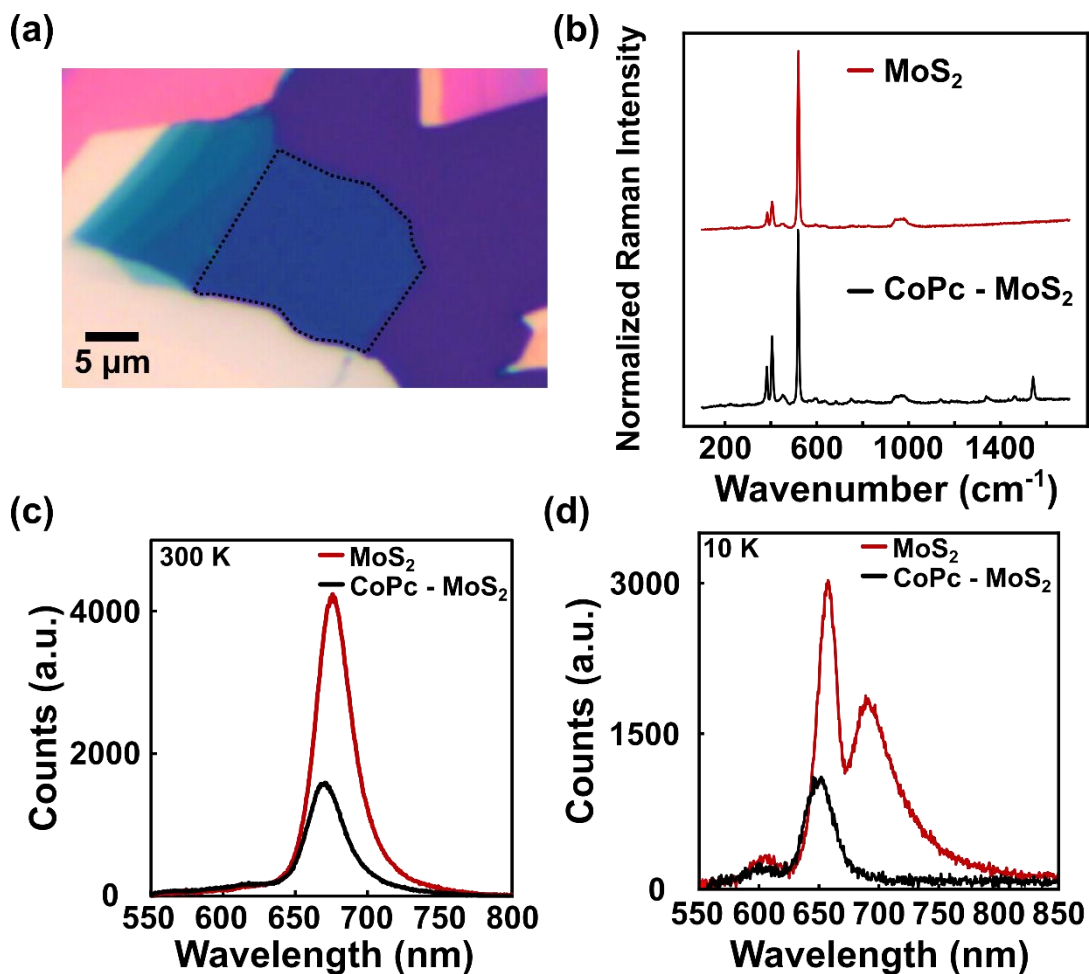


Figure 3.2 (a) Optical micrograph of mechanically exfoliated MoS<sub>2</sub> with the monolayer region highlighted. (b) Raman spectra of monolayer MoS<sub>2</sub> before and after deposition of 1 nm CoPc. The separation of the A<sub>1g</sub> and E<sub>2g</sub> is  $\sim 19$  cm<sup>-1</sup>, indicating monolayer MoS<sub>2</sub>. Raman modes that appear in the 1100 – 1500 cm<sup>-1</sup> range are characteristic of CoPc. (c) 300 K PL spectra of mechanically exfoliated MoS<sub>2</sub> and MoS<sub>2</sub> - 1 nm CoPc. The A-exciton and associated trion are prominent at 675 nm, and a small higher-energy shoulder is visible due to the B-exciton (d) 10 K photoluminescence of MoS<sub>2</sub> and MoS<sub>2</sub> – 1 nm CoPc. At this temperature, the MoS<sub>2</sub> defect emission becomes apparent at 700 nm in addition to the A- and B- excitons at 660 nm and 600 nm, respectively. The defect PL is completely quenched by the CoPc and the A- exciton is partially quenched.

the overlapping neutral MoS<sub>2</sub> A-exciton and trion emissions are prominent at 670 nm, as well as a higher energy shoulder assignable to the B-exciton (Figure 3.2c). Following CoPc deposition, the

MoS<sub>2</sub> PL is partially quenched. This is likely due to mutual charge transfer via formation of a type-II heterojunction.<sup>165</sup> In addition, the PL is shifted to lower wavelengths, likely a result of an increased ratio of neutral excitons to trions resulting from depletion of free MoS<sub>2</sub> carriers as a result of the CoPc overlayer. At cryogenic temperatures, the MoS<sub>2</sub> defect emission becomes apparent above 700 nm, in addition to the previously observed A- and B- excitons (Figure 3.2d). The A- and B- excitons have shifted to shorter wavelengths (650 nm and 600 nm respectively) as expected for MoS<sub>2</sub> excitons at low temperature.<sup>315</sup> Following deposition of CoPc/creation of the heterojunction, the MoS<sub>2</sub> A-exciton and trion PL are quenched as in the room temperature PL, and complete quenching of the defect PL is also observed. Furthermore, the excitonic PL is also quenched, as at room temperature.

To investigate the mechanism of defect PL quenching, the variation in defect PL was compared over a wide range of MPc derivatives (M = Co, Cu, Zn, H<sub>2</sub>). For a direct comparison between different molecules, the MoS<sub>2</sub> growth technique was changed to chemical vapor deposition (CVD), which yields a higher concentration of defects.<sup>317</sup> This makes the defect PL an order of magnitude more intense than the A-exciton and thus accentuates the differences in the quenching behavior between different MPcs. To avoid spatial inhomogeneity, MPc films were deposited in different regions of a large area MoS<sub>2</sub> monolayer film via shadow masking (Figure 3.3a). Since the crystalline quality and stoichiometry of CVD-derived MoS<sub>2</sub> can vary along the growth direction, this masking approach allows the defect PL to be compared between pristine MoS<sub>2</sub> and the nearby MPc – MoS<sub>2</sub> heterojunction that has nominally the same growth quality.

Figure 3.3b compares the defect PL quenching efficiency of different MPc-structures. As expected from higher defect density in CVD MoS<sub>2</sub>, the defect emission is more intense than the excitonic emission in these samples compared with mechanically exfoliated samples in Figure 3.2d. There is a clear trend in intensity of the defect PL peak between MPcs, with CoPc being the

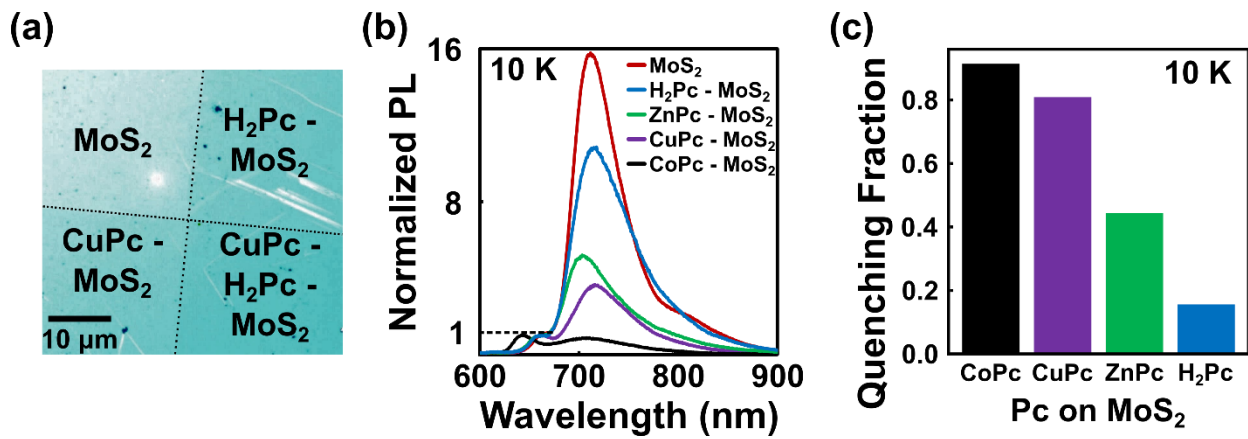


Figure 3.3 (a) Optical microscopy of representative MPc films on monolayer CVD MoS<sub>2</sub>. PL spectra of MoS<sub>2</sub> were collected near the edges of the MPc film to ensure the observed quenching was not due to inhomogeneity in CVD growth. (b) Low temperature photoluminescence spectra of representative CVD MoS<sub>2</sub> and MoS<sub>2</sub> with 1 nm films of H<sub>2</sub>Pc, ZnPc, CuPc, and CoPc. The spectra are normalized to the intensity of the MoS<sub>2</sub> A exciton peak. (c) Comparison of quenching fraction of each MPc.

strongest quencher, followed by CuPc, ZnPc, and finally H<sub>2</sub>Pc showing the least quenching efficiency. This is compared graphically in Figure 3.3c, using the quenching fraction, which is defined as in eq. 1. Here QF is the quenching fraction, PL(MPc - MoS<sub>2</sub>) is the PL spectrum of the

$$QF = 1 - \frac{\sum_{675}^{900} PL(MPc - MoS_2)}{\sum_{675}^{900} PL(MoS_2)} \quad (1)$$

MPc - MoS<sub>2</sub> heterojunction, PL(MoS<sub>2</sub>) is the PL of the nearby bare MoS<sub>2</sub>, and the  $\Sigma$  operator denotes a Riemann sum of the curves over the indicated wavelengths. A quenching fraction of 1 means complete disappearance of the defect PL peak and 0.0 indicates no change in the defect PL.

Thus, the peak areas follow the same trend as the peak height shown in Figure 3.3b, with the quenching fraction following the order,  $\text{CoPc} > \text{CuPc} > \text{ZnPc} > \text{H}_2\text{Pc}$ . The non-normalized PL plots, including the  $\text{MoS}_2$  reference PL used for each  $\text{MPc} - \text{MoS}_2$  are shown in Figure 3.4.

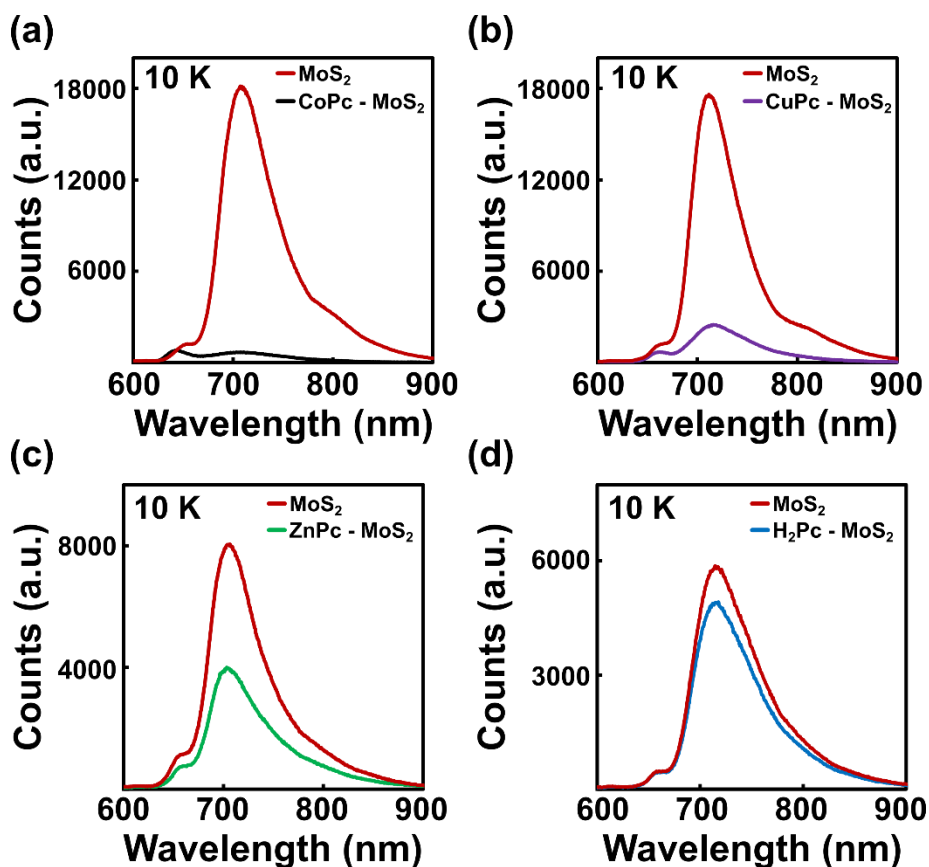


Figure 3.4 Non-normalized PL spectra comparing (a) CoPc, (b) CuPc, (c) ZnPc, and (d)  $\text{H}_2\text{Pc}$  with a nearby clean  $\text{MoS}_2$ . There is a clear trend in quenching efficiency, with  $\text{CoPc} > \text{CuPc} > \text{ZnPc} > \text{H}_2\text{Pc}$ . Within the MPc, the quenching efficiency follows the Periodic Table, becoming less efficient as d-electrons are added to the central metal center in the MPcs. Note that the shape of the defect emission does vary between spectra due to inhomogeneity in the CVD  $\text{MoS}_2$ . All comparisons in this figure are done for  $\text{MoS}_2 - \text{Pc}$  areas within  $10 \mu\text{m}$  of the representative pristine  $\text{MoS}_2$  in a given spectrum. Thus the  $\text{MoS}_2$  varies between panels but is comparable within a given panel.

To verify the observed PL quenching behavior, time-resolved PL measurements were carried out at low temperatures (10 K) using time correlated single photon counting (TCSPC), as shown in Figure 3.5. The defect PL in pristine MoS<sub>2</sub> is known to have a lifetime of several  $\mu$ s--far longer than the exciton lifetime of  $\sim$ 100 ps.<sup>81</sup> Due to instrumental limitations, we are only able to collect TCSPC traces out to 2  $\mu$ s, which does not allow accurate fitting of the long defect PL decay times.

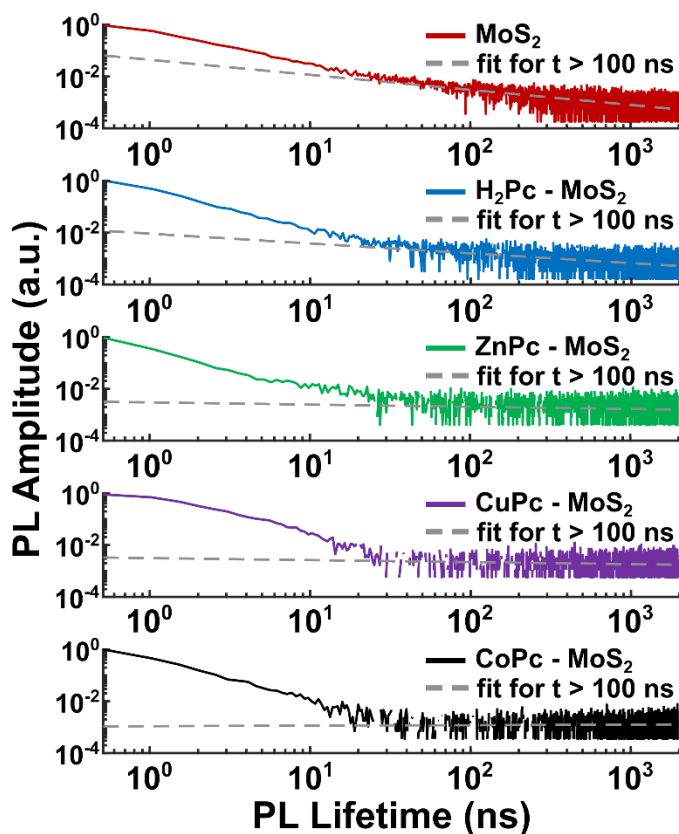


Figure 3.5 Time correlated single photon counting (TCSPC) traces collected at 10 K with a 450 nm laser showing the photoluminescence decay for MoS<sub>2</sub> and the MoS<sub>2</sub> – MPc systems. Due to instrumentation limits, the  $\mu$ s-scale decay of the defect emission cannot be accurately fit but can allow qualitative comparisons by using a linear fit to the median intensity for times  $>$  100 ns.

However, a qualitative estimation of defect-associated exciton decay rates can be obtained by fitting to the trace for times greater than 100 ns since the exciton emission has a significantly shorter lifetime (600 ps at 300 K, 150 ps at 77 K)<sup>81</sup> and is not expected to contribute at these longer times. The slopes of these lines then represent the relative magnitude of defect PL decay occurring due to MPc - MoS<sub>2</sub> heterojunction related processes. The pristine MoS<sub>2</sub> shows the expected  $\mu$ s scale decay of the defect signal,<sup>81</sup> while MoS<sub>2</sub>-H<sub>2</sub>Pc exhibits a smaller slope, and ZnPc, CuPc, and CoPc are qualitatively similar, revealing no  $\mu$ s decay dynamics associated with defect-bound MoS<sub>2</sub> excitons. This result indicates that the MPcs are either creating a new decay pathway that outcompetes radiative decay from defect-bound excitons, or they are eliminating the defect-bound exciton radiative decay pathway altogether.

The mechanisms for quenching the defect PL include creating faster, competing recombination pathways through energy or charge transfer, or by eliminating the defect-exciton recombination pathway altogether, either through changing the Fermi level or altering the chemistry of the defect itself. Let us first consider nonradiative energy transfer (NRET), in which the defect excited state transfers to the MPc, where it decays without emitting a photon. For systems in the weak electronic coupling regime, the rate of energy transfer is proportional to the spectral overlap of the donor PL spectrum and the acceptor absorbance spectrum.<sup>318</sup> These overlaps are shown in Figure 3.13 in Chapter 3.6 and calculated in Table 3.1; they indicate that the observed quenching fraction has no correlation with the spectral overlap, implying that NRET is not the mechanism of defect PL quenching. Damping of the MoS<sub>2</sub> dielectric function by the MPcs is a similar PL quenching mechanism,<sup>319,320</sup> but this too does not reproduce the observed trend in

quenching fraction ( $\text{Co} > \text{Cu} > \text{Zn} > \text{H}_2$ ), instead predicting more quenching of the defect PL by  $\text{H}_2\text{Pc}$  than  $\text{CuPc}$  (Figure 3.13). More information about this mechanism can be found in Chapter 3.6.

The possible mechanism of defect PL quenching was further probed by studying the gate voltage dependence of the defect emission at a low temperature (10 K) which allows tuning of well-defined Fermi level by quenching thermionic processes. Bare  $\text{MoS}_2$  devices (Figure 3.6a) show expected Fermi level dependence, with defect emission dramatically increasing with decreasing gate voltage, in agreement with the literature.<sup>89</sup> In contrast,  $\text{CoPc} - \text{MoS}_2$  devices (Figure 3.6b) suppress defect emission out to large negative gate voltages, only showing

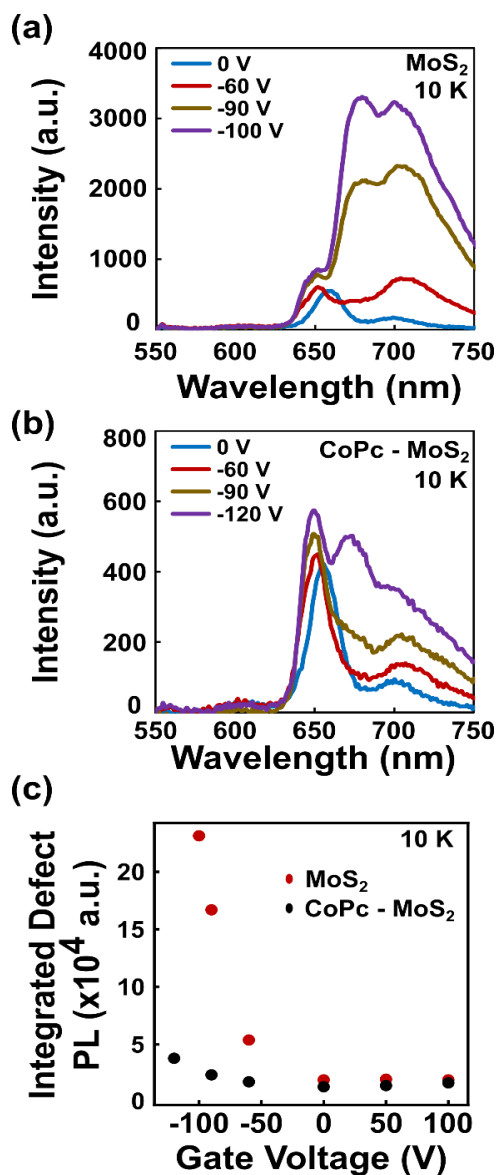


Figure 3.6 Low temperature PL with applied gate voltages of (a) mechanically exfoliated MoS<sub>2</sub> alone and (b) CoPc – MoS<sub>2</sub>. Negative gate voltages enhance the defect emission in MoS<sub>2</sub>, but this effect is suppressed by CoPc. (c) Comparison of defect PL integration for MoS<sub>2</sub> and CoPc – MoS<sub>2</sub> at the measured gate voltages.

substantial defect emission below -100 V. These results are summarized in Figure 3.6c.

Note that at positive gate voltage both MoS<sub>2</sub> and CoPc - MoS<sub>2</sub> show little change in defect PL emission (Figure 3.7), however CoPc - MoS<sub>2</sub> shows a greater shift in excitonic emission to lower energy. This is consistent with CoPc having a larger population of neutral excitons at 0 V,

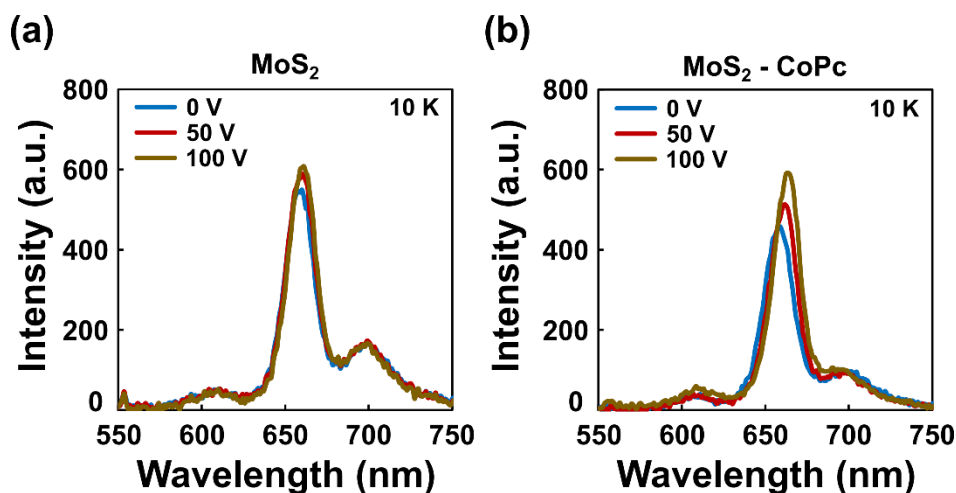


Figure 3.7 (a) MoS<sub>2</sub> with positive voltages shows no change in the defect PL except for lower energy emission from trions. (b) MoS<sub>2</sub>-CoPc at positive voltages show a larger shift to lower energy emission at high gate voltages, suggesting a lower initial population of trions at 0 V due to p-doping from CoPc.

as observed in Figures 3.3 and 3.8, which shifts to trion dominated emission at 100 V, while the MoS<sub>2</sub> alone is trion dominated at both 0 V and 100 V, causing a greater apparent shift for MoS<sub>2</sub> - CoPc. This is to be explained by MoS<sub>2</sub> being naturally electron doped and able to accommodate a greater fraction of trions at zero gate voltage versus the depleted MoS<sub>2</sub>-CoPc p-n heterojunction diode. This observation rules out doping as an explanation of the observed defect quenching. The shift in neutral exciton to trion ratio in CoPc - MoS<sub>2</sub> can be explained by reduced density of free carriers in the depleted heterojunction. From this perspective, one should expect more defect PL following CoPc deposition since charge depletion or doping should have the same effect as a

negative gate bias as in Figure 3.6a. Comparing the MoS<sub>2</sub> excitonic PL energy before and after MPc deposition (Figure 3.8), we see that all of the investigated MPcs form depleted heterojunctions to varying degrees. This is in agreement with electrical measurements on MPc – MoS<sub>2</sub> field-effect transistors, which all exhibit an increase in threshold voltage consistent with reduced free carriers following MPc deposition.<sup>243,258,307</sup> This rules out doping or ground state charge transfer as an underlying mechanism for any of the observed defect PL quenching.

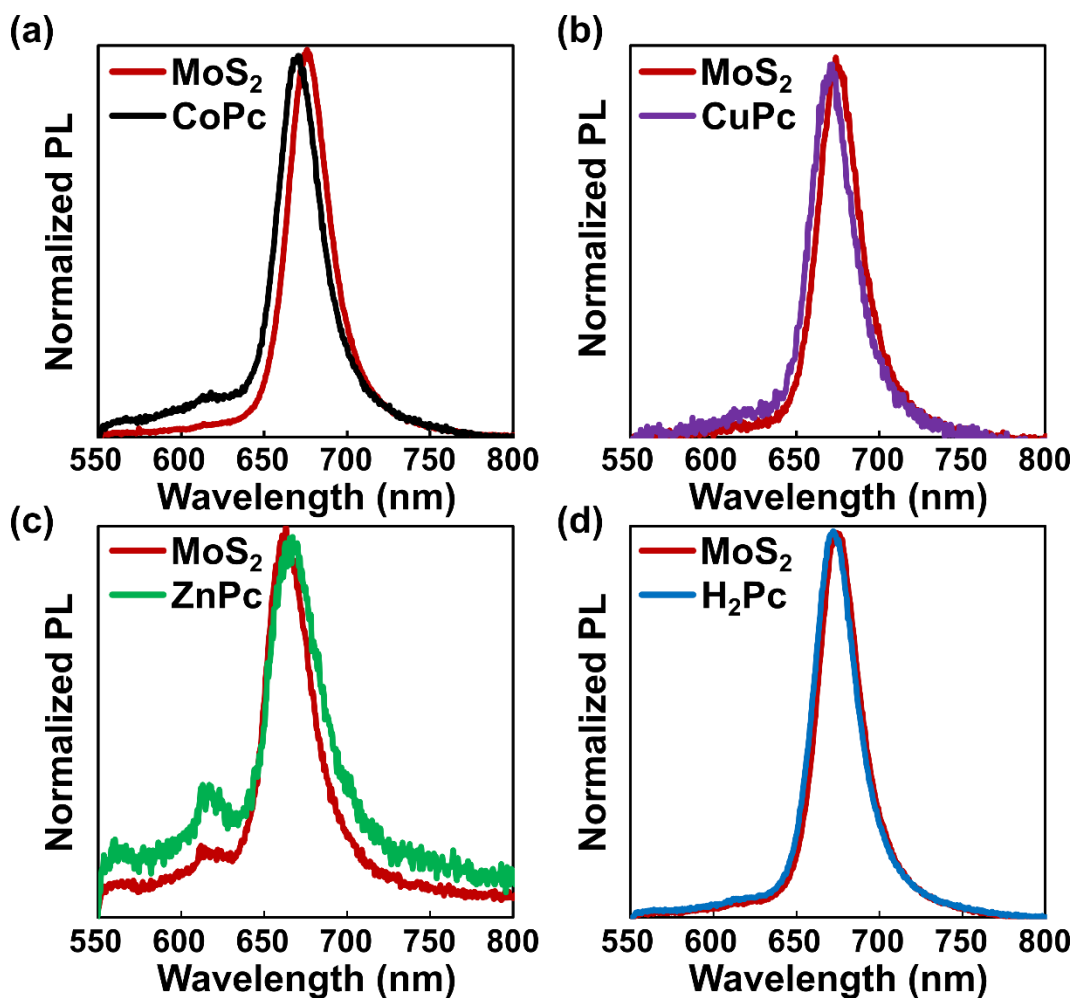


Figure 3.8 Normalized room temperature photoluminescence comparison with and without MPc films for (a) CoPc (b) CuPc (c) ZnPc and (d) H<sub>2</sub>Pc. For all spectra there is either no change to the

energy of the exciton emission or a slight shift to lower wavelengths due to a decrease in trion emission characteristic of p-doping. This is also consistent with the low temperature results in Fig 2.

To narrow the possible mechanisms of the observed defect PL quenching, detailed DFT analysis was applied. First, the interaction between MPc molecules and MoS<sub>2</sub> point defects was verified to be energetically favorable. Figure 3.9 shows that the MPc binding energy is positive at both sulfur vacancies (S<sub>vac</sub>) and oxygen substitutions (O<sub>sub</sub>), with the outer carbon aromatic ring directly above the defect being the most energetically favorable position.

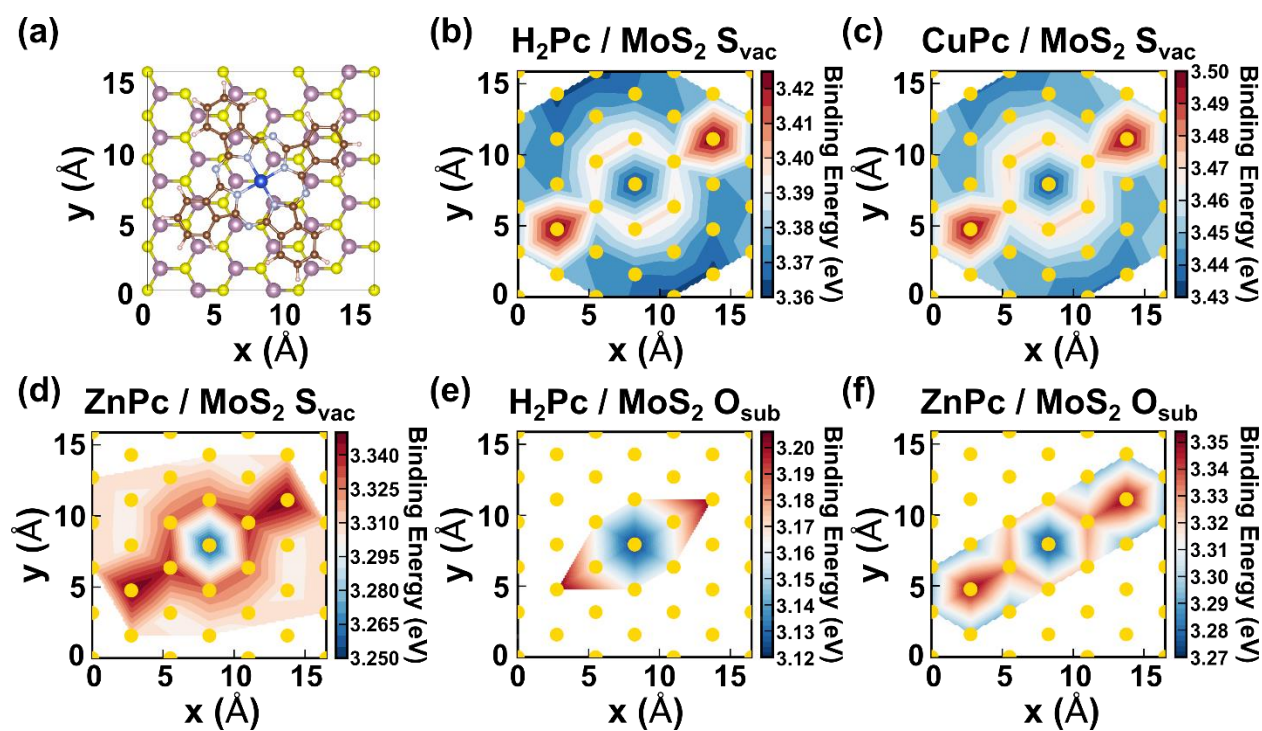


Figure 3.9 Binding energy calculation of Pc on MoS<sub>2</sub> defects at different locations relative to the Pc. (a) Schematic of the MPc structure on MoS<sub>2</sub> used for the binding energy calculations. The yellow sulfurs correspond to the yellow dots, which indicate the location of the defect used in each binding energy calculation for (b) H<sub>2</sub>Pc on S<sub>vac</sub>, (c) CuPc on S<sub>vac</sub>, (d) ZnPc on S<sub>vac</sub>, (e) H<sub>2</sub>Pc on an oxygen substitution (O<sub>sub</sub>), and (f) ZnPc on O<sub>sub</sub>.

As mentioned above, another potential mechanism of defect quenching is charge transfer. While thermally activated electron transfer processes are typically vibration-coupled and thus require more thermal energy than is available at 10 K ( $k_B T \approx 7 \text{ cm}^{-1}$ ), charge transfer can still occur by tunneling mechanisms.<sup>321</sup> To investigate the possibility of tunneling-assisted charge transfer in the heterostructure systems, we calculate the project density of states (pDOS) of localized defect states (Figure 3.14a and 3.14b). Next, we obtain orbital energy levels for the MPc and H<sub>2</sub>Pc on MoS<sub>2</sub> (Figure 3.14c) by applying self-energy corrections to the orbital energies of MPc molecules from OT-RSH calculations and to band edges of MoS<sub>2</sub> from PBE in order to account for non-local dielectric screening effects. Using these energy levels, the expected tunneling currents do not match our observed trends in quenching efficiency, thus ruling out charge transfer as a mechanism of the defect quenching. See Chapter 3.6 for further discussion.

Next, the energy of defect formation with and without MPc adsorption was investigated. Figure 3.10 shows the different charged states as a function of Fermi energy for the S<sub>vac</sub>s. A similar calculation was also performed for the O<sub>subs</sub> in Figure 3.11. The major change induced by the MPc is a shift in the Fermi level at which the lowest energy defect charge state changes from 0 to -1. When looking at S<sub>vac</sub> defects in MoS<sub>2</sub> alone, we see a crossover from 0 to -1 charge when the Fermi level approaches the conduction band minimum (CBM). This corresponds to the gate voltage dependent defect PL in Figure 3.6a and observed by others.<sup>89</sup> At higher gate voltages, the Fermi level is near the CBM, the defect PL is low, and the defects are negatively charged. As the gate voltage is lowered, the defect PL increases as the defect charge changes from negative to neutral. Furthermore, it can be seen in the CoPc – MoS<sub>2</sub> case that the 0 to -1 crossover occurs at

lower Fermi levels than the bare MoS<sub>2</sub> case, and in the H<sub>2</sub>Pc – MoS<sub>2</sub> case it occurs at a Fermi level between the CoPc – MoS<sub>2</sub> and the bare MoS<sub>2</sub>, reproducing our observed quenching trend in Figure 3.3c (Co > Cu > Zn > H<sub>2</sub>). In the Pc – MoS<sub>2</sub>, the population of negative (dark) defects is greater, and a far lower gate voltage is needed to drive the defects to neutral (bright), in agreement with the observations in Figure 3.6b. Having ruled out other potential PL quenching mechanisms, our results suggest that the MPC quench defect PL by altering the charge of the defects themselves, rather than creating competing nonradiative decay paths.

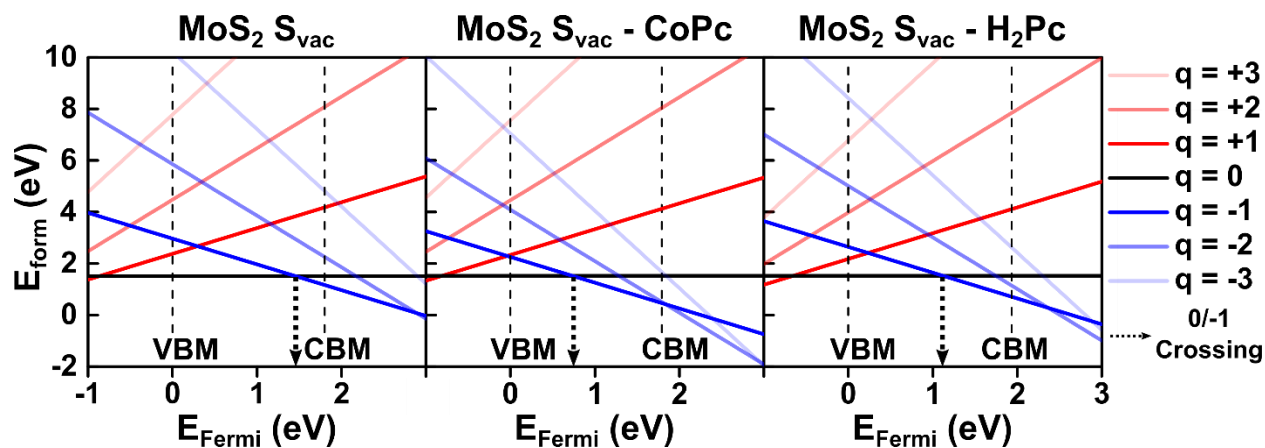


Figure 3.10 Formation energy of neutral and charged  $S_{vac}$  vs Fermi energy for MoS<sub>2</sub> alone, CoPc - MoS<sub>2</sub> and H<sub>2</sub>Pc - MoS<sub>2</sub>. For a given Fermi energy, the dominant defect state is the charged state corresponding to the lowest energy line. For the MoS<sub>2</sub> case, at the VBM this is neutral, while at the CBM this is -1. At a Fermi level near the CBM, the formation energy of the negative

$S_{\text{vac}}$  is  $\text{CoPc} < \text{H}_2\text{Pc} < \text{MoS}_2$  only. The Fermi energy where the defect charge changes from neutral to negative is highlighted with a gray arrow.

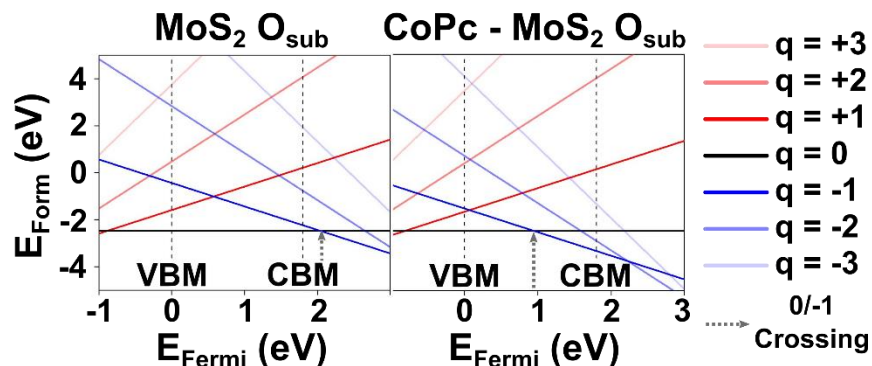


Figure 3.11 Formation energy of charged and neutral  $\text{O}_{\text{sub}}$  versus Fermi energy for  $\text{MoS}_2$  alone and  $\text{CoPc} - \text{MoS}_2$ . (b) pDOS of  $\text{MoS}_2$  with charged and neutral oxygen substitutions ( $\text{O}_{\text{sub}}$ ).

### 3.4. Conclusion

We have demonstrated quenching of the defect photoluminescence of the  $\text{MoS}_2$  by deposition of MPc thin films, with the quenching efficiency depending sensitively on the central transition metal. Experiments rule out non-radiative energy transfer, charge depletion, and charge transfer as the mechanism of this quenching. Gate-voltage dependent measurements and DFT analysis suggest the mechanism is stabilization of negatively charged defects by MPc. The different quenching behavior of the various MPc suggest a powerful route to controlling defect chemistry through molecular adsorbates. This result has significant implications for improving  $\text{MoS}_2$  based single photon emitters by quenching background defect PL and may also be used to manipulate populations of defect-bound excitons to increase PLQY at high excitation powers.

### 3.5. Methods

#### *Preparation of Monolayer $\text{MoS}_2$*

Monolayer samples of MoS<sub>2</sub> were exfoliated via micromechanical exfoliation using Scotch tape on SiO<sub>2</sub>/Si substrates. To improve the yield of monolayer MoS<sub>2</sub>, the substrate was heated while in contact with tape for 15 min at 60 °C and gently exfoliated while still warm. MoS<sub>2</sub> monolayers were identified via optical microscopy based on color contrast and then confirmed with Raman microscopy. Identified monolayer samples were then annealed for 4 h at 400 °C in an Ar/H<sub>2</sub> environment (constant flow of 600/200 sccm respectively) to remove unwanted tape residues and improve layer adhesion to the SiO<sub>2</sub>.

#### *Chemical Vapor Deposition of MoS<sub>2</sub> Films*

Monolayer flakes of MoS<sub>2</sub> were synthesized using an atmospheric pressure chemical vapor deposition process in which 5 mg of MoO<sub>3</sub> (Sigma-Aldrich) powder was spread evenly within an alumina boat and capped with two 1 cm<sup>2</sup> SiO<sub>2</sub>/Si (300 nm oxide) substrates. The alumina boat was placed inside a 1” diameter quartz tube located in the center of a tube furnace. Then, 300 mg of sulfur pieces (Alfa-Aesar) were similarly placed in a second alumina boat which was located upstream and outside of the tube furnace. After purging the sealed quartz tube for 15 min with argon gas, the center of the furnace was heated from room temperature to 700 °C over a span of 40 min. The temperature was then held constant for 3 minutes. During this entire process, the argon flow rate was maintained at 13 sccm. When the furnace temperature reached 575°C during the ramp process, the alumina boat containing the sulfur was moved to a region inside the furnace where the temperature was approximately 150°C as verified by a thermocouple. This movement

was enabled using two magnets. Once the growth process was completed, the furnace was allowed to cool to room temperature.

#### *Metallophthalocyanine Film Deposition*

Metallophthalocyanines were purchased from Sigma-Aldrich and purified by temperature gradient sublimation by heating one end of a tube furnace containing the crude material under a vacuum of  $<10^{-2}$  Torr. Films were grown by thermal evaporation at a pressure below  $10^{-5}$  Torr at a rate of 0.1 – 0.2 Å/s, as monitored by a calibrated quartz crystal microbalance, to obtain thicknesses of 1.0 nm.

#### *Low Temperature Photoluminescence Measurements*

Photoluminescence (PL) at room temperature (300 K) and low temperature (10 K) was characterized in a vacuum environment within a variable temperature optical cryostat (ARS DE204PF), using a 532 nm laser as excitation source (Lighthouse Photonics - Sprout). The excitation spot was  $\sim 1$   $\mu\text{m}$  with a 100x objective (Nikon T-PLAN with NA 0.6), with incident power at  $\sim 100$   $\mu\text{W}$ . and a 20 s integration time. Emission spectra were collected on a spectrometer (Andor SHAMROCK SR-750 with i-DUS Camera DU-420A).

#### *Raman Microscopy*

Confocal Raman microscopy spectra were collected using a Horiba Raman Xplora with a 532 nm laser, 150  $\mu\text{W}$  power, a 100x objective, and a 1800 grooves/mm diffraction grating.

#### *TCSPC Microscopy*

Low temperature Time Correlated Single Photon Counting (TCSPC) was carried out in a variable temperature optical cryostat (Montana Instruments Cryostation S100). A 450 nm pulsed

laser (Picoquant PDL200b) operating at 500 kHz excited the sample through an objective lens (Zeiss Epiplan-Neofluar 100x/0.90 NA), and the collected fluorescence was directed to an avalanche photodiode detector (APD; Micro Photon Devices PDM). The timing electronics (Picoquant Picoharp 300) measures the relative time between the arrival of a photon at the APD and a trigger signal from the pulsed laser.

### *Theoretical*

The defect formation energy and pDOS calculations were performed by employing spin-polarized density functional theory (DFT) implemented in Vienna Ab initio Simulation Package (VASP) code.<sup>322,323</sup> The structural optimization and self-consistent total energy calculations were based on the generalized gradient approximation (GGA) with the Perdew-Burke-Ernzerhof (PBE) exchange-correlation functional along with the projector-augmented wave (PAW) potentials. Electronic wave functions were expanded in a plane wave basis set with the kinetic energy cutoff of 400 eV. For the Brillouin zone integration a  $2 \times 2 \times 1$  Monkhorst-Pack k-point mesh was used and the k-point density is approximately  $32 \text{ \AA}^{-3}$ . The energy convergence criterion for the electronic wavefunction was set to be  $10^{-5}$  eV. A vacuum layer of about 13.6 Å (periodic length in  $z$  direction =20 Å) was chosen to guarantee that no spurious interaction occurred between the layers in monolayer simulations using periodic boundary conditions.

The defect formation energy  $E_{form}^q$  at charge state  $q$  is calculated by eq 2, where  $E_{defect}^q$  and

$$E_{form}^q = E_{defect}^q - E_{perfect} - \sum_i n_i \mu_i + q E_{Fermi} + E_{2D\_corr} \quad (2)$$

and  $E_{perfect}$  are the total energy of the system with charged defect and perfect one, respectively.  $n_i$  is the number of atoms added/removed by the defect,  $\mu_i$  is the chemical potential, and  $E_{Fermi}$  is the Fermi level energy.  $E_{2D\_corr}$  is the correction term to overcome the energy divergence in charged 2D system, and here we apply the scheme developed by Freysoldt and Neugebauer.<sup>324</sup>

For the electronic structure of mixed-dimensional 0D/2D heterojunctions, an electrostatic model that has been found to provide results comparable to full screened range-separated hybrid functional (SRSH) calculations and experimental band gaps, was used and was found to be superior over standard DFT calculations. Specifically, we apply self-energy corrections following Neaton et al<sup>325,326</sup> to the molecular levels of gas-phase phthalocyanine molecules obtained from optimally-tuned range-separated hybrid functional (OT-RSH),<sup>151</sup> and to band edges of MoS<sub>2</sub> to account for the non-local dielectric screening effect. Effects of the interface charge redistribution on the energy levels are obtained from DFT calculations with PBE functional for the 0D/2D heterojunctions. Binding energies of phthalocyanine molecules on MoS<sub>2</sub> with S-vacancy and O-substitutions are calculated with van der Waals interactions.

### 3.6. Supporting Information – Charge and Energy Transfer

#### *Energy Transfer*

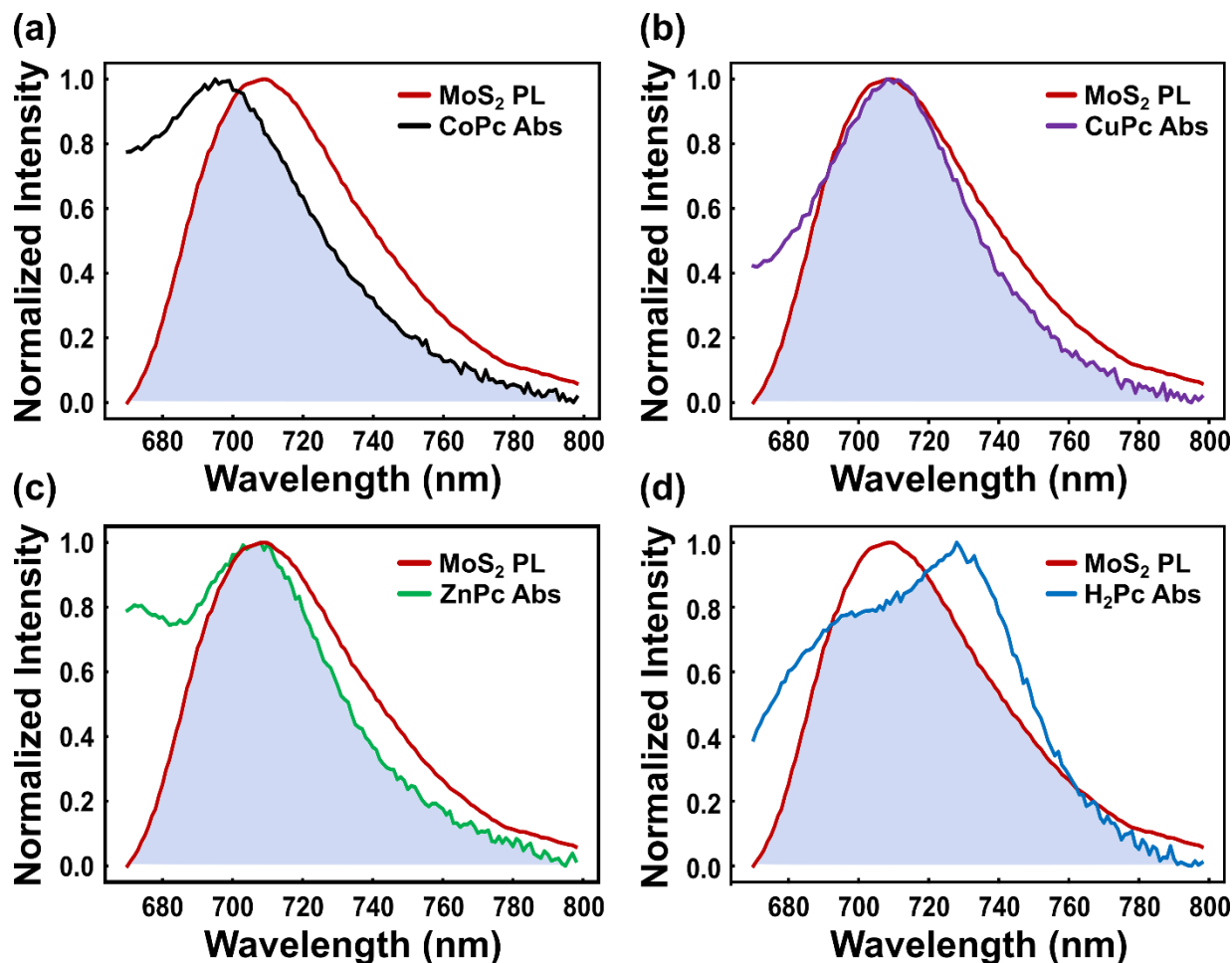


Figure 3.12 Spectra of MoS<sub>2</sub> defect PL and MPc absorption, normalized to a maximum value of 1.0 for ease of comparison, of (a) CoPc, (b) CuPc, (c) ZnPc, (d) H<sub>2</sub>Pc. The overlap area is highlighted in blue. Absorption spectra were collected by subtracting the absorption of CVD MoS<sub>2</sub> on sapphire and 4 Å of the MPc on MoS<sub>2</sub> on sapphire. This was done to account for the large shift in Pc absorption upon deposition on MoS<sub>2</sub> documented elsewhere.<sup>66</sup> MoS<sub>2</sub> defect PL spectra are the same as presented in Figures 3.2b-e, using CVD MoS<sub>2</sub> on SiO<sub>2</sub> at 10 K. Both absorption and PL spectra were normalized to 1.0 as their maxima.

Spectral overlap integrals  $J$  are calculated using the formula,

$$(3) \quad J = \int_0^{\infty} F_D(\lambda) \varepsilon_A(\lambda) \lambda^4 d\lambda$$

Where  $F_D$  is the normalized donor (MoS<sub>2</sub>) PL,  $\lambda$  is wavelength, and  $\varepsilon_A$  is acceptor (Pc) molar extinction coefficients.  $\varepsilon_A$  was calculated from the Pc absorption spectra (A) using Beer's Law ( $\varepsilon = A / c l$ ), where the concentration,  $c$ , was 2.7 M for all Pc as calculated from the density of solid Pc, and  $l$ , the path length was 0.4 nm for all Pc.

Table 3.1 Calculated Overlap Integrals and Quenching Factors

	CoPc	CuPc	ZnPc	H <sub>2</sub> Pc
Overlap Integral (M <sup>-1</sup> cm <sup>-1</sup> nm <sup>4</sup> x 10 <sup>15</sup> )	9.4	8.8	8.6	11
Quenching Factor	0.914	0.809	0.444	0.156

### *Dielectric Screening Model*

Another factor of non-radiative energy transfer (NRET) is dielectric screening of the dipole of the donor, which has been found to affect the NRET rate significantly in the mixed-dimensional quantum dot/2D systems.<sup>320</sup> Here we investigate the dielectric screening effect of the MPc films on the rate of NRET from MoS<sub>2</sub> to MPc, by using an electromagnetic model<sup>320</sup> where the key factors are the in-plane and out-of-plane dielectric tensor ( $\varepsilon = \varepsilon' + i\varepsilon''$ ) for both the donor and acceptor at the wavelength of the photoluminescence, the distance between the acceptor and donor  $h$ , and thickness of the acceptor layer  $d$ . From previously published spectroscopic ellipsometry

data of CuPc,<sup>327</sup> and H<sub>2</sub>Pc,<sup>328</sup> we obtain in-plane (out-of-plane) dielectric function of  $\epsilon_{//}=3.9+1.9i$  ( $\epsilon_{\perp}=4.9+3.0i$ ), and  $\epsilon_{//}=3.3+2.9i$  ( $\epsilon_{\perp}=5.4+2.5i$ ) for CuPc and H<sub>2</sub>Pc, respectively, at the defect emission wavelength of  $\sim 691$  nm. At the A-exciton emission wavelength of  $\sim 650$  nm, the dielectric functions are  $\epsilon_{//}=3.71+2.2i$  ( $\epsilon_{\perp}=4.93+2.4i$ ), and  $\epsilon_{//}=2.7+2.8i$  ( $\epsilon_{\perp}=4.8+1.8i$ ), respectively, for CuPc and H<sub>2</sub>Pc. The dielectric function for MoS<sub>2</sub> is  $\epsilon_{//}=18+9.3i$  ( $\epsilon_{\perp}=16+2.2i$ ).<sup>320</sup> The interlayer distances  $h$  as obtained from DFT calculations are 0.64 nm for both CuPc and H<sub>2</sub>Pc, which is the distance from the Pc layer to the center of monolayer MoS<sub>2</sub>. The ratio of NRET rate at MoS<sub>2</sub> defect emission to that at A-exciton emission as a function of Pc thickness is shown in Figure 3.13. Based on these calculations, we would expect greater quenching from H<sub>2</sub>Pc than CuPc, in opposition to our observed trend, indicating no form of NRET explains the quenching of the MoS<sub>2</sub> defect emission.

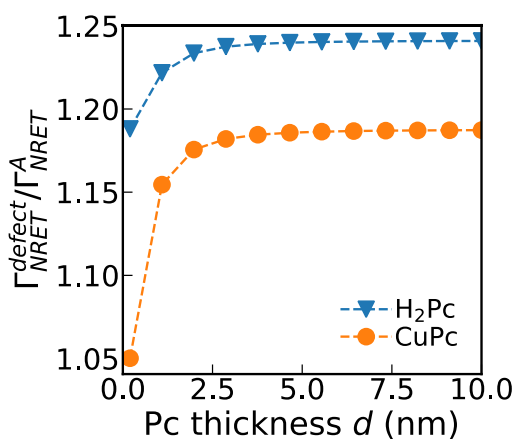


Figure 3.13 Ratio of NRET rates of the MoS<sub>2</sub> defect to A exciton induced by H<sub>2</sub>Pc and CuPc as a function of Pc thickness. The greater expected quenching of the defect by H<sub>2</sub>Pc vs CuPc contradicts the observed patterns.

## Charge Transfer

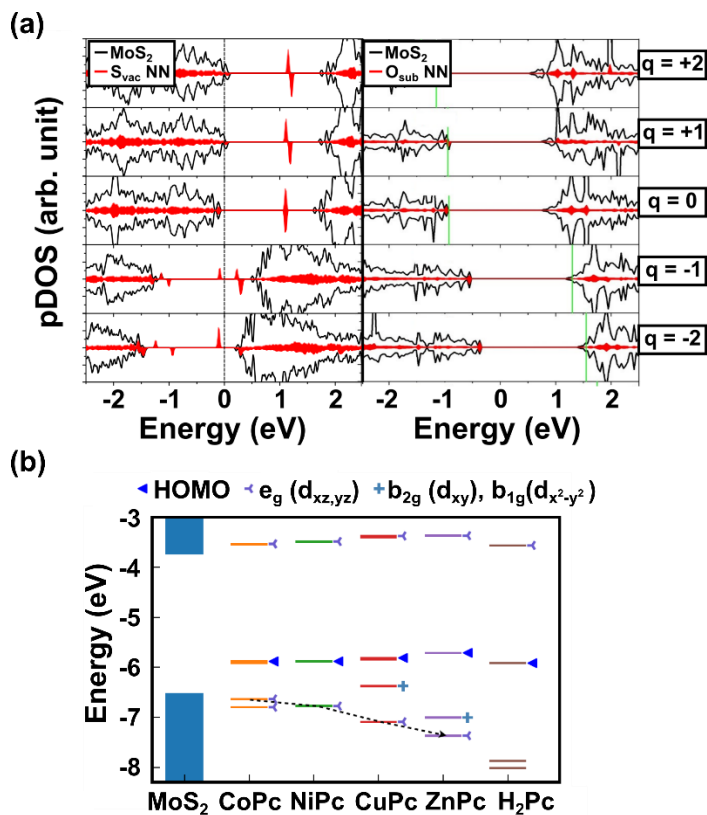


Figure 3.14 (a) Projected density of states (pDOS) of MoS<sub>2</sub> with sulfur vacancies or oxygen substitutions of different charge. The S<sub>vac</sub> or O<sub>sub</sub> nearest neighbor (NN) orbitals correspond to the localized states induced by the S<sub>vac</sub> or O<sub>sub</sub>. (b) Band alignment diagram showing the energy of the out-of-plane MPC d<sub>xz</sub> and d<sub>yz</sub> orbitals moving from the valence band edge in the case of CoPc to lower energy in the case of CuPc and ZnPc, while H<sub>2</sub>Pc has no such orbitals.

As Figure 3.14a shows, the S<sub>vac</sub> induces localized states below the conduction band and near the valence band edge, while O<sub>sub</sub> induces states near the valence band edge. These are the potential charge donor sites. The Pc orbitals shown in the Figure S8b are potential acceptor states. As discussed in the main text, thermally assisted charge transfer will not be possible at 10 K,<sup>321</sup> but so any charge transfer will have to occur through tunneling. We can predict the relative

rates of tunneling using the following expression the tunneling current  $I$  through a vacuum gap<sup>329</sup>

$$(4) \quad I = (2\pi e/\hbar) \sum_{\mu\nu} f(E_\mu)[1 - f(E_\nu)] \times |M_{\mu\nu}|^2 \delta(E_\mu - E_\nu)$$

Where  $f(E)$  is the Fermi function,  $M_{\mu\nu}$  is the tunneling matrix element between states  $\varphi_\nu$  in the acceptor and  $\varphi_\mu$  in the donor,  $E_\mu$  is the energy of state  $\varphi_\mu$ , and  $\delta$  is the Kronecker delta function. Given the delta function, we only expect tunneling to be significant to MPc orbitals near the localized states of the defects. Based on Figure S8 this immediately rules out charge transfer from  $S_{\text{vac}}$  trapped electrons near the conduction band. This similarly rules out hole tunneling to the MPc HOMO, which is much higher energy than the valence band localized states of the  $O_{\text{sub}}$  and  $S_{\text{vac}}$ .

At first glance the HOMO-1 states of the MPc are good candidates as hole transfer acceptors from valence band edge defect states. They have significant out-of-plane electron density (highlighted in Figure S8b) which should increase their tunneling matrix elements, and their alignment to the valence band edge reproduces the trend in PL quenching factors. Closer inspection, however, reveals this to be implausible. The HOMO-1 energy decreases by 0.5 eV from CoPc to ZnPc (0.9 eV if only counting out-of-plane d-orbitals). According to the delta function dependence, the tunneling rate to ZnPc should be near zero, but its quenching fraction is above 0.4. This could be explained by ‘spreading’ of the ZnPc states due to interfacial band bending<sup>241</sup> or increased bandwidth from film thickness,<sup>330</sup> but neither of these effects should create states more than 200 meV above the orbital of the isolated molecule.

\*Chapter 3 is a preprint version of an article that will be submitted for publication in 2021.

## 4. Tailoring the Optical Response of Pentacene Thin Films via Templated Growth on Hexagonal Boron Nitride

### 4.1. Abstract

The optoelectronic properties of organic thin films are strongly dependent on their molecular orientation and packing, which in turn is sensitive to the underlying substrate. Hexagonal boron nitride (hBN) and other van der Waals (vdW) materials are known to template different organic thin film growth from conventional inorganic substrates such as SiO<sub>2</sub>. Here the morphology and temperature-dependent optical properties of pentacene films grown on hBN are reported.

Pentacene deposited on hBN forms large-grain films with a molecular  $\pi$ -face-on orientation in contrast to the dendritic edge-on thin-film phase on SiO<sub>2</sub>. This pentacene/hBN film exhibits a 40 meV lower free exciton emission than pentacene/SiO<sub>2</sub> and an unconventional temperature dependence of emission energy. Time-resolved photoluminescence (PL) decay measurements show a long-lived signal in the  $\pi$ -face-on phase related to delayed emission from triplet-triplet fusion. This work demonstrates that growth on vdW materials provides an informative pathway for controlling optoelectronic functionality in molecular thin films.

### 4.2. Introduction

Pentacene is a technologically relevant organic semiconductor, both for its high mobility in thin-film transistors<sup>216</sup> and as a model system for carrier multiplication in organic photovoltaics via singlet fission.<sup>208</sup> Since the optoelectronic properties of pentacene thin films strongly depend on their morphology,<sup>194,204,210</sup> control over their growth microstructure has been an area of intense

study.<sup>182,187,331,332</sup> However, the relationship between thin-film structure and optical properties of pentacene films has been investigated primarily on conventional inorganic substrates, most commonly amorphous SiO<sub>2</sub>. These studies have demonstrated some degree of control over optical anisotropy through constrained growth<sup>196</sup> and tunable molecular orientation,<sup>202,333</sup> but require fabrication or annealing procedures that are unique to the interface between pentacene and amorphous SiO<sub>2</sub> and do not exploit molecular templating that could be enabled by atomically well-defined substrates.

Layered van der Waals (vdW) materials have attracted significant interest as substrates for organic thin-film growth to create mixed-dimensional heterostructures,<sup>228</sup> which combine the well-understood features of the component materials to engender emergent properties not possible in either isolated system.<sup>66,165,246,304,306,334</sup> Pentacene films have been studied on graphene<sup>187,331</sup> and MoS<sub>2</sub>,<sup>231,233</sup> however the charge transfer processes with the underlying semimetallic or semiconducting substrate complicate identification of new morphological-optical relationships within the pentacene films. In contrast, due to its electrically insulating character and exceptionally low density of trapped charges, hexagonal boron nitride (hBN) substrates have the potential to address these issues. Moreover, hBN has been shown to template the epitaxial growth of organic films,<sup>138</sup> making it an exemplary model system to investigate structure-property relationships in organic-vdW heterojunctions.

Prior reports of pentacene film growth on hBN are limited to investigations of structural and electrical properties.<sup>184,205,335,336</sup> Pentacene film growth on hBN yields long needle-like crystals, a different morphology than the dendrites formed on SiO<sub>2</sub>.<sup>184,335</sup> A similar needle-like phase with  $\pi$ -

face-on molecular orientation has also been observed in pentacene grown on HOPG.<sup>337</sup> This orientation was found to significantly alter the pentacene ionization energy compared to the thin-film molecular edge-on phase on SiO<sub>2</sub>,<sup>337</sup> suggesting other pentacene optical properties may also change in the needle-like phase. While the low-temperature photoluminescence (PL) of the dendritic pentacene phase (commonly referred to as the thin-film phase) has been thoroughly analyzed,<sup>183,210</sup> it is not yet known whether and to what degree the different needle-like pentacene morphology on hBN alters the optoelectronic response. Given the importance of structural parameters such as stacking geometry and angle for singlet fission,<sup>338</sup> control over the pentacene thin-film phase with a vdW substrate is expected to have implications for pentacene photonic applications including the design of emerging organic-vdW optoelectronic devices.

Here we report that PL in pentacene thin films grown on hBN exhibit free exciton emission at a substantially lower energy and with a narrower linewidth than pentacene on amorphous SiO<sub>2</sub>. This difference is accentuated at 10 K, where the PL of pentacene thin films on hBN approaches the limiting case of emission from single-crystal pentacene.<sup>210,211</sup> In addition, the PL emission energy from the pentacene/hBN thin-film phase increases with elevated temperatures, whereas PL from the pentacene/SiO<sub>2</sub> thin-film phase exhibits the opposite trend. The PL of pentacene/hBN also possesses a long-lived emission component that is not present for pentacene/SiO<sub>2</sub>. Attributed to recombination from singlets formed by delayed triplet-triplet fusion, this long-lived component has implications for the harvesting of carriers produced by singlet fission in carrier multiplication devices. Overall, this work highlights that vdW-templated growth of pentacene thin films provides unique optical property control that can be utilized for fundamental studies and photonic

applications.

### 4.3. Results and Discussion

To fabricate pentacene/hBN thin-film samples, hBN was mechanically exfoliated onto 300-nm SiO<sub>2</sub>/Si substrates and then coated with 20 nm of pentacene by thermal evaporation at a base pressure of  $\sim 5 \times 10^{-6}$  Torr. Figure 4.1a shows an optical micrograph of pentacene covering both an hBN flake and the surrounding SiO<sub>2</sub> substrate. Large, needle-like crystals of pentacene are visible only on the hBN (Figure 4.1a). AFM profilometry shows that the needles have a width of 1-2  $\mu\text{m}$  and a height of 10 - 20 nm (Figure 4.2a).

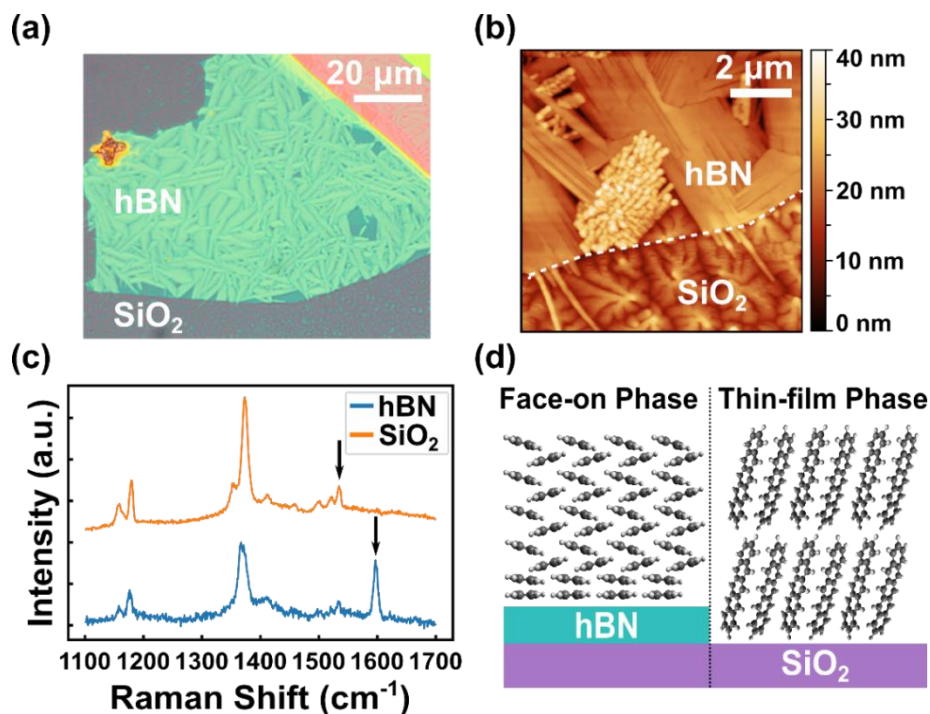


Figure 4.1 (a) Optical images showing the assembly of thermally evaporated pentacene into needle-like grains on 5-10 nm hBN. (b) AFM topographic image showing the transition from predominantly needle-like pentacene on hBN to the dendritic structure on SiO<sub>2</sub>. (c) Raman spectra of pentacene grown on hBN and SiO<sub>2</sub> using a 532 nm excitation wavelength, normalized

to the respective maxima at  $1370\text{ cm}^{-1}$  and vertically offset to highlight the different modes. Arrows indicate the  $A_g$  vibration at  $1533\text{ cm}^{-1}$  in pentacene/ $\text{SiO}_2$  and the  $B_{3g}$  vibration at  $1597\text{ cm}^{-1}$  in pentacene/hBN. (d) Schematic illustration of the  $\pi$ -face-on growth of pentacene/hBN and the edge-on growth of the pentacene/ $\text{SiO}_2$  thin-film phase.

Note that this morphology is only apparent when the hBN is cleaned to be free of polymer residues. AFM images of the hBN– $\text{SiO}_2$  interface in Figure 4.1b indicate an abrupt change in the pentacene morphology. The dendritic structures on  $\text{SiO}_2$  are typical of the well-known pentacene thin-film phase with characteristic 1.6 nm terraces (Figure 4.2b)<sup>182,183,339</sup> and a molecular tilt angle of  $17^\circ$  with respect to the surface normal.<sup>38</sup> The coverage of the needle-like phase on hBN is not complete in some cases, likely due to polymer residues that are known to limit achievable grain size in similar organic-vdW heterojunctions,<sup>340</sup> and the gaps between the crystals exhibit either a dendritic thin-film phase or nanoscale grains of indeterminate phase. To avoid this ambiguity, subsequent measurements were carried out only on regions with full needle coverage.

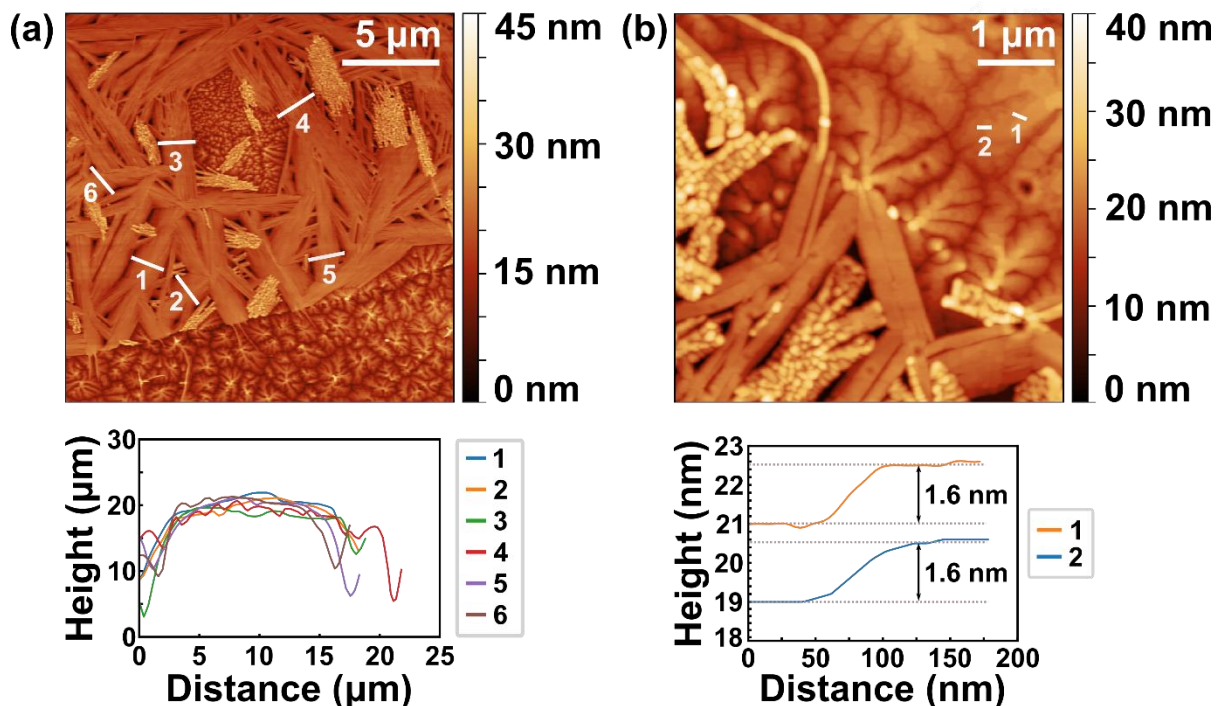


Figure 4.2 (a) AFM profilometry of large pentacene needles on hBN showing heights of 10 – 20 nm and widths of 1 – 2  $\mu\text{m}$ . (b) AFM profilometry of pentacene terraces on  $\text{SiO}_2$ . The step height is 1.6 nm, consistent with the thin-film phase.

Similar needle-like growth occurs for pentacene thin films on  $\text{WS}_2$  and  $\text{MoS}_2$  as observed in optical and AFM images (Figure 4.3). This result suggests that the atomically abrupt and dangling bond-free surfaces of layered vdW substrates promote the needle-like phase of pentacene. Special care must be taken to ensure that the substrate is free of polymer residue in order to observe the needle-like phase (see Experimental Methods), which accounts for its absence in some prior reports of pentacene/ $\text{MoS}_2$  heterojunctions.<sup>231,233</sup> Similarly, recent work has shown that highly defective hBN also disrupts the formation of epitaxial films of pentacene.<sup>205</sup>

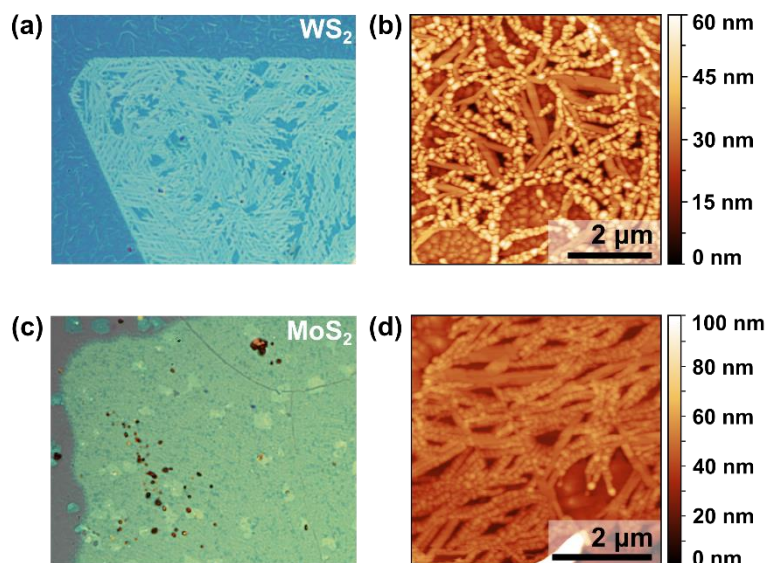


Figure 4.3  $\pi$ -Face-on and thin-film phase of pentacene on semiconducting vdW materials. (a,c) Optical images at 100x magnification of pentacene on  $\text{WS}_2$  (a) and  $\text{MoS}_2$  (c). (b, d) AFM scans of (a, c) respectively. Needle-like structures are apparent on both. They also show a greater coverage of nanoscale grains and dendritic thin-film phase than on hBN.

Figure 4.1c shows the Raman spectra of the two pentacene phases. The ratio of the intensities of the two highlighted vibrational modes,  $B_{3g}$  ( $1597\text{ cm}^{-1}$ ) to  $A_g$  ( $1533\text{ cm}^{-1}$ ), is determined by the orientation of the pentacene with respect to the surface normal. The dominant  $B_{3g}$  Raman mode indicates that the pentacene is lying flat on the substrate, whereas the dominant  $A_g$  Raman mode indicates that the pentacene is oriented in an edge-on geometry, with the long axis perpendicular to the substrate.<sup>341,342</sup> Therefore, the Raman spectra confirm that pentacene thin films grow  $\pi$ -face-on for hBN but predominantly edge-on for  $\text{SiO}_2$ , as shown schematically in Figure 4.1d. This agrees with prior observations of pentacene needle-like growth on highly oriented pyrolytic graphite (HOPG), which also has a  $\pi$ -face-on molecular orientation,<sup>337</sup> as well as structural transitions of similar systems such as 6-hexaparaphenyl films grown on graphene flakes on an  $\text{SiO}_2$  substrate.<sup>343</sup> We expect the  $\pi$ -face-on phase to transition to an edge-on orientation at greater

film thickness, in accordance with prior observations.<sup>184</sup> Throughout this discussion, we will refer to pentacene/hBN as the  $\pi$ -face-on phase and pentacene/SiO<sub>2</sub> as the thin-film phase to match with prior literature.<sup>183,333,339</sup> While growth of  $\pi$ -face-on pentacene/SiO<sub>2</sub> has also been reported,<sup>202,333</sup> it requires precise temperature control and involved thermal annealing. In contrast, the present films are grown at 25 °C, and measured without further processing, highlighting a key advantage of vdW substrates for achieving the  $\pi$ -face-on pentacene phase.

The 298 K PL spectra of pentacene on hBN and SiO<sub>2</sub> (Figure 4.4a) have low intensities since ultrafast singlet fission is the dominant decay pathway, resulting in low-yield fluorescence from the singlet state.<sup>177</sup> At 10 K, each PL spectrum is better resolved (Figure 4.4b) and exhibits the peaks corresponding to free excitons (FE) and self-trapped excitons (STE) near 1.8 eV and 1.65 eV, respectively, typical of pentacene single-crystals and thin-films.<sup>210-212</sup> In addition, there is a broad low-energy shoulder extending through 1.5 eV that can be assigned to extrinsic defects in pentacene crystals,<sup>212</sup> as well as a broad peak near 2.1 eV that has been attributed to the recombination of charge transfer excitons in neighboring pentacene molecules.<sup>197</sup> Note that the FE and STE emission peaks are 40 meV lower in the  $\pi$ -face-on phase than in the thin-film phase. This difference is similar to the difference in free exciton emission energies between the pentacene single-crystal and thin-film phases (1.78 eV vs 1.82 eV),<sup>210,211</sup> further corroborating that the observed shift is the result of the different crystal structures of the two phases. A similar shift in the emission energy is also observed for pentacene thin films on WS<sub>2</sub> and MoS<sub>2</sub> (Figure 4.5), suggesting that this feature is intrinsic to the vdW-templated  $\pi$ -face-on phase and not due to coupling with a particular vdW substrate.

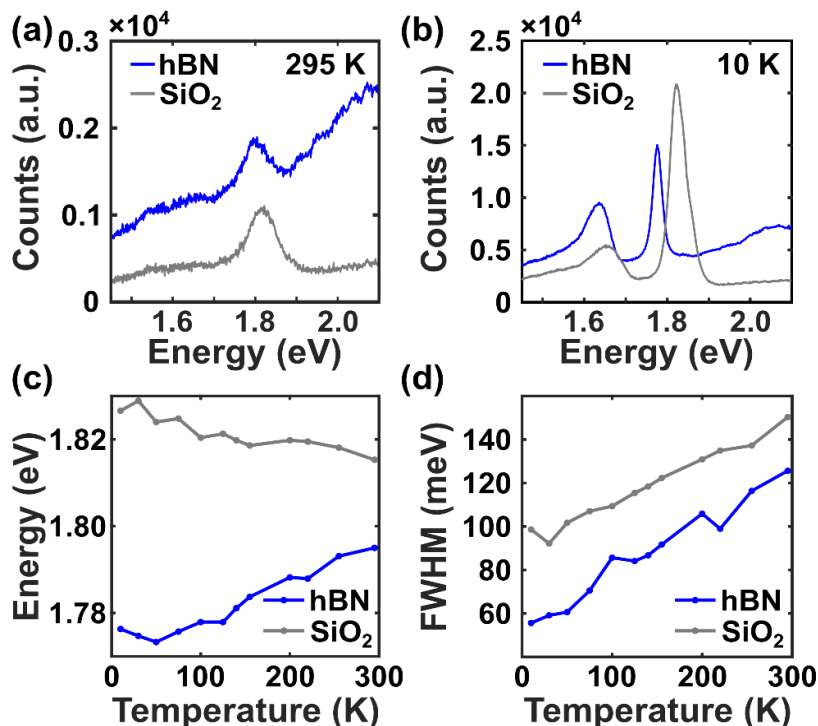


Figure 4.4 (a) Comparison of the 298 K photoluminescence spectra of  $\pi$ -face-on pentacene/hBN and thin-film phase pentacene/SiO<sub>2</sub>. (b) Photoluminescence spectral comparison of pentacene/hBN and pentacene/SiO<sub>2</sub> at 10 K. The higher and lower energy peaks are assigned to pentacene free exciton (FE) emission and self-trapped exciton (STE) emission, respectively. Emission from pentacene/hBN (blue) has a narrower linewidth and a lower energy relative to pentacene/SiO<sub>2</sub> (gray). (c) Temperature dependence of the FE emission energy for the two pentacene phases extracted from Gaussian fits. (d) Temperature dependence of the FE emission full-width at half maximum (FWHM), showing that both phases have narrower emission at lower temperatures.

The PL from pentacene thin films on hBN ( $\pi$ -face-on) and on SiO<sub>2</sub> (thin-film) also exhibit different temperature dependencies (Figure 4.4c). The optical bandgap of pentacene is known to change with temperature depending on substrate and thickness.<sup>183,194</sup> In bulk pentacene, as with most molecular solids, the bandgap decreases due to thermal contraction increasing the orbital overlap.<sup>194</sup> In thinner pentacene films such as those investigated here, the thermal expansion

mismatch between the film and substrate can induce strain that changes the temperature dependence of the optical response.<sup>183,332</sup> The observed pentacene/hBN PL behavior closely

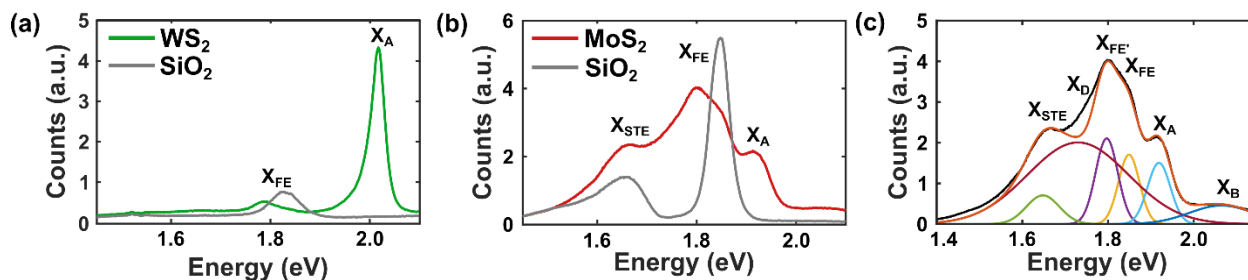


Figure 4.5 (a,b) PL spectra at 10 K of pentacene thin films on the indicated vdW substrates compared to SiO<sub>2</sub>. Red-shift of the pentacene peak on WS<sub>2</sub> is apparent since the WS<sub>2</sub> exciton is well-separated from the pentacene emission. The pentacene/MoS<sub>2</sub> spectrum is more complicated since the pentacene emission overlaps spectrally with the MoS<sub>2</sub> emission. X<sub>A</sub> denotes the A-exciton emission of the vdW material, X<sub>FE</sub> denotes the pentacene free exciton emission, and X<sub>STE</sub> denotes the pentacene self-trapped exciton. The STE emission of pentacene on WS<sub>2</sub> is hidden by the large intensity of the A-exciton emission. (c) The pentacene/MoS<sub>2</sub> spectrum broken down by a series of peak functions in order to better identify the constituent components of the broad, convoluted emission. In addition to the peaks in (b), there is contribution from the MoS<sub>2</sub> B-exciton (X<sub>B</sub>), the MoS<sub>2</sub> defect emission (X<sub>D</sub>), and both the thin-film and  $\pi$ -face-on phase pentacene FE emission (X<sub>FE</sub> and X<sub>FE'</sub> respectively).

follows that of pentacene/polyethyleneterephthalate (PET),<sup>183</sup> in accord with the similar in-plane thermal expansion coefficients of  $5\text{-}15 \times 10^{-5} \text{ K}^{-1}$  for PET<sup>344</sup> and  $2\text{-}4 \times 10^{-5} \text{ K}^{-1}$  for hBN,<sup>345</sup> both of which are close to the bulk pentacene value of  $1.1 \times 10^{-4} \text{ K}^{-1}$  along the *a*-direction and  $2.9 \times 10^{-5} \text{ K}^{-1}$  along the *b*-direction.<sup>183</sup> The significantly lower coefficient of thermal expansion for SiO<sub>2</sub> ( $5 \times 10^{-7} \text{ K}^{-1}$ )<sup>346</sup> leads to a larger strain in the pentacene film at lower temperature, which shifts the PL to higher energy. A similar but lower magnitude temperature shift is observed in pentacene/WS<sub>2</sub> (Figure 4.6), which supports the conclusion that thermal expansion mismatch is the principal driver of this phenomenon since WS<sub>2</sub> has an approximate in-plane thermal expansion coefficient of  $10^{-6} \text{ K}^{-1}$ , based on temperature-dependent Raman measurements,<sup>347</sup> which is between

that of hBN and SiO<sub>2</sub>. The temperature dependence of the PL linewidths for pentacene/hBN and pentacene/SiO<sub>2</sub> are similar (Figure 4.4d). However, the PL band of the  $\pi$ -face-on phase is narrower at all temperatures, suggesting a higher degree of ordering and fewer defects.<sup>210</sup> The narrower linewidth and lower energy FE emission show that the  $\pi$ -face-on phase pentacene/hBN approaches the limiting case of pentacene single-crystals, except with a slightly larger PL linewidth due to the presence of grain boundaries within the laser spot.<sup>210</sup>

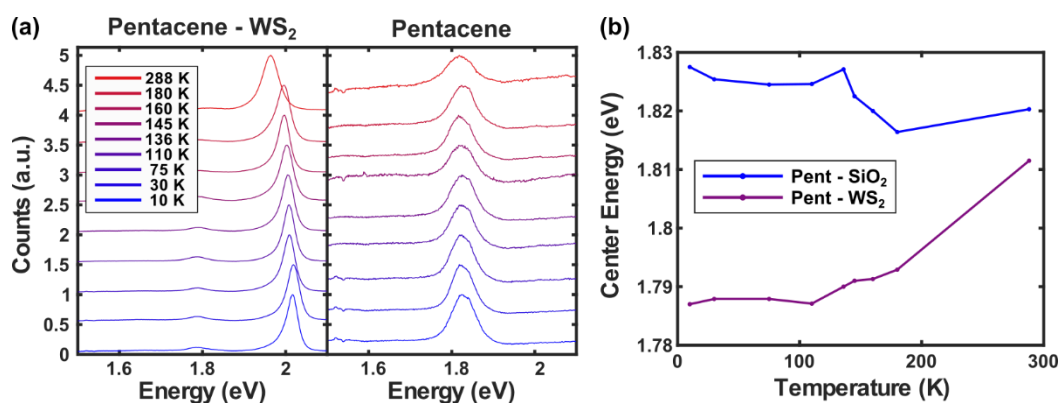


Figure 4.6 Temperature-dependent PL of pentacene/WS<sub>2</sub>. (a) PL plots of the pentacene thin films on WS<sub>2</sub> and SiO<sub>2</sub>. The WS<sub>2</sub> exciton emission at 2 eV is more efficient than the pentacene free exciton at 1.8 eV. (b) Energy of pentacene free exciton emission versus temperature. The epitaxial film on WS<sub>2</sub> behaves similarly to the film on hBN, although with a lower overall energy shift. The in-plane thermal expansion coefficient of WS<sub>2</sub> is on the order of  $10^{-6} \text{ K}^{-1}$ , based on temperature-dependent Raman measurements.<sup>347</sup> This thermal expansion coefficient is between hBN ( $2 - 4 \times 10^{-5} \text{ K}^{-1}$ )<sup>345</sup> and SiO<sub>2</sub> ( $5 \times 10^{-7} \text{ K}^{-1}$ ),<sup>346</sup> which aligns with the temperature-dependent PL shift of pentacene/WS<sub>2</sub> being between those two other substrates.

Figure 4.7a shows a PL decay lifetime map of pentacene/hBN and the surrounding SiO<sub>2</sub> substrate 298 K. The PL decay of the pentacene on SiO<sub>2</sub> can be fit with a biexponential function, where an instrument response function (IRF) limited ( $<50$  ps) component accounts for more than 99% of the decay, and a component with lifetime 400 ps accounts for the remainder (Figure 4.7b). The emission from pentacene/hBN is more intense than that of pentacene/SiO<sub>2</sub>. The PL decay of

pentacene/hBN consists of the two components already mentioned plus a third 3.2-ns component (see Table 4.1 for a full table of fitting parameters).

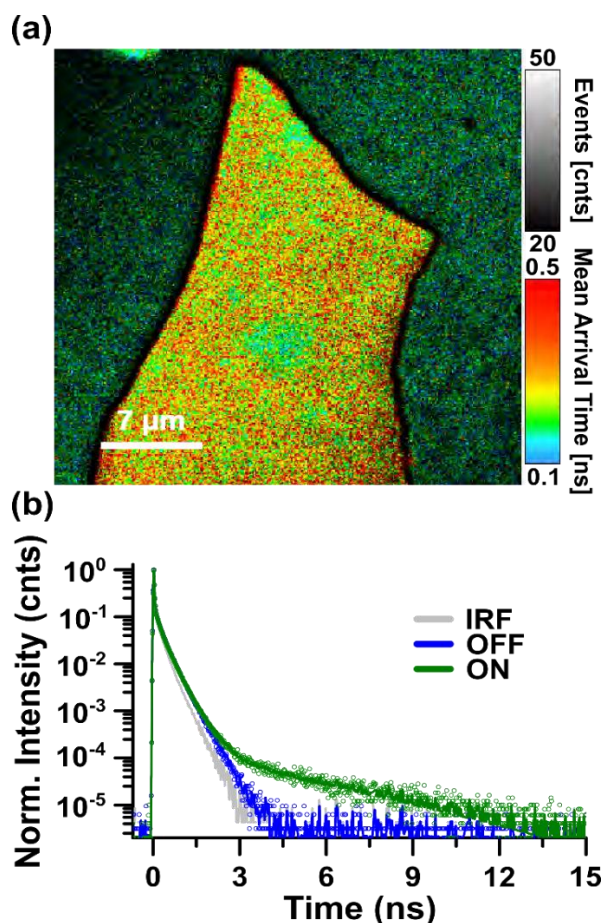


Figure 4.7 (a) PL map of the pentacene/hBN thin film, acquired with an excitation wavelength of 570 nm and detection range 650-950 nm. The grayscale bar indicates the signal intensity and the color bar indicates the average PL lifetime (ns) at each pixel. (b) Decay of PL intensity at representative spots ON (green) and OFF (blue) the hBN flake, along with IRF (gray). The “fastest” two components of PL decay (i.e., <50 ps and 400 ps; convolved with the IRF) in both phases correspond to a singlet fission process, while the 3.2 ns component of the PL from pentacene deposited on top of hBN arises from triplet-triplet recombination.

Table 4.1 Fitting parameters for the photoluminescence decay histograms of pentacene deposited on an hBN flake and on a non-hBN part of the substrate, excited at 570 nm. Three spots were evaluated at each region on the image. The IRF was fitted to a Gaussian ( $a_1$ ,  $\tau_1$ ) and a biexponential decay ( $a_2$ ,  $\tau_2$ ,  $a_3$ ,  $\tau_3$ ).

Spot	$a_1$ [%]	$\tau_1$ [ps]	$a_2$ [%]	$\tau_2$ [ns]	$a_3$ [%]	$\tau_3$ [ns]	$\langle \tau \rangle$ [ps]
Off 1	> 99.99	< 50	< 0.01	0.40±0.02	---	---	< 50
Off 2	> 99.99	< 50	< 0.01	0.40±0.03	---	---	< 50
Off 3	> 99.99	< 50	< 0.01	0.39±0.02	---	---	< 50
On 1	> 99.99	< 50	< 0.01	0.40±0.02	< 0.01	3.20±0.28	< 50
On 2	> 99.99	< 50	< 0.01	0.40±0.02	< 0.01	3.10±0.24	< 50
On 3	> 99.99	< 50	< 0.01	0.40±0.02	< 0.01	3.10±0.19	< 50
Wrinkle 1	> 99.99	< 50	< 0.01	1.20±0.11	< 0.01	4.20±0.18	60±10
Wrinkle 2	99.97±0.01	< 50	0.03±0.02	0.85±0.03	< 0.01	3.40±0.14	200±10
Wrinkle 3	> 99.99	< 50	< 0.01	1.10±0.14	< 0.01	4.10±0.17	< 50
IRF	(Gaussian)	29±1	95.6±0.3	0.011±0.001	4.4±0.1	0.219±0.001	

The photophysics of pentacene and most of its derivatives are dominated by ultrafast singlet fission to a coherent triplet pair on the 100-fs timescale.<sup>177</sup> Other studies reported that the PL decay of pentacene thin films on SiO<sub>2</sub> occur with components of 3 ps and 52 ps.<sup>348</sup> Because our experimental IRF is 220 ps, it is likely that singlet fission is the principal cause for the >99% IRF-limited decay in pentacene films on both SiO<sub>2</sub> and hBN. The 400-ps component may also arise from the singlet fission process convolved with the IRF (see Experimental Methods).

In addition to the biexponential PL decay observed for both pentacene/SiO<sub>2</sub> and pentacene/hBN, there is a 3.2-ns decay component for pentacene/hBN. Such long-lived PL from pentacene has been assigned to two sources: decay of isolated pentacene molecules<sup>199,348,349</sup> and delayed emission from the singlet state formed after triplet-triplet annihilation (where the triplet is formed by singlet fission).<sup>177,213,350</sup> Since these experiments are conducted on pure pentacene films, rather than pentacene in a matrix of other molecules, we do not expect to see decay dynamics of isolated molecules. Ruling out this pathway, we suggest that delayed triplet-triplet recombination following singlet fission is the source of the 3.2-ns feature. A number of factors could make this recombination pathway more favorable for pentacene/hBN thin films than for pentacene/SiO<sub>2</sub>. Bimolecular recombination, including the fusion of non-geminate triplets, would be enhanced by the increased order (indicated by narrower PL linewidths) in the  $\pi$ -face-on phase compared to the thin-film phase.<sup>351</sup> Furthermore, greater charge mobility, which growth on hBN substrates promotes,<sup>187,352</sup> should increase the likelihood of triplet-triplet encounters. Finally, greater optical absorption by the  $\pi$ -face-on phase molecular orientation<sup>353</sup> increases the density of excitons and promotes bimolecular recombination pathways. The production of a higher density of mobile triplets by the  $\pi$ -face-on phase suggests that the use of hBN as a templating substrate or charge transport layer in pentacene devices may enhance the yield of mobile carriers from singlet fission.

#### 4.4. Conclusions

We have demonstrated that thermal evaporation results in a needle-like  $\pi$ -face-on pentacene thin-film phase on hBN. The optical response of this phase differs from that of the usual thin-film phase on SiO<sub>2</sub>, as evidenced by a narrower, lower energy free exciton emission, a qualitatively

different photoluminescence temperature dependence, and an emergent delayed emission state that is not present in the thin-film phase. This result will inform the future design of organic optoelectronic devices on hBN and points to compelling opportunities for using layered vdW materials to template unique phases of organic thin films in mixed-dimensional heterostructures. We anticipate the discovery of other emergent optical processes in such films that are likely to have implications for the creation of anisotropic optical devices and the design of solid-state systems for singlet fission, triplet upconversion, and other spintronic applications.

#### 4.5. Experimental Methods

hBN samples were prepared using micromechanical exfoliation from bulk crystals on 285 nm thick SiO<sub>2</sub>/Si substrates. Suitable samples of 5 – 10 nm thickness were identified by optical microscopy. To maximize surface quality, samples of desired thicknesses and sizes were annealed at 400 °C for 3 h in an Ar/H<sub>2</sub> (~70%/30%) environment. After annealing, samples were again inspected by optical microscopy for any remaining tape-adhesive residues on the hBN flakes or the surrounding SiO<sub>2</sub> substrate, and then annealed again for 3 h if any residues remained. No chemical treatments were performed on the samples to avoid introducing any potential external contaminants on the material surfaces. Samples that are contaminated with residual polymers do not exhibit the large needle-like grains of pentacene characteristic of the  $\pi$ -face-on phase.

Pentacene was purchased from Sigma-Aldrich and purified by temperature gradient sublimation. Films were deposited by thermal evaporation. In particular, the pentacene powder in an alumina-coated tungsten boat and the target substrate were loaded into a bell jar in an N<sub>2</sub> glovebox and evacuated below 10<sup>-5</sup> Torr. The pentacene was resistively heated, and thin films were

grown at a rate of  $1.0 - 3.0 \text{ \AA} / \text{s}$ , monitored by quartz crystal microbalance, to a final thickness of 20 nm.

Raman spectra were collected with a Horiba Raman Xplora using a 532 nm laser at  $150 \mu\text{W}$  power with a 100x microscope object and 1800 grooves/mm diffraction grating. AFM was performed in tapping mode with an Asylum Cypher AFM using a Si cantilever with a resonant frequency  $\sim 300 \text{ kHz}$ . Temperature-dependent PL measurements were taken in vacuum using a continuous wave 532 nm laser at  $150 \mu\text{W}$  with a 50x microscope objective. A cryogen-free cryostat (Advanced Research Systems DE204PF) was used to vary the sample temperature from 7 K to 295 K. PL spectra were filtered by a 550 nm long-pass filter and recorded by a spectrometer (Andor Shamrock SR-750) equipped with a thermo-electrically cooled CCD (Andor iDUS DU420-A).

PL lifetime imaging microscopy experiments were carried out in a custom-built microscope equipped with a piezo scanner (NanoPI, Physik Instrumente), an APD detector (MicroPhoton Devices), and a photon counting board (PicoHarp300, PicoQuant) where correlation times between the excitation pulses and detected photons were recorded. The excitation pulses were synchronized from an amplified Yb laser head (Pharos) that pumped an OPA (Orpheus) tuned to 570 nm. The pulses, at a repetition rate of 200 kHz, were focused with a long working distance objective (0.7 NA, 100X, Mitutoyo), and the detected PL was filtered with a long-pass dichroic (Chroma ZT640rdc-UF1) and a long-pass filter (Thorlabs FLG610). The IRF of the instrument was measured by reflecting an attenuated excitation pulse with a silver mirror placed in the sample plane. The fit of the IRF with one Gaussian and two exponential functions yields a width of

0.030 ns and decays of 0.011 ns (95.6%) and a 0.219 ns (4.4%). It should be noted that the lifetime analysis convolves this IRF in the fit of recorded kinetic traces. Image reconstruction and lifetime analysis were carried out using commercial software (SymphoTime 64, PicoQuant).

\*This chapter was originally published in the *Journal of Physical Chemistry Letters*. Reprinted with permission from <sup>201</sup>. Copyright 2021 American Chemical Society.

## 5. Summary and Future Outlook

### 5.1. Thesis Summary

This thesis provided several examples of systematic exploration of the properties of organic – 2D heterojunctions, showing emergent behavior that would not appear in either material in isolation. These examples provide valuable information about the specific systems studied, as well as more general guidance about how to think about design of future molecule – 2D interfaces.

Chapter 2 discussed the electronic coupling between metallophthalocyanines (MPc) and MoS<sub>2</sub>, as revealed through absorption and Raman spectroscopy. A significant red-shifting of the MPc absorption Q-band results from delocalization of the  $\pi$ -electrons into the MoS<sub>2</sub>. This

coupling of electrons also manifests as Raman enhancement of the MPc by MoS<sub>2</sub>. The magnitude of this Raman enhancement was found to depend on the identity of the Pc metal, with the enhancement decreasing in the order CoPc, NiPc, CuPc, ZnPc, and with little enhancement of metal-free H<sub>2</sub>Pc. Density functional theory (DFT) calculations show a similar trend in the mixing of the MPc LUMO and HOMO-1 orbitals with the MoS<sub>2</sub> conduction and valence bands, pointing to the chemical origins of these spectroscopic features.

The MPc - MoS<sub>2</sub> heterojunction was also the topic of Chapter 3, this time focusing on the interaction of the MPc molecules with defects in MoS<sub>2</sub>. MPc were found to quench the low temperature (10 K) photoluminescence (PL) associated with defect-bound excitons in MoS<sub>2</sub>, while H<sub>2</sub>Pc was found not to quench those defects. Furthermore, a similar trend was found in the quenching efficacy as in the Raman enhancement, with quenching decreasing in the order CoPc, CuPc, ZnPc, and H<sub>2</sub>Pc. Room temperature PL and low temperature gate-voltage dependent PL ruled out charge depletion or doping as a potential mechanism of this quenching, while careful consideration of spectral overlap and dielectric constants of the films ruled out nonradiative energy transfer. The DFT calculation of the electronic structure show that charge transfer is an unlikely quenching mechanism, which points to chemical changes in the nature of the MoS<sub>2</sub> defects induced by the MPc as the mechanism of defect PL quenching. This was confirmed by DFT calculation of the energy of formation of defects with different charges, which found that MPc stabilize negatively charged non-emissive defects over bright neutral defects. Adsorbate-defect interactions in MoS<sub>2</sub> are still poorly understood, and this work represents an advance in

both fundamental knowledge of this topic, as well as a potential route to fine-tuning the optical and electronic responses of these defects.

The focus of Chapter 4 moved to a larger scale view of these heterojunctions, focusing on the morphology changes in organic thin films that are templated by 2D material substrates, and how these morphologies may result in new optical properties. The material system studied was the pentacene – hexagonal boron nitride (hBN) heterojunction. Pentacene films grown by thermal evaporation on hBN form a long, needle-like morphology, in contrast to the dendritic structure typically observed in thin-film phase pentacene on SiO<sub>2</sub>. Raman measurements show that the pentacene lies  $\pi$ -face-on to the hBN, in contrast to edge-on to SiO<sub>2</sub>. PL measurements of the pentacene at 10 K reveals that both the free-exciton (FE) and self-trapped exciton (STE) emissions are shifted to lower energy in the  $\pi$ -face-on phase. Further comparisons of the temperature dependence of the FE and STE emission of pentacene films grown on hBN and SiO<sub>2</sub> show contrasting behavior due to thermal-expansion induced strain. This results in relatively strain-free films on hBN, versus highly strained films on SiO<sub>2</sub>. Finally, time-dependent PL measurements of the pentacene films show the presence of a long-lived PL decay only in the  $\pi$ -face-on phase, likely a result of long-lived triplet states fusing back into singlets and recombining. This work connects pentacene – hBN interactions from morphology to molecular orientation to optical properties and electronic structure and demonstrates the power in using hBN as a templating substrate to discover new structures even in materials as well studied as pentacene.

## 5.2. Future Directions: Tuning Organic / 2D Heterojunctions Beyond Band Alignment

The surface sensitivity and lack of dielectric screening in 2D materials provide numerous opportunities to tailor their properties using adsorbed  $\pi$ -electron organic molecules. These organic-2D mixed-dimensional heterojunctions are often considered solely in terms of their energy level alignment – i.e., the relative energies of the frontier molecular orbitals versus the 2D material conduction and valence band edges. While this simple model is frequently adequate to describe doping and photoinduced charge transfer, the tools of molecular chemistry enable additional manipulation of properties in organic-2D heterojunctions that are not accessible in other solid-state systems. Fully exploiting these possibilities requires consideration of the details of the organic adlayer beyond its energy level alignment, including hybridization and electrostatics, molecular orientation and thin-film morphology, non-frontier orbitals and defects, excitonic states, spin, and chirality. This chapter explores how these relatively overlooked molecular properties offer unique opportunities for tuning optical and electronic characteristics, thereby guiding the rational design of organic-2D mixed-dimensional heterojunctions with emergent properties.

Mixed-dimensional heterojunctions between zero-dimensional (0D) organic molecules and atomically thin two-dimensional (2D) materials are a rapidly growing area of scientific and technological research interest.<sup>228,246,354</sup> The aim of studying these organic-2D heterojunctions is to understand and leverage the unique properties of their constituent materials in order to realize physical phenomena not possible with either material alone. When predicting the properties of interfaces between dissimilar materials, including organic-2D mixed-dimensional heterojunctions, the simplest initial model reduces the system to an energy level diagram. In the organic-2D case,

the relevant energy levels are the highest occupied molecular orbital (HOMO) and lowest unoccupied molecular orbital (LUMO) relative to the 2D material valence band maximum (VBM) and conduction band minimum (CBM). From this energy level alignment, the likely flow of charges in the ground and excited states can be anticipated. Indeed, this approach is often used to identify candidate organic-2D material combinations for photovoltaic cells, photodetectors, diodes, and related electronic and optical devices.

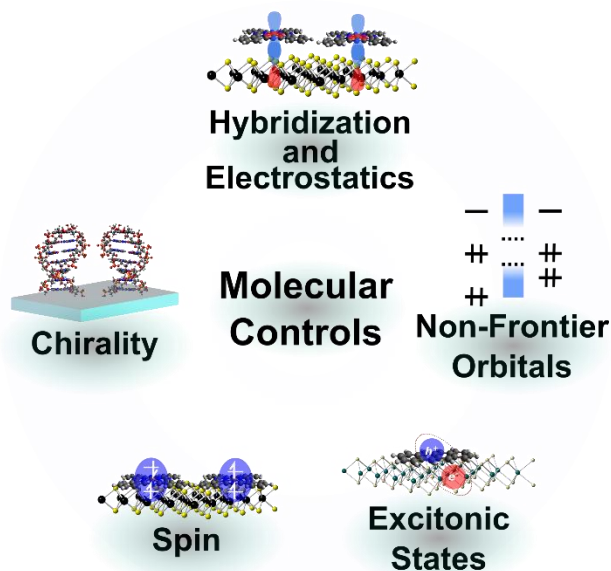


Figure 5.1 Summary of molecular characteristics beyond frontier orbital energy level alignment that can provide tunability over the electronic and optical properties of organic-2D mixed-dimensional heterojunctions.

While this simple model provides a useful first-order approximation, it does not fully capture many of the relevant details of the heterojunction. The band and orbital energies, for instance, are not static and will be displaced when the molecule and 2D material are in intimate contact due to electrostatic and hybridization effects. In addition, beyond the frontier HOMO and

LUMO, non-frontier molecular orbitals can participate in the photophysical dynamics of the organic-2D heterojunction. Furthermore, electrons and holes may not be free carriers in the heterojunction but can instead exist in bound electron-hole-pair excitonic states. Simple energy level alignment also fails to capture details related to magnetism or molecular spin states, molecular orientation, thin-film morphology, or chirality. These additional molecular characteristics present significant opportunities for further tuning the properties of organic-2D heterojunctions.

As summarized in Figure 5.1, this Perspective explores the current understanding and implementation of these relatively overlooked molecular properties (i.e., hybridization and electrostatics, orientation and morphology, non-frontier orbitals, excitonic states, spin, and chirality) in organic-2D mixed-dimensional heterojunctions. While most of the prominent examples are heterojunctions between 2D transition metal dichalcogenides (TMDs) and conjugated metallophthalocyanines (Pcs), perylenes, or acenes, the conclusions of this perspective article can be applied more generally to the broader array of synthetically available 2D materials and  $\pi$ -electron organic molecules. The aim is not an exhaustive review, but rather to highlight informative model systems that are representative of the larger field. Ultimately, by focusing on key fundamental issues, this perspective article will help define general design rules for next-generation organic-2D mixed-dimensional heterojunctions.

### 5.2.1. Hybridization and Electrostatics

When two disparate materials are brought into contact in a heterojunction, their electronic states are not static. Even in van der Waals (vdW) interfaces that are only weakly

bonded, interactions between orbitals can perturb the energy level alignment. The impacts of hybridization, charge transfer, and electrostatics are discussed in more detail in Chapter 1.4.1.

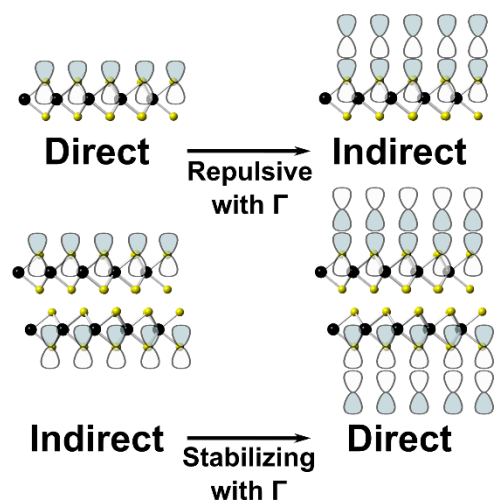


Figure 5.2 Proposed hybridization-driven direct-to-indirect bandgap transition in monolayer MoS<sub>2</sub> or indirect-to-direct bandgap transition in bilayer MoS<sub>2</sub>. Repulsion between out-of-plane MoS<sub>2</sub> p<sub>z</sub> orbitals drives the direct-to-indirect transition in monolayer to bilayer MoS<sub>2</sub>. Similarly, by designing molecular systems that have strong bonding or antibonding interactions with the MoS<sub>2</sub> p<sub>z</sub> orbitals, the energy at  $\Gamma$  in the valence band structure can be raised or lowered while leaving  $K$  relatively unchanged.

While it is known that hybridization with organic adlayers can influence the band structure of 2D materials, the fundamental limit of this effect remains unknown. To develop and verify chemical intuition about this topic, systematic DFT and ARPES studies of a wide variety of organic-2D heterojunctions are needed. In this manner, hybridization can be more systematically exploited to open new avenues of band engineering in 2D materials. For instance, it is known that the direct-to-indirect bandgap transition in monolayer to bilayer MoS<sub>2</sub> is induced by repulsion between out-of-plane S p<sub>z</sub> orbitals at the valence band  $\Gamma$  point.<sup>52</sup> A monolayer of strongly interacting molecules could potentially have a similar effect. In particular, repulsive interactions

between organic adsorbates and the S  $p_z$  orbitals may allow a direct-to-indirect bandgap transition in monolayer MoS<sub>2</sub>, or conversely stabilizing interactions may induce an indirect-to-direct bandgap transition in bilayer MoS<sub>2</sub> (Figure 5.2).

Variations in the underlying 2D material band structure can also change the interaction strength with organic molecules. Moiré patterns in 2D materials are an excellent demonstration of this phenomenon. For instance, sub-monolayer films of phthalocyanines follow the Moiré patterns of graphene grown on certain metal surfaces,<sup>355–357</sup> indicating that the periodic changes to the graphene electronic structure drive molecular assembly. Twistronics, the emerging field that is exploring the impact of twist angle between the two planes in 2D-2D heterostructures, is rapidly growing. In the same way that 2D-2D heterostructures preceded work on organic-2D heterostructures, the intriguing addition of organic adsorbates to twistronic 2D-2D heterostructures is a logical next step of investigation. The addition of a third layer to a twistronic heterostructure has been proposed as a means of modifying the Moiré potential.<sup>358</sup> Instead of using another 2D material for this purpose, organics may find use as a precise means of introducing periodic changes in the electron density, doping characteristics, dielectric constant, dipole moment, and/or spin within these heterostructures.

### 5.2.2. Adlayer Orientation and Morphology

Given the anisotropy of electronic transport and optical properties in organic solids, detailed understanding of molecular orientation is critical for the design of organic-2D heterojunction. For experiments that seek to isolate other effects, molecules with more isotropic geometries such as fullerenes should be ideal.<sup>359</sup> The role of orientation and morphology in organic

charge transport has been studied heavily in the organic photovoltaic (OPV) literature.<sup>360</sup> While not every insight from OPVs will apply to hybrid organic-2D heterojunctions, the state-of-the-art in OPVs should be a source of inspiration. For instance, the tools and approaches used to understand the complex, disordered interfaces in OPV bulk heterojunctions may be useful in understanding the behavior of bulk heterojunction films consisting of organics and liquid-phase-exfoliated 2D materials.<sup>361,362</sup> Furthermore, next-generation non-fullerene acceptors such as the ITIC and Y6 families may find use in organic-2D photodetectors and photovoltaics.

A key question within the organic-2D heterojunction field is whether simple descriptors can predict growth orientation. While it is tempting to assume that all large aromatic systems will lie  $\pi$ -face-on, the difference in orientation between H<sub>2</sub>Pc and CuPc on MoS<sub>2</sub> indicates that additional factors need to be considered. While some work on this topic has been performed,<sup>205,363</sup> many questions remain unanswered. One difficulty in studying organic adlayer orientation and morphology is the common presence of surface contaminants. For example, polymer residues from exfoliation or lithography are known to disrupt the formation of films on 2D surfaces,<sup>201,340</sup> and high densities of defects in the 2D substrate can also alter film growth morphology.<sup>242</sup> Given the impact of orientation and morphology on the optoelectronic properties of organic-2D heterojunctions, it is critical to employ clean, high-quality 2D materials whenever possible. Experimental details on material synthesis, handling, cleaning, and fabrication must be published in detail since careful control of all of these factors are essential for reproducibility.

### 5.2.3. Non-Frontier Orbitals

Orbitals beyond the HOMO and LUMO, including non-frontier molecular orbital defect states in 2D materials, often play important roles in the electronic structure of organic-2D heterojunctions. Careful consideration of these effects is essential to understanding the optoelectronic response of organic-2D heterojunctions, and potentially permits enabling or tuning functionality beyond charge or energy transfer. When considering charge transfer in organic-2D heterojunctions, it is often neither the HOMO nor LUMO that has the optimal alignment with the 2D band edges. For instance, hole transfer rates from MoS<sub>2</sub> to PTB7 depends on the density of states below the PTB7 HOMO,<sup>245</sup> and hole transfer from MoS<sub>2</sub> to pentacene is fastest to the HOMO-1 near the VBM (Figures 5.3a and 5.3b).<sup>364</sup> Other optical responses are also affected by these non-frontier orbitals such as the Raman enhancement of MoS<sub>2</sub>-Pc heterojunctions arising partially from mixing of the phthalocyanine HOMO-1 orbital with the MoS<sub>2</sub> VBM.<sup>66</sup>

An area where non-frontier orbitals are critical is so-called ‘ping-pong’ energy transfer, where an excited state in a non-frontier molecular orbital is transferred to the 2D substrate and then back to a lower energy state on the molecule. This form of energy transfer is possible in organic-2D heterojunctions when two conditions are met: (1) Charge transfer occurs on femtosecond timescales that are faster than internal conversion; (2) Sufficiently large energetic separation exists between different molecular orbitals, which is not possible in 2D bands alone. As a specific illustration, consider a molecule that has a LUMO below the 2D CBM but a LUMO + 1 that is above the 2D CBM. Exciting to the LUMO + 1 would normally result in efficient internal conversion to the LUMO, but in this case it is faster for the LUMO + 1 electron to instead transfer

to the 2D CBM. Since the LUMO is below the CBM, a driving force exists for back electron transfer from the 2D material to the LUMO. This ping-pong energy transfer has been observed in MoS<sub>2</sub> heterojunctions with porphyrins<sup>365,366</sup> and graphene quantum dots.<sup>367</sup>

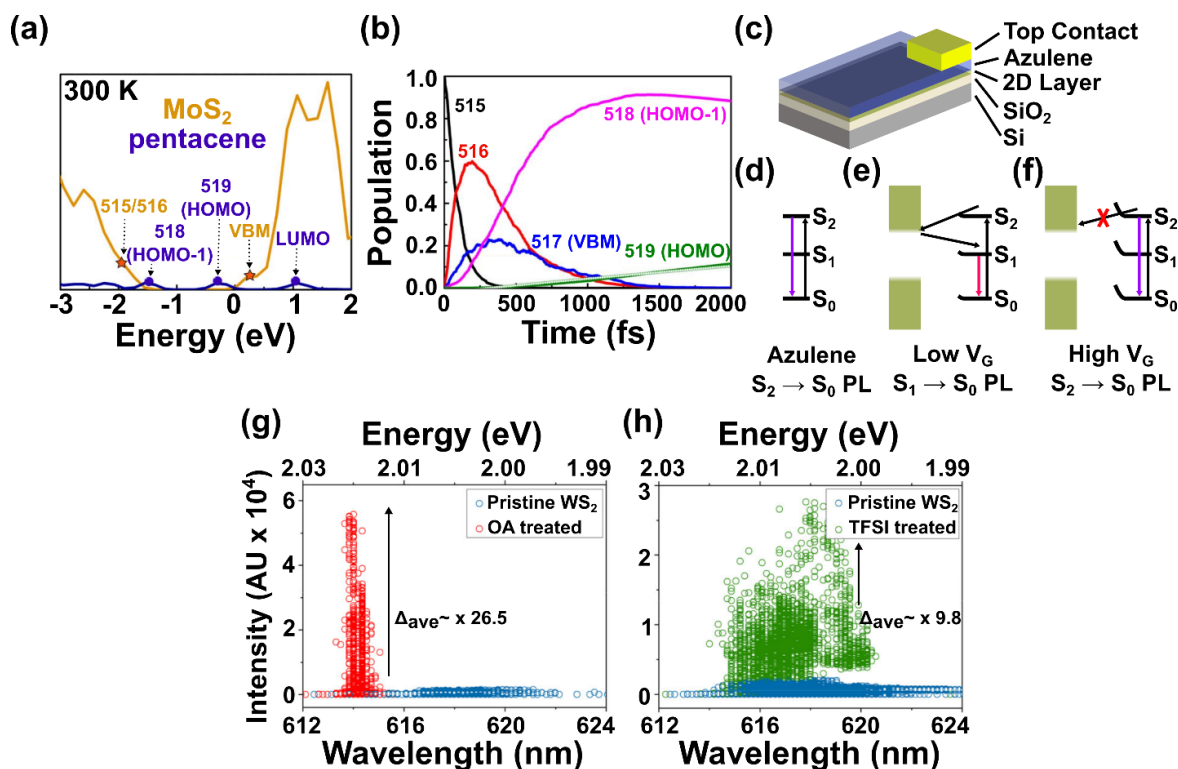


Figure 5.3 (a) Calculated density of states (DOS) of a pentacene-MoS<sub>2</sub> heterojunction at 300 K using the HSE06 functional. (b) Calculated time-dependent state populations from nonadiabatic dynamic simulations of interfacial hole transfer in a pentacene-MoS<sub>2</sub> heterojunction. Hole transfer proceeds from the MoS<sub>2</sub> VBM to the pentacene HOMO-1 on ultrafast timescales before relaxing to the pentacene HOMO over the following picoseconds. (c) Schematic proposal of an azulene-2D heterojunction that utilizes ping-pong electron transfers to allow gate-tunable emission at two wavelengths. (d) Azulene exhibits bright fluorescence from its S<sub>2</sub> state in isolation. (e) If the S<sub>1</sub> state is within the bandgap of a 2D semiconductor, photoexcited azulene would likely undergo back electron transfer via S<sub>2</sub> → CB → S<sub>1</sub>, allowing emission from the S<sub>1</sub> state. (f) At high gate voltages, band bending may prevent electron transfer from the azulene, allowing it to fluoresce from its S<sub>2</sub> state as it does under normal conditions. (g,h) Photoluminescence intensity and wavelength histograms of WS<sub>2</sub> treated with (g) Oleic acid and (f) Bis(trifluoromethane)sulfonimide (TFSI). Both treatments dramatically increase the WS<sub>2</sub> photoluminescence quantum yield (PLQY), but the narrowness of the emission from the oleic acid

treatment suggests chemical specificity in the defect passivation. (a) and (b) reprinted with permission from <sup>364</sup>. Copyright 2019 American Chemical Society. (g) and (h) reprinted with permission from <sup>253</sup>. Copyright 2019 American Chemical Society.

A potential application of these ping-pong energy transfers is shown in Figure 5.3c. Azulene is a famous exception to Kasha's Rule, showing bright fluorescence from the  $S_2$  state. If azulene is deposited on an appropriately chosen 2D semiconductor such that its  $S_2$  state is above the CBM but its  $S_1$  state is in the bandgap, it would likely undergo a ping-pong transfer and fluoresce from the  $S_1$  state. An external stimulus, such as an applied gate voltage can manipulate the interfacial band bending, thus allowing modification of the rate of charge transfer from the  $S_2$  state to the CBM. In this manner, the fluorescence could be dynamically tuned between the  $S_2$  and the  $S_1$  state. For information processing applications, this phenomenon would allow conversion of binary electrical signals to optical information. In addition, it could be used for lighting applications by tuning the ratio of  $S_2$  and  $S_1$  fluorescence, thereby allowing the hue of the emission to be altered by the voltage within a single device.

Like non-frontier orbitals, 2D material defects are often not considered within a simple energy level alignment picture despite their importance to the electrical and optical properties of organic-2D heterojunctions. While a wide range of defects in 2D materials have been identified,<sup>59</sup> the relative abundance and role of specific defects remain topics of debate.<sup>62,63</sup> Organic molecules often interact strongly with defects,<sup>256,299</sup> further complicating the effects of defects in organic-2D heterojunctions. An example of the need to understand the chemistry of adsorbate-defect interactions is the study of  $\text{MoS}_2$  photoluminescence quantum yield (PLQY). At room temperature and low excitation powers, an effective strategies for enhancing  $\text{MoS}_2$  PLQY have included

superacid treatments<sup>84</sup> or applied voltages<sup>368</sup> to suppress the formation of negative trions, which can contribute to nonradiative recombination in MoS<sub>2</sub>.<sup>91</sup> At higher excitation powers, exciton-exciton annihilation (EEA) further limits PLQY,<sup>254,368</sup> which in turn has hindered the use of MoS<sub>2</sub> in lasing applications. At high temperatures, neutral excitons are in thermal equilibrium with defect-bound excitons that luminesce at cryogenic temperatures.<sup>81</sup> It is believed that EEA is promoted by these defect-bound excitons.<sup>254</sup> Substrate choice has been shown to play a major role in EEA,<sup>254</sup> and defect photoluminescence has been shown to have partially extrinsic character,<sup>89</sup> suggesting that organic layers could be used to tune the energetic distribution of defect states and thus limit the impact of EEA at high powers.

Fundamental questions about the chemical identity and energy levels of 2D defects are beginning to be answered. While a number of organic materials have been used to passivate defects,<sup>256,257,299,369</sup> relatively little work has focused on molecular design to target specific defects in 2D materials. An important exception is the passivation of WS<sub>2</sub> defects with oleic acid, which results in greater PLQY and narrower emission than TFSI treatments (Figures 5.3g and 5.3h).<sup>253</sup> The next level of sophistication in these schemes would be to go beyond passivation to fine-tuning of the defect levels and their occupancy. In addition to altering the defect energy for suppressing EEA, potential uses of this approach include influencing defect drift kinetics in TMD memristors<sup>370</sup> and/or altering the wavelength of single photon emitting defects.<sup>312</sup>

#### 5.2.4. Excitonic States

Both organic and 2D materials have high exciton binding energies and as such can host diverse excitonic and many-body phenomena. In the case of organic materials, low dielectric

screening reflects their inherently low dielectric constants, whereas the reduced dimensionality of 2D materials increases electron-hole Coulomb interactions.<sup>85,371</sup> By combining organic and 2D materials, excitons can be tuned or even new types of bound states can be hosted at their interfaces. For example, doping 2D materials with strongly electron donating or accepting molecules can change the neutral exciton to trion ratio,<sup>88,90,92</sup> which in turn tunes PLQY since radiative recombination is more efficient in neutral excitons than trions.<sup>91</sup> The density of excitons in the 2D layer can also be changed by energy transfer with organic adsorbates.<sup>251</sup>

While neutral excitons and trions have been studied extensively, 2D materials can also host higher order excitonic states such as biexcitons (i.e., bound states consisting of two electrons and two holes). Biexcitons have drawn interest in quantum information sciences since their radiative recombination can produce entangled photon pairs.<sup>93</sup> Although the combination of two neutral excitons can form a biexciton, it has been found that biexcitons can be more efficiently generated by combining a charged trion with an oppositely charged free carrier.<sup>95</sup> Efficient generation of excited-state biexcitons has been demonstrated in graphene-WS<sub>2</sub> heterostructures. In this case, exciton dissociation at the graphene-WS<sub>2</sub> interface transfers electrons to graphene, leaving behind positive holes to bind to negative trions in WS<sub>2</sub> as shown schematically in Figure 5.4a.<sup>372</sup> By carefully controlling the hole and negative trion populations by an applied gate voltage, the emission can be biased towards biexcitons as shown in Figure 5.4b.

Since molecular adsorbates can control carrier type and density in 2D materials, organic-2D heterojunctions provide significant opportunities for tailoring biexciton populations and resulting emission. For example, the direction of doping induced by a molecule and the charge that

it injects via excited-state charge transfer are independent. As a specific case, a properly oriented molecule with a large dipole moment and a high LUMO could act as a p-type dopant electrostatically but also donate free electrons when photoexcited. Molecular adlayers can also play a role in the study of electron-hole liquids and plasmas in 2D materials at high exciton densities. These excited states have recently been observed in  $\text{MoS}_2$ <sup>373,374</sup> and  $\text{MoTe}_2$ <sup>375</sup> at high

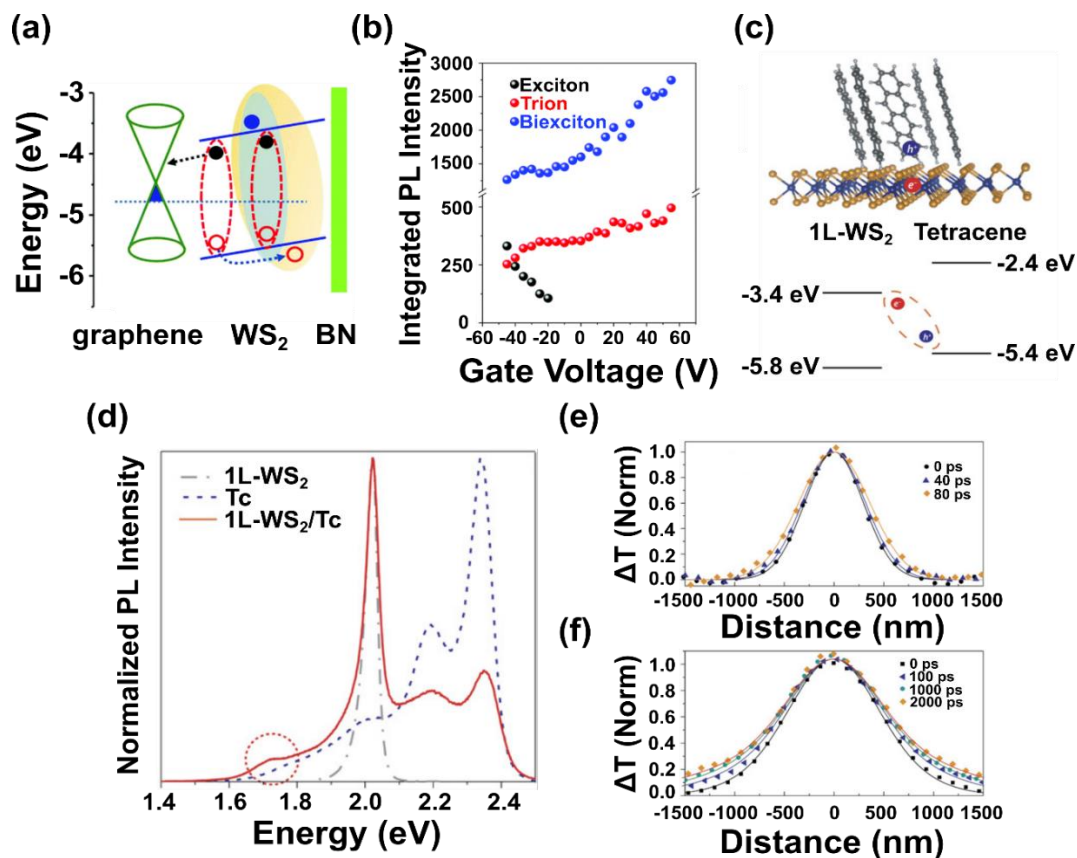


Figure 5.4 (a) Schematic band diagram of a graphene- $\text{WS}_2$ -hBN heterostructure for excited-state biexciton formation. Electrons from photoexcited neutral excitons in the  $\text{WS}_2$  transfer to the graphene, leaving behind free holes that can combine with negative trions (light grey shaded area) to form an excited-state biexciton (light orange shaded area). (b) Integrated PL intensity of the excitonic emission from the heterostructure in (a) as a function of gate voltage. Higher gate voltage increases the negative trion population, promoting formation and emission of biexcitons (X). (c) Schematic of a tetracene- $\text{WS}_2$  heterojunction, its energy level alignment, and the energy levels of a charge transfer exciton. (d) Photoluminescence spectrum of the tetracene- $\text{WS}_2$

heterojunction. An extra peak is present near 1.7 eV that is attributed to recombination of the charge transfer exciton. (e,f) Exciton population profiles of (e) WS<sub>2</sub> and (f) tetracene-WS<sub>2</sub>. The excitons diffuse further in the case of the tetracene-WS<sub>2</sub> heterojunction due to equilibrium with the long-lived charge transfer exciton. (a) and (b) reproduced from <sup>372</sup>. Copyright 2019 Royal Society of Chemistry. (c), (d), (e) and (f) reproduced from <sup>252</sup>. Copyright 2018 The Authors, American Association for the Advancement of Science, licensed under CC BY-NC.

optical pumping powers. Rather than using high powers on a 2D monolayer that could potentially damage it, another route could be pumping a wide-bandgap organic adsorbate in a type-I heterojunction with the 2D layer, which can greatly increase the charge carrier density through energy transfer.<sup>251</sup> The low dielectric constant of the organic adlayer will minimally screen Coulomb interactions and could permit study of these many-body states at lower powers.

In addition to promoting the formation of bound states within 2D layers, organic-2D heterojunctions can also host their own emergent excitonic phenomena. Prominent examples are interlayer or charge transfer (CT) excitons, in which one charge carrier is localized on the 2D material and the other is localized on the organic molecule, as has been observed in tetracene-WS<sub>2</sub> heterojunctions.<sup>252</sup> The energy levels of the CT exciton can be approximated using the HOMO and CBM (as in Figure 5.4c) or the LUMO and VBM, depending on which has the smaller energy spacing. CT excitons often exhibit PL, which appears as a new peak in the spectrum that is not attributable to either the 2D material or the molecule alone (Figure 5.4d). In the case of tetracene-WS<sub>2</sub> heterojunctions, the CT excitons are highly mobile with long lifetimes, as shown in the exciton population profiles in Figures 5.4e and 5.4f.

Since CT exciton emission is often weak and convoluted with trions, biexcitons, and defects, photoelectron spectroscopy presents an alternative means for identifying CT states.<sup>241,285</sup> The large

and oriented dipole moments for CT excitons also suggest that they should be particularly responsive to applied voltages perpendicular to the heterojunction plane, which allows them to be differentiated from other in-plane excitonic states that do not have intrinsic orientation. Other classes of interlayer excited states may also be possible in organic-2D heterojunctions. While most work has focused on neutral CT excitons, interlayer trions and biexcitons have been observed in 2D-2D heterojunctions,<sup>376,377</sup> which suggests that they should be achievable in organic-2D heterojunctions. High-temperature superfluidity and exotic forms of superconductivity have also been predicted in interlayer exciton systems, and thus represent future targets for organic-2D heterojunction research.

#### 5.2.5. Spin Degree of Freedom

Studies of magnetically ordered 2D materials is accelerating,<sup>378</sup> although there has been comparatively little work on the interactions of 2D materials with molecular spins in heterojunctions. Molecules provide a diversity of spin states and magnetic phases that are tunable during synthesis and through their interactions with the environment. This tunability and reconfigurability enable unique capabilities and introduce new physical possibilities for organic-2D heterojunctions that are not possible in conventional 2D-2D heterojunctions. Organic or metal-organic paramagnets on thin metal films are promising model systems for identifying opportunities for on-surface magnetochemistry.<sup>160</sup> The spin configuration of metal complexes on surfaces is dependent on the metal-surface distance,<sup>379</sup> and modification of this configuration can be achieved through axial coordination of ligands.<sup>380</sup> For example, FePc on Au(111) can transition from high spin to low spin via coordination of H atoms.<sup>381</sup> These spin changes can also alter electrical

transport in metal films through the Kondo effect.<sup>382</sup> The Kondo effect has also been observed for H<sub>2</sub>Pc on Ag despite the diamagnetic molecular ground state since electron donation from Ag creates a sufficiently large spin on H<sub>2</sub>Pc.<sup>383</sup>

Changes to molecular spin configuration induced by surface interactions have been observed in organic-2D heterojunctions. Representative examples include spin crossover in MPc molecules hybridized with graphene defects (Figures 5.5a and 5.5b)<sup>384,385</sup> in addition to measurable transport effects from spin crossover being observed in graphene-nanoparticle heterojunctions.<sup>386</sup> Moreover, magnetoresistance in MoS<sub>2</sub> FETs can be changed with adsorbed free radicals, including

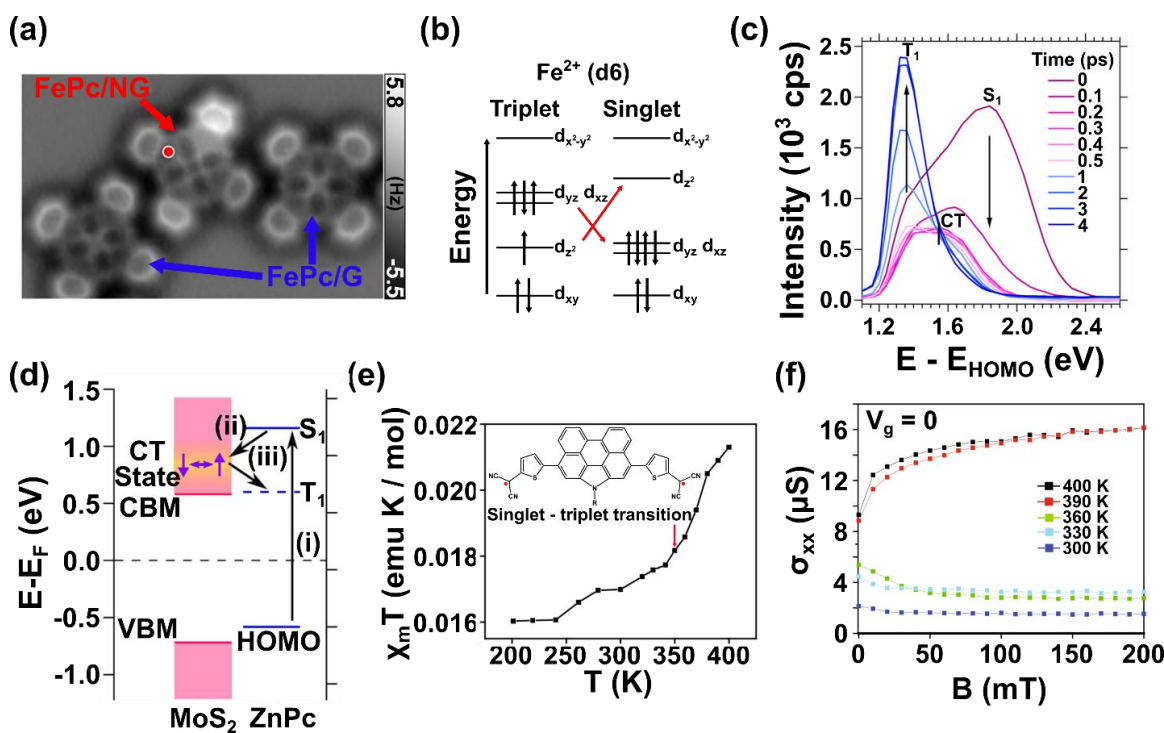


Figure 5.5 (a) Constant height AFM images of FePc molecules on nitrogen-doped graphene show a change in electron density in the FePc adsorbed above an N-dopant, corresponding to triplet FePc on graphene and singlet FePc above the dopant. (b) Proposed change in electronic

structure of  $\text{Fe}^{2+}$  d-orbitals when adsorbed on an N-dopant. On graphene, the  $d_{yz}$ ,  $d_{xz}$ , and  $d_z^2$  orbitals are not strongly split and form a high-spin triplet ground state. Repulsion from the N-dopant results in a higher energy  $d_z^2$  orbital and a low-spin singlet ground state. (c) Two-photon photoemission spectra at selected delay times in a ZnPc-MoS<sub>2</sub> heterostructure. Upon photoexcitation, the emission evolves through three states as depicted in (d). Upon photoexcitation of ZnPc (i), charge transfer occurs (ii), followed by back electron transfer to the ZnPc triplet state (iii). (e) Structure of quinoidal dithienyl perylenequinodimethane (QDTP) and SQUID measurements showing a spin transition around 360 K as QDTP switches from a singlet to a triplet state. (f) Temperature-dependent magnetoconductivity of a QDTP-MoS<sub>2</sub> heterojunction. A clear transition from negative to positive magnetoconductivity is observed as the QDTP switches from a singlet to a triplet spin state. (a) and (b) reprinted from <sup>385</sup>. Copyright 2018 The Authors, Springer Nature under a CC-BY license. (c) and (d) reprinted with permission from <sup>285</sup>. Copyright 2017 American Chemical Society. (e) and (f) reprinted from <sup>387</sup>. Copyright 2017 The Authors, Springer Nature, under a CC-BY license.

dynamic change in response to temperature (Figures 5.5c and 5.5d).<sup>387</sup> Spin crossover will likely see continued interest as a means of dynamically altering the properties of organic-2D heterojunctions, either by modulating magnetoresistance or in combination with other properties discussed below.

Other thin-film magnetic effects may also be induced by organic adsorbates. For example, Kondo scattering and Ruderman–Kittel–Kasuya–Yosida (RKKY) interactions are enabled by hybridization of spins with a 2D band. Specifically, Kondo scattering has been observed in gated MoS<sub>2</sub> due to unpaired spins at defects.<sup>388</sup> The tunability of both orbital energetics and symmetry will be critical in designing molecules for these applications. Experiments with magnetically ordered 2D metal halides or superconducting 2D materials are also an area of significant promise. In particular, hydrazine adsorbed on superconducting NbSe<sub>2</sub> has been shown to induce coexisting ferromagnetic and superconducting phases.<sup>389</sup> While research on these magnetic and

superconducting heterojunctions remains in an exploratory phase, the growing number of 2D materials in this family will accelerate progress along these lines.

The valley physics of TMDs also present opportunities for integration with organic molecular spins. Since small magnetic fields from ferromagnetic materials in a heterojunction with WSe<sub>2</sub> or MoS<sub>2</sub> are known to greatly influence valley polarization,<sup>390,391</sup> ferromagnetic organic adlayers are expected to display similar effects. Another application that may leverage the unique properties of organic molecules is adsorbate-mediated intervalley spin-flip scattering.<sup>392,393</sup> An organic paramagnet with unpaired spins of appropriate symmetry and energy could participate in this type of process. By pumping a TMD with circularly polarized light, it should be possible to orient the spins of organic molecules by creating unequal rates of spin-flip scattering. In this manner, the spin orientation of the organic layer can be optically aligned, potentially inducing magnetic ordering in molecules that were previously disordered.

Even for diamagnetic molecules, spin can play a role in organic-2D heterojunctions. Due to its large spin-orbit coupling, MoS<sub>2</sub> facilitates singlet-to-triplet transitions in ZnPc by back electron transfer as shown in Figures 5.5e and 5.5f.<sup>285</sup> Since this process of back electron transfer may allow populating triplet states in molecules that may otherwise have slow intersystem crossing, MoS<sub>2</sub> and other high spin-orbit TMDs are attractive sensitizers for solid-state triplet upconversion.<sup>394</sup> A diphenylanthracene-TMD heterojunction is a promising candidate for this process, although any upconversion experiment will require care in understanding the thickness and orientation dependent energy level alignment. Large spin-orbit coupling in the organic layer is another interesting and tunable parameter, potentially enabling bright phosphorescence or spin-valley split

hybridization in organic-2D heterojunctions. A library of phosphorescent metal complexes that have been developed for organic light emitting diodes may be especially useful for this application.

Exciton recombination is also influenced by spin. Excitons can be classified as bright or dark depending on whether their radiative recombination is spin-forbidden. In cases of large spin-orbit coupling, these bright and dark excitons have different energies. In particular, tungsten-based TMDs have dark excitons that are lower in energy and thus have limited PLQY.<sup>395</sup> Nevertheless, the dark excitons can still undergo energy transfer,<sup>396</sup> providing one route for interaction with organics. Furthermore, they can be brightened by external magnetic fields,<sup>397</sup> which could be achieved with organic ferromagnets. Dark-to-bright exciton interconversion by adsorbate scattering has also been shown in carbon nanotubes (CNTs).<sup>398</sup> With greater control over excited state decay pathways, it is likely that molecular adsorbates can be designed to amplify dark-to-bright scattering in organic-2D heterojunctions.

#### 5.2.6. Chirality Effects

Despite many potential applications, chirality is an underexplored degree of freedom in organic-2D heterojunctions. Early work in this direction includes the liquid phase exfoliation of MoS<sub>2</sub> in the presence of chiral molecules that has been shown to induce a chiral buckling in the resulting nanoplatelets that leads to measurable circular dichroism (Figures 5.6a and 5.6b).<sup>399</sup> Chiral buckling has also been observed in graphene quantum dots and results in chirality-dependent cytotoxicity,<sup>400</sup> which suggests that chiral functionalization of 2D materials may be a fruitful area of research for biomedical applications. In addition, chiral-functionalized MoS<sub>2</sub> and WS<sub>2</sub> show enantioselectivity in certain chemical reactions.<sup>401</sup> Achiral molecules may also exhibit

chirality when they are confined to a 2D surface,<sup>402</sup> allowing them to seed chiral supramolecular structure growth such as covalent organic frameworks.<sup>403</sup> The ability to seed larger scale chirality has potential uses in optics and enantioselective catalysis.

The link between spin and chirality, through the chiral-induced spin selectivity (CISS) effect, has yet to be explored the context of organic-2D heterojunctions. This effect is known to promote spin-dependent tunneling probabilities through chiral molecules, as well as spin-selective polarization of chiral molecules adsorbed on ferromagnetic surfaces.<sup>404</sup> The latter effect has been shown to result in chirality-dependent magnetic orientation in thin-film heterojunctions consisting of chiral molecules, metals, and ferromagnetic materials (Figure 5.6c-e).<sup>405</sup> Since spin-chirality linkage is surface sensitive, magnetic 2D materials are prime candidates for exploring thin-film

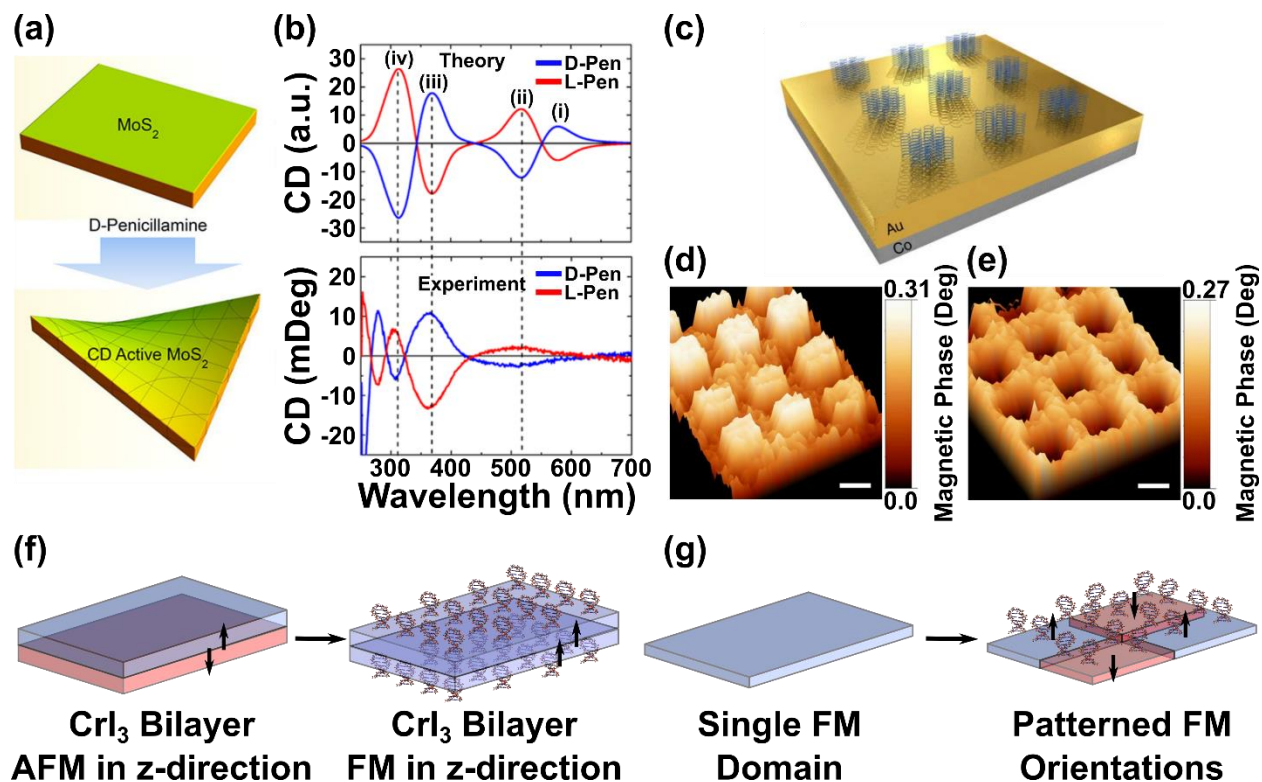


Figure 5.6 (a) Liquid phase exfoliation of MoS<sub>2</sub> in the presence of chiral penicillamine induces chiral bending in the resulting nanoplatelets. (b) Circular dichroism spectra of these platelets shows that the bent nanoplatelets are optically active and oppositely polarized for the D- and L-enantiomers. (c) Schematic of patterned chiral  $\alpha$ -helix polyaniline molecules (AHPA-L and AHPA-D) on a ferromagnetic thin film, separated by a conductive gold layer. (d,e) Magnetic force microscopy (MFM) of patterned AHPA-L and AHPA-D, respectively, show opposite magnetization orientation of the Co thin film induced by the chiral molecule. (f,g) Schematic proposals to use chirality to manipulate magnetically ordered 2D materials. (f) CrI<sub>3</sub> bilayers are known to be antiferromagnetically (AFM) oriented in the z-direction. By coating both sides of a CrI<sub>3</sub> bilayer with a conductive layer of molecules of the same chirality in a manner similar to (c), it may be possible to induce a ferromagnetic (FM) phase transition. (g) A ferromagnetic monolayer is patterned with a conductive layer and domains of opposite chirality. (a) and (b) reprinted with permission from <sup>399</sup>. Copyright 2018 American Chemical Society. (c), (d), and (e) reprinted from <sup>405</sup>. Copyright 2017 American Chemical Society.

CISS. Demonstrations of this effect could include changing the out-of-plane magnetic ordering of bilayer CrI<sub>3</sub> from antiferromagnetic to ferromagnetic by coating both sides with molecules of the same chirality (Figure 5.6f) or patterning domains of different chirality on a ferromagnetic

monolayer to create domains of opposite spin orientation (Figure 5.6g). Furthermore, these effects might be dynamically controlled by altering the chirality of the adsorbate (e.g., by using the B-Z transition of DNA). The deposition of chiral molecules onto valleytronic 2D materials may also be a fruitful research direction. Moreover, there is evidence that chiral molecules can alter the superconducting symmetry of Nb films from s-wave to p-wave or d-wave.<sup>406</sup> Since the previous section noted that organic-2D superconductor interfaces have already shown interesting effects, chiral paramagnets on NbSe<sub>2</sub> or FeSe are likely to display rich physical phenomena.

#### 5.2.7. Summary of Future Directions

This perspective has focused on many underexplored areas of molecular tunability in organic-2D heterojunctions including hybridization and electrostatics, molecular orientation and thin-film morphology, non-frontier orbitals and defects, excitonic states, spin, and chirality. All of these phenomena can be further tuned and enhanced through structural and/or electronic reconfigurability, which is a rapidly growing field in mixed-dimensional heterojunctions.<sup>237,259,260</sup> Since many organic molecules can be driven to undergo conformation changes (e.g., photoisomerization), nearly every molecular feature that was discussed in this Perspective offers the potential to be dynamically altered. Consequently, organic-2D heterojunctions are likely to be of high interest to application areas that rely on reconfigurability such as non-volatile memory,<sup>108</sup> neuromorphic computing,<sup>407</sup> and quantum information sciences.<sup>408</sup>

While the fundamental understanding of charge transfer and doping in organic-2D heterojunctions is maturing, there are areas where deeper investigation is needed. Specific examples include the role and potential uses of hybridization, rules for vdW templating of organic

morphology, and the chemistry of defects. Furthermore, other aspects of organic-2D heterojunctions are at a more nascent stage such as manipulating higher order excitonic states, spin, and chirality to realize new physics and chemistry. Overall, organic adlayers in mixed-dimensional heterostructures must be understood at a level beyond HOMO and LUMO energetics, and molecular properties should not be considered in isolation from the 2D material. While this reality increases the complexity of designing organic-2D heterojunctions, it also implies a richness that has only begun to be harnessed.

\*Chapter 5.2 adapted with permission from <sup>262</sup>. Copyright 2021 American Chemical Society.

## 6. References

- (1) Novoselov, K. S.; Geim, A. K.; Morozov, S. V.; Jiang, D.; Katsnelson, M. I.; Grigorieva, I. V.; Dubonos, S. V.; Firsov, A. A. Two-Dimensional Gas of Massless Dirac Fermions in Graphene. *Nature* **2005**, *438* (7065), 197–200. <https://doi.org/10.1038/nature04233>.
- (2) Novoselov, K. S.; Geim, A. K.; Morozov, S. V.; Jiang, D.; Zhang, Y.; Dubonos, S. V.; Grigorieva, I. V.; Firsov, A. A. Electric Field Effect in Atomically Thin Carbon Films. *Science* (80-. ). **2004**, *306* (5696).
- (3) Mannix, A. J.; Zhou, X. F.; Kiraly, B.; Wood, J. D.; Alducin, D.; Myers, B. D.; Liu, X.; Fisher, B. L.; Santiago, U.; Guest, J. R.; et al. Synthesis of Borophenes: Anisotropic, Two-Dimensional Boron Polymorphs. *Science* (80-. ). **2015**, *350* (6267), 1513–1516. <https://doi.org/10.1126/science.aad1080>.
- (4) Al Balushi, Z. Y.; Wang, K.; Ghosh, R. K.; Vilá, R. A.; Eichfeld, S. M.; Caldwell, J. D.; Qin, X.; Lin, Y. C.; Desario, P. A.; Stone, G.; et al. Two-Dimensional Gallium Nitride Realized via Graphene Encapsulation. *Nat. Mater.* **2016**, *15* (11), 1166–1171. <https://doi.org/10.1038/nmat4742>.
- (5) Sarkar, A. S.; Stratakis, E. Recent Advances in 2D Metal Monochalcogenides. *Adv. Sci.* **2020**, *7* (21), 2001655. <https://doi.org/10.1002/advs.202001655>.
- (6) Manzeli, S.; Ovchinnikov, D.; Pasquier, D.; Yazyev, O. V.; Kis, A. 2D Transition Metal Dichalcogenides. *Nature Reviews Materials*. Nature Publishing Group June 13, 2017, pp 1–15. <https://doi.org/10.1038/natrevmats.2017.33>.
- (7) Chen, Q.; Ding, Q.; Wang, Y.; Xu, Y.; Wang, J. Electronic and Magnetic Properties of a Two-Dimensional Transition Metal Phosphorous Chalcogenide TMPS4. *J. Phys. Chem. C* **2020**, *124* (22), 12075–12080. <https://doi.org/10.1021/acs.jpcc.0c02432>.
- (8) Kumbhakar, P.; Chowde Gowda, C.; Mahapatra, P. L.; Mukherjee, M.; Malviya, K. D.; Chaker, M.; Chandra, A.; Lahiri, B.; Ajayan, P. M.; Jariwala, D.; et al. Emerging 2D Metal Oxides and Their Applications. *Mater. Today* **2021**.

<https://doi.org/10.1016/j.mattod.2020.11.023>.

- (9) Och, M.; Martin, M.-B.; Dlubak, B.; Seneor, P.; Mattevi, C. Synthesis of Emerging 2D Layered Magnetic Materials. *Nanoscale* **2021**. <https://doi.org/10.1039/D0NR07867K>.
- (10) Chaudhari, N. K.; Jin, H.; Kim, B.; San Baek, D.; Joo, S. H.; Lee, K. MXene: An Emerging Two-Dimensional Material for Future Energy Conversion and Storage Applications. *Journal of Materials Chemistry A*. Royal Society of Chemistry December 5, 2017, pp 24564–24579. <https://doi.org/10.1039/c7ta09094c>.
- (11) Liu, H.; Du, Y.; Deng, Y.; Ye, P. D. Semiconducting Black Phosphorus: Synthesis, Transport Properties and Electronic Applications. *Chemical Society Reviews*. Royal Society of Chemistry May 7, 2015, pp 2732–2743. <https://doi.org/10.1039/c4cs00257a>.
- (12) Mannix, A. J.; Kiraly, B.; Hersam, M. C.; Guisinger, N. P. Synthesis and Chemistry of Elemental 2D Materials. *Nature Reviews Chemistry*. Nature Publishing Group January 11, 2017, pp 1–14. <https://doi.org/10.1038/s41570-016-0014>.
- (13) M. V., V.; Nageswaran, G. Review—2D Layered Metal Organic Framework Nanosheets as an Emerging Platform for Electrochemical Sensing. *J. Electrochem. Soc.* **2020**, *167* (13), 136502. <https://doi.org/10.1149/1945-7111/abb4f5>.
- (14) Li, X.; Yadav, P.; Loh, K. P. Function-Oriented Synthesis of Two-Dimensional (2D) Covalent Organic Frameworks—from 3D Solids to 2D Sheets. *Chemical Society Reviews*. Royal Society of Chemistry July 21, 2020, pp 4835–4866. <https://doi.org/10.1039/d0cs00236d>.
- (15) Grancini, G.; Nazeeruddin, M. K. Dimensional Tailoring of Hybrid Perovskites for Photovoltaics. *Nature Reviews Materials*. Nature Publishing Group January 1, 2019, pp 4–22. <https://doi.org/10.1038/s41578-018-0065-0>.
- (16) Castellanos-Gomez, A. Why All the Fuss about 2D Semiconductors? *Nat Phot.* **2016**, *10* (4), 202–204.
- (17) Novoselov, K. S.; Fal'ko, V. I.; Colombo, L.; Gellert, P. R.; Schwab, M. G.; Kim, K. A Roadmap for Graphene. *Nature* **2012**, *490* (7419), 192–200.
- (18) Jain, A.; Bharadwaj, P.; Heeg, S.; Parzefall, M.; Taniguchi, T.; Watanabe, K.; Novotny, L. Minimizing Residues and Strain in 2D Materials Transferred from PDMS. *Nanotechnology* **2018**, *29* (26), 265203. <https://doi.org/10.1088/1361-6528/aabd90>.
- (19) Huang, Y.; Pan, Y. H.; Yang, R.; Bao, L. H.; Meng, L.; Luo, H. L.; Cai, Y. Q.; Liu, G. D.; Zhao, W. J.; Zhou, Z.; et al. Universal Mechanical Exfoliation of Large-Area 2D Crystals. *Nat. Commun.* **2020**, *11* (1), 1–9. <https://doi.org/10.1038/s41467-020-16266-w>.
- (20) Gao, E.; Lin, S. Z.; Qin, Z.; Buehler, M. J.; Feng, X. Q.; Xu, Z. Mechanical Exfoliation of

- Two-Dimensional Materials. *J. Mech. Phys. Solids* **2018**, *115*, 248–262.  
<https://doi.org/10.1016/j.jmps.2018.03.014>.
- (21) Onodera, M.; Masubuchi, S.; Moriya, R.; MacHida, T. Assembly of van Der Waals Heterostructures: Exfoliation, Searching, and Stacking of 2D Materials. *Japanese Journal of Applied Physics*. Institute of Physics Publishing January 1, 2020, p 010101.  
<https://doi.org/10.7567/1347-4065/ab5ee0>.
- (22) Liu, X.; Gu, J.; Ding, K.; Fan, D.; Hu, X.; Tseng, Y.-W.; Lee, Y.-H.; Menon, V.; Forrest, S. R. Photoresponse of an Organic Semiconductor/Two-Dimensional Transition Metal Dichalcogenide Heterojunction. *Nano Lett.* **2017**, *17* (5), 3176–3181.  
<https://doi.org/10.1021/acs.nanolett.7b00695>.
- (23) Durand, C.; Zhang, X.; Fowlkes, J.; Najmaei, S.; Lou, J.; Li, A.-P. Defect-Mediated Transport and Electronic Irradiation Effect in Individual Domains of CVD-Grown Monolayer MoS<sub>2</sub>. *J. Vac. Sci. Technol. B, Nanotechnol. Microelectron. Mater. Process. Meas. Phenom.* **2015**, *33* (2), 02B110. <https://doi.org/10.1116/1.4906331>.
- (24) Muñoz, R.; Gómez-Aleixandre, C. Review of CVD Synthesis of Graphene. *Chem. Vap. Depos.* **2013**, *19* (10-11-12), 297–322. <https://doi.org/10.1002/cvde.201300051>.
- (25) Zhang, K.; Feng, Y.; Wang, F.; Yang, Z.; Wang, J. Two Dimensional Hexagonal Boron Nitride (2D-HBN): Synthesis, Properties and Applications. *Journal of Materials Chemistry C*. Royal Society of Chemistry November 30, 2017, pp 11992–12022.  
<https://doi.org/10.1039/c7tc04300g>.
- (26) Zhang, Y.; Yao, Y.; Sendeku, M. G.; Yin, L.; Zhan, X.; Wang, F.; Wang, Z.; He, J. Recent Progress in CVD Growth of 2D Transition Metal Dichalcogenides and Related Heterostructures. *Adv. Mater.* **2019**, *31* (41), 1901694.  
<https://doi.org/10.1002/adma.201901694>.
- (27) Kang, J.; Sangwan, V. K.; Wood, J. D.; Hersam, M. C. Solution-Based Processing of Monodisperse Two-Dimensional Nanomaterials. *Acc. Chem. Res.* **2017**, *50* (4), 943–951.  
<https://doi.org/10.1021/acs.accounts.6b00643>.
- (28) Kang, J.; Wells, S. A.; Sangwan, V. K.; Lam, D.; Liu, X.; Luxa, J.; Sofer, Z.; Hersam, M. C. Solution-Based Processing of Optoelectronically Active Indium Selenide. *Adv. Mater.* **2018**, *30* (38), 1802990. <https://doi.org/10.1002/adma.201802990>.
- (29) Biccari, S.; Barwich, S.; Boland, D.; Harvey, A.; Hanlon, D.; McEvoy, N.; Coleman, J. N. Exfoliation of 2D Materials by High Shear Mixing. *2D Mater.* **2019**, *6* (1), 015008.  
<https://doi.org/10.1088/2053-1583/aae7e3>.
- (30) Bellani, S.; Petroni, E.; Del Rio Castillo, A. E.; Curreli, N.; Martín-García, B.; Oropesa-Nuñez, R.; Prato, M.; Bonaccorso, F. Scalable Production of Graphene Inks via Wet-Jet

- Milling Exfoliation for Screen-Printed Micro-Supercapacitors. *Adv. Funct. Mater.* **2019**, *29* (14), 1807659. <https://doi.org/10.1002/adfm.201807659>.
- (31) Eda, G.; Yamaguchi, H.; Voiry, D.; Fujita, T.; Chen, M.; Chhowalla, M. Photoluminescence from Chemically Exfoliated MoS<sub>2</sub>. *Nano Lett.* **2011**, *11* (12), 5111–5116. <https://doi.org/10.1021/nl201874w>.
- (32) Liu, N.; Kim, P.; Kim, J. H.; Ye, J. H.; Kim, S.; Lee, C. J. Large-Area Atomically Thin MoS<sub>2</sub> Nanosheets Prepared Using Electrochemical Exfoliation. *ACS Nano* **2014**, *8* (7), 6902–6910. <https://doi.org/10.1021/nm5016242>.
- (33) Secor, E. B.; Hersam, M. C. Emerging Carbon and Post-Carbon Nanomaterial Inks for Printed Electronics. *J. Phys. Chem. Lett.* **2015**, *6* (4), 620–626. <https://doi.org/10.1021/jz502431r>.
- (34) Torrisi, F.; Coleman, J. N. Electrifying Inks with 2D Materials. *Nat. Nanotechnol.* **2014**, *9* (10), 738–739. <https://doi.org/10.1038/nnano.2014.218>.
- (35) Chen, K. S.; Balla, I.; Luu, N. S.; Hersam, M. C. Emerging Opportunities for Two-Dimensional Materials in Lithium-Ion Batteries. *ACS Energy Letters*. American Chemical Society September 8, 2017, pp 2026–2034. <https://doi.org/10.1021/acsenerylett.7b00476>.
- (36) Cai, X.; Luo, Y.; Liu, B.; Cheng, H. M. Preparation of 2D Material Dispersions and Their Applications. *Chemical Society Reviews*. Royal Society of Chemistry August 21, 2018, pp 6224–6266. <https://doi.org/10.1039/c8cs00254a>.
- (37) Wilson, J. A.; Yoffe, A. D. The Transition Metal Dichalcogenides Discussion and Interpretation of the Observed Optical, Electrical and Structural Properties. *Adv. Phys.* **1969**, *18* (73), 193–335. <https://doi.org/10.1080/00018736900101307>.
- (38) Voiry, D.; Mohite, A.; Chhowalla, M. Phase Engineering of Transition Metal Dichalcogenides. *Chemical Society Reviews*. Royal Society of Chemistry May 7, 2015, pp 2702–2712. <https://doi.org/10.1039/c5cs00151j>.
- (39) Staley, N. E.; Wu, J.; Eklund, P.; Liu, Y.; Li, L.; Xu, Z. Electric Field Effect on Superconductivity in Atomically Thin Flakes of NbSe<sub>2</sub>. *Phys. Rev. B - Condens. Matter Mater. Phys.* **2009**, *80* (18), 184505. <https://doi.org/10.1103/PhysRevB.80.184505>.
- (40) Ma, Y.; Kou, L.; Li, X.; Dai, Y.; Smith, S. C.; Heine, T. Quantum Spin Hall Effect and Topological Phase Transition in Two-Dimensional Square Transition-Metal Dichalcogenides. *Phys. Rev. B - Condens. Matter Mater. Phys.* **2015**, *92* (8), 085427. <https://doi.org/10.1103/PhysRevB.92.085427>.
- (41) Mak, K. F.; Lee, C.; Hone, J.; Shan, J.; Heinz, T. F. Atomically Thin MoS<sub>2</sub>: A New Direct-Gap Semiconductor. *Phys. Rev. Lett.* **2010**, *105* (13), 136805. <https://doi.org/10.1103/PhysRevLett.105.136805>.

- (42) Schönfeld, B.; Huang, J. J.; Moss, S. C. Anisotropic Mean-square Displacements (MSD) in Single-crystals of 2H- and 3R-MoS<sub>2</sub>. *Acta Crystallogr. Sect. B* **1983**, *39* (4), 404–407. <https://doi.org/10.1107/S0108768183002645>.
- (43) Wang, H. W.; Skeldon, P.; Thompson, G. E.; Wood, G. C. Synthesis and Characterization of Molybdenum Disulphide Formed from Ammonium Tetrathiomolybdate. *J. Mater. Sci.* **1997**, *32* (2), 497–502. <https://doi.org/10.1023/A:1018538424373>.
- (44) Jiang, T.; Liu, H.; Huang, D.; Zhang, S.; Li, Y.; Gong, X.; Shen, Y. R.; Liu, W. T.; Wu, S. Valley and Band Structure Engineering of Folded MoS<sub>2</sub> Bilayers. *Nat. Nanotechnol.* **2014**, *9* (10), 825–829. <https://doi.org/10.1038/nnano.2014.176>.
- (45) Shi, J.; Yu, P.; Liu, F.; He, P.; Wang, R.; Qin, L.; Zhou, J.; Li, X.; Zhou, J.; Sui, X.; et al. 3R MoS<sub>2</sub> with Broken Inversion Symmetry: A Promising Ultrathin Nonlinear Optical Device. *Adv. Mater.* **2017**, *29* (30), 1701486. <https://doi.org/10.1002/adma.201701486>.
- (46) Enyashin, A. N.; Seifert, G. Density-Functional Study of Li<sub>x</sub>MoS<sub>2</sub> Intercalates (0 ≤ x ≤ 1). *Comput. Theor. Chem.* **2012**, *999*, 13–20. <https://doi.org/10.1016/j.comptc.2012.08.005>.
- (47) Tsai, H. L.; Heising, J.; Schindler, J. L.; Kannewurf, C. R.; Kanatzidis, M. G. Exfoliated-Restacked Phase of WS<sub>2</sub>. *Chem. Mater.* **1997**, *9* (4), 879–882. <https://doi.org/10.1021/cm960579t>.
- (48) Voiry, D.; Salehi, M.; Silva, R.; Fujita, T.; Chen, M.; Asefa, T.; Shenoy, V. B.; Eda, G.; Chhowalla, M. Conducting MoS<sub>2</sub> Nanosheets as Catalysts for Hydrogen Evolution Reaction. *Nano Lett.* **2013**, *13* (12), 6222–6227. <https://doi.org/10.1021/nl403661s>.
- (49) Bissessur, R.; Kanatzidis, M. G.; Schindler, J. L.; Kannewurf, C. R. Encapsulation of Polymers into MoS<sub>2</sub> and Metal to Insulator Transition in Metastable MoS<sub>2</sub>. *J. Chem. Soc. Chem. Commun.* **1993**, No. 20, 1582–1585. <https://doi.org/10.1039/C39930001582>.
- (50) Acerce, M.; Voiry, D.; Chhowalla, M. Metallic 1T Phase MoS<sub>2</sub> Nanosheets as Supercapacitor Electrode Materials. *Nat. Nanotechnol.* **2015**, *10* (4), 313–318. <https://doi.org/10.1038/nnano.2015.40>.
- (51) Padilha, J. E.; Peelaers, H.; Janotti, A.; Van De Walle, C. G. Nature and Evolution of the Band-Edge States in MoS<sub>2</sub>: From Monolayer to Bulk. *Phys. Rev. B - Condens. Matter Mater. Phys.* **2014**, *90* (20). <https://doi.org/10.1103/PhysRevB.90.205420>.
- (52) Chang, C.-H.; Fan, X.; Lin, S.-H.; Kuo, J.-L. Orbital Analysis of Electronic Structure and Phonon Dispersion in MoS<sub>2</sub>, MoSe<sub>2</sub>, WS<sub>2</sub>, and WSe<sub>2</sub> Monolayers under Strain. *Phys. Rev. B* **2013**, *88* (19), 195420. <https://doi.org/10.1103/PhysRevB.88.195420>.
- (53) Xiao, D.; Liu, G. Bin; Feng, W.; Xu, X.; Yao, W. Coupled Spin and Valley Physics in Monolayers of MoS<sub>2</sub> and Other Group-VI Dichalcogenides. *Phys. Rev. Lett.* **2012**, *108* (19), 196802. <https://doi.org/10.1103/PhysRevLett.108.196802>.

- (54) Cao, T.; Wang, G.; Han, W.; Ye, H.; Zhu, C.; Shi, J.; Niu, Q.; Tan, P.; Wang, E.; Liu, B.; et al. Valley-Selective Circular Dichroism of Monolayer Molybdenum Disulfide. *Nat. Commun.* **2012**, *3*, 887. <https://doi.org/10.1038/ncomms1882>.
- (55) Zeng, H.; Dai, J.; Yao, W.; Xiao, D.; Cui, X. Valley Polarization in MoS<sub>2</sub> Monolayers by Optical Pumping. *Nat. Nanotechnol.* **2012**, *7* (8), 490–493. <https://doi.org/10.1038/nnano.2012.95>.
- (56) Mak, K. F.; He, K.; Shan, J.; Heinz, T. F. Control of Valley Polarization in Monolayer MoS<sub>2</sub> by Optical Helicity. *Nat. Nanotechnol.* **2012**, *7* (8), 494–498. <https://doi.org/10.1038/nnano.2012.96>.
- (57) Mak, K. F.; Xiao, D.; Shan, J. Light–Valley Interactions in 2D Semiconductors. *Nature Photonics*. Nature Publishing Group August 1, 2018, pp 451–460. <https://doi.org/10.1038/s41566-018-0204-6>.
- (58) Schaibley, J. R.; Yu, H.; Clark, G.; Rivera, P.; Ross, J. S.; Seyler, K. L.; Yao, W.; Xu, X.; Rycerz, A.; Tworzydło, J.; et al. Valleytronics in 2D Materials. *Nat. Rev. Mater.* **2016**, *1* (11). <https://doi.org/10.1038/natrevmats.2016.55>.
- (59) Haldar, S.; Vovusha, H.; Yadav, M. K.; Eriksson, O.; Sanyal, B. Systematic Study of Structural, Electronic, and Optical Properties of Atomic-Scale Defects in the Two-Dimensional Transition Metal Dichalcogenides MX<sub>2</sub> (M = Mo, W; X = S, Se, Te). *Phys. Rev. B* **2015**, *92* (23), 235408. <https://doi.org/10.1103/PhysRevB.92.235408>.
- (60) Lu, H.; Kummel, A.; Robertson, J. Passivating the Sulfur Vacancy in Monolayer MoS<sub>2</sub>. *APL Mater.* **2018**, *6* (6), 066104. <https://doi.org/10.1063/1.5030737>.
- (61) Zhou, W.; Zou, X.; Najmaei, S.; Liu, Z.; Shi, Y.; Kong, J.; Lou, J.; Ajayan, P. M.; Yakobson, B. I.; Idrobo, J.-C. Intrinsic Structural Defects in Monolayer Molybdenum Disulfide. *Nano Lett.* **2013**, *13* (6), 2615–2622. <https://doi.org/10.1021/nl4007479>.
- (62) Barja, S.; Refaely-Abramson, S.; Schuler, B.; Qiu, D. Y.; Pulkin, A.; Wickenburg, S.; Ryu, H.; Ugeda, M. M.; Kastl, C.; Chen, C.; et al. Identifying Substitutional Oxygen as a Prolific Point Defect in Monolayer Transition Metal Dichalcogenides. *Nat. Commun.* **2019**, *10* (1), 1–8. <https://doi.org/10.1038/s41467-019-11342-2>.
- (63) Petó, J.; Ollár, T.; Vancsó, P.; Popov, Z. I.; Magda, G. Z.; Dobrik, G.; Hwang, C.; Sorokin, P. B.; Tapasztó, L. Spontaneous Doping of the Basal Plane of MoS<sub>2</sub> Single Layers through Oxygen Substitution under Ambient Conditions. *Nat. Chem.* **2018**, *10* (12), 1246–1251. <https://doi.org/10.1038/s41557-018-0136-2>.
- (64) Huang, B.; Tian, F.; Shen, Y.; Zheng, M.; Zhao, Y.; Wu, J.; Liu, Y.; Pennycook, S. J.; Thong, J. T. L. Selective Engineering of Chalcogen Defects in MoS<sub>2</sub> by Low-Energy Helium Plasma. *ACS Appl. Mater. Interfaces* **2019**, *11* (27), 24404–24411.

- <https://doi.org/10.1021/acsami.9b05507>.
- (65) Magda, G. Z.; Pető, J.; Dobrik, G.; Hwang, C.; Biró, L. P.; Tapasztó, L. Exfoliation of Large-Area Transition Metal Chalcogenide Single Layers. *Sci. Rep.* **2015**, *5* (1), 1–5. <https://doi.org/10.1038/srep14714>.
- (66) Amsterdam, S. H.; Stanev, T. K.; Zhou, Q.; Lou, A. J.-T.; Bergeron, H.; Darancet, P.; Hersam, M. C.; Stern, N. P.; Marks, T. J. Electronic Coupling in Metallophthalocyanine–Transition Metal Dichalcogenide Mixed-Dimensional Heterojunctions. *ACS Nano* **2019**, *13* (4), 4183–4190. <https://doi.org/10.1021/acs.nano.8b09166>.
- (67) Liu, H. F.; Wong, S. L.; Chi, D. Z. CVD Growth of MoS<sub>2</sub>-Based Two-Dimensional Materials. *Chem. Vap. Depos.* **2015**, *21* (10-11-12), 241–259. <https://doi.org/10.1002/cvde.201500060>.
- (68) Shastry, T. A.; Balla, I.; Bergeron, H.; Amsterdam, S. H.; Marks, T. J.; Hersam, M. C. Mutual Photoluminescence Quenching and Photovoltaic Effect in Large-Area Single-Layer MoS<sub>2</sub>–Polymer Heterojunctions. *ACS Nano* **2016**, *10* (11), 10573–10579. <https://doi.org/10.1021/acs.nano.6b06592>.
- (69) Kang, K.; Xie, S.; Huang, L.; Han, Y.; Huang, P. Y.; Mak, K. F.; Kim, C. J.; Muller, D.; Park, J. High-Mobility Three-Atom-Thick Semiconducting Films with Wafer-Scale Homogeneity. *Nature* **2015**, *520* (7549), 656–660. <https://doi.org/10.1038/nature14417>.
- (70) Wang, W.; Shu, H.; Wang, J.; Cheng, Y.; Liang, P.; Chen, X. Defect Passivation and Photoluminescence Enhancement of Monolayer MoS<sub>2</sub> Crystals through Sodium Halide-Assisted Chemical Vapor Deposition Growth. *ACS Appl. Mater. Interfaces* **2020**, *12* (8), 9563–9571. <https://doi.org/10.1021/acsami.9b19224>.
- (71) Mun, J.; Park, H.; Park, J.; Joung, D.; Lee, S.-K.; Leem, J.; Myoung, J.-M.; Park, J.; Jeong, S.-H.; Chegal, W.; et al. High-Mobility MoS<sub>2</sub> Directly Grown on Polymer Substrate with Kinetics-Controlled Metal–Organic Chemical Vapor Deposition. *ACS Appl. Electron. Mater.* **2019**, *1* (4), 608–616. <https://doi.org/10.1021/acsaelm.9b00078>.
- (72) Cwik, S.; Mitoraj, D.; Mendoza Reyes, O.; Rogalla, D.; Peeters, D.; Kim, J.; Schütz, H. M.; Bock, C.; Beranek, R.; Devi, A. Direct Growth of MoS<sub>2</sub> and WS<sub>2</sub> Layers by Metal Organic Chemical Vapor Deposition. *Adv. Mater. Interfaces* **2018**, *5* (16), 1800140. <https://doi.org/10.1002/admi.201800140>.
- (73) Tan, L. K.; Liu, B.; Teng, J. H.; Guo, S.; Low, H. Y.; Loh, K. P. Atomic Layer Deposition of a MoS<sub>2</sub> Film. *Nanoscale* **2014**, *6* (18), 10584–10588. <https://doi.org/10.1039/c4nr02451f>.
- (74) Kwack, Y. J.; Choi, W. S. Chemical Vapor Deposition-Free Solution-Processed Synthesis Method for Two-Dimensional MoS<sub>2</sub> Atomic Layer Films. *Nanotechnology* **2019**, *30* (38),

385201. <https://doi.org/10.1088/1361-6528/ab2494>.
- (75) Jawaid, A.; Nepal, D.; Park, K.; Jespersen, M.; Qualley, A.; Mirau, P.; Drummy, L. F.; Vaia, R. A. Mechanism for Liquid Phase Exfoliation of MoS<sub>2</sub>. *Chem. Mater.* **2016**, *28* (1), 337–348. <https://doi.org/10.1021/acs.chemmater.5b04224>.
- (76) Varrla, E.; Backes, C.; Paton, K. R.; Harvey, A.; Gholamvand, Z.; McCauley, J.; Coleman, J. N. Large-Scale Production of Size-Controlled MoS<sub>2</sub> Nanosheets by Shear Exfoliation. *Chem. Mater.* **2015**, *27* (3), 1129–1139. <https://doi.org/10.1021/cm5044864>.
- (77) Ben Amara, I.; Ben Salem, E.; Jaziri, S. Optoelectronic Response and Excitonic Properties of Monolayer MoS<sub>2</sub>. *J. Appl. Phys.* **2016**, *120* (5), 051707. <https://doi.org/10.1063/1.4958948>.
- (78) Molina-Sánchez, A.; Sangalli, D.; Hummer, K.; Marini, A.; Wirtz, L. Effect of Spin-Orbit Interaction on the Optical Spectra of Single-Layer, Double-Layer, and Bulk MoS<sub>2</sub>. *Phys. Rev. B - Condens. Matter Mater. Phys.* **2013**, *88* (4), 045412. <https://doi.org/10.1103/PhysRevB.88.045412>.
- (79) Bernardi, M.; Palumbo, M.; Grossman, J. C. Extraordinary Sunlight Absorption and One Nanometer Thick Photovoltaics Using Two-Dimensional Monolayer Materials. *Nano Lett.* **2013**, *13* (8), 3664–3670. <https://doi.org/10.1021/nl401544y>.
- (80) Pandey, J.; Soni, A. Unraveling Biexciton and Excitonic Excited States from Defect Bound States in Monolayer MoS<sub>2</sub>. *Appl. Surf. Sci.* **2019**, *463*, 52–57. <https://doi.org/10.1016/j.apsusc.2018.08.205>.
- (81) Goodman, A. J.; Willard, A. P.; Tisdale, W. A. Exciton Trapping Is Responsible for the Long Apparent Lifetime in Acid-Treated MoS<sub>2</sub>. *Phys. Rev. B* **2017**, *96* (12), 121404. <https://doi.org/10.1103/PhysRevB.96.121404>.
- (82) Lee, C.; Yan, H.; Brus, L. E.; Heinz, T. F.; Hone, J.; Ryu, S. Anomalous Lattice Vibrations of Single- and Few-Layer MoS<sub>2</sub>. *ACS Nano* **2010**, *4* (5), 2695–2700. <https://doi.org/10.1021/nn1003937>.
- (83) Splendiani, A.; Sun, L.; Zhang, Y.; Li, T.; Kim, J.; Chim, C.-Y.; Galli, G.; Wang, F. Emerging Photoluminescence in Monolayer MoS<sub>2</sub>. *Nano Lett.* **2010**, *10* (4), 1271–1275. <https://doi.org/10.1021/nl903868w>.
- (84) Amani, M.; Taheri, P.; Addou, R.; Ahn, G. H.; Kiriya, D.; Lien, D. H.; Ager, J. W.; Wallace, R. M.; Javey, A. Recombination Kinetics and Effects of Superacid Treatment in Sulfur- and Selenium-Based Transition Metal Dichalcogenides. *Nano Lett.* **2016**, *16* (4), 2786–2791. <https://doi.org/10.1021/acs.nanolett.6b00536>.
- (85) Chernikov, A.; Berkelbach, T. C.; Hill, H. M.; Rigosi, A.; Li, Y.; Aslan, O. B.; Reichman, D. R.; Hybertsen, M. S.; Heinz, T. F. Exciton Binding Energy and Nonhydrogenic

- Rydberg Series in Monolayer WS<sub>2</sub>. *Phys. Rev. Lett.* **2014**, *113* (7), 076802.  
<https://doi.org/10.1103/PhysRevLett.113.076802>.
- (86) Mak, K. F.; He, K.; Lee, C.; Lee, G. H.; Hone, J.; Heinz, T. F.; Shan, J. Tightly Bound Trions in Monolayer MoS<sub>2</sub>. *Nat. Mater.* **2012**, *12* (3), 207–211.  
<https://doi.org/10.1038/nmat3505>.
- (87) Lee, H. S.; Kim, M. S.; Kim, H.; Lee, Y. H. Identifying Multiexcitons in MoS<sub>2</sub> Monolayers at Room Temperature. *Phys. Rev. B* **2016**, *93* (14), 140409.  
<https://doi.org/10.1103/PhysRevB.93.140409>.
- (88) Pradeepa, H. L.; Mondal, P.; Bid, A.; Basu, J. K. Electrical and Chemical Tuning of Exciton Lifetime in Monolayer MoS<sub>2</sub> for Field-Effect Transistors. *ACS Appl. Nano Mater.* **2020**, *3* (1), 641–647. <https://doi.org/10.1021/acsanm.9b02170>.
- (89) Greben, K.; Arora, S.; Harats, M. G.; Bolotin, K. I. Intrinsic and Extrinsic Defect-Related Excitons in TMDCs. *Nano Lett.* **2020**, *20* (4), 2544–2550.  
<https://doi.org/10.1021/acs.nanolett.9b05323>.
- (90) Oh, H. M.; Jeong, H.; Han, G. H.; Kim, H.; Kim, J. H.; Lee, S. Y.; Jeong, S. Y.; Jeong, S.; Park, D. J.; Kim, K. K.; et al. Modulating Electronic Properties of Monolayer MoS<sub>2</sub> via Electron-Withdrawing Functional Groups of Graphene Oxide. *ACS Nano* **2016**, *acsnano.6b06319*. <https://doi.org/10.1021/acsnano.6b06319>.
- (91) Ghimire, G.; Adhikari, S.; Jo, S. G.; Kim, H.; Jiang, J.; Joo, J.; Kim, J. Local Enhancement of Exciton Emission of Monolayer MoS<sub>2</sub> by Copper Phthalocyanine Nanoparticles. *J. Phys. Chem. C* **2018**, *122* (12), 6794–6800.  
<https://doi.org/10.1021/acs.jpcc.8b00092>.
- (92) Zhang, W.; Matsuda, K.; Miyauchi, Y. PH-Dependent Photoluminescence Properties of Monolayer Transition-Metal Dichalcogenides Immersed in an Aqueous Solution. *J. Phys. Chem. C* **2018**, *122* (24), 13175–13181. <https://doi.org/10.1021/acs.jpcc.8b03427>.
- (93) He, Y. M.; Iff, O.; Lundt, N.; Baumann, V.; Davanco, M.; Srinivasan, K.; Höfling, S.; Schneider, C. Cascaded Emission of Single Photons from the Biexciton in Monolayered WSe<sub>2</sub>. *Nat. Commun.* **2016**, *7* (1), 1–6. <https://doi.org/10.1038/ncomms13409>.
- (94) Wang, W.; Sui, N.; Ni, M.; Chi, X.; Pan, L.; Zhang, H.; Kang, Z.; Zhou, Q.; Wang, Y. Studying of the Biexciton Characteristics in Monolayer MoS<sub>2</sub>. *J. Phys. Chem. C* **2020**, *124* (2), 1749–1754. <https://doi.org/10.1021/acs.jpcc.9b11582>.
- (95) Pei, J.; Yang, J.; Wang, X.; Wang, F.; Mokkaapati, S.; Lü, T.; Zheng, J. C.; Qin, Q.; Neshev, D.; Tan, H. H.; et al. Excited State Biexcitons in Atomically Thin MoSe<sub>2</sub>. *ACS Nano* **2017**, *11* (7), 7468–7475. <https://doi.org/10.1021/acsnano.7b03909>.
- (96) Yu, Y.; Dang, J.; Qian, C.; Sun, S.; Peng, K.; Xie, X.; Wu, S.; Song, F.; Yang, J.; Xiao, S.;

- et al. Many-Body Effect of Mesoscopic Localized States in MoS<sub>2</sub> Monolayer. *Phys. Rev. Mater.* **2019**, 3 (5), 051001. <https://doi.org/10.1103/PhysRevMaterials.3.051001>.
- (97) Liu, X.; Balla, I.; Bergeron, H.; Campbell, G. P.; Bedzyk, M. J.; Hersam, M. C. Rotationally Commensurate Growth of MoS<sub>2</sub> on Epitaxial Graphene. *ACS Nano* **2016**, 10 (1), 1067–1075. <https://doi.org/10.1021/acsnano.5b06398>.
- (98) Radisavljevic, B.; Kis, A. Mobility Engineering and a Metal-Insulator Transition in Monolayer MoS<sub>2</sub>. *Nat. Mater.* **2013**, 12 (9), 815–820. <https://doi.org/10.1038/nmat3687>.
- (99) Novoselov, K. S.; Jiang, D.; Schedin, F.; Booth, T. J.; Khotkevich, V. V.; Morozov, S. V.; Geim, A. K. Two-Dimensional Atomic Crystals. *Proc. Natl. Acad. Sci. U. S. A.* **2005**, 102 (30), 10451–10453. <https://doi.org/10.1073/pnas.0502848102>.
- (100) Ghatak, S.; Pal, A. N.; Ghosh, A. Nature of Electronic States in Atomically Thin MoS<sub>2</sub> Field-Effect Transistors. *ACS Nano* **2011**, 5 (10), 7707–7712. <https://doi.org/10.1021/nn202852j>.
- (101) Lee, G. H.; Cui, X.; Kim, Y. D.; Arefe, G.; Zhang, X.; Lee, C. H.; Ye, F.; Watanabe, K.; Taniguchi, T.; Kim, P.; et al. Highly Stable, Dual-Gated MoS<sub>2</sub> Transistors Encapsulated by Hexagonal Boron Nitride with Gate-Controllable Contact, Resistance, and Threshold Voltage. *ACS Nano* **2015**, 9 (7), 7019–7026. <https://doi.org/10.1021/acsnano.5b01341>.
- (102) Kaasbjerg, K.; Thygesen, K. S.; Jacobsen, K. W. Phonon-Limited Mobility in n-Type Single-Layer MoS<sub>2</sub> from First Principles. *Phys. Rev. B - Condens. Matter Mater. Phys.* **2012**, 85 (11), 115317. <https://doi.org/10.1103/PhysRevB.85.115317>.
- (103) Bertolazzi, S.; Brivio, J.; Kis, A. Stretching and Breaking of Ultrathin MoS<sub>2</sub>. *ACS Nano* **2011**, 5 (12), 9703–9709. <https://doi.org/10.1021/nn203879f>.
- (104) Pu, J.; Yomogida, Y.; Liu, K. K.; Li, L. J.; Iwasa, Y.; Takenobu, T. Highly Flexible MoS<sub>2</sub> Thin-Film Transistors with Ion Gel Dielectrics. *Nano Lett.* **2012**, 12 (8), 4013–4017. <https://doi.org/10.1021/nl301335q>.
- (105) Li, J.; Naiini, M. M.; Vaziri, S.; Lemme, M. C.; Östling, M. Inkjet Printing of MoS<sub>2</sub>. *Adv. Funct. Mater.* **2014**, 24 (41), 6524–6531. <https://doi.org/10.1002/adfm.201400984>.
- (106) Britnell, L.; Gorbachev, R. V.; Jalil, R.; Belle, B. D.; Schedin, F.; Mishchenko, A.; Georgiou, T.; Katsnelson, M. I.; Eaves, L.; Morozov, S. V.; et al. Field-Effect Tunneling Transistor Based on Vertical Graphene Heterostructures. *Science (80-. )*. **2012**, 335 (6071), 947–950. <https://doi.org/10.1126/science.1218461>.
- (107) Sangwan, V. K.; Jariwala, D.; Kim, I. S.; Chen, K. S.; Marks, T. J.; Lauhon, L. J.; Hersam, M. C. Gate-Tunable Memristive Phenomena Mediated by Grain Boundaries in Single-Layer MoS<sub>2</sub>. *Nat. Nanotechnol.* **2015**, 10 (5), 403–406. <https://doi.org/10.1038/nnano.2015.56>.

- (108) Lee, H. S.; Sangwan, V. K.; Rojas, W. A. G.; Bergeron, H.; Jeong, H. Y.; Yuan, J.; Su, K.; Hersam, M. C. Dual-Gated MoS<sub>2</sub> Memtransistor Crossbar Array. *Adv. Funct. Mater.* **2020**, *30* (45), 2003683. <https://doi.org/10.1002/adfm.202003683>.
- (109) da Silveira Firmiano, E. G.; Rabelo, A. C.; Dalmaschio, C. J.; Pinheiro, A. N.; Pereira, E. C.; Schreiner, W. H.; Leite, E. R. Supercapacitor Electrodes Obtained by Directly Bonding 2D MoS<sub>2</sub> on Reduced Graphene Oxide. *Adv. Energy Mater.* **2014**, *4* (6), 1301380. <https://doi.org/10.1002/aenm.201301380>.
- (110) David, L.; Bhandavat, R.; Singh, G. MoS<sub>2</sub>/Graphene Composite Paper for Sodium-Ion Battery Electrodes. *ACS Nano* **2014**, *8* (2), 1759–1770. <https://doi.org/10.1021/nn406156b>.
- (111) Jariwala, D.; Davoyan, A. R.; Tagliabue, G.; Sherrott, M. C.; Wong, J.; Atwater, H. A. Near-Unity Absorption in van Der Waals Semiconductors for Ultrathin Optoelectronics. *Nano Lett.* **2016**, *acs.nanolett.6b01914*. <https://doi.org/10.1021/acs.nanolett.6b01914>.
- (112) Wi, S.; Kim, H.; Chen, M.; Nam, H.; Guo, L. J.; Meyhofer, E.; Liang, X. Enhancement of Photovoltaic Response in Multilayer MoS<sub>2</sub> Induced by Plasma Doping. *ACS Nano* **2014**, *8* (5), 5270–5281. <https://doi.org/10.1021/nn5013429>.
- (113) Wang, L.; Huang, L.; Tan, W. C.; Feng, X.; Chen, L.; Huang, X.; Ang, K.-W. 2D Photovoltaic Devices: Progress and Prospects. *Small Methods* **2018**, *2* (3), 1700294. <https://doi.org/10.1002/smt.201700294>.
- (114) Wang, S.; Zhang, D.; Li, B.; Zhang, C.; Du, Z.; Yin, H.; Bi, X.; Yang, S. Ultrastable In-Plane 1T-2H MoS<sub>2</sub> Heterostructures for Enhanced Hydrogen Evolution Reaction. *Adv. Energy Mater.* **2018**, *8* (25), 1801345. <https://doi.org/10.1002/aenm.201801345>.
- (115) Kakavelakis, G.; Del Rio Castillo, A. E.; Pellegrini, V.; Ansaldo, A.; Tzourmpakis, P.; Brescia, R.; Prato, M.; Stratakis, E.; Kymakis, E.; Bonaccorso, F. Size-Tuning of WSe<sub>2</sub> Flakes for High Efficiency Inverted Organic Solar Cells. *ACS Nano* **2017**, *11* (4), 3517–3531. <https://doi.org/10.1021/acsnano.7b00323>.
- (116) Nalwa, H. S. A Review of Molybdenum Disulfide (MoS<sub>2</sub>) Based Photodetectors: From Ultra-Broadband, Self-Powered to Flexible Devices. *RSC Advances*. Royal Society of Chemistry August 19, 2020, pp 30529–30602. <https://doi.org/10.1039/d0ra03183f>.
- (117) Li, Z.; Meng, X.; Zhang, Z. Recent Development on MoS<sub>2</sub>-Based Photocatalysis: A Review. *Journal of Photochemistry and Photobiology C: Photochemistry Reviews*. Elsevier B.V. June 1, 2018, pp 39–55. <https://doi.org/10.1016/j.jphotochemrev.2017.12.002>.
- (118) Ding, Q.; Song, B.; Xu, P.; Jin, S. Efficient Electrocatalytic and Photoelectrochemical Hydrogen Generation Using MoS<sub>2</sub> and Related Compounds. *Chem.* Elsevier Inc

- November 10, 2016, pp 699–726. <https://doi.org/10.1016/j.chempr.2016.10.007>.
- (119) Li, L. H.; Chen, Y. Atomically Thin Boron Nitride: Unique Properties and Applications. *Adv. Funct. Mater.* **2016**, *26* (16), 2594–2608. <https://doi.org/10.1002/adfm.201504606>.
- (120) Watanabe, K.; Taniguchi, T.; Kanda, H. Direct-Bandgap Properties and Evidence for Ultraviolet Lasing of Hexagonal Boron Nitride Single Crystal. *Nat. Mater.* **2004**, *3* (6), 404–409. <https://doi.org/10.1038/nmat1134>.
- (121) Jo, I.; Pettes, M. T.; Kim, J.; Watanabe, K.; Taniguchi, T.; Yao, Z.; Shi, L. Thermal Conductivity and Phonon Transport in Suspended Few-Layer Hexagonal Boron Nitride. *Nano Lett.* **2013**, *13* (2), 550–554. <https://doi.org/10.1021/nl304060g>.
- (122) Kim, S. M.; Hsu, A.; Park, M. H.; Chae, S. H.; Yun, S. J.; Lee, J. S.; Cho, D. H.; Fang, W.; Lee, C.; Palacios, T.; et al. Synthesis of Large-Area Multilayer Hexagonal Boron Nitride for High Material Performance. *Nat. Commun.* **2015**, *6* (1), 1–11. <https://doi.org/10.1038/ncomms9662>.
- (123) Nagashima, A.; Tejima, N.; Gamou, Y.; Kawai, T.; Oshima, C. Electronic Structure of Monolayer Hexagonal Boron Nitride Physisorbed on Metal Surfaces. *Phys. Rev. Lett.* **1995**, *75* (21), 3918–3921. <https://doi.org/10.1103/PhysRevLett.75.3918>.
- (124) Blase, X.; Rubio, A.; Louie, S. G.; Cohen, M. L. Quasiparticle Band Structure of Bulk Hexagonal Boron Nitride and Related Systems. *Phys. Rev. B* **1995**, *51* (11), 6868–6875. <https://doi.org/10.1103/PhysRevB.51.6868>.
- (125) Shi, Y.; Hamsen, C.; Jia, X.; Kim, K. K.; Reina, A.; Hofmann, M.; Hsu, A. L.; Zhang, K.; Li, H.; Juang, Z. Y.; et al. Synthesis of Few-Layer Hexagonal Boron Nitride Thin Film by Chemical Vapor Deposition. *Nano Lett.* **2010**, *10* (10), 4134–4139. <https://doi.org/10.1021/nl1023707>.
- (126) Hua Li, L.; Chen, Y.; Cheng, B. M.; Lin, M. Y.; Chou, S. L.; Peng, Y. C. Photoluminescence of Boron Nitride Nanosheets Exfoliated by Ball Milling. *Appl. Phys. Lett.* **2012**, *100* (26), 261108. <https://doi.org/10.1063/1.4731203>.
- (127) Tran, T. T.; Bray, K.; Ford, M. J.; Toth, M.; Aharonovich, I. Quantum Emission from Hexagonal Boron Nitride Monolayers. *Nat. Nanotechnol.* **2016**, *11* (1), 37–41. <https://doi.org/10.1038/nnano.2015.242>.
- (128) Gorbachev, R. V.; Riaz, I.; Nair, R. R.; Jalil, R.; Britnell, L.; Belle, B. D.; Hill, E. W.; Novoselov, K. S.; Watanabe, K.; Taniguchi, T.; et al. Hunting for Monolayer Boron Nitride: Optical and Raman Signatures. *Small* **2011**, *7* (4), 465–468. <https://doi.org/10.1002/sml.201001628>.
- (129) Geick, R.; Perry, C. H.; Rupprecht, G. Normal Modes in Hexagonal Boron Nitride. *Phys. Rev.* **1966**, *146* (2), 543–547. <https://doi.org/10.1103/PhysRev.146.543>.

- (130) Song, L.; Ci, L.; Lu, H.; Sorokin, P. B.; Jin, C.; Ni, J.; Kvashnin, A. G.; Kvashnin, D. G.; Lou, J.; Yakobson, B. I.; et al. Large Scale Growth and Characterization of Atomic Hexagonal Boron Nitride Layers. *Nano Lett.* **2010**, *10* (8), 3209–3215. <https://doi.org/10.1021/nl1022139>.
- (131) Zastrow, M. Meet the Crystal Growers Who Sparked a Revolution in Graphene Electronics. *Nature* **2019**, *572* (7770), 429–432. <https://doi.org/10.1038/d41586-019-02472-0>.
- (132) Lee, K. H.; Shin, H. J.; Lee, J.; Lee, I. Y.; Kim, G. H.; Choi, J. Y.; Kim, S. W. Large-Scale Synthesis of High-Quality Hexagonal Boron Nitride Nanosheets for Large-Area Graphene Electronics. *Nano Lett.* **2012**, *12* (2), 714–718. <https://doi.org/10.1021/nl203635v>.
- (133) Wood, G. E.; Marsden, A. J.; Mudd, J. J.; Walker, M.; Asensio, M.; Avila, J.; Chen, K.; Bell, G. R.; Wilson, N. R. Van Der Waals Epitaxy of Monolayer Hexagonal Boron Nitride on Copper Foil: Growth, Crystallography and Electronic Band Structure. *2D Mater.* **2015**, *2* (2), 025003. <https://doi.org/10.1088/2053-1583/2/2/025003>.
- (134) Dean, C. R.; Young, A. F.; Meric, I.; Lee, C.; Wang, L.; Sorgenfrei, S.; Watanabe, K.; Taniguchi, T.; Kim, P.; Shepard, K. L.; et al. Boron Nitride Substrates for High-Quality Graphene Electronics. *Nat. Nanotechnol.* **2010**, *5* (10), 722–726. <https://doi.org/10.1038/nnano.2010.172>.
- (135) Arora, H.; Jung, Y.; Venanzi, T.; Watanabe, K.; Taniguchi, T.; Hübner, R.; Schneider, H.; Helm, M.; Hone, J. C.; Erbe, A. Effective Hexagonal Boron Nitride Passivation of Few-Layered InSe and GaSe to Enhance Their Electronic and Optical Properties. *ACS Appl. Mater. Interfaces* **2019**, *11* (46), 43480–43487. <https://doi.org/10.1021/acsami.9b13442>.
- (136) Shcherbakov, D.; Stepanov, P.; Weber, D.; Wang, Y.; Hu, J.; Zhu, Y.; Watanabe, K.; Taniguchi, T.; Mao, Z.; Windl, W.; et al. Raman Spectroscopy, Photocatalytic Degradation, and Stabilization of Atomically Thin Chromium Tri-Iodide. *Nano Lett.* **2018**, *18* (7), 4214–4219. <https://doi.org/10.1021/acs.nanolett.8b01131>.
- (137) Seitz, M.; Gant, P.; Castellanos-Gomez, A.; Prins, F. Long-Term Stabilization of Two-Dimensional Perovskites by Encapsulation with Hexagonal Boron Nitride. *Nanomater.* **2019**, *Vol. 9, Page 1120* **2019**, *9* (8), 1120. <https://doi.org/10.3390/NANO9081120>.
- (138) Kratzer, M.; Matkovic, A.; Teichert, C. Adsorption and Epitaxial Growth of Small Organic Semiconductors on Hexagonal Boron Nitride. *J. Phys. D. Appl. Phys.* **2019**, *52* (38), 383001. <https://doi.org/10.1088/1361-6463/AB29CB>.
- (139) Veeralingam, S.; Durai, L.; Yadav, P.; Badhulika, S. Record-High Responsivity and Detectivity of a Flexible Deep-Ultraviolet Photodetector Based on Solid State-Assisted Synthesized HBN Nanosheets. *ACS Appl. Electron. Mater.* **2021**, *3* (3), 1162–1169.

- <https://doi.org/10.1021/acsaelm.0c01021>.
- (140) Aldalbahi, A.; Feng, P. Development of 2-D Boron Nitride Nanosheets UV Photoconductive Detectors. *IEEE Trans. Electron Devices* **2015**, *62* (6), 1885–1890. <https://doi.org/10.1109/TED.2015.2423253>.
- (141) Tran, T. T.; Elbadawi, C.; Totonjian, D.; Lobo, C. J.; Grosso, G.; Moon, H.; Englund, D. R.; Ford, M. J.; Aharonovich, I.; Toth, M. Robust Multicolor Single Photon Emission from Point Defects in Hexagonal Boron Nitride. In *2017 Conference on Lasers and Electro-Optics, CLEO 2017 - Proceedings*; Institute of Electrical and Electronics Engineers Inc., 2017; Vol. 2017-January, pp 1–2. <https://doi.org/10.1021/acsnano.6b03602>.
- (142) Löbber, G. Phthalocyanines. In *Ullmann's Encyclopedia of Industrial Chemistry*; Wiley-VCH Verlag GmbH & Co. KGaA: Weinheim, Germany, 2000. [https://doi.org/10.1002/14356007.a20\\_213](https://doi.org/10.1002/14356007.a20_213).
- (143) Erk, P.; Hengelsberg, H. *The Porphyrin Handbook Volume 19: Applications of Phthalocyanines*; Kadish, K. M., Smith, K. M., Guillard, R., Eds.; Academic Press: Amsterdam, 2003.
- (144) Gregory, P. Industrial Applications of Phthalocyanines. *J. Porphyr. Phthalocyanines* **2000**, *04* (04), 432–437. [https://doi.org/10.1002/\(sici\)1099-1409\(200006/07\)4:4<432::aid-jpp254>3.0.co;2-n](https://doi.org/10.1002/(sici)1099-1409(200006/07)4:4<432::aid-jpp254>3.0.co;2-n).
- (145) Sperl, A.; Kröger, J.; Berndt, R. Electronic Superstructure of Lead Phthalocyanine on Lead Islands. *J. Phys. Chem. A* **2011**, *115* (25), 6973–6978. <https://doi.org/10.1021/jp112169s>.
- (146) Galanin, N. E.; Yakubov, L. A.; Shaposhnikov, G. P. Synthesis and Spectral Properties of Sandwich Meso- Tetramethyltetrabenzoporphyrin-Phthalocyanine Complexes with Lutetium, Erbium, Yttrium, and Lanthanum. *Russ. J. Org. Chem.* **2008**, *44* (6), 921–926. <https://doi.org/10.1134/S1070428008060237>.
- (147) Zyskowski, C. D.; Kennedy, V. O. Compounds in the Series from Boron Subphthalocyanine to Boron Subnaphthalocyanine. *J. Porphyr. Phthalocyanines* **2000**, *4* (8), 707–712. [https://doi.org/10.1002/1099-1409\(200012\)4:8<707::AID-JPP285>3.0.CO;2-V](https://doi.org/10.1002/1099-1409(200012)4:8<707::AID-JPP285>3.0.CO;2-V).
- (148) Rawling, T.; Xiao, H.; Lee, S. T.; Colbran, S. B.; McDonagh, A. M. Optical and Redox Properties of Ruthenium Phthalocyanine Complexes Tuned with Axial Ligand Substituents. *Inorg. Chem.* **2007**, *46* (7), 2805–2813. <https://doi.org/10.1021/ic061866u>.
- (149) Griffiths, C. H.; Walker, M. S.; Goldstein, P. Polymorphism in Vanadyl Phthalocyanine. *Mol Cryst Liq Cryst* **1976**, *33* (1–2), 149–170.

- <https://doi.org/10.1080/15421407608083878>.
- (150) Hong, J.; Fauvell, T. J.; Helweh, W.; Zhang, X.; Chen, L. X. Investigation of the Photoinduced Axial Ligation Process in the Excited State of Nickel(II) Phthalocyanine. *J. Photochem. Photobiol. A Chem.* **2019**, *372*, 270–278. <https://doi.org/10.1016/j.jphotochem.2018.12.026>.
- (151) Zhou, Q.; Liu, Z. F.; Marks, T. J.; Darancet, P. Electronic Structure of Metallophthalocyanines, MPc (M = Fe, Co, Ni, Cu, Zn, Mg) and Fluorinated MPc†. *ChemRxiv*. ChemRxiv October 23, 2020. <https://doi.org/10.26434/chemrxiv.13135676.v1>.
- (152) Koji Miyake, \*, †; Yukari Hori, ‡; Taichi Ikeda, ‡, §; Masumi Asakawa, ‡; Toshimi Shimizu, ‡ and; Shinya Sasaki†, ¶. Alkyl Chain Length Dependence of the Self-Organized Structure of Alkyl-Substituted Phthalocyanines. **2008**. <https://doi.org/10.1021/LA702564M>.
- (153) Sakamoto, K.; Ohno, E. Synthesis and Electron Transfer Property of Phthalocyanine Derivatives. *Prog. Org. Coatings* **1997**, *31* (1–2), 139–145. [https://doi.org/10.1016/S0300-9440\(97\)00029-5](https://doi.org/10.1016/S0300-9440(97)00029-5).
- (154) Greulich, K.; Belser, A.; Bölke, S.; Grüninger, P.; Karstens, R.; Sättele, M. S.; Ovsyannikov, R.; Giangrisostomi, E.; Basova, T. V.; Klyamer, D.; et al. Charge Transfer from Organic Molecules to Molybdenum Disulfide: Influence of the Fluorination of Iron Phthalocyanine. *J. Phys. Chem. C* **2020**, *124* (31), 16990–16999. <https://doi.org/10.1021/acs.jpcc.0c03862>.
- (155) Jiang, H.; Ye, J.; Hu, P.; Wei, F.; Du, K.; Wang, N.; Ba, T.; Feng, S.; Kloc, C. Fluorination of Metal Phthalocyanines: Single-Crystal Growth, Efficient N-Channel Organic Field-Effect Transistors, and Structure-Property Relationships. *Sci. Rep.* **2014**, *4* (1), 1–6. <https://doi.org/10.1038/srep07573>.
- (156) McKeown, N. B. Phthalocyanine-Containing Polymers. *Journal of Materials Chemistry*. Royal Society of Chemistry January 1, 2000, pp 1979–1995. <https://doi.org/10.1039/b000793p>.
- (157) Kezilebieke, S.; Amokrane, A.; Abel, M.; Bucher, J. P. Hierarchy of Chemical Bonding in the Synthesis of Fe-Phthalocyanine on Metal Surfaces: A Local Spectroscopy Approach. *J. Phys. Chem. Lett.* **2014**, *5* (18), 3175–3182. <https://doi.org/10.1021/jz5015696>.
- (158) Piantek, M.; Serrate, D.; Moro-Lagares, M.; Algarabel, P.; Pascual, J. I.; Ibarra, M. R. Manganese Phthalocyanine Derivatives Synthesized by On-Surface Cyclotetramerization. *J. Phys. Chem. C* **2014**, *118* (31), 17895–17899. <https://doi.org/10.1021/jp506652j>.
- (159) Gottfried, J. M. Surface Chemistry of Porphyrins and Phthalocyanines. *Surf. Sci. Rep.* **2015**, *70* (3), 259–379. <https://doi.org/10.1016/j.surfrep.2015.04.001>.

- (160) Ballav, N.; Wäckerlin, C.; Siewert, D.; Oppeneer, P. M.; Jung, T. A. Emergence of On-Surface Magnetochemistry. *J. Phys. Chem. Lett.* **2013**, *4* (14), 2303–2311. <https://doi.org/10.1021/jz400984k>.
- (161) Liao, M.-S.; Scheiner, S. Electronic Structure and Bonding in Metal Phthalocyanines, Metal=Fe, Co, Ni, Cu, Zn, Mg. *J. Chem. Phys.* **2001**, *114* (22), 9780–9791. <https://doi.org/10.1063/1.1367374>.
- (162) Nyokong, T.; Isago, H. The Renaissance in Optical Spectroscopy of Phthalocyanines and Other Tetraazaporphyrins. *Journal of Porphyrins and Phthalocyanines*. Society of Porphyrins and Phthalocyanines (SPP) May 2, 2004, pp 1083–1090. <https://doi.org/10.1142/S1088424604000453>.
- (163) Krichevsky, D. M.; Zasedatelev, A. V.; Tolbin, A. Y.; Luchkin, S. Y.; Karpo, A. B.; Krasovskii, V. I.; Tomilova, L. G. Highly Transparent Low-Symmetry Zinc Phthalocyanine-Based Monolayers for NO<sub>2</sub> Gas Detection. *Thin Solid Films* **2017**, *642*, 295–302. <https://doi.org/10.1016/j.tsf.2017.10.001>.
- (164) Tackley, D. R.; Dent, G.; Smith, W. E. Phthalocyanines: Structure and Vibrations. *Phys. Chem. Chem. Phys.* **2001**, *3* (8), 1419–1426. <https://doi.org/10.1039/b007763l>.
- (165) Padgaonkar, S.; Amsterdam, S. H.; Bergeron, H.; Su, K.; Marks, T. J.; Hersam, M. C.; Weiss, E. A. Molecular-Orientation-Dependent Interfacial Charge Transfer in Phthalocyanine/MoS<sub>2</sub> Mixed-Dimensional Heterojunctions. *J. Phys. Chem. C* **2019**, *123* (21), 13337–13343. <https://doi.org/10.1021/acs.jpcc.9b04063>.
- (166) Bovill, A. J.; McConnell, A. A.; Nimmo, J. A.; Smith, W. E. Resonance Raman Spectra of  $\alpha$ -Copper Phthalocyanine. *J. Phys. Chem.* **1986**, *90* (4), 569–575. <https://doi.org/10.1021/j100276a017>.
- (167) Murray, C.; Dozova, N.; McCaffrey, J. G.; FitzGerald, S.; Shafizadeh, N.; Crépin, C. Infra-Red and Raman Spectroscopy of Free-Base and Zinc Phthalocyanines Isolated in Matrices. *Phys. Chem. Chem. Phys.* **2010**, *12* (35), 10406–10422. <https://doi.org/10.1039/c0cp00055h>.
- (168) Jeong, J.; Park, S.; Kang, S. J.; Lee, H.; Yi, Y. Impacts of Molecular Orientation on the Hole Injection Barrier Reduction: CuPc/HAT-CN/Graphene. *J. Phys. Chem. C* **2016**, *120* (4), 2292–2298. <https://doi.org/10.1021/acs.jpcc.5b11535>.
- (169) Walter, M. G.; Rudine, A. B.; Wamser, C. C. Porphyrins and Phthalocyanines in Solar Photovoltaic Cells. *J. Porphy. Phthalocyanines* **2010**, *14* (9), 759–792. <https://doi.org/10.1142/S1088424610002689>.
- (170) Tang, C. W. Two-Layer Organic Photovoltaic Cell. *Appl. Phys. Lett.* **1986**, *48* (2), 183–185. <https://doi.org/10.1063/1.96937>.

- (171) Lee, M. H.; Dunietz, B. D.; Geva, E. Donor-to-Donor vs Donor-to-Acceptor Interfacial Charge Transfer States in the Phthalocyanine-Fullerene Organic Photovoltaic System. *J. Phys. Chem. Lett.* **2014**, *5* (21), 3810–3816. <https://doi.org/10.1021/jz5017203>.
- (172) Wang, N.; Yu, J.; Zang, Y.; Huang, J.; Jiang, Y. Effect of Buffer Layers on the Performance of Organic Photovoltaic Cells Based on Copper Phthalocyanine and C60. *Sol. Energy Mater. Sol. Cells* **2010**, *94* (2), 263–266. <https://doi.org/10.1016/j.solmat.2009.09.012>.
- (173) Wang, C.; Chen, X.; Chen, F.; Shao, J. Organic Photodetectors Based on Copper Phthalocyanine Films Prepared by a Multiple Drop Casting Method. *Org. Electron.* **2019**, *66*, 183–187. <https://doi.org/10.1016/j.orgel.2018.12.035>.
- (174) Hohnholz, D.; Steinbrecher, S.; Hanack, M. Applications of Phthalocyanines in Organic Light Emitting Devices. *J. Mol. Struct.* **2000**, *521* (1–3), 231–237. [https://doi.org/10.1016/S0022-2860\(99\)00438-X](https://doi.org/10.1016/S0022-2860(99)00438-X).
- (175) Bao, Z.; Lovinger, A. J.; Dodabalapur, A. Organic Field-Effect Transistors with High Mobility Based on Copper Phthalocyanine. *Appl. Phys. Lett.* **1996**, *69* (20), 3066–3068. <https://doi.org/10.1063/1.116841>.
- (176) Waqas Alam, M. Current Progress in Electrode/Pentacene Interfaces of Pentacene-Based Organic Thin Films Transistors: A Review. *Mater. Express* **2019**, *9* (7), 691–703. <https://doi.org/10.1166/mex.2019.1574>.
- (177) Wilson, M. W. B.; Rao, A.; Clark, J.; Kumar, R. S. S.; Brida, D.; Cerullo, G.; Friend, R. H. Ultrafast Dynamics of Exciton Fission in Polycrystalline Pentacene. *J. Am. Chem. Soc.* **2011**, *133* (31), 11830–11833. <https://doi.org/10.1021/ja201688h>.
- (178) Rao, A.; Friend, R. H. Harnessing Singlet Exciton Fission to Break the Shockley-Queisser Limit. *Nature Reviews Materials*. Nature Publishing Group October 4, 2017, pp 1–12. <https://doi.org/10.1038/natrevmats.2017.63>.
- (179) Campbell, R. B.; Robertson, J. M.; Trotter, J. The Crystal and Molecular Structure of Pentacene. *Acta Crystallogr.* **1961**, *14* (7), 705–711. <https://doi.org/10.1107/s0365110x61002163>.
- (180) Holmes, D.; Kumaraswamy, S.; Matzger, A. J.; Vollhardt, K. P. C. On the Nature of Nonplanarity in the [N]Phenylenes. *Chem. - A Eur. J.* **1999**, *5* (11), 3399–3412. [https://doi.org/10.1002/\(SICI\)1521-3765\(19991105\)5:11<3399::AID-CHEM3399>3.0.CO;2-V](https://doi.org/10.1002/(SICI)1521-3765(19991105)5:11<3399::AID-CHEM3399>3.0.CO;2-V).
- (181) Mattheus, C. C.; Dros, A. B.; Baas, J.; Meetsma, A.; De Boer, J. L.; Palstra, T. T. M. Polymorphism in Pentacene. *Acta Crystallogr. Sect. C Cryst. Struct. Commun.* **2001**, *57* (8), 939–941. <https://doi.org/10.1107/S010827010100703X>.

- (182) Ruiz, R.; Choudhary, D.; Nickel, B.; Toccoli, T.; Chang, K. C.; Mayer, A. C.; Clancy, P.; Blakely, J. M.; Headrick, R. L.; Iannotta, S.; et al. Pentacene Thin Film Growth. *Chemistry of Materials*. American Chemical Society November 16, 2004, pp 4497–4508. <https://doi.org/10.1021/cm049563q>.
- (183) Helzel, J.; Jankowski, S.; El Helou, M.; Witte, G.; Heimbrodt, W. Temperature Dependent Optical Properties of Pentacene Films on Zinc Oxide. *Appl. Phys. Lett.* **2011**, *99* (21), 211102. <https://doi.org/10.1063/1.3663863>.
- (184) Park, B.; Kim, K.; Park, J.; Lim, H.; Lanh, P. T.; Jang, A. R.; Hyun, C.; Myung, C. W.; Park, S.; Kim, J. W.; et al. Anomalous Ambipolar Transport of Organic Semiconducting Crystals via Control of Molecular Packing Structures. *ACS Appl. Mater. Interfaces* **2017**, *9* (33), 27839–27846. <https://doi.org/10.1021/acsami.7b05129>.
- (185) Lee, W. H.; Park, J.; Sim, S. H.; Lim, S.; Kim, K. S.; Hong, B. H.; Cho, K. Surface-Directed Molecular Assembly of Pentacene on Monolayer Graphene for High-Performance Organic Transistors. *J. Am. Chem. Soc.* **2011**, *133* (12), 4447–4454. <https://doi.org/10.1021/ja1097463>.
- (186) Casalis, L.; Danisman, M. F.; Nickel, B.; Bracco, G.; Toccoli, T.; Iannotta, S.; Scoles, G. Hyperthermal Molecular Beam Deposition of Highly Ordered Organic Thin Films. *Phys. Rev. Lett.* **2003**, *90* (20), 4. <https://doi.org/10.1103/PhysRevLett.90.206101>.
- (187) Kim, K.; Santos, E. J. G.; Lee, T. H.; Nishi, Y.; Bao, Z. Epitaxially Grown Strained Pentacene Thin Film on Graphene Membrane. *Small* **2015**, *11* (17), 2037–2043. <https://doi.org/10.1002/sml.201403006>.
- (188) Nguyen, N. N.; Lee, H. C.; Kang, B.; Jo, M.; Cho, K. Electric-Field-Tunable Growth of Organic Semiconductor Crystals on Graphene. *Nano Lett.* **2019**, *19* (3), 1758–1766. <https://doi.org/10.1021/acs.nanolett.8b04764>.
- (189) Hodas, M.; Siffalovic, P.; Nádaždy, P.; Mrkyvková, N.; Bodík, M.; Halahovets, Y.; Duva, G.; Reisz, B.; Konovalov, O.; Ohm, W.; et al. Real-Time Monitoring of Growth and Orientational Alignment of Pentacene on Epitaxial Graphene for Organic Electronics. *ACS Appl. Nano Mater.* **2018**, *1* (6), 2819–2826. <https://doi.org/10.1021/acsanm.8b00473>.
- (190) Sadowski, J. T.; Nagao, T.; Yaginuma, S.; Fujikawa, Y.; Al-Mahboob, A.; Nakajima, K.; Sakurai, T.; Thayer, G. E.; Tromp, R. M. Thin Bismuth Film as a Template for Pentacene Growth. *Appl. Phys. Lett.* **2005**, *86* (7), 1–3. <https://doi.org/10.1063/1.1865350>.
- (191) Lanzilotto, V.; Sanchez-Sanchez, C.; Bavdek, G.; Cvetko, D.; Lopez, M. F.; Martin-Gago, J. A.; Floreano, L. Planar Growth of Pentacene on the Dielectric TiO<sub>2</sub>(110) Surface. *J. Phys. Chem. C* **2011**, *115* (11), 4664–4672. <https://doi.org/10.1021/jp111011z>.
- (192) Söhnchen, S.; Lukas, S.; Witte, G. Epitaxial Growth of Pentacene Films on Cu(110). *J.*

- Chem. Phys.* **2004**, *121* (1), 525–534. <https://doi.org/10.1063/1.1760076>.
- (193) Gajewski, W.; Huth, M.; Buth, F.; Nickel, B.; Stutzmann, M.; Garrido, J. A. Photoresponse and Morphology of Pentacene Thin Films Modified by Oxidized and Reduced Diamond Surfaces. *Phys. Rev. B - Condens. Matter Mater. Phys.* **2009**, *80* (23), 235311. <https://doi.org/10.1103/PhysRevB.80.235311>.
- (194) Faltermeier, D.; Gompf, B.; Dressel, M.; Tripathi, A. K.; Pflaum, J. Optical Properties of Pentacene Thin Films and Single Crystals. *Phys. Rev. B - Condens. Matter Mater. Phys.* **2006**, *74* (12), 125416. <https://doi.org/10.1103/PhysRevB.74.125416>.
- (195) Ostroverkhova, O.; Shcherbina, S.; Cooke, D. G.; Egerton, R. F.; Hegmann, F. A.; Tykwinski, R. R.; Parkin, S. R.; Anthony, J. E. Optical and Transient Photoconductive Properties of Pentacene and Functionalized Pentacene Thin Films: Dependence on Film Morphology. *J. Appl. Phys.* **2005**, *98* (3), 033701. <https://doi.org/10.1063/1.1949711>.
- (196) Babusenar, A.; Jena, S.; Ray, D.; Bhattacharyya, J. Optical Polarization Anisotropy Induced by Molecular Alignment in Pentacene Films Confined in Micron Sized Grooves Etched in SiO<sub>2</sub> Substrate. *Mater. Res. Express* **2019**, *6* (4), 46402. <https://doi.org/10.1088/2053-1591/aaf911>.
- (197) Anger, F.; Oss, J. O.; Heinemeyer, U.; Broch, K.; Scholz, R.; Gerlach, A.; Schreiber, F. Photoluminescence Spectroscopy of Pure Pentacene, Perfluoropentacene, and Mixed Thin Films. *J. Chem. Phys.* **2012**, *136* (5), 054701. <https://doi.org/10.1063/1.3677839>.
- (198) Park, S. P.; Kim, S. S.; Kim, J. H.; Whang, C. N.; Im, S. Optical and Luminescence Characteristics of Thermally Evaporated Pentacene Films on Si. *Appl. Phys. Lett.* **2002**, *80* (16), 2872–2874. <https://doi.org/10.1063/1.1471929>.
- (199) Broch, K.; Dieterle, J.; Branchi, F.; Hestand, N. J.; Olivier, Y.; Tamura, H.; Cruz, C.; Nichols, V. M.; Hinderhofer, A.; Beljonne, D.; et al. Robust Singlet Fission in Pentacene Thin Films with Tuned Charge Transfer Interactions. *Nat. Commun.* **2018**, *9* (1), 954. <https://doi.org/10.1038/s41467-018-03300-1>.
- (200) Meyenburg, I.; Breuer, T.; Karthäuser, A.; Chatterjee, S.; Witte, G.; Heimbrodt, W. Temperature-Resolved Optical Spectroscopy of Pentacene Polymorphs: Variation of Herringbone Angles in Single-Crystals and Interface-Controlled Thin Films. *Phys. Chem. Chem. Phys.* **2016**, *18* (5), 3825–3831. <https://doi.org/10.1039/c5cp07836a>.
- (201) Amsterdam, S. H.; LaMountain, T.; Stanev, T. K.; Sangwan, V. K.; López-Arteaga, R.; Padgaonkar, S.; Watanabe, K.; Taniguchi, T.; Weiss, E. A.; Marks, T. J.; et al. Tailoring the Optical Response of Pentacene Thin Films via Templated Growth on Hexagonal Boron Nitride. *J. Phys. Chem. Lett.* **2021**, *12* (1), 26–31. <https://doi.org/https://doi.org/10.1021/acs.jpcllett.0c03132>.

- (202) Duva, G.; Mann, A.; Pithan, L.; Beyer, P.; Hagenlocher, J.; Gerlach, A.; Hinderhofer, A.; Schreiber, F. Template-Free Orientation Selection of Rod-Like Molecular Semiconductors in Polycrystalline Films. *J. Phys. Chem. Lett.* **2019**, *10* (5), 1031–1036. <https://doi.org/10.1021/acs.jpcllett.9b00304>.
- (203) Knipp, D.; Street, R. A.; Völkel, A.; Ho, J. Pentacene Thin Film Transistors on Inorganic Dielectrics: Morphology, Structural Properties, and Electronic Transport. *J. Appl. Phys.* **2003**, *93* (1), 347–355. <https://doi.org/10.1063/1.1525068>.
- (204) Kim, C.; Facchetti, A.; Marks, T. J. Gate Dielectric Microstructural Control of Pentacene Film Growth Mode and Field-Effect Transistor Performance. *Adv. Mater.* **2007**, *19* (18), 2561–2566. <https://doi.org/10.1002/adma.200700101>.
- (205) Gunder, D.; Watanabe, K.; Taniguchi, T.; Witte, G. Van Der Waals Bound Organic/2D Insulator Hybrid Structures: Epitaxial Growth of Acene Films on HBN(001) and the Influence of Surface Defects. *ACS Appl. Mater. Interfaces* **2020**, *12* (34), 38757–38767. <https://doi.org/10.1021/acsami.0c09527>.
- (206) Matković, A.; Genser, J.; Lüftner, D.; Kratzer, M.; Gajić, R.; Puschnig, P.; Teichert, C. Epitaxy of Highly Ordered Organic Semiconductor Crystallite Networks Supported by Hexagonal Boron Nitride. *Sci. Rep.* **2016**, *6* (1), 1–10. <https://doi.org/10.1038/srep38519>.
- (207) Yamagata, H.; Norton, J.; Hontz, E.; Olivier, Y.; Beljonne, D.; Brédas, J. L.; Silbey, R. J.; Spano, F. C. The Nature of Singlet Excitons in Oligoacene Molecular Crystals. *J. Chem. Phys.* **2011**, *134* (20), 204703. <https://doi.org/10.1063/1.3590871>.
- (208) Wilson, M. W. B.; Rao, A.; Ehrler, B.; Friend, R. H. Singlet Exciton Fission in Polycrystalline Pentacene: From Photophysics toward Devices. *Acc. Chem. Res.* **2013**, *46* (6), 1330–1338. <https://doi.org/10.1021/ar300345h>.
- (209) Sebastian, L.; Weiser, G.; Bäessler, H. Charge Transfer Transitions in Solid Tetracene and Pentacene Studied by Electroabsorption. *Chem. Phys.* **1981**, *61* (1–2), 125–135. [https://doi.org/10.1016/0301-0104\(81\)85055-0](https://doi.org/10.1016/0301-0104(81)85055-0).
- (210) He, R.; Tassi, N. G.; Blanchet, G. B.; Pinczuk, A. Intense Photoluminescence from Pentacene Monolayers. *Appl. Phys. Lett.* **2010**, *96* (26), 263303. <https://doi.org/10.1063/1.3458816>.
- (211) Aoki-Matsumoto, T.; Furuta, K.; Yamada, T.; Moriya, H.; Mizuno, K.; Matsui, A. H. Excitonic Photoluminescence in Pentacene Single Crystal. In *International Journal of Modern Physics B*; World Scientific Publishing Co. Pte Ltd, 2001; Vol. 15, pp 3753–3756. <https://doi.org/10.1142/s0217979201008585>.
- (212) He, R.; Chi, X.; Pinczuk, A.; Lang, D. V.; Ramirez, A. P. Extrinsic Optical Recombination in Pentacene Single Crystals: Evidence of Gap States. *Appl. Phys. Lett.*

- 2005, 87 (21), 1–3. <https://doi.org/10.1063/1.2135494>.
- (213) Basel, B. S.; Zirzmeier, J.; Hetzer, C.; Phelan, B. T.; Krzyaniak, M. D.; Reddy, S. R.; Coto, P. B.; Horwitz, N. E.; Young, R. M.; White, F. J.; et al. Unified Model for Singlet Fission within a Non-Conjugated Covalent Pentacene Dimer. *Nat. Commun.* **2017**, 8 (1), 15171. <https://doi.org/10.1038/ncomms15171>.
- (214) Jurchescu, O. D.; Baas, J.; Palstra, T. T. M. Effect of Impurities on the Mobility of Single Crystal Pentacene. *Appl. Phys. Lett.* **2004**, 84 (16), 3061–3063. <https://doi.org/10.1063/1.1704874>.
- (215) Kitamura, M.; Arakawa, Y. Pentacene-Based Organic Field-Effect Transistors. *J. Phys. Condens. Matter* **2008**, 20 (18), 184011. <https://doi.org/10.1088/0953-8984/20/18/184011>.
- (216) Lin, Y. Y.; Gundlach, D. J.; Nelson, S. F.; Jackson, T. N. Stacked Pentacene Layer Organic Thin-Film Transistors with Improved Characteristics. *IEEE Electron Device Lett.* **1997**, 18 (12), 606–608. <https://doi.org/10.1109/55.644085>.
- (217) Han, C. Y.; Tang, W. M.; Lai, P. T. High-Mobility Pentacene Organic Thin-Film Transistor with  $\text{La}_x\text{Nb}_{(1-x)}\text{O}_y$  Gate Dielectric Fabricated on Vacuum Tape. *IEEE Trans. Electron Devices* **2017**, 64 (4), 1716–1722. <https://doi.org/10.1109/TED.2017.2661806>.
- (218) Morino, Y.; Yokota, Y.; Hara, H.; Bando, K. I.; Ono, S.; Imanishi, A.; Okada, Y.; Matsui, H.; Uemura, T.; Takeya, J.; et al. Rapid Improvements in Charge Carrier Mobility at Ionic Liquid/Pentacene Single Crystal Interfaces by Self-Cleaning. *Phys. Chem. Chem. Phys.* **2020**, 22 (11), 6131–6135. <https://doi.org/10.1039/d0cp00149j>.
- (219) Han, C. Y.; Tang, W. M.; Lai, P. T. High-Mobility Pentacene Organic Thin-Film Transistors Achieved by Reducing Remote Phonon Scattering and Surface-Roughness Scattering. *Appl. Surf. Sci.* **2021**, 544, 148656. <https://doi.org/10.1016/j.apsusc.2020.148656>.
- (220) Naibi Lakshminarayana, A.; Ong, A.; Chi, C. Modification of Acenes for N-Channel OFET Materials. *Journal of Materials Chemistry C*. Royal Society of Chemistry April 5, 2018, pp 3551–3563. <https://doi.org/10.1039/c8tc00146d>.
- (221) Iwasawa, M.; Tsuruta, R.; Nakayama, Y.; Sasaki, M.; Hosokai, T.; Lee, S.; Fukumoto, K.; Yamada, Y. Exciton Dissociation and Electron Transfer at a Well-Defined Organic Interface of an Epitaxial C60 Layer on a Pentacene Single Crystal. *J. Phys. Chem. C* **2020**, 124 (25), 13572–13579. <https://doi.org/10.1021/acs.jpcc.0c02796>.
- (222) Hansmann, A.-K.; Döring, R. C.; Rinn, A.; Giesen, S. M.; Fey, M.; Breuer, T.; Berger, R.; Witte, G.; Chatterjee, S. Charge Transfer Excitation and Asymmetric Energy Transfer at the Interface of Pentacene–Perfluoropentacene Heterostacks. *ACS Appl. Mater. Interfaces* **2021**, 13 (4), 5284–5292. <https://doi.org/10.1021/acsami.0c16172>.

- (223) Alam, B.; Morrison, A. F.; Herbert, J. M. Charge Separation and Charge Transfer in the Low-Lying Excited States of Pentacene. *J. Phys. Chem. C* **2020**, *124* (45), 24653–24666. <https://doi.org/10.1021/acs.jpcc.0c07932>.
- (224) Casillas, R.; Papadopoulos, I.; Ullrich, T.; Thiel, D.; Kunzmann, A.; Guldi, D. M. Molecular Insights and Concepts to Engineer Singlet Fission Energy Conversion Devices. *Energy and Environmental Science*. Royal Society of Chemistry September 1, 2020, pp 2741–2804. <https://doi.org/10.1039/d0ee00495b>.
- (225) Thompson, N. J.; Congreve, D. N.; Goldberg, D.; Menon, V. M.; Baldo, M. A. Slow Light Enhanced Singlet Exciton Fission Solar Cells with a 126% Yield of Electrons per Photon. *Appl. Phys. Lett.* **2013**, *103* (26), 263302. <https://doi.org/10.1063/1.4858176>.
- (226) Yang, L.; Tabachnyk, M.; Bayliss, S. L.; Böhm, M. L.; Broch, K.; Greenham, N. C.; Friend, R. H.; Ehrler, B. Solution-Processable Singlet Fission Photovoltaic Devices. *Nano Lett.* **2015**, *15* (1), 354–358. <https://doi.org/10.1021/nl503650a>.
- (227) Kunzmann, A.; Gruber, M.; Casillas, R.; Tykewinski, R. R.; Costa, R. D.; Guldi, D. M. Tuning Pentacene Based Dye-Sensitized Solar Cells. *Nanoscale* **2018**, *10* (18), 8515–8525. <https://doi.org/10.1039/c8nr01502c>.
- (228) Jariwala, D.; Marks, T. J.; Hersam, M. C. Mixed-Dimensional van Der Waals Heterostructures. *Nat. Mater.* **2017**, *16* (2), 170–181. <https://doi.org/10.1038/nmat4703>.
- (229) Kiriya, D.; Tosun, M.; Zhao, P.; Kang, J. S.; Javey, A. Air-Stable Surface Charge Transfer Doping of MoS<sub>2</sub> by Benzyl Viologen. *J. Am. Chem. Soc.* **2014**, *136* (22), 7853–7856. <https://doi.org/10.1021/ja5033327>.
- (230) Wang, J.; Ji, Z.; Yang, G.; Chuai, X.; Liu, F.; Zhou, Z.; Lu, C.; Wei, W.; Shi, X.; Niu, J.; et al. Charge Transfer within the F4TCNQ - MoS<sub>2</sub> van Der Waals Interface: Toward Electrical Properties Tuning and Gas Sensing Application. *Adv. Funct. Mater.* **2018**, *28* (51), 1806244. <https://doi.org/10.1002/adfm.201806244>.
- (231) Homan, S. B.; Sangwan, V. K.; Balla, I.; Bergeron, H.; Weiss, E. A.; Hersam, M. C.; Bettis Homan, S.; Sangwan, V. K.; Balla, I.; Bergeron, H.; et al. Ultrafast Exciton Dissociation and Long-Lived Charge Separation in a Photovoltaic Pentacene–MoS<sub>2</sub> van Der Waals Heterojunction. *Nano Lett.* **2017**, *17* (1), 164–169. <https://doi.org/10.1021/acs.nanolett.6b03704>.
- (232) Zhong, C.; Sangwan, V. K.; Wang, C.; Bergeron, H.; Hersam, M. C.; Weiss, E. A. Mechanisms of Ultrafast Charge Separation in a PTB7/Monolayer MoS<sub>2</sub> van Der Waals Heterojunction. *J. Phys. Chem. Lett.* **2018**, *9* (10), 2484–2491. <https://doi.org/10.1021/acs.jpcllett.8b00628>.
- (233) Jariwala, D.; Howell, S. L.; Chen, K.-S. S.; Kang, J.; Sangwan, V. K.; Filippone, S. A.;

- Turrisi, R.; Marks, T. J.; Lauhon, L. J.; Hersam, M. C. Hybrid, Gate-Tunable, van Der Waals p–n Heterojunctions from Pentacene and MoS<sub>2</sub>. *Nano Lett.* **2016**, *16* (1), 497–503. <https://doi.org/10.1021/acs.nanolett.5b04141>.
- (234) Najmaei, S.; Zou, X.; Er, D.; Li, J.; Jin, Z.; Gao, W.; Zhang, Q.; Park, S.; Ge, L.; Lei, S.; et al. Tailoring the Physical Properties of Molybdenum Disulfide Monolayers by Control of Interfacial Chemistry. *Nano Lett.* **2014**, *14* (3), 1354–1361. <https://doi.org/10.1021/nl404396p>.
- (235) Obaidulla, S. M.; Habib, M. R.; Khan, Y.; Kong, Y.; Liang, T.; Xu, M. MoS<sub>2</sub> and Perylene Derivative Based Type-II Heterostructure: Bandgap Engineering and Giant Photoluminescence Enhancement. *Adv. Mater. Interfaces* **2020**, *7* (3), 1901197. <https://doi.org/10.1002/admi.201901197>.
- (236) Li, Y.; Xu, C. Y.; Hu, P.; Zhen, L. Carrier Control of MoS<sub>2</sub> Nanoflakes by Functional Self-Assembled Monolayers. *ACS Nano* **2013**, *7* (9), 7795–7804. <https://doi.org/10.1021/nn402682j>.
- (237) Zhao, Y.; Bertolazzi, S.; Maglione, M. S.; Rovira, C.; Mas-Torrent, M.; Samori, P. Molecular Approach to Electrochemically Switchable Monolayer MoS<sub>2</sub> Transistors. *Adv. Mater.* **2020**, *32*, 2000740. <https://doi.org/10.1002/adma.202000740>.
- (238) Pagaduan, J. N.; Hight-Huf, N.; Datar, A.; Nagar, Y.; Barnes, M.; Naveh, D.; Ramasubramaniam, A.; Katsumata, R.; Emrick, T. Electronic Tuning of Monolayer Graphene with Polymeric “Zwitterists.” *ACS Nano* **2021**, *15* (2), 2762–2770. <https://doi.org/10.1021/acsnano.0c08624>.
- (239) Habib, M. R.; Li, H.; Kong, Y.; Liang, T.; Obaidulla, S. M.; Xie, S.; Wang, S.; Ma, X.; Su, H.; Xu, M. Tunable Photoluminescence in a van Der Waals Heterojunction Built from a MoS<sub>2</sub> Monolayer and a PTCDA Organic Semiconductor. *Nanoscale* **2018**, *10* (34), 16107–16115. <https://doi.org/10.1039/c8nr03334j>.
- (240) Mrkyvkova, N.; Hodas, M.; Hagara, J.; Nadazdy, P.; Halahovets, Y.; Bodik, M.; Tokar, K.; Chai, J. W.; Wang, S. J.; Chi, D. Z.; et al. Diindenoperylene Thin-Film Structure on MoS<sub>2</sub> Monolayer. *Appl. Phys. Lett.* **2019**, *114* (25), 251906. <https://doi.org/10.1063/1.5100282>.
- (241) Kafle, T. R.; Kattel, B.; Yao, P.; Zereshki, P.; Zhao, H.; Chan, W.-L. Effect of the Interfacial Energy Landscape on Photoinduced Charge Generation at the ZnPc/MoS<sub>2</sub> Interface. *J. Am. Chem. Soc.* **2019**, *141* (28), 11328–11336. <https://doi.org/10.1021/jacs.9b05893>.
- (242) Breuer, T.; Maßmeyer, T.; Mänz, A.; Zoerb, S.; Harbrecht, B.; Witte, G. Structure of van Der Waals Bound Hybrids of Organic Semiconductors and Transition Metal Dichalcogenides: The Case of Acene Films on MoS<sub>2</sub>. *Phys. status solidi - Rapid Res. Lett.*

- 2016, 10 (12), 905–910. <https://doi.org/10.1002/pssr.201600320>.
- (243) Pak, J.; Jang, J.; Cho, K.; Kim, T.-Y.; Kim, J.-K.; Song, Y.; Hong, W.-K.; Min, M.; Lee, H.; Lee, T. Enhancement of Photodetection Characteristics of MoS<sub>2</sub> Field Effect Transistors Using Surface Treatment with Copper Phthalocyanine. *Nanoscale* **2015**, 7 (44), 18780–18788. <https://doi.org/10.1039/C5NR04836B>.
- (244) Rijal, K.; Rudayni, F.; Kafle, T. R.; Chan, W. L. Collective Effects of Band Offset and Wave Function Dimensionality on Impeding Electron Transfer from 2D to Organic Crystals. *J. Phys. Chem. Lett.* **2020**, 11 (18), 7495–7501. <https://doi.org/10.1021/acs.jpcclett.0c01796>.
- (245) Liu, X. Y.; Chen, W. K.; Fang, W. H.; Cui, G. Nonadiabatic Dynamics Simulations Reveal Distinct Effects of the Thickness of PTB7 on Interfacial Electron and Hole Transfer Dynamics in PTB7@MoS<sub>2</sub> Heterostructures. *J. Phys. Chem. Lett.* **2019**, 10 (11), 2949–2956. <https://doi.org/10.1021/acs.jpcclett.9b01066>.
- (246) Padgaonkar, S.; Olding, J. N.; Lauhon, L. J.; Hersam, M. C.; Weiss, E. A. Emergent Optoelectronic Properties of Mixed-Dimensional Heterojunctions. *Acc. Chem. Res.* **2020**, 53 (4), 763–772. <https://doi.org/10.1021/acs.accounts.9b00581>.
- (247) Ling, X.; Fang, W.; Lee, Y.-H.; Araujo, P. T.; Zhang, X.; Rodriguez-Nieva, J. F.; Lin, Y.; Zhang, J.; Kong, J.; Dresselhaus, M. S. Raman Enhancement Effect on Two-Dimensional Layered Materials: Graphene, h-BN and MoS<sub>2</sub>. *Nano Lett.* **2014**, 14 (6), 3033–3040. <https://doi.org/10.1021/nl404610c>.
- (248) Muehlethaler, C.; Considine, C. R.; Menon, V.; Lin, W.-C.; Lee, Y.-H.; Lombardi, J. R. Ultrahigh Raman Enhancement on Monolayer MoS<sub>2</sub>. *ACS Photonics* **2016**, acsphotronics.6b00213. <https://doi.org/10.1021/acsphotronics.6b00213>.
- (249) Lombardi, J. R.; Birke, R. L. Theory of Surface-Enhanced Raman Scattering in Semiconductors. *J. Phys. Chem. C* **2014**, 118 (20), 11120–11130. <https://doi.org/10.1021/jp5020675>.
- (250) Barros, E. B.; Dresselhaus, M. S. Theory of Raman Enhancement by Two-Dimensional Materials: Applications for Graphene-Enhanced Raman Spectroscopy. *Phys. Rev. B* **2014**, 90 (3), 035443. <https://doi.org/10.1103/PhysRevB.90.035443>.
- (251) Zhang, L.; Sharma, A.; Zhu, Y.; Zhang, Y.; Wang, B.; Dong, M.; Nguyen, H. T.; Wang, Z.; Wen, B.; Cao, Y.; et al. Efficient and Layer-Dependent Exciton Pumping across Atomically Thin Organic–Inorganic Type-I Heterostructures. *Adv. Mater.* **2018**, 30 (40), 1803986. <https://doi.org/10.1002/adma.201803986>.
- (252) Zhu, T.; Yuan, L.; Zhao, Y.; Zhou, M.; Wan, Y.; Mei, J.; Huang, L. Highly Mobile Charge-Transfer Excitons in Two-Dimensional WS<sub>2</sub>/Tetracene Heterostructures. *Sci. Adv.*

- 2018, 4 (1). <https://doi.org/10.1126/sciadv.aao3104>.
- (253) Tanoh, A. O. A.; Alexander-Webber, J.; Xiao, J.; Delport, G.; Williams, C. A.; Bretscher, H.; Gauriot, N.; Allardice, J.; Pandya, R.; Fan, Y.; et al. Enhancing Photoluminescence and Mobilities in WS<sub>2</sub> Monolayers with Oleic Acid Ligands. *Nano Lett.* **2019**, 19 (9), 6299–6307. <https://doi.org/10.1021/acs.nanolett.9b02431>.
- (254) Goodman, A. J.; Lien, D. H.; Ahn, G. H.; Spiegel, L. L.; Amani, M.; Willard, A. P.; Javey, A.; Tisdale, W. A. Substrate-Dependent Exciton Diffusion and Annihilation in Chemically Treated MoS<sub>2</sub> and WS<sub>2</sub>. *J. Phys. Chem. C* **2020**, 124 (22), 12175–12184. <https://doi.org/10.1021/acs.jpcc.0c04000>.
- (255) Mutz, N.; Park, S.; Schultz, T.; Sadofev, S.; Dalgleish, S.; Reissig, L.; Koch, N.; List-Kratochvil, E. J. W.; Blumstengel, S. Excited-State Charge Transfer Enabling MoS<sub>2</sub>/Phthalocyanine Photodetectors with Extended Spectral Sensitivity. *J. Phys. Chem. C* **2020**, 124 (5), 2837–2843. <https://doi.org/10.1021/acs.jpcc.9b10877>.
- (256) Park, J. H.; Sanne, A.; Guo, Y.; Amani, M.; Zhang, K.; Movva, H. C. P. P.; Robinson, J. A.; Javey, A.; Robertson, J.; Banerjee, S. K.; et al. Defect Passivation of Transition Metal Dichalcogenides via a Charge Transfer van Der Waals Interface. *Sci. Adv.* **2017**, 3 (10), 1–7. <https://doi.org/10.1126/sciadv.1701661>.
- (257) Cho, K.; Pak, J.; Chung, S.; Lee, T. Recent Advances in Interface Engineering of Transition-Metal Dichalcogenides with Organic Molecules and Polymers. *ACS Nano* **2019**, 13 (9), 9713–9734. <https://doi.org/10.1021/acsnano.9b02540>.
- (258) Huang, Y.; Zhuge, F.; Hou, J.; Lv, L.; Luo, P.; Zhou, N.; Gan, L.; Zhai, T. Van Der Waals Coupled Organic Molecules with Monolayer MoS<sub>2</sub> for Fast Response Photodetectors with Gate-Tunable Responsivity. *ACS Nano* **2018**, 12 (4), 4062–4073. <https://doi.org/10.1021/acsnano.8b02380>.
- (259) Zhao, Y.; Ippolito, S.; Samori, P. Functionalization of 2D Materials with Photosensitive Molecules: From Light-Responsive Hybrid Systems to Multifunctional Devices. *Adv. Opt. Mater.* **2019**, 7 (16), 1900286. <https://doi.org/10.1002/adom.201900286>.
- (260) Padgaonkar, S.; Eckdahl, C. T.; Sowa, J. K.; López-Arteaga, R.; Westmoreland, D. E.; Woods, E. F.; Irgen-Giorgio, S.; Nagasing, B.; Seideman, T.; Hersam, M. C.; et al. Light-Triggered Switching of Quantum Dot Photoluminescence through Excited-State Electron Transfer to Surface-Bound Photochromic Molecules. *Nano Lett.* **2021**, 21 (1), 854–860. <https://doi.org/10.1021/acs.nanolett.0c04611>.
- (261) Tang, Z.; George, A.; Winter, A.; Kaiser, D.; Neumann, C.; Weimann, T.; Turchanin, A. Optically Triggered Control of the Charge Carrier Density in Chemically Functionalized Graphene Field Effect Transistors. *Chem. – A Eur. J.* **2020**, chem.202000431. <https://doi.org/10.1002/chem.202000431>.

- (262) Amsterdam, S. H.; Marks, T. J.; Hersam, M. C. Leveraging Molecular Properties to Tailor Mixed-Dimensional Heterostructures beyond Energy Level Alignment. *J. Phys. Chem. Lett.* **2021**, 4543–4557. <https://doi.org/10.1021/acs.jpcclett.1c00799>.
- (263) Jariwala, D.; Sangwan, V. K.; Lauhon, L. J.; Marks, T. J.; Hersam, M. C. Emerging Device Applications for Semiconducting Two-Dimensional Transition Metal Dichalcogenides. *ACS Nano* **2014**, 8 (2), 1102–1120. <https://doi.org/10.1021/nm500064s>.
- (264) Wang, Q. H.; Kalantar-Zadeh, K.; Kis, A.; Coleman, J. N.; Strano, M. S. Electronics and Optoelectronics of Two-Dimensional Transition Metal Dichalcogenides. *Nature Nanotechnology*. Nature Publishing Group November 6, 2012, pp 699–712. <https://doi.org/10.1038/nnano.2012.193>.
- (265) Wang, H.; Li, C.; Fang, P.; Zhang, Z.; Zhang, J. Z. Synthesis, Properties, and Optoelectronic Applications of Two-Dimensional MoS<sub>2</sub> and MoS<sub>2</sub>-Based Heterostructures. *Chem. Soc. Rev.* **2018**, 47 (16), 6101–6127. <https://doi.org/10.1039/c8cs00314a>.
- (266) Radisavljevic, B.; Radenovic, A.; Brivio, J.; Giacometti, V.; Kis, A. Single-Layer MoS<sub>2</sub> Transistors. *Nat. Nanotechnol.* **2011**, 6 (3), 147–150. <https://doi.org/10.1038/nnano.2010.279>.
- (267) Wei, G.; Stanev, T. K.; Czaplewski, D. A.; Jung, I. W.; Stern, N. P. Silicon-Nitride Photonic Circuits Interfaced with Monolayer MoS<sub>2</sub>. *Appl. Phys. Lett.* **2015**, 107 (9), 091112. <https://doi.org/10.1063/1.4929779>.
- (268) Howell, S. L.; Jariwala, D.; Wu, C. C.; Chen, K. S.; Sangwan, V. K.; Kang, J.; Marks, T. J.; Hersam, M. C.; Lauhon, L. J. Investigation of Band-Offsets at Monolayer-Multilayer MoS<sub>2</sub> Junctions by Scanning Photocurrent Microscopy. *Nano Lett.* **2015**, 15 (4), 2278–2284. <https://doi.org/10.1021/nl504311p>.
- (269) Jia, Y.; Stanev, T. K.; Lenferink, E. J.; Stern, N. P. Enhanced Conductivity along Lateral Homojunction Interfaces of Atomically Thin Semiconductors. *2D Mater.* **2017**, 4 (2), 021012. <https://doi.org/10.1088/2053-1583/4/2/021012>.
- (270) Rivera, P.; Schaibley, J. R.; Jones, A. M.; Ross, J. S.; Wu, S.; Aivazian, G.; Klement, P.; Seyler, K.; Clark, G.; Ghimire, N. J.; et al. Observation of Long-Lived Interlayer Excitons in Monolayer MoSe<sub>2</sub> - WSe<sub>2</sub> Heterostructures. *Nat. Commun.* **2015**, 6 (1), 1–6. <https://doi.org/10.1038/ncomms7242>.
- (271) Ross, J. S.; Rivera, P.; Schaibley, J.; Lee-Wong, E.; Yu, H.; Taniguchi, T.; Watanabe, K.; Yan, J.; Mandrus, D.; Cobden, D.; et al. Interlayer Exciton Optoelectronics in a 2D Heterostructure p–n Junction. *Nano Lett.* **2017**, acs.nanolett.6b03398. <https://doi.org/10.1021/acs.nanolett.6b03398>.

- (272) Chow, C. M.; Yu, H.; Jones, A. M.; Yan, J.; Mandrus, D. G.; Taniguchi, T.; Watanabe, K.; Yao, W.; Xu, X. Unusual Exciton-Phonon Interactions at van Der Waals Engineered Interfaces. *Nano Lett.* **2017**, *17* (2), 1194–1199. <https://doi.org/10.1021/acs.nanolett.6b04944>.
- (273) Valley, N.; Greeneltch, N.; Van Duyne, R. P.; Schatz, G. C. A Look at the Origin and Magnitude of the Chemical Contribution to the Enhancement Mechanism of Surface-Enhanced Raman Spectroscopy (SERS): Theory and Experiment. *J. Phys. Chem. Lett.* **2013**, *4* (16), 2599–2604. <https://doi.org/10.1021/jz4012383>.
- (274) Arillo-Flores, O. I.; Fadlallah, M. M.; Schuster, C.; Eckern, U.; Romero, A. H. Magnetic, Electronic, and Vibrational Properties of Metal and Fluorinated Metal Phthalocyanines. *Phys. Rev. B - Condens. Matter Mater. Phys.* **2013**, *87* (16), 165115. <https://doi.org/10.1103/PhysRevB.87.165115>.
- (275) Marom, N.; Hod, O.; Scuseria, G. E.; Kronik, L. Electronic Structure of Copper Phthalocyanine: A Comparative Density Functional Theory Study. *J. Chem. Phys.* **2008**, *128* (16), 164107. <https://doi.org/10.1063/1.2898540>.
- (276) Isago, H. “Prototypical” Optical Absorption Spectra of Phthalocyanines and Their Theoretical Background; Springer, Tokyo, 2015; pp 21–40. [https://doi.org/10.1007/978-4-431-55102-7\\_2](https://doi.org/10.1007/978-4-431-55102-7_2).
- (277) Yin, Y.; Miao, P.; Zhang, Y.; Han, J.; Zhang, X.; Gong, Y.; Gu, L.; Xu, C.; Yao, T.; Xu, P.; et al. Significantly Increased Raman Enhancement on MoX<sub>2</sub> (X = S, Se) Monolayers upon Phase Transition. *Adv. Funct. Mater.* **2017**, *27* (16), 1606694. <https://doi.org/10.1002/adfm.201606694>.
- (278) Lee, Y.; Kim, H.; Lee, J.; Yu, S. H.; Hwang, E.; Lee, C.; Ahn, J. H.; Cho, J. H. Enhanced Raman Scattering of Rhodamine 6G Films on Two-Dimensional Transition Metal Dichalcogenides Correlated to Photoinduced Charge Transfer. *Chem. Mater.* **2016**, *28* (1), 180–187. <https://doi.org/10.1021/acs.chemmater.5b03714>.
- (279) Quan, L.; Song, Y.; Lin, Y.; Zhang, G.; Dai, Y.; Wu, Y.; Jin, K.; Ding, H.; Pan, N.; Luo, Y.; et al. The Raman Enhancement Effect on a Thin GaSe Flake and Its Thickness Dependence. *J. Mater. Chem. C* **2015**, *3* (42), 11129–11134. <https://doi.org/10.1039/c5tc02209f>.
- (280) Lin, J.; Liang, L.; Ling, X.; Zhang, S.; Mao, N.; Zhang, N.; Sumpter, B. G.; Meunier, V.; Tong, L.; Zhang, J. Enhanced Raman Scattering on In-Plane Anisotropic Layered Materials. **2015**.
- (281) Lee, J.; Mak, K. F.; Shan, J. Electrical Control of the Valley Hall Effect in Bilayer MoS<sub>2</sub> Transistors. *Nat. Nanotechnol.* **2016**, *11* (5), 421–425. <https://doi.org/10.1038/nnano.2015.337>.

- (282) Prins, F.; Goodman, A. J.; Tisdale, W. A. Reduced Dielectric Screening and Enhanced Energy Transfer in Single- and Few-Layer MoS<sub>2</sub>. *Nano Lett.* **2014**, *14* (11), 6087–6091. <https://doi.org/10.1021/nl5019386>.
- (283) Zhang, L.; Yang, Y.; Huang, H.; Lyu, L.; Zhang, H.; Cao, N.; Xie, H.; Gao, X.; Niu, D.; Gao, Y. Thickness-Dependent Air-Exposure-Induced Phase Transition of CuPc Ultrathin Films to Well-Ordered One-Dimensional Nanocrystals on Layered Substrates. *J. Phys. Chem. C* **2015**, *119* (8), 4217–4223. <https://doi.org/10.1021/jp512613z>.
- (284) Nguyen, E. P.; Carey, B. J.; Harrison, C. J.; Atkin, P.; Berean, K. J.; Della Gaspera, E.; Ou, J. Z.; Kaner, R. B.; Kalantar-Zadeh, K.; Daeneke, T. Excitation Dependent Bidirectional Electron Transfer in Phthalocyanine-Functionalised MoS<sub>2</sub> Nanosheets. *Nanoscale* **2016**, *8* (36), 16276–16283. <https://doi.org/10.1039/c6nr04326g>.
- (285) Kafle, T. R.; Kattel, B.; Lane, S. D.; Wang, T.; Zhao, H.; Chan, W. L. Charge Transfer Exciton and Spin Flipping at Organic-Transition-Metal Dichalcogenide Interfaces. *ACS Nano* **2017**, *11* (10), 10184–10192. <https://doi.org/10.1021/acsnano.7b04751>.
- (286) Wagner, S. R.; Huang, B.; Park, C.; Feng, J.; Yoon, M.; Zhang, P. Growth of Metal Phthalocyanine on Deactivated Semiconducting Surfaces Steered by Selective Orbital Coupling. *Phys. Rev. Lett.* **2015**, *115* (9), 096101. <https://doi.org/10.1103/PhysRevLett.115.096101>.
- (287) Heyd, J.; Scuseria, G. E.; Ernzerhof, M. Hybrid Functionals Based on a Screened Coulomb Potential. *J. Chem. Phys.* **2003**, *118* (18), 8207–8215. <https://doi.org/10.1063/1.1564060>.
- (288) Tkatchenko, A.; Scheffler, M. Accurate Molecular van Der Waals Interactions from Ground-State Electron Density and Free-Atom Reference Data. *Phys. Rev. Lett.* **2009**, *102* (7), 073005. <https://doi.org/10.1103/PhysRevLett.102.073005>.
- (289) Adrian, F. J. Charge Transfer Effects in Surface-Enhanced Raman Scattering. *J. Chem. Phys.* **1982**, *77* (11), 5302–5314. <https://doi.org/10.1063/1.443800>.
- (290) Hilty, F. W.; Kuhlman, A. K.; Pauly, F.; Zayak, A. T. Raman Scattering from a Molecule-Semiconductor Interface Tuned by an Electric Field: Density Functional Theory Approach. *J. Phys. Chem. C* **2015**, *119* (40), 23113–23118. <https://doi.org/10.1021/acs.jpcc.5b08089>.
- (291) Lippitsch, M. E. Ground-State Charge Transfer as a Mechanism for Surface-Enhanced Raman Scattering. *Phys. Rev. B* **1984**, *29* (6), 3101–3110. <https://doi.org/10.1103/PhysRevB.29.3101>.
- (292) Morton, S. M.; Jensen, L. Understanding the Molecule-Surface Chemical Coupling in SERS. *J. Am. Chem. Soc.* **2009**, *131* (11), 4090–4098. <https://doi.org/10.1021/ja809143c>.

- (293) Ling, X.; Wu, J.; Xie, L.; Zhang, J. Graphene-Thickness-Dependent Graphene-Enhanced Raman Scattering. *J. Phys. Chem. C* **2013**, *117* (5), 2369–2376. <https://doi.org/10.1021/jp310564d>.
- (294) Dou, W.; Huang, S.; Zhang, R. Q.; Lee, C. S. Molecule-Substrate Interaction Channels of Metal-Phthalocyanines on Graphene on Ni(111) Surface. *J. Chem. Phys.* **2011**, *134* (9), 094705. <https://doi.org/10.1063/1.3561398>.
- (295) Lee, S. Y.; Kim, U. J.; Chung, J.; Nam, H.; Jeong, H. Y.; Han, G. H.; Kim, H.; Oh, H. M.; Lee, H.; Kim, H.; et al. Large Work Function Modulation of Monolayer MoS<sub>2</sub> by Ambient Gases. *ACS Nano* **2016**, *10* (6), 6100–6107. <https://doi.org/10.1021/acsnano.6b01742>.
- (296) Giannozzi, P.; Andreussi, O.; Brumme, T.; Bunau, O.; Buongiorno Nardelli, M.; Calandra, M.; Car, R.; Cavazzoni, C.; Ceresoli, D.; Cococcioni, M.; et al. Advanced Capabilities for Materials Modelling with Quantum ESPRESSO. *J. Phys. Condens. Matter* **2017**, *29* (46), 465901. <https://doi.org/10.1088/1361-648X/aa8f79>.
- (297) Perdew, J. P.; Burke, K.; Ernzerhof, M. Generalized Gradient Approximation Made Simple. *Phys. Rev. Lett.* **1996**, *77* (18), 3865–3868. <https://doi.org/10.1103/PhysRevLett.77.3865>.
- (298) Hamann, D. R. Optimized Norm-Conserving Vanderbilt Pseudopotentials. *Phys. Rev. B - Condens. Matter Mater. Phys.* **2013**, *88* (8), 085117. <https://doi.org/10.1103/PhysRevB.88.085117>.
- (299) Choudhury, P.; Ravavarapu, L.; Dekle, R.; Chowdhury, S. Modulating Electronic and Optical Properties of Monolayer MoS<sub>2</sub> Using Nonbonded Phthalocyanine Molecules. *J. Phys. Chem. C* **2017**, *121* (5), 2959–2967. <https://doi.org/10.1021/acs.jpcc.6b11239>.
- (300) Singh, E.; Singh, P.; Kim, K. S.; Yeom, G. Y.; Nalwa, H. S. Flexible Molybdenum Disulfide (MoS<sub>2</sub>) Atomic Layers for Wearable Electronics and Optoelectronics. *ACS Appl. Mater. Interfaces* **2019**, *11* (12), 11061–11105. <https://doi.org/10.1021/acsami.8b19859>.
- (301) Barua, S.; Dutta, H. S.; Gogoi, S.; Devi, R.; Khan, R. Nanostructured MoS<sub>2</sub>-Based Advanced Biosensors: A Review. *ACS Appl. Nano Mater.* **2018**, *1* (1), 2–25. <https://doi.org/10.1021/acsanm.7b00157>.
- (302) Brar, V. W.; Sherrott, M. C.; Jariwala, D. Emerging Photonic Architectures in Two-Dimensional Opto-Electronics. *Chem. Soc. Rev.* **2018**, *47* (17), 6824–6844. <https://doi.org/10.1039/c8cs00206a>.
- (303) Ding, Q.; Song, B.; Xu, P.; Jin, S. Efficient Electrocatalytic and Photoelectrochemical Hydrogen Generation Using MoS<sub>2</sub> and Related Compounds. *Chem* **2016**, *1* (5), 699–726. <https://doi.org/10.1016/j.chempr.2016.10.007>.

- (304) Gobbi, M.; Orgiu, E.; Samorì, P. When 2D Materials Meet Molecules: Opportunities and Challenges of Hybrid Organic/Inorganic van Der Waals Heterostructures. *Adv. Mater.* **2018**, *30* (18), 1706103. <https://doi.org/10.1002/adma.201706103>.
- (305) Huang, Y. L.; Zheng, Y. J.; Song, Z.; Chi, D.; Wee, A. T. S.; Quek, S. Y. The Organic-2D Transition Metal Dichalcogenide Heterointerface. *Chem. Soc. Rev.* **2018**, *47* (9), 3241–3264. <https://doi.org/10.1039/c8cs00159f>.
- (306) Sun, J.; Choi, Y.; Choi, Y. J.; Kim, S.; Park, J.; Lee, S.; Cho, J. H. 2D–Organic Hybrid Heterostructures for Optoelectronic Applications. *Adv. Mater.* **2019**, *31* (34), 1803831. <https://doi.org/10.1002/adma.201803831>.
- (307) Choi, J.; Zhang, H.; Choi, J. H. Modulating Optoelectronic Properties of Two-Dimensional Transition Metal Dichalcogenide Semiconductors by Photoinduced Charge Transfer. *ACS Nano* **2016**, *10* (1), 1671–1680. <https://doi.org/10.1021/acsnano.5b07457>.
- (308) Zhou, M.; Wang, W.; Lu, J.; Ni, Z. How Defects Influence the Photoluminescence of TMDCs. *Nano Res.* **2021**, *14* (1), 29–39. <https://doi.org/10.1007/s12274-020-3037-9>.
- (309) Qiu, H.; Xu, T.; Wang, Z.; Ren, W.; Nan, H.; Ni, Z.; Chen, Q.; Yuan, S.; Miao, F.; Song, F.; et al. Hopping Transport through Defect-Induced Localized States in Molybdenum Disulphide. *Nat. Commun.* **2013**, *4* (1), 1–6. <https://doi.org/10.1038/ncomms3642>.
- (310) Murthy, A. A.; Stanev, T. K.; Dos Reis, R.; Hao, S.; Wolverton, C.; Stern, N. P.; Dravid, V. P. Direct Visualization of Electric-Field-Induced Structural Dynamics in Monolayer Transition Metal Dichalcogenides. *ACS Nano* **2020**, *14* (2), 1569–1576. <https://doi.org/10.1021/acsnano.9b06581>.
- (311) Saigal, N.; Ghosh, S. Evidence for Two Distinct Defect Related Luminescence Features in Monolayer MoS<sub>2</sub>. *Appl. Phys. Lett.* **2016**, *109* (12), 122105. <https://doi.org/10.1063/1.4963133>.
- (312) Barthelmi, K.; Klein, J.; Hötger, A.; Sigl, L.; Sigger, F.; Mitterreiter, E.; Rey, S.; Gyger, S.; Lorke, M.; Florian, M.; et al. Atomistic Defects as Single-Photon Emitters in Atomically Thin MoS<sub>2</sub>. *Appl. Phys. Lett.* **2020**, *117* (7), 070501. <https://doi.org/10.1063/5.0018557>.
- (313) Klein, J.; Lorke, M.; Florian, M.; Sigger, F.; Sigl, L.; Rey, S.; Wierzbowski, J.; Cerne, J.; Müller, K.; Mitterreiter, E.; et al. Site-Selectively Generated Photon Emitters in Monolayer MoS<sub>2</sub> via Local Helium Ion Irradiation. *Nat. Commun.* **2019**, *10* (1), 1–8. <https://doi.org/10.1038/s41467-019-10632-z>.
- (314) Cadiz, F.; Courtade, E.; Robert, C.; Wang, G.; Shen, Y.; Cai, H.; Taniguchi, T.; Watanabe, K.; Carrere, H.; Lagarde, D.; et al. Excitonic Linewidth Approaching the Homogeneous Limit in MoS<sub>2</sub>-Based van Der Waals Heterostructures. *Phys. Rev. X* **2017**,

- 7 (2), 021026. <https://doi.org/10.1103/PhysRevX.7.021026>.
- (315) Tongay, S.; Suh, J.; Ataca, C.; Fan, W.; Luce, A.; Kang, J. S.; Liu, J.; Ko, C.; Raghunathanan, R.; Zhou, J.; et al. Defects Activated Photoluminescence in Two-Dimensional Semiconductors: Interplay between Bound, Charged, and Free Excitons. *Sci. Rep.* **2013**, *3* (1), 1–5. <https://doi.org/10.1038/srep02657>.
- (316) Sivaram, S. V.; Hanbicki, A. T.; Rosenberger, M. R.; Jernigan, G. G.; Chuang, H. J.; McCreary, K. M.; Jonker, B. T. Spatially Selective Enhancement of Photoluminescence in MoS<sub>2</sub> by Exciton-Mediated Adsorption and Defect Passivation. *ACS Appl. Mater. Interfaces* **2019**, *11* (17), 16147–16155. <https://doi.org/10.1021/acsami.9b00390>.
- (317) Hong, J.; Hu, Z.; Probert, M.; Li, K.; Lv, D.; Yang, X.; Gu, L.; Mao, N.; Feng, Q.; Xie, L.; et al. Exploring Atomic Defects in Molybdenum Disulphide Monolayers. *Nat. Commun.* **2015**, *6* (1), 1–8. <https://doi.org/10.1038/ncomms7293>.
- (318) Taghipour, N.; Martinez, P. L. H.; Ozden, A.; Olutas, M.; Dede, D.; Gungor, K.; Erdem, O.; Perkgoz, N. K.; Demir, H. V. Near-Unity Efficiency Energy Transfer from Colloidal Semiconductor Quantum Wells of CdSe/CdS Nanoplatelets to a Monolayer of MoS<sub>2</sub>. *ACS Nano* **2018**, *12* (8), 8547–8554. <https://doi.org/10.1021/acs.nano.8b04119>.
- (319) Haldar, A.; Cortes, C. L.; Darancet, P.; Sharifzadeh, S. Microscopic Theory of Plasmons in Substrate-Supported Borophene. *Nano Lett.* **2020**, *20* (5), 2986–2992. <https://doi.org/10.1021/acs.nanolett.9b04789>.
- (320) Raja, A.; Montoya-Castillo, A.; Zultak, J.; Zhang, X. X.; Ye, Z.; Roquelet, C.; Chenet, D. A.; Van Der Zande, A. M.; Huang, P.; Jockusch, S.; et al. Energy Transfer from Quantum Dots to Graphene and MoS<sub>2</sub>: The Role of Absorption and Screening in Two-Dimensional Materials. *Nano Lett.* **2016**, *16* (4), 2328–2333. <https://doi.org/10.1021/acs.nanolett.5b05012>.
- (321) Barbara, P. F.; Meyer, T. J.; Ratner, M. A. Contemporary Issues in Electron Transfer Research. *J. Phys. Chem.* **1996**, *100* (31), 13148–13168. <https://doi.org/10.1021/jp9605663>.
- (322) Kresse, G.; Joubert, D. From Ultrasoft Pseudopotentials to the Projector Augmented-Wave Method. *Phys. Rev. B - Condens. Matter Mater. Phys.* **1999**, *59* (3), 1758–1775. <https://doi.org/10.1103/PhysRevB.59.1758>.
- (323) Kresse, G.; Furthmüller, J. Efficient Iterative Schemes for Ab Initio Total-Energy Calculations Using a Plane-Wave Basis Set. *Phys. Rev. B - Condens. Matter Mater. Phys.* **1996**, *54* (16), 11169–11186. <https://doi.org/10.1103/PhysRevB.54.11169>.
- (324) Freysoldt, C.; Neugebauer, J. First-Principles Calculations for Charged Defects at Surfaces, Interfaces, and Two-Dimensional Materials in the Presence of Electric Fields.

- Phys. Rev. B* **2018**, *97* (20), 205425. <https://doi.org/10.1103/PhysRevB.97.205425>.
- (325) Neaton, J. B.; Hybertsen, M. S.; Louie, S. G. Renormalization of Molecular Electronic Levels at Metal-Molecule Interfaces. *Phys. Rev. Lett.* **2006**, *97* (21), 216405. <https://doi.org/10.1103/PhysRevLett.97.216405>.
- (326) Cho, Y.; Berkelbach, T. C. Environmentally Sensitive Theory of Electronic and Optical Transitions in Atomically Thin Semiconductors. *Phys. Rev. B* **2018**, *97* (4), 041409. <https://doi.org/10.1103/PhysRevB.97.041409>.
- (327) Debe, M. K. Variable Angle Spectroscopic Ellipsometry Studies of Oriented Phthalocyanine Films. II. Copper Phthalocyanine. *J. Vac. Sci. Technol. A Vacuum, Surfaces, Film.* **1992**, *10* (4), 2816–2821. <https://doi.org/10.1116/1.577916>.
- (328) Debe, M. K.; Field, D. R. Variable Angle Spectroscopic Ellipsometry Studies of Oriented Phthalocyanine Films. *J. Vac. Sci. Technol. A Vacuum, Surfaces, Film.* **1991**, *9* (3), 1265–1271. <https://doi.org/10.1116/1.577610>.
- (329) Tersoff, J.; Hamann, D. R. Theory and Application for the Scanning Tunneling Microscope. *Phys. Rev. Lett.* **1983**, *50* (25), 1998–2001. <https://doi.org/10.1103/PhysRevLett.50.1998>.
- (330) Yanagisawa, S.; Yamauchi, K.; Inaoka, T.; Oguchi, T.; Hamada, I. Origin of the Band Dispersion in a Metal Phthalocyanine Crystal. *Phys. Rev. B - Condens. Matter Mater. Phys.* **2014**, *90* (24), 245141. <https://doi.org/10.1103/PhysRevB.90.245141>.
- (331) Götzen, J.; Käfer, D.; Wöll, C.; Witte, G. Growth and Structure of Pentacene Films on Graphite: Weak Adhesion as a Key for Epitaxial Film Growth. *Phys. Rev. B - Condens. Matter Mater. Phys.* **2010**, *81* (8), 085440. <https://doi.org/10.1103/PhysRevB.81.085440>.
- (332) Von Helden, L.; Breuer, T.; Witte, G. Anisotropic Thermal Expansion in Pentacene and Perfluoropentacene: Effects of Molecular Packing Motif and Fixation at the Interface. *Appl. Phys. Lett.* **2017**, *110* (14), 141904. <https://doi.org/10.1063/1.4979650>.
- (333) Shioya, N.; Murdey, R.; Nakao, K.; Yoshida, H.; Koganezawa, T.; Eda, K.; Shimoaka, T.; Hasegawa, T. Alternative Face-on Thin Film Structure of Pentacene. *Sci. Rep.* **2019**, *9* (1), 1–7. <https://doi.org/10.1038/s41598-018-37166-6>.
- (334) Li, S.; Zhong, C.; Henning, A.; Sangwan, V. K.; Zhou, Q.; Liu, X.; Rahn, M. S.; Wells, S. A.; Park, H. Y.; Luxa, J.; et al. Molecular-Scale Characterization of Photoinduced Charge Separation in Mixed-Dimensional InSe-Organic van Der Waals Heterostructures. *ACS Nano* **2020**, *14* (3), 3509–3518. <https://doi.org/10.1021/acsnano.9b09661>.
- (335) Lee, C.-H.; Schiros, T.; Santos, E. J. G.; Kim, B.; Yager, K. G.; Kang, S. J.; Lee, S.; Yu, J.; Watanabe, K.; Taniguchi, T.; et al. Epitaxial Growth of Molecular Crystals on van Der Waals Substrates for High-Performance Organic Electronics. *Adv. Mater.* **2014**, *26* (18),

- 2812–2817. <https://doi.org/10.1002/adma.201304973>.
- (336) Zhang, Y.; Qiao, J.; Gao, S.; Hu, F.; He, D.; Wu, B.; Yang, Z.; Xu, B.; Li, Y.; Shi, Y.; et al. Probing Carrier Transport and Structure-Property Relationship of Highly Ordered Organic Semiconductors at the Two-Dimensional Limit. *Phys. Rev. Lett.* **2016**, *116* (1), 016602. <https://doi.org/10.1103/PhysRevLett.116.016602>.
- (337) Yoshida, H.; Yamada, K.; Tsutsumi, J.; Sato, N. Complete Description of Ionization Energy and Electron Affinity in Organic Solids: Determining Contributions from Electronic Polarization, Energy Band Dispersion, and Molecular Orientation. *Phys. Rev. B - Condens. Matter Mater. Phys.* **2015**, *92* (7), 075145. <https://doi.org/10.1103/PhysRevB.92.075145>.
- (338) Felter, K. M.; Grozema, F. C. Singlet Fission in Crystalline Organic Materials: Recent Insights and Future Directions. *Journal of Physical Chemistry Letters*. American Chemical Society November 21, 2019, pp 7208–7214. <https://doi.org/10.1021/acs.jpcclett.9b00754>.
- (339) Dimitrakopoulos, C. D.; Brown, A. R.; Pomp, A. Molecular Beam Deposited Thin Films of Pentacene for Organic Field Effect Transistor Applications. *J. Appl. Phys.* **1996**, *80* (4), 2501–2508. <https://doi.org/10.1063/1.363032>.
- (340) Kratzer, M.; Bayer, B. C.; Kidambi, P. R.; Matković, A.; Gajić, R.; Cabrero-Vilatela, A.; Weatherup, R. S.; Hofmann, S.; Teichert, C. Effects of Polymethylmethacrylate-Transfer Residues on the Growth of Organic Semiconductor Molecules on Chemical Vapor Deposited Graphene. *Appl. Phys. Lett.* **2015**, *106* (10), 103101. <https://doi.org/10.1063/1.4913948>.
- (341) Seto, K.; Furukawa, Y. Study on Solid Structure of Pentacene Thin Films Using Raman Imaging. *J. Raman Spectrosc.* **2012**, *43* (12), 2015–2019. <https://doi.org/10.1002/jrs.4090>.
- (342) Hosoi, Y.; Deyra, D. M.; Nakajima, K.; Furukawa, Y. Micro-Raman Spectroscopy on Pentacene Thin-Film Transistors. In *Molecular Crystals and Liquid Crystals*; Taylor & Francis Group, 2008; Vol. 491, pp 317–323. <https://doi.org/10.1080/15421400802331083>.
- (343) Kratzer, M.; Klima, S.; Teichert, C.; Vasić, B.; Matković, A.; Ralević, U.; Gajić, R. Temperature Dependent Growth Morphologies of Parahexaphenyl on SiO<sub>2</sub> Supported Exfoliated Graphene. *J. Vac. Sci. Technol. B, Nanotechnol. Microelectron. Mater. Process. Meas. Phenom.* **2013**, *31* (4), 04D114. <https://doi.org/10.1116/1.4813895>.
- (344) Bikiaris, D. N.; Karayannidis, G. P. Thermomechanical Analysis of Chain-extended PET and PBT. *J. Appl. Polym. Sci.* **1996**, *60* (1), 55–61. [https://doi.org/10.1002/\(SICI\)1097-4628\(19960404\)60:1<55::AID-APP7>3.0.CO;2-U](https://doi.org/10.1002/(SICI)1097-4628(19960404)60:1<55::AID-APP7>3.0.CO;2-U).

- (345) Yates, B.; Overy, M. J.; Pirgon, O. The Anisotropic Thermal Expansion of Boron Nitride: I. Experimental Results and Their Analysis. *Philos. Mag.* **1975**, *32* (4), 847–857. <https://doi.org/10.1080/14786437508221624>.
- (346) Blech, I.; Cohen, U. Effects of Humidity on Stress in Thin Silicon Dioxide Films. *J. Appl. Phys.* **1982**, *53* (6), 4202–4207. <https://doi.org/10.1063/1.331244>.
- (347) Huang, X.; Gao, Y.; Yang, T.; Ren, W.; Cheng, H. M.; Lai, T. Quantitative Analysis of Temperature Dependence of Raman Shift of Monolayer WS<sub>2</sub>. *Sci. Rep.* **2016**, *6* (1), 1–8. <https://doi.org/10.1038/srep32236>.
- (348) Toccoli, T.; Bettotti, P.; Cassinese, A.; Gottardi, S.; Kubozono, Y.; Loi, M. A.; Manca, M.; Verucchi, R. Photophysics of Pentacene-Doped Picene Thin Films. *J. Phys. Chem. C* **2018**, *122* (29), 16879–16886. <https://doi.org/10.1021/acs.jpcc.8b02978>.
- (349) Niu, M.; Zheng, F.; Yang, X.; Bi, P.; Feng, L.; Hao, X. Molecular Packing Correlated Fluorescence in TIPS-Pentacene Films. *Org. Electron.* **2017**, *49*, 340–346. <https://doi.org/https://doi.org/10.1016/j.orgel.2017.07.007>.
- (350) Zhu, T.; Wan, Y.; Huang, L. Direct Imaging of Frenkel Exciton Transport by Ultrafast Microscopy. *Acc. Chem. Res.* **2017**, *50* (7), 1725–1733. <https://doi.org/10.1021/acs.accounts.7b00155>.
- (351) Greenham, N. C.; Bobbert, P. A. Two-Dimensional Electron-Hole Capture in a Disordered Hopping System. *Phys. Rev. B - Condens. Matter Mater. Phys.* **2003**, *68* (24), 245301. <https://doi.org/10.1103/PhysRevB.68.245301>.
- (352) He, D.; Zhang, Y.; Wu, Q.; Xu, R.; Nan, H.; Liu, J.; Yao, J.; Wang, Z.; Yuan, S.; Li, Y.; et al. Two-Dimensional Quasi-Freestanding Molecular Crystals for High-Performance Organic Field-Effect Transistors. *Nat. Commun.* **2014**, *5* (1), 1–7. <https://doi.org/10.1038/ncomms6162>.
- (353) Kim, D. K.; Lubert-Perquel, D.; Heutz, S. Comparison of Organic and Inorganic Layers for Structural Templating of Pentacene Thin Films. *Mater. Horizons* **2020**, *7* (1), 289–298. <https://doi.org/10.1039/c9mh00355j>.
- (354) Bertolazzi, S.; Gobbi, M.; Zhao, Y.; Backes, C.; Samori, P. Molecular Chemistry Approaches for Tuning the Properties of Two-Dimensional Transition Metal Dichalcogenides. *Chem. Soc. Rev.* **2018**, *47* (17), 6845–6888. <https://doi.org/10.1039/c8cs00169c>.
- (355) Mao, J.; Zhang, H.; Jiang, Y.; Pan, Y.; Gao, M.; Xiao, W.; Gao, H. J. Tunability of Supramolecular Kagome Lattices of Magnetic Phthalocyanines Using Graphene-Based Moiré Patterns as Templates. *J. Am. Chem. Soc.* **2009**, *131* (40), 14136–14137. <https://doi.org/10.1021/ja904907z>.

- (356) Zhang, H. G.; Sun, J. T.; Low, T.; Zhang, L. Z.; Pan, Y.; Liu, Q.; Mao, J. H.; Zhou, H. T.; Guo, H. M.; Du, S. X.; et al. Assembly of Iron Phthalocyanine and Pentacene Molecules on a Graphene Monolayer Grown on Ru(0001). *Phys. Rev. B - Condens. Matter Mater. Phys.* **2011**, *84* (24), 245436. <https://doi.org/10.1103/PhysRevB.84.245436>.
- (357) Yang, K.; Xiao, W. D.; Jiang, Y. H.; Zhang, H. G.; Liu, L. W.; Mao, J. H.; Zhou, H. T.; Du, S. X.; Gao, H.-J. Molecule–Substrate Coupling between Metal Phthalocyanines and Epitaxial Graphene Grown on Ru(0001) and Pt(111). *J. Phys. Chem. C* **2012**, *116* (26), 14052–14056. <https://doi.org/10.1021/jp304068a>.
- (358) Tong, Q.; Chen, M.; Xiao, F.; Yu, H.; Yao, W. Interferences of Electrostatic Moiré Potentials and Bichromatic Superlattices of Electrons and Excitons in Transition Metal Dichalcogenides. *2D Mater.* **2021**, *8* (2), 025007. <https://doi.org/10.1088/2053-1583/abd006>.
- (359) Liu, T.; Troisi, A. What Makes Fullerene Acceptors Special as Electron Acceptors in Organic Solar Cells and How to Replace Them. *Adv. Mater.* **2013**, *25* (7), 1038–1041. <https://doi.org/10.1002/adma.201203486>.
- (360) Ramirez, I.; Causa', M.; Zhong, Y.; Banerji, N.; Riede, M. Key Tradeoffs Limiting the Performance of Organic Photovoltaics. *Adv. Energy Mater.* **2018**, *8* (28), 1703551. <https://doi.org/10.1002/aenm.201703551>.
- (361) Savoie, B. M.; Rao, A.; Bakulin, A. A.; Gelinas, S.; Movaghar, B.; Friend, R. H.; Marks, T. J.; Ratner, M. A. Unequal Partnership: Asymmetric Roles of Polymeric Donor and Fullerene Acceptor in Generating Free Charge. *J. Am. Chem. Soc.* **2014**, *136* (7), 2876–2884. <https://doi.org/10.1021/ja411859m>.
- (362) Wang, G.; Swick, S. M.; Matta, M.; Mukherjee, S.; Strzalka, J. W.; Logsdon, J. L.; Fabiano, S.; Huang, W.; Aldrich, T. J.; Yang, T.; et al. Photovoltaic Blend Microstructure for High Efficiency Post-Fullerene Solar Cells. To Tilt or Not to Tilt? *J. Am. Chem. Soc.* **2019**, *141* (34), 13410–13420. <https://doi.org/10.1021/jacs.9b03770>.
- (363) Dreher, M.; Günder, D.; Zörb, S.; Witte, G. Van Der Waals Bound Organic Semiconductor/2D-Material Hybrid Heterosystems: Intrinsic Epitaxial Alignment of Perfluoropentacene Films on Transition Metal Dichalcogenides. *Chem. Mater.* **2020**, *32* (20), 9034–9043. <https://doi.org/10.1021/acs.chemmater.0c03482>.
- (364) Xie, X. Y.; Liu, X. Y.; Fang, Q.; Fang, W. H.; Cui, G. Photoinduced Carrier Dynamics at the Interface of Pentacene and Molybdenum Disulfide. *J. Phys. Chem. A* **2019**, *123* (36), 7693–7703. <https://doi.org/10.1021/acs.jpca.9b04728>.
- (365) Canton-Vitoria, R.; Scharl, T.; Stergiou, A.; Cadranel, A.; Arenal, R.; Guldi, D. M.; Tagmatarchis, N. Ping-Pong Intercomponent Energy Transfer in Covalently Linked Porphyrin-MoS<sub>2</sub> Architectures. *Angew. Chemie Int. Ed.* **2019**.

- <https://doi.org/10.1002/anie.201914494>.
- (366) Canton-Vitoria, R.; Scharl, T.; Stergiou, A.; Cadranel, A.; Arenal, R.; Guldi, D. M.; Tagmatarchis, N. Ping-Pong Energy Transfer in Covalently Linked Porphyrin-MoS<sub>2</sub> Architectures. *Angew. Chemie Int. Ed.* **2020**, *59* (10), 3976–3981. <https://doi.org/10.1002/anie.201914494>.
- (367) Shan, H.; Yu, Y.; Zhang, R.; Cheng, R.; Zhang, D.; Luo, Y.; Wang, X.; Li, B.; Zu, S.; Lin, F.; et al. Electron Transfer and Cascade Relaxation Dynamics of Graphene Quantum Dots/MoS<sub>2</sub> Monolayer Mixed-Dimensional van Der Waals Heterostructures. *Mater. Today* **2019**, *24*, 10–16. <https://doi.org/10.1016/j.mattod.2019.01.015>.
- (368) Lien, D. H.; Uddin, S. Z.; Yeh, M.; Amani, M.; Kim, H.; Ager, J. W.; Yablonoitch, E.; Javey, A. Electrical Suppression of All Nonradiative Recombination Pathways in Monolayer Semiconductors. *Science (80-. )*. **2019**, *364* (6439), 468–471. <https://doi.org/10.1126/science.aaw8053>.
- (369) Cai, Y.; Zhou, H.; Zhang, G.; Zhang, Y.-W. Modulating Carrier Density and Transport Properties of MoS<sub>2</sub> by Organic Molecular Doping and Defect Engineering. *Chem. Mater.* **2016**, *28* (23), 8611–8621. <https://doi.org/10.1021/acs.chemmater.6b03539>.
- (370) Hus, S. M.; Ge, R.; Chen, P. A.; Liang, L.; Donnelly, G. E.; Ko, W.; Huang, F.; Chiang, M. H.; Li, A. P.; Akinwande, D. Observation of Single-Defect Memristor in an MoS<sub>2</sub> Atomic Sheet. *Nat. Nanotechnol.* **2021**, *16* (1), 58–62. <https://doi.org/10.1038/s41565-020-00789-w>.
- (371) Sharma, A.; Yan, H.; Zhang, L.; Sun, X.; Liu, B.; Lu, Y. Highly Enhanced Many-Body Interactions in Anisotropic 2D Semiconductors. *Acc. Chem. Res.* **2018**, *51* (5), 1164–1173. <https://doi.org/10.1021/acs.accounts.7b00504>.
- (372) Li, Y.; Stolte, N.; Li, B.; Li, H.; Cheng, G.; Pan, D.; Wang, J. Interface Charge-Transfer Induced Intralayer Excited-State Biexcitons in Graphene/WS<sub>2</sub> van Der Waals Heterostructures. *Nanoscale* **2019**, *11* (28), 13552–13557. <https://doi.org/10.1039/c9nr02862e>.
- (373) Yu, Y.; Bataller, A. W.; Younts, R.; Yu, Y.; Li, G.; Puretzky, A. A.; Geohegan, D. B.; Gundogdu, K.; Cao, L. Room Temperature Electron-Hole Liquid in Monolayer MoS<sub>2</sub>. *ACS Nano* **2019**, *13* (9), 10351–10358. <https://doi.org/10.1021/acs.nano.9b04124>.
- (374) Younts, R.; Bataller, A.; Ardekani, H.; Yu, Y.; Cao, L.; Gundogdu, K. Near Band-Edge Optical Excitation Leading to Catastrophic Ionization and Electron–Hole Liquid in Room-Temperature Monolayer MoS<sub>2</sub>. *Phys. status solidi* **2019**, *256* (11), 1900223. <https://doi.org/10.1002/pssb.201900223>.
- (375) Arp, T. B.; Pleskot, D.; Aji, V.; Gabor, N. M. Electron–Hole Liquid in a van Der Waals

- Heterostructure Photocell at Room Temperature. *Nat. Photonics* **2019**, *13* (4), 245–250. <https://doi.org/10.1038/s41566-019-0349-y>.
- (376) Deilmann, T.; Thygesen, K. S. Interlayer Trions in the MoS<sub>2</sub>/WS<sub>2</sub> van Der Waals Heterostructure. *Nano Lett.* **2018**, *18* (2), 1460–1465. <https://doi.org/10.1021/acs.nanolett.7b05224>.
- (377) Li, W.; Lu, X.; Dubey, S.; Devenica, L.; Srivastava, A. Dipolar Interactions between Localized Interlayer Excitons in van Der Waals Heterostructures. *Nat. Mater.* **2020**, *19* (6), 624–629. <https://doi.org/10.1038/s41563-020-0661-4>.
- (378) Gibertini, M.; Koperski, M.; Morpurgo, A. F.; Novoselov, K. S. Magnetic 2D Materials and Heterostructures. *Nat. Nanotechnol.* **2019**, *14* (5), 408–419. <https://doi.org/10.1038/s41565-019-0438-6>.
- (379) Arruda, L. M.; Ali, M. E.; Bernien, M.; Nickel, F.; Kopprasch, J.; Czekelius, C.; Oppeneer, P. M.; Kuch, W. Modifying the Magnetic Anisotropy of an Iron Porphyrin Molecule by an On-Surface Ring-Closure Reaction. *J. Phys. Chem. C* **2019**, *123* (23), 14547–14555. <https://doi.org/10.1021/acs.jpcc.9b03126>.
- (380) Hieringer, W.; Flechtner, K.; Kretschmann, A.; Seufert, K.; Auwärter, W.; Barth, J. V.; Görling, A.; Steinrück, H. P.; Gottfried, J. M. The Surface Trans Effect: Influence of Axial Ligands on the Surface Chemical Bonds of Adsorbed Metalloporphyrins. *J. Am. Chem. Soc.* **2011**, *133* (16), 6206–6222. <https://doi.org/10.1021/ja1093502>.
- (381) Wang, Y.; Li, X.; Zheng, X.; Yang, J. Spin Switch in Iron Phthalocyanine on Au(111) Surface by Hydrogen Adsorption. *J. Chem. Phys.* **2017**, *147* (13), 134701. <https://doi.org/10.1063/1.4996970>.
- (382) Tsukahara, N.; Minamitani, E.; Kim, Y.; Kawai, M.; Takagi, N. Controlling Orbital-Selective Kondo Effects in a Single Molecule through Coordination Chemistry. *J. Chem. Phys.* **2014**, *141* (5), 054702. <https://doi.org/10.1063/1.4890654>.
- (383) Granet, J.; Sicot, M.; Gerber, I. C.; Kremer, G.; Pierron, T.; Kierren, B.; Moreau, L.; Fagot-Revurat, Y.; Lamare, S.; Chérioux, F.; et al. Adsorption-Induced Kondo Effect in Metal-Free Phthalocyanine on Ag(111). *J. Phys. Chem. C* **2020**, *124* (19), 10441–10452. <https://doi.org/10.1021/acs.jpcc.9b11141>.
- (384) Wang, Y.; Li, X.; Yang, J. Electronic and Magnetic Properties of CoPc and FePc Molecules on Graphene: The Substrate, Defect, and Hydrogen Adsorption Effects. *Phys. Chem. Chem. Phys.* **2019**, *21* (10), 5424–5434. <https://doi.org/10.1039/C8CP07091A>.
- (385) de la Torre, B.; Švec, M.; Hapala, P.; Redondo, J.; Krejčí, O.; Lo, R.; Manna, D.; Sarmah, A.; Nachtigallová, D.; Tuček, J.; et al. Non-Covalent Control of Spin-State in Metal-Organic Complex by Positioning on N-Doped Graphene. *Nat. Commun.* **2018**, *9* (1), 1–9.

<https://doi.org/10.1038/s41467-018-05163-y>.

- (386) Dugay, J.; Aarts, M.; Gimenez-Marqués, M.; Kozlova, T.; Zandbergen, H. W.; Coronado, E.; Van Der Zant, H. S. J. Phase Transitions in Spin-Crossover Thin Films Probed by Graphene Transport Measurements. *Nano Lett.* **2017**, *17* (1), 186–193. <https://doi.org/10.1021/acs.nanolett.6b03780>.
- (387) Datta, S.; Cai, Y.; Yudhistira, I.; Zeng, Z.; Zhang, Y. W.; Zhang, H.; Adam, S.; Wu, J.; Loh, K. P. Tuning Magnetoresistance in Molybdenum Disulphide and Graphene Using a Molecular Spin Transition. *Nat. Commun.* **2017**, *8* (1), 1–8. <https://doi.org/10.1038/s41467-017-00727-w>.
- (388) Wu, J.; Liu, Y.; Liu, Y.; Liu, Y.; Cai, Y.; Zhao, Y.; Ng, H. K.; Watanabe, K.; Taniguchi, T.; Zhang, G.; et al. Large Enhancement of Thermoelectric Performance in MoS<sub>2</sub>/h-BN Heterostructure Due to Vacancy-Induced Band Hybridization. *Proc. Natl. Acad. Sci. U. S. A.* **2020**, *117* (25), 13929–13936. <https://doi.org/10.1073/pnas.2007495117>.
- (389) Zhu, X.; Guo, Y.; Cheng, H.; Dai, J.; An, X.; Zhao, J.; Tian, K.; Wei, S.; Cheng Zeng, X.; Wu, C.; et al. Signature of Coexistence of Superconductivity and Ferromagnetism in Two-Dimensional NbSe<sub>2</sub> Triggered by Surface Molecular Adsorption. *Nat. Commun.* **2016**, *7* (1), 1–8. <https://doi.org/10.1038/ncomms11210>.
- (390) Zou, C.; Cong, C.; Shang, J.; Zhao, C.; Eginligil, M.; Wu, L.; Chen, Y.; Zhang, H.; Feng, S.; Zhang, J.; et al. Probing Magnetic-Proximity-Effect Enlarged Valley Splitting in Monolayer WSe<sub>2</sub> by Photoluminescence. *Nano Res.* **2018**, *11* (12), 6252–6259. <https://doi.org/10.1007/s12274-018-2148-z>.
- (391) Seyler, K. L.; Zhong, D.; Huang, B.; Linpeng, X.; Wilson, N. P.; Taniguchi, T.; Watanabe, K.; Yao, W.; Xiao, D.; McGuire, M. A.; et al. Valley Manipulation by Optically Tuning the Magnetic Proximity Effect in WSe<sub>2</sub>/CrI<sub>3</sub> Heterostructures. *Nano Lett.* **2018**, *18* (6), 3823–3828. <https://doi.org/10.1021/acs.nanolett.8b01105>.
- (392) Slobodeniuk, A. O.; Basko, D. M. Spin–Flip Processes and Radiative Decay of Dark Intravalley Excitons in Transition Metal Dichalcogenide Monolayers. *2D Mater.* **2016**, *3* (3), 035009. <https://doi.org/10.1088/2053-1583/3/3/035009>.
- (393) Shao, B.; Schüler, M.; Schönhoff, G.; Frauenheim, T.; Czycholl, G.; Wehling, T. O. Optically and Electrically Controllable Adatom Spin–Orbital Dynamics in Transition Metal Dichalcogenides. *Nano Lett.* **2017**, *17* (11), 6721–6726. <https://doi.org/10.1021/acs.nanolett.7b02785>.
- (394) Vanorman, Z. A.; Bieber, A. S.; Wieghold, S.; Nienhaus, L. A Perspective on Triplet Fusion Upconversion: Triplet Sensitizers beyond Quantum Dots. *MRS Commun.* **2019**, *9* (3), 924–935. <https://doi.org/10.1557/mrc.2019.115>.

- (395) Steinleitner, P.; Merkl, P.; Graf, A.; Nagler, P.; Watanabe, K.; Taniguchi, T.; Zipfel, J.; Schüller, C.; Korn, T.; Chernikov, A.; et al. Dielectric Engineering of Electronic Correlations in a van Der Waals Heterostructure. *Nano Lett.* **2018**, *18* (2), 1402–1409. <https://doi.org/10.1021/acs.nanolett.7b05132>.
- (396) Wu, L.; Chen, Y.; Zhou, H.; Zhu, H. Ultrafast Energy Transfer of Both Bright and Dark Excitons in 2D van Der Waals Heterostructures beyond Dipolar Coupling. *ACS Nano* **2019**, *13* (2), 2341–2348. <https://doi.org/10.1021/acsnano.8b09059>.
- (397) Zhang, X. X.; Cao, T.; Lu, Z.; Lin, Y. C.; Zhang, F.; Wang, Y.; Li, Z.; Hone, J. C.; Robinson, J. A.; Smirnov, D.; et al. Magnetic Brightening and Control of Dark Excitons in Monolayer WSe<sub>2</sub>. *Nat. Nanotechnol.* **2017**, *12* (9), 883–888. <https://doi.org/10.1038/nnano.2017.105>.
- (398) Ishii, A.; Machiya, H.; Kato, Y. K. High Efficiency Dark-to-Bright Exciton Conversion in Carbon Nanotubes. *Phys. Rev. X* **2019**, *9* (4), 41048. <https://doi.org/10.1103/PhysRevX.9.041048>.
- (399) Purcell-Milton, F.; McKenna, R.; Brennan, L. J.; Cullen, C. P.; Guillemeney, L.; Tepliakov, N. V.; Baimuratov, A. S.; Rukhlenko, I. D.; Perova, T. S.; Duesberg, G. S.; et al. Induction of Chirality in Two-Dimensional Nanomaterials: Chiral 2D MoS<sub>2</sub> Nanostructures. *ACS Nano* **2018**, *12* (2), 954–964. <https://doi.org/10.1021/acsnano.7b06691>.
- (400) Suzuki, N.; Wang, Y.; Elvati, P.; Qu, Z. B.; Kim, K.; Jiang, S.; Baumeister, E.; Lee, J.; Yeom, B.; Bahng, J. H.; et al. Chiral Graphene Quantum Dots. *ACS Nano* **2016**, *10* (2), 1744–1755. <https://doi.org/10.1021/acsnano.5b06369>.
- (401) Zhang, H.; He, H.; Jiang, X.; Xia, Z.; Wei, W. Preparation and Characterization of Chiral Transition-Metal Dichalcogenide Quantum Dots and Their Enantioselective Catalysis. *ACS Appl. Mater. Interfaces* **2018**, *10* (36), 30680–30688. <https://doi.org/10.1021/acsami.8b10594>.
- (402) Snegir, S.; Dappe, Y. J.; Kapitanchuk, O. L.; Coursault, D.; Lacaze, E. Kinked Row-Induced Chirality Driven by Molecule-Substrate Interactions. *Phys. Chem. Chem. Phys.* **2020**, *22* (14), 7259–7267. <https://doi.org/10.1039/c9cp06519a>.
- (403) Tahara, K.; Kubo, Y.; Hashimoto, S.; Ishikawa, T.; Kaneko, H.; Brown, A.; Hirsch, B. E.; Feyter, S. De; Tobe, Y. Porous Self-Assembled Molecular Networks as Templates for Chiral-Position-Controlled Chemical Functionalization of Graphitic Surfaces. *J. Am. Chem. Soc.* **2020**, *142* (16), 7699–7708. <https://doi.org/10.1021/jacs.0c02979>.
- (404) Naaman, R.; Paltiel, Y.; Waldeck, D. H. Chiral Molecules and the Electron Spin. *Nat. Rev. Chem.* **2019**, *3* (4), 250–260. <https://doi.org/10.1038/s41570-019-0087-1>.

- (405) Ben Dor, O.; Yochelis, S.; Radko, A.; Vankayala, K.; Capua, E.; Capua, A.; Yang, S. H.; Baczewski, L. T.; Parkin, S. S. P.; Naaman, R.; et al. Magnetization Switching in Ferromagnets by Adsorbed Chiral Molecules without Current or External Magnetic Field. *Nat. Commun.* **2017**, *8* (1), 1–7. <https://doi.org/10.1038/ncomms14567>.
- (406) Alpern, H.; Katzir, E.; Yochelis, S.; Katz, N.; Paltiel, Y.; Millo, O. Unconventional Superconductivity Induced in Nb Films by Adsorbed Chiral Molecules. *New J. Phys.* **2016**, *18* (11), 113048. <https://doi.org/10.1088/1367-2630/18/11/113048>.
- (407) Sangwan, V. K.; Hersam, M. C. Neuromorphic Nanoelectronic Materials. *Nat. Nanotechnol.* **2020**, *15* (7), 517–528. <https://doi.org/10.1038/s41565-020-0647-z>.
- (408) Liu, X.; Hersam, M. C. 2D Materials for Quantum Information Science. *Nat. Rev. Mater.* **2019**, *4* (10), 669–684. <https://doi.org/10.1038/s41578-019-0136-x>.

## 7. Vita

### Email

samuelamsterdam2015@u.northwestern.edu

### Education

2015 – 2021 **Ph.D.** in Chemistry, Northwestern University

2011 – 2014 **B.S.** in Chemistry, Carnegie Mellon University

### Publications

**Amsterdam, S. H.**; Marks, T. J.; Hersam, M. C. Leveraging Molecular Properties to Tailor Mixed-Dimensional Heterostructures beyond Energy Level Alignment. *J. Phys. Chem. Lett.* **2021**, 4543-4557.

**Amsterdam, S. H.**; LaMountain, T.; Stanev, T. K.; Sangwan, V. K.; López-Arteaga, R.; Padgaonkar, S.; Watanabe, K.; Taniguchi, T.; Weiss, E. A.; Marks, T. J.; Hersam, M. C.; Stern, N. P. Tailoring the Optical Response of Pentacene Thin Films via Templated Growth on Hexagonal Boron Nitride. *J. Phys. Chem. Lett.* **2021**, 12 (1), 26-31.

**Amsterdam, S. H.**; Stanev, T. K.; Zhou, Q.; Wang, L.; Irgen-Gioro, S.; Padgaonkar, S.; Murthy, A. A.; Sangwan, V. K.; Dravid, V. P.; Weiss, E. A.; Chan, M.; Darancet, P.; Hersam, M. C.; Stern, N. P.; Marks, T. J. Mechanistic Investigation of MoS<sub>2</sub> Defect Photoluminescence Quenching by Adsorbed Metallophthalocyanines. **2021**, *in preparation*.

LaMountain, T.; Nelson, J.; Lenferink, E. J.; **Amsterdam, S. H.**; Murthy, A. A.; Marks, T. J.; Dravid, V. P.; Hersam, M. C.; Stern, N. P. Valley-Selective Optical Stark Effect of Exciton-Polaritons in a Monolayer Semiconductor. **2021**, *in review*.

Zhu, W.; Spencer, A. P.; Mukherjee, S.; Alzola, J. M.; Sangwan, V. K.; **Amsterdam, S. H.**; Swick, S. M.; Jones, L. O.; Heiber, M. C.; Herzing, A. A.; Li, G.; Stern, C. L.; DeLongchamp, D. M.; Kohlstedt, K. L.; Hersam, M. C.; Schatz, G. C.; Wasielewski, M. R.; Chen, L. X.; Facchetti, A.; Marks, T. J. Crystallography, Morphology, Electronic Structure, and Transport in Non-Fullerene/Non-Indacenodithienothiophene Polymer: Y6 Solar Cells. *JACS.* **2020**, 142, 14532-14547.

Swick, S. M.; Alzola, J. M.; Sangwan, V. K.; **Amsterdam, S. H.**; Zhu, W.; Jones, L. O.; Powers-Riggs, N.; Facchetti, A.; Kohlstedt, K. L.; Schatz, G. C.; Hersam, M. C.; Wasielewski, M. R.; Marks, T. J. Fluorinating  $\pi$ -Extended Molecular Acceptors Yields Highly Connected Crystal

Structures and Low Reorganization Energies for Efficient Solar Cells. *Adv. Ener. Mater.* **2020**, 2000635.

**Amsterdam, S. H.**; Stanev, T. K.; Zhou, Q.; Lou, A. J. T.; Bergeron, H.; Darancet, P.; Hersam, M. C.; Stern, N. P.; Marks, T. J. Electronic Coupling in Metallophthalocyanine–Transition Metal Dichalcogenide Mixed-Dimensional Heterojunctions. *ACS Nano* **2019**, *13*, 4183-4190.

Padgaonkar, S.; **Amsterdam, S. H.**; Bergeron, H.; Su, K.; Marks, T. J.; Hersam, M. C.; Weiss, E. A. Molecular-Orientation-Dependent Interfacial Charge Transfer in Phthalocyanine/MoS<sub>2</sub> Mixed-Dimensional Heterojunctions. *J. Phys. Chem. C* **2019**, *123*, 13337-13343.

Gottlieb, E.; Kagalwala, H. N.; Mohin, J.; Budwal, N.; **Amsterdam, S.**; Lamson, M.; Matyjaszewski, K.; Bernhard, S.; Kowalewski, T. Common Carbons as Water-Reducing Catalysts in Photo-Driven Hydrogen Evolution with Nitrogen-Dependent Activity. *ChemNanoMat*. **2018**, *4*, 1039-1042.

Shastri, T. A.; Balla, I.; Bergeron, H.; **Amsterdam, S. H.**; Marks, T. J.; Hersam, M. C. Mutual Photoluminescence Quenching and Photovoltaic Effect in Large-Area Single-Layer MoS<sub>2</sub>-Polymer Heterojunctions. *ACS Nano* **2016**, *10*, 10573-10579.

Qiu, Y.; Worch, J. C.; Chirdon, D. N.; Kaur, A.; Maurer, A. B.; **Amsterdam, S.**; Collins, C. R.; Pintauer, T.; Yaron, D.; Bernhard, S.; Noonan, K. J. T. Tuning Thiophene with Phosphorus: Synthesis and Electronic Properties of Benzobisthiaphospholes. *Chem. – Eur. J.* **2014**, *20*, 7746-7751.

### **Honors and Awards**

National Defense Science and Engineering Graduate Fellowship (NDSEG) (2016)

Northwestern University Ryan Fellowship (2015)

Carnegie Mellon Department of Chemistry American Institute of Chemists Student Award (2015)

Phi Beta Kappa Honor Society (2015)

New York University Materials Research Science and Engineering Center Research Experience for Undergraduates Fellowship (NYU-MRSEC REU) (2014)